Dissertation

Submitted to the

Combined Faculty of Natural Sciences and Mathematics

Of the Ruperto Carola University Heidelberg, Germany

For the degree of

Doctor of Natural Sciences

Presented by

Jessica Michelle Devant, M.Sc.

From Darmstadt, Germany

Oral examination 29.06.2020

Deciphering structural variations within the norovirus capsid

Referees:

1st Examiner: Prof. Dr. Dr. Henri-Jaques Delecluse

2nd Examiner: Dr. Grant S. Hansman

Abstract

Norovirus is one of the most common agents associated with acute gastroenteritis. Despite its discovery 50 years ago, as of now there is no cure or treatment, and knowledge about the infection cycle of norovirus is still limited.

Using cryo-electron microscopy, we determined the structure of different clinically relevant GII.4 genotype virus like particles (VLPs), and an engineered version of GII.4 that is in use as vaccine candidate. Unexpectedly, we found that these empty particles were composed of 240 copies of the capsid protein instead of the typical 180. We could show that this conformation is only adopted by GII.4 VLPs, and that norovirus virions most likely assemble into T=3 icosahedral particles. Conversely, the capsid protein of GII.17, another genotype that has become clinically relevant in the last years, assembled into the characteristic T=3 icosahedral capsid.

Moreover, we characterized a panel of GII.4 specific Nanobodies and determined their binding sites and influence on particle integrity using cryo-EM. Several Nanobodies had a strong inhibition potential in surrogate assays against GII.4 VLPs, but cross-reactivity to other genotypes was low. Structures of Nanobody/VLP complexes revealed that the Nanobodies bound to a similar site on the lower part of the P domain. The structures showed that the P domains were flexibly rotated to distinct positions, but generally particle conformation remained intact.

Likewise, we worked on three GI.1 specific Nanobodies and found two Nanobodies with high inhibition potential. Importantly, we found that combination of Nanobody with the human milk oligosaccharide 2'FL was able to synergistically improve attachment inhibition of VLPs to histo-blood group antigens, suggesting the use of combinational treatment against norovirus infection.

In another study, we found that murine norovirus, which is commonly used as a model system for human norovirus, was undergoing severe structural rearrangements after incubation with ions, such as Mg^{2+} and Ca^{2+}. The normally extended P domains were collapsing onto the shell, accompanied by a rotational movement. Most likely, this movement is important to facilitate infection. Importantly, we also characterized a Nanobody that was binding to the lower part of the P domain, effectively inhibiting MNV infection by blocking this movement.

Taken together, these results gives insight on general norovirus structure and how noroviruses are interacting with antivirals and cofactors. Our research broadens the understanding of norovirus-internal differences and capsid flexibilities, and can ultimately aid in the development of a more effective treatment for norovirus infections.

Aims and objectives

Our main aim was to broaden the understanding of norovirus on a structural level. Here we focused on different targets:

1) Comparison of structures from different genotypes, based on intact VLPs.

2) Determine the structure of norovirus VLPs in complex with potential antivirals to characterize the influence the binding in context of the intact particle.

3) Solve the structure of norovirus capsids in complex with potential binding factors to shed light on how noroviruses are interacting with host cells.

Zusammenfassung

Norovirus-Infektionen sind eine der häufigsten Ursachen für akute Gastroenteritis. Trotz der Entdeckung des Norovirus vor fast 50 Jahren, gibt es bisher keine zugelassenen Impfungen oder Medikamente, und viele Fragen zum Infektionszyklus des Norovirus sind noch offen.

Mittels Kryo-Elektronenmikroskopie konnten wir die Struktur virus-ähnlicher Partikel des klinisch relevanten Stammes GII.4, sowie einer gentechnisch veränderten Variante (GII.4c) die derzeit als Impfstoffkandidat in klinischen Studien getestet wird, bestimmen. Überraschenderweise wurde hierbei festgestellt, dass die Partikel aus 240 Untereinheiten des Kapsidproteins VP1 bestanden, die Kapside wiesen somit eine T=4 ikosaedrische Symmetrie auf. Diese Morphologie wiederspricht der typischen Norovirus-Struktur, die aus nur 180 Untereinheiten assembliert und damit T=3 Symmetrie aufweist. Wir konnten zeigen, dass diese vergrößerte Struktur nur in Isolaten des GII.4 Stammes vorkommt und über einen weiten Zeitraum hinweg konserviert ist. Im Gegensatz dazu deuteten Versuche mit intakten GII.4 Viren darauf hin, dass diese in ein T=3 ikosaedrisches Kapsid assemblieren.

Weiterhin untersuchten wir Viruspartikel des GII.17 Genotyps, der in den letzten Jahren klinische Relevanz entwickelte. Hierbei fanden wir, dass dessen Kapsidprotein in Partikel mit der Norovirus-typischen T=3 ikosaedrischen Symmetrie assemblierte.

In einer weiteren Studie analysierten wir GI.1 spezifische konventionelle Antikörper sowie Einzeldomänenantikörper (Nanokörper). Interessanterweise konnten wir zeigen, dass eine Kombination aus einem inhibierenden Nanokörper und dem humanen Milchzucker 2'Fukosyllaktose synergistisch inhibierend wirkte. Dies könnte einen neuartigen Therapieansatz gegen Norovirus darstellen.

In einer weiteren Studie charakterisierten wir GII.4 spezifische Nanokörper. Viele der getesteten Nanokörper waren in der Lage, die Bindung von Viruspartikeln an Histo-Blutgruppenantigene zu unterbinden, jedoch war die Kreuzreaktivität zu anderen Genotypen nur gering. Mittels Kryo-Elektronenmikroskopie wurde die Struktur von mehreren Nanokörpern im Komplex mit GII.4 Kapsiden gelöst, um deren Bindestelle zu bestimmen und den Einfluss der Bindung auf das Kapsid zu untersuchen. Interessanterweise banden alle Nanokörper an die untere Seite der P Domäne, trotz verschiedener Kreuzreaktivitäten. Weiterhin zeigten die Strukturen, dass die Affinität der Nanokörper stark genug ist, um die P Domäne in verschiedene Positionen zu bringen, die die volle Belegung aller Bindestellen erlaubten.

Das fünfte Kapitel beschäftigt sich mit strukturellen Variationen des murinen Norovirus, welches als Modellsystem für das humane Norovirus genutzt wird. Wurden diese Viren mit Kationen inkubiert, kollabierte die normalerweise gestreckte Verbindungsregion zwischen P- und S Domäne. Es gibt Hinweise dass diese Konformationsänderung notwendig ist, um eine effiziente Infektion zu ermöglichen. Weiterhin konnten wir einen Nanokörper identifizieren, der an der unteren Seite der P Domäne band und somit eine Infektion *in vitro* verhindern konnte. Unsere Ergebnisse deuten darauf hin, dass die Bindung des Nanokörpers den Kollaps der P Domäne verhindert, was eine Infektion unterdrückt.

Allgemein tragen die Ergebnisse dieser Studien dazu bei, strukturelle Variationen in der Norovirus Familie aufzuzeigen. Variationen können durch die Unterschiede zwischen den Stämmen oder auch durch die Interaktionen mit Bindungsfaktoren oder antiviralen Molekülen auftreten. Strukturelle Modifikationen des Kapsids innerhalb der Norovirus-Familie wurden bisher nur wenig untersucht; Informationen über Unterschiede und infektionsrelevante Konformationsänderungen können daher dazu beitragen, das Wissen über Norovirus-Infektionen zu erweitern und letztendlich effektive Prophylaxe- oder Behandlungsstrategien gegen Norovirus-Infektionen zu entwickeln.

Abbreviations

2'FL	2' fucosyllactose
Å	Ångstrom
AA	Amino acid
A-Tri	A-trisaccharide
Bp	Base pairs
CDR	Complementary determined regions
CTF	Contrast transfer fuction
CsCl	Cesium chloride
DNA	Deoxyribonucleic acid
DMEM	Dulbeccos modified eagle medium
E. coli	*Escherichia coli*
EDTA	Ethylenediaminetetraacetic acid
ELISA	Enzyme linked immunosorbent assay
EM	Electron microscopy
EMDB	Electron Microscopy Data Bank
FCV	Feline calicivirus
FSC	Fourier shell correlation
FUT	Fucosyltransferase
GCDCA	Sodium glycochenodeoxycholate
GFB	Gelfiltration buffer
h	Hour
HBGA	Histo-blood group antigens
HMO	Human milk oligosaccharides
IC_{50}	Half maximal inhibiton value
IgG	Immunoglobulin G
IPTG	Isopropyl -β -D-thiogalactopyranosid
kDa	Kilo Dalton
keV	Kilo electron volt
LB	Lysogeny broth
MAb	Monoclonal antibody
MBP	Maltose binding protein
min	Minute
MNV	Murine norovirus
NB	Nanobody
NV	Norovirus
OD	Optical density
ORF	Open reading frame
PBS	Phosphate-buffered saline
PBS-T	Phosphate-buffered saline –Tween
PCR	Polymerase chain reaction
PDB	Protein Data Bank
PGM	Porcine gastric mucin
RHDV	Rabbit hemorrhagic disease virus
RNA	Ribonucleic acid
s	Second
SDS-PAGE	Sodium dodecyl sulfate polyacrylamid gelelectrophoresis
SOC	Super optimal broth with catabolite repression
TAE	Tris-acetate-EDTA
TB	Terrific broth
TBS	Tris-buffered saline
TBS-T	Tris-buffered saline –Tween
TES	Tris-EDTA-Sucrose
Tris	Tris(hydroxymethyl)aminomethane
VHH	Variable domain of the heavy chain of heavy chain only antibodies
VLP	Virus-like particle
VP1	Viral protein 1
VP2	Viral protein 2
w/v	Weight/volume

Table of Contents

List of figures

List of tables

1. Introduction

1.1. Norovirus pathogenicity and symptoms

Noroviruses are non-enveloped viruses belonging to the *Caliciviridae* family that are the major cause of non-bacterial gastroenteritis outbreaks. Norovirus was first described after an outbreak in a school in Norwalk, Ohio in 1968 (1) and identified in 1972 (83). Norovirus is transmitted mainly through the fecal-oral route. Environmental transmissions also occur, via contaminated food, water or surfaces (4, 37, 215). Following a short incubation, the infection causes nausea, severe diarrhea, vomiting or fever (1). The illness can affect all age groups but is usually self-limiting, with symptoms resolving within three to five days (125). Nevertheless, norovirus infections are a severe threat for the young, elderly and immunocompromised. Moreover, it has been shown that patients can shed virions for more than two months after infection (4), and also asymptomatically infected individuals can shed virions (156). The virus is highly contagious, with only a few particles (<100) needed to cause the disease (205). Combined with its remarkable environmental stability, this makes the virus challenging to control, particularly in confined environments such as hospitals, nursing homes and cruise ships (138). Approximately 20% of all reported gastroenteritis cases are caused by norovirus (10). With 200,000 deaths per year, mainly due to complications caused by dehydration and malnutrition, human norovirus-associated infections are recognized as the most common cause of death from foodborne gastroenteritis (8, 32, 155).

1.2. Genome organization and variability within the *Caliciviridae*

Next to *Norovirus*, the *Caliciviridae* family contains 10 other genera that can infect a wide range of different species. Mammals can be infected by seven different genera, namely *Sapovirus, Lagovirus, Vesivirus*, *Nebovirus Valovirus, Recovirus* and *Norovirus* (217). *Norovirus* and *Sapovirus* are the only genera known to infect humans and cause outbreaks of acute gastroenteritis (149). Other genera have been shown to infect fish (*Minovirus* and *Salovirus*) or bird species (*Nacovirus* and *Bavorirus*).

The most studied non-human calicivirus is the murine norovirus (MNV). MNV was discovered in 2003 (85) and since then several genotypes have been described. MNV is classified in the *Norovirus* genus and shares several characteristics with human noroviruses, i.e. fecal-oral transmission; and certain strains caused mild diarrhea in mice (143). As a

pathogen, MNV has been detected in various research institutions and is one of the most prevalent viruses in mouse facilities (75, 142). One of the major differences between mouse and human norovirus is the genetic variability. MNV are more genetically stable than human noroviruses, with all genotypes segregated into a single genogroup (206). Due to the availability of well-established tissue culture and reverse genetics systems, MNV has become the main model system to study norovirus infection (223, 224).

Caliciviridae have a linear, single stranded positive sensed RNA genome of 7.3-8.5 kb with a 5' VPg (genome linked viral protein) cap and a polyadenylated tail at the 3' end (59).

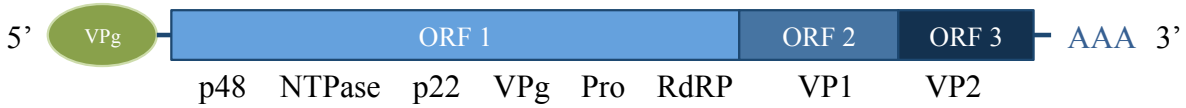

Figure 1-1 | Schematic representation of the norovirus genome. The genome is connected to VPg at the 5' end, and is polyadenylated at the 3' end. Usually, caliciviruses have 3 ORFs: ORF1 encodes six non-structural proteins as a polyprotein that is post-translationally cleaved. ORF2 and ORF3 encode for the major and minor capsid protein, respectively, termed VP1 and VP2.

The calicivirus genome usually contains three open reading frames (ORFs), designated as ORF1-3 (Figure 1-1). MNV contains an additional ORF4, which encodes for a virulence factor (137). ORF1 encodes for a polyprotein that is post-translationally cleaved into six nonstructural proteins [p48, NTPase, p22, VPg, 3C-like protease ($3CL^{pro}$) and RNA dependent RNA polymerase (RdRp)] (70). ORF2 encodes the major capsid protein VP1 that forms the capsid and ORF3 encodes the minor capsid protein VP2. VP2 is expressed in substoichiometric proportions of ~2-8 molecules per virion. So far, the role of VP2 has not been fully defined, but there is evidence for its involvement in capsid assembly and genome encapsidation (218). Moreover, studies suggested that the presence of VP2 enhances capsid stability and homogeneity in size (12), and in feline calicivirus (FCV), presence of VP2 was necessary to establish infection (32, 193).

Noroviruses undergo a high degree of genetic drift and new strains are emerging every other year (187). Currently, the *Norovirus* genus is divided into seven genogroups. Noroviruses are further classified into different genogroups and based on their capsid protein and polymerase sequence. To increase its genetic diversity, norovirus is known to recombine genetic segments from different genotypes and genogroups (47, 126).

Genogroup I (GI), GII and GIV can cause infections in humans. GI is only contagious to humans, but GII and GIV comprise genotypes that can also infect cats, dogs and pigs (216) (Figure 1-2).

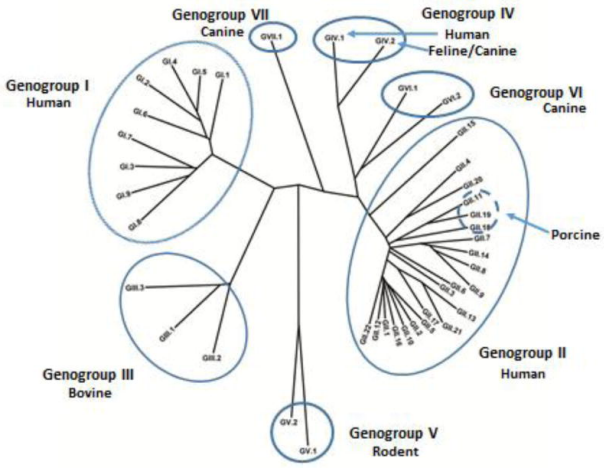

Figure 1-2 | Phylogenetic tree of *Norovirus*, based on the VP1 sequence. Most genogroups target distinct hosts, except GII and GIV, which target humans as well as pigs, cats and dogs, respectively. Figure adapted from (34).

Genogroup II is the most predominant group of noroviruses and is responsible for most reported cases all over the world. Within this genogroup, GII genotype 4 (GII.4) has caused multiple epidemics and therefore has been recognized as the most prevalent and clinically important genotype (42, 165). One reason for the predominance of this genotype could be the high genetic diversity of GII noroviruses, and in particular GII.4, that evolve much more rapidly than GI noroviruses, which exhibit a comparably stable genome (154). However, another GII genotype, GII.17, was found to cause major outbreaks, in mainly Asian countries (135, 151). Although GII.17 has already been discovered in 1978 (164), only in the last years this genotype has become prevalent. A single amino acid substitution permitted GII.17 variants to bind to histo-blood group antigens (HBGAs), which might have contributed to its high infectivity today (188). Moreover, one study suggested that the number of mutations in the GII.17 capsid gene per site and year was one order of magnitude higher than in other strains, which could support their fast emergence and spread (23). Recently, GII.17 outbreaks have been reported in regions outside Asia and epidemiologists speculate that the GII.17 genotype could become more predominant than GII.4 in the future (36, 146).

1.3. Structural organization of caliciviruses

Several structures of *Caliciviridae* members have been solved using X-ray crystallography and cryo-EM (13, 24, 31, 69, 162). These studies revealed a common overall architecture of the capsid. In general, calicivirus capsids are composed of 180 copies of the ~58 kDa major capsid protein VP1, and exhibit T=3 icosahedral symmetry.

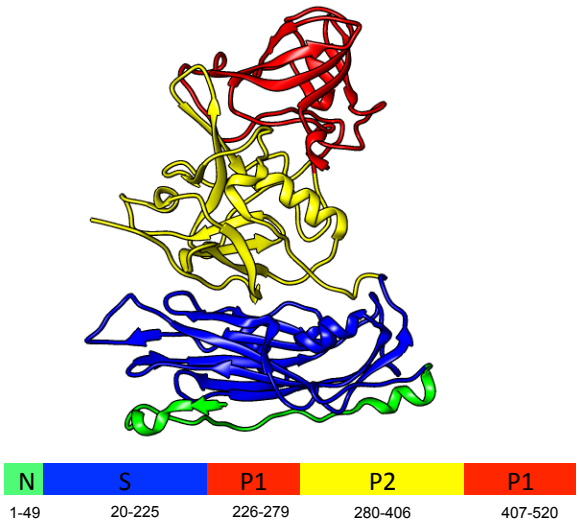

Figure 1-3 | Ribbon model of GI.1 VP1, colored by domains. The N-terminus (aa 1-49) is colored green, the S domain (aa 20-225) is colored in blue, and the P domain, separated in P1 (aa 226-279 and 407-520) and P2 (aa 280-406) is colored in red and yellow, respectively.

VP1 can be divided into two different domains, a shell (S) domain and a protruding (P) domain (162) (Figure 1-3). The S domain is the N-terminal part of the protein (aa 1-225 in GI.1 numbering) and forms a continuous scaffold surrounding the RNA genome (129). The S domain is relatively rigid and exhibits the lowest sequence variability between the different genotypes. Structurally, the S domain adopts an eight-stranded β-barrel fold. It is connected to the P domain by a flexible hinge region that is typically 12-14 amino acids in size. In the assembled capsid, the P domain is the outermost part of VP1, forming dimeric, arch-like protrusions (Figure 1-4). These characterize the typical norovirus shape and are even visible in negative stain EM images (84). The protrusions are arranged in a symmetrical manner on the capsid, giving the impression of 32 cup-shaped depressions that gave the virus family their name (calyx, lat.: cup) (62). The P domain can be further subdivided into the P1 and P2 subdomains. P1 is the lower part of the P domain, and P2 is an insertion into P1 and constitutes the outermost part of the capsid that contains cofactor and receptor binding sites (19, 21, 29, 66, 90). Most amino acid variations are occurring in this surface exposed subdomain under the pressure of herd immunity, which contributes to the high antigenic variability of noroviruses. The general fold of the P domains is conserved among the *Caliciviridae* and is unique for this virus family (162). The P1 domain forms three β-strands at the N-terminal part, followed by an antiparallel four-stranded β-sheet, and a single α-helix. The P2 domain is formed by a β-barrel composed of six antiparallel β-strands. These are connected by loops that are varying in size between the different genotypes. Isolated

P domains can be expressed in *E. coli,* where they retain biological functions, such as binding to HBGAs (199).

To adopt T=3 icosahedral symmetry, VP1 forms three quasiequivalent conformers that are termed A, B and C. These give rise to two different kinds of dimers, A/B and C/C. 60 A/B dimers are located at the quasi two-fold icosahedral symmetry axes, whereas the C subunits assemble into 30 C/C dimers, positioned at the strict two-fold axes. Usually, the S domains of the A/B dimer are bent, whereas the S domains of the C/C dimer are in a flat conformation. This difference in packing is commonly observed in other T=3 viruses and is thought to enable the virus to form a contiguously closed shell.

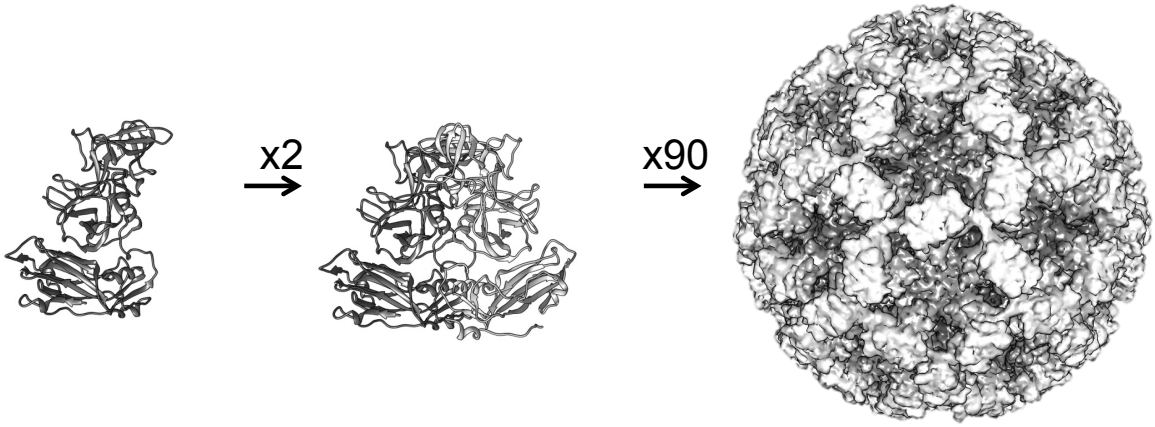

Figure 1-4 | Model of the calicivirus structure, using the example of norovirus GI.1. The major capsid protein VP1 dimerizes, which leads to the formation of the typical arch like structures. 90 dimers assemble into an intact T=3 icosahedral capsid. The figure was generated from the crystal structure of the GI.1 VLP (1IHM).

Remarkably, there is evidence that this T=3 icosahedral form is not the only conformation in which the virus capsid can exist. In different studies, smaller VLPs have been reported, presumably of T=1 icosahedral symmetry, and composed of only 60 VP1 copies. Such particles have been observed in human stool samples (202), as well as in a recently developed enteroid cell culture system for norovirus propagation (49).

Despite the similarity in the general structure, there are still several differences observable between structures of different calicivirus genotypes (Figure 1-5). The first high-resolution structure of a human norovirus VLP, GI.1, was solved in 1999 (162). In this model, the hinge region formed a loop and the P domain was located in close vicinity to the S domain. In contrast, the P domains of GII.10 VLPs are rotated in respect to the GI.1 P domain, and floating 15 Å over the shell, raised by an extended hinge region (69). Elevated P domains appear to be common in caliciviruses, as MNV, FCV and rabbit hemorrhagic disease virus (RHDV) share this conformational arrangement (86, 87).

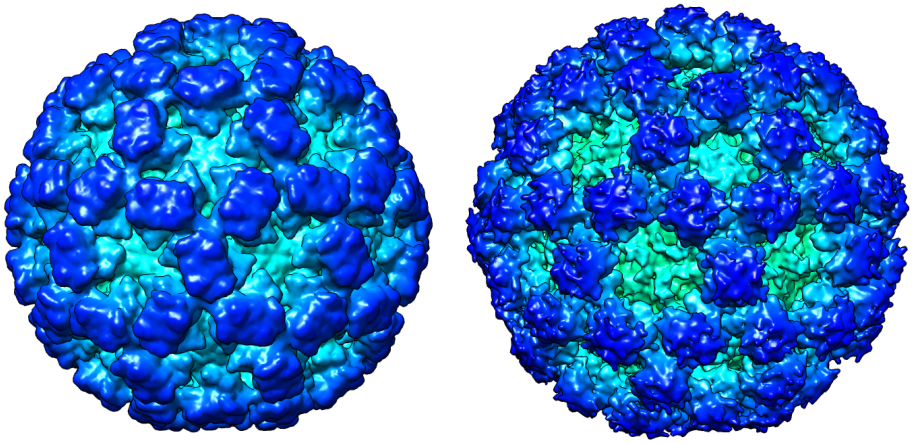

Figure 1-5 | Capsid structure of GI.1 (left) and GII.10 (right). The P domains (dark blue) of GI.1 are lowered onto the shell (turquoise), whereas the GII.10 P domain dimers (blue) are floating above the shell. The figures of the particles were generated from the crystal structure of the GI.1 VLP (PDB: 1IHM) and the cryo-EM structure of the GII.10 VLP (EMDB-5374).

Recently it has been shown that MNV P domains are structurally rearranging from the elevated form to a collapsed form after incubation with bile acid, a binding cofactor known to enable efficient infection (183). This suggests that the raised and lowered conformations could be interchangeable and are not characteristic features for certain genogroups. Nevertheless, it is yet undetermined why this collapse is crucial for infection. Moreover, structural information on human noroviruses is still scarce and it is not known, whether these conformational changes are occurring in human norovirus as well, or if this is a specific feature of MNV.

1.4. Norovirus infection cycle

So far, not all steps in the norovirus cycle of infection have been elucidated (Figure 1-6). As only recently a human norovirus cell culture system has been developed (49), most studies on the life cycle have been done on related surrogate systems, such as MNV or FCV. What is known, is that the virus uses HBGAs and bile acids as cofactors for attachment (49, 200). Bile salts are cholesterol derivates that are produced in the liver and secreted into the gastrointestinal tract. They are involved in regulation of cellular metabolism, maintenance of intestinal homeostasis or facilitation of lipid absorption (27). For several caliciviruses [MNV (150), FCV (128) and Hom-1 Calicivirus (194)], proteinaceous receptors have been identified. Therefore, it is likely that human noroviruses similarly engage a protein receptor, which remains to be identified.

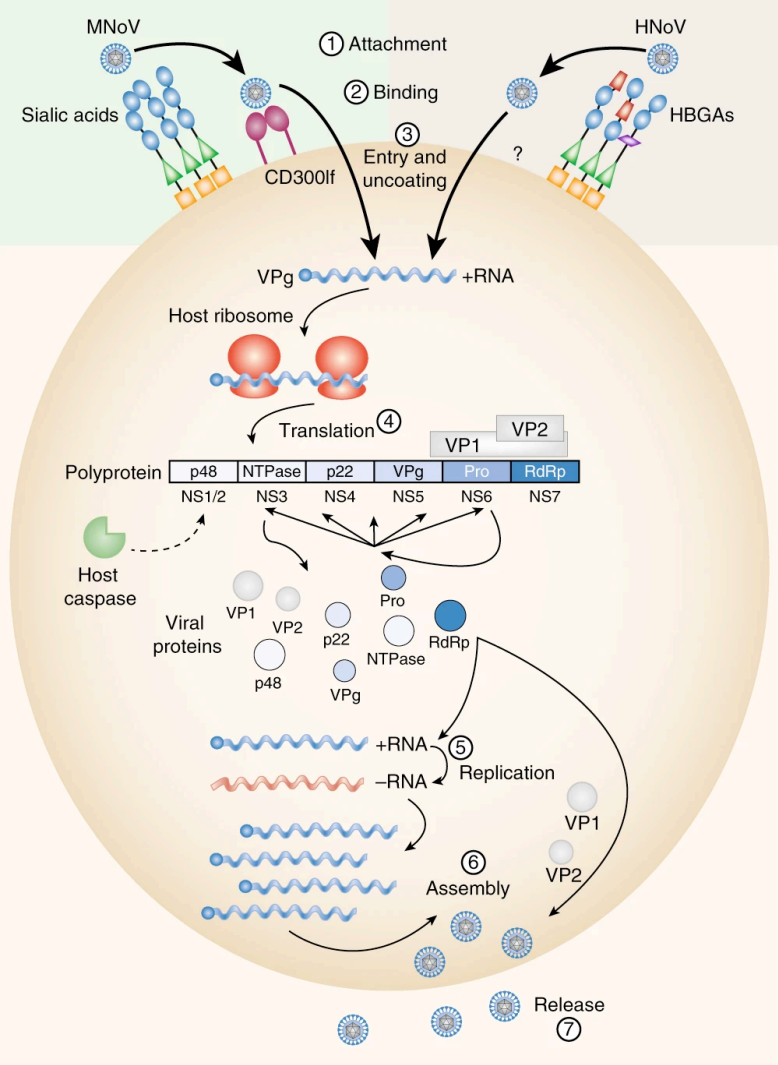

Figure 1-6 | Model of the norovirus infection cycle. The virus is attaching to the cell, using either proteinaceous receptors or cofactors, such as HBGAs. MNV attaches to sialic acids and CD300lf, human norovirus attaches to HBGAs. Cell entry and uncoating mechanisms are so far unknown. The genome linked protein VPg initiates RNA translation. The viral RdRp replicates RNA and the replicated genomes are either used for further translation in the replication complex or packaged into the newly forming capsids. Figure adapted from (71).

The virion is internalized though a presently unknown mechanism, and subsequently uncoated and disassembled. FCV has been shown to have a both clathrin- and pH-dependent entry pathway (186, 197). Conversely, MNV cell entry is dependent on cholesterol and dynamin, but independent of pH (57, 158). Only for FCV, a model of genome release is available so far. Cryo-EM studies revealed that upon receptor binding, 12 VP2 molecules assemble at a single three-fold axis to form a portal vertex (32). Further structural rearrangements lead to the formation of a pore in the shell, and the hydrophobic tip of the VP2 molecules is thought to facilitate membrane penetration, to allow subsequent release of the RNA. VPg, an RNA-attached, nonstructural protein, recruits host translational factors to initiate the translation of the viral RNA that takes place in the cytoplasm of the host cell. Genomic RNA is used as the

template for initial translation of the nonstructural proteins (207). After synthesis of the nonstructural proteins, the replication of the genome occurs via the RdRp in replication complexes. Thereby, also subgenomic +RNA is produced that is utilized for translation of the structural proteins VP1 and VP2 (168). VP1 and VP2 are encapsidating the accumulated genomic RNA to form new virions, which are released in a yet unknown manner.

1.5. Histo-blood group antigens and their role in norovirus infections

The attachment of a virus to its host cell is a crucial step in the infection cycle. HBGAs serve as binding cofactors for human noroviruses and this interaction was shown to be necessary to establish norovirus infection. HBGAs are carbohydrate-based antigens that include the ABO- and Lewis antigens. HBGAs are present on red blood cells, epithelial and endothelial cells as part of the glycocalyx, but can also occur soluble in most bodily fluids, such as saliva, milk or blood, except the cerebrospinal fluid. HBGAs are synthesized in a stepwise manner, by addition of monosaccharides to precursor molecules by various glycosyltransferases (Figure 1-7). The variances in activity of these enzymes contribute to the great variety of carbohydrates that make up the individual HBGA composition. These glycosyltransferases are part of three major gene families, the ABO-, secretor- and Lewis family. The simplest antigens are the H antigens, which are specific for blood group O. H antigens are produced by two distinct fucosyltransferases, FUT1 and FUT2, which add a fucose in an α-1,2-linkage to various precursor disaccharides. 20% of Europeans and Northern Americans are homozygous recessive for an inactivating nonsense mutation in the FUT2 gene, making them so-called nonsecretors (133). This phenotype is characterized by the lack of ABH antigens on cell surfaces and in bodily fluids. The H antigens are substrates for A- or B-glycosyltransferases, which convert their substrate to A- or B antigens, by addition of an α-1,3-linked N-acetylgalactosamine or galactose, respectively. Fucosylation of N-acetylglucosamine by FUT3 converts ABO antigens into Lewis antigens. Differential expression of HBGAs in individuals is highly associated with susceptibility towards various infectious diseases and noroviruses were the first viral human pathogen for which HBGA dependence was discovered (29). It is known that numerous pathogens attach to HBGAs and the interplay between these pathogens and this group of antigens is thought to have facilitated the HBGA diversity (78, 132).

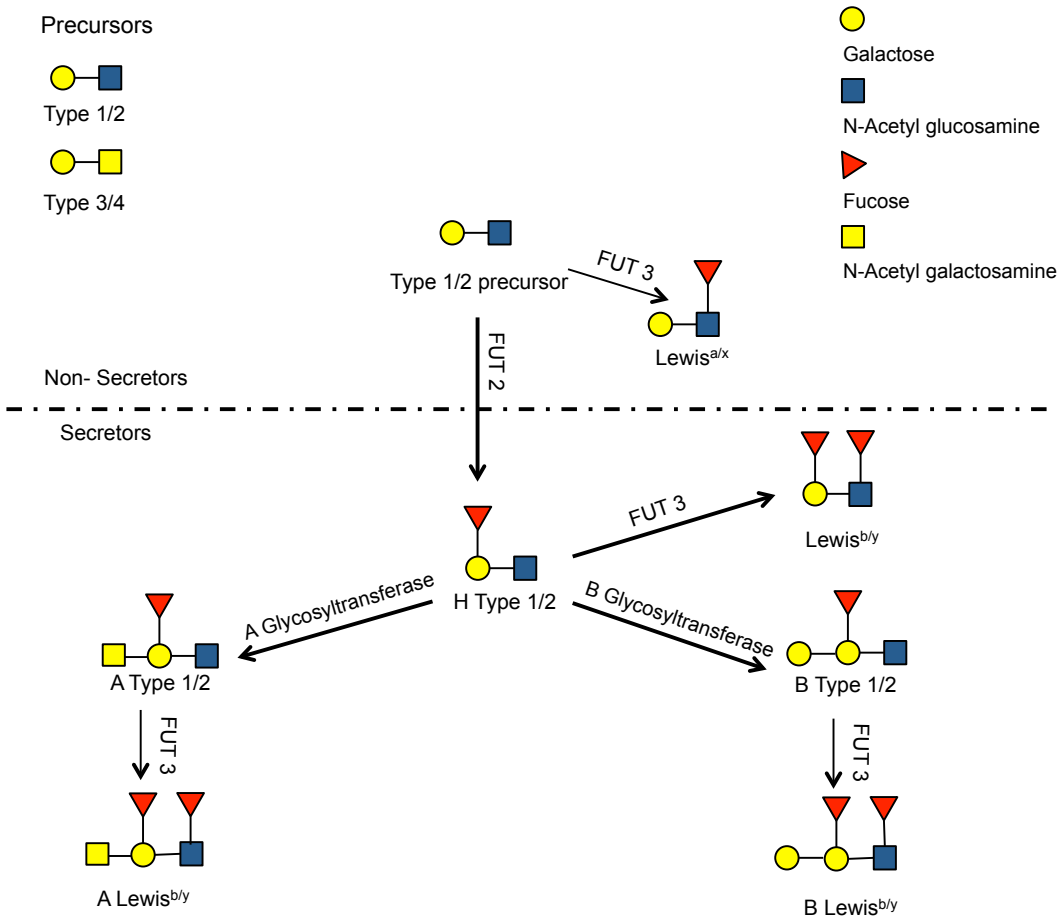

Figure 1-7 | HBGA synthesis pathway, at the example of type 1/2 HBGAs. HBGAs are assembled from galactose (yellow circle), N-acetyl glucosamine (blue square), fucose (red triangle) and N-acetylgalactosamine (yellow square). Nonsecretors lack the FUT2 enzyme and can only synthesize the smallest Lewis antigens. In secretor positive individuals, FUT2 fucosylates the precursors, to produce the H-type antigen. A- or B glycosyltransferases can modify the H antigen to form A- and B antigens, respectively. FUT3 can add fucose to the N-acetylglucosamine, of H-, A- and B type antigens, producing Lewis antigens.

Several studies provided proof that different norovirus genotypes exhibit distinct HBGA binding patterns. People with blood group O were shown to be more susceptible towards infection with GI noroviruses, whereas individuals with blood group B were partially immune against GI infection (78, 115). In contrast, GII noroviruses have a broader binding profile and do not discriminate between different blood groups (76). GII.4 genotypes in particular are promiscuous concerning the HBGA usage, a fact that could contribute to their prevalence (77). It has been suggested that GII.4 not only alters its antigenic landscape to evade herd immunity, but also adapts its HBGA binding pattern to allow infection of previously immune populations (117).

The differences in specificity between GI and GII viruses can be explained by the distinct binding modes. In both genogroups, HBGA binding exclusively involves residues of the P2 domain. However, GI noroviruses detect HBGAs through a binding site located on a single

P domain monomer, whereas GII noroviruses contain a distinct binding site for HBGAs at the dimeric interface of the P domain dimer, involving residues from both VP1 molecules in a dimer (19, 21, 29). This binding site preferentially recognizes α-fucose, thereby explaining the broad binding range (29, 201) Furthermore, studies indicated that the secretor status plays a crucial role in sensitivity towards norovirus infection: Secretor negative individuals with a non-functioning FUT2 allele were resistant to norovirus infection in challenge studies and *in vitro* assays (22, 55, 78, 116).

Also for other members of the *Caliciviridae,* HBGA interaction has been reported. For example RHDV bound H- and B type antigens (177) and Tulane virus was able to detect B type antigens (50). Additionally, MNV and FCV are able to detect sialic acids, which are HBGA related ligands, indicating that carbohydrate binding is a common feature within the *Caliciviridae* (198, 203).

1.6. Potential inhibitors for norovirus infection

So far, no antivirals against norovirus infection have been approved. Potential antivirals could target different steps in the viral replication cycle, such as attachment, cell entry, genome release, replication and translation, or assembly and release of virions. As many of these steps are still poorly characterized in norovirus, attachment to HBGAs has been one of the prime targets in past efforts to develop antivirals. A lot of work is done for example on the discovery of potentially inhibiting norovirus-specific antibodies. A wide array of different monoclonal antibodies (mAbs) have been described to block the VLP attachment to HBGAs in surrogate assays (3, 119, 221), and in a recent study, one of those antibodies was shown to be neutralizing in cell culture (102). One problem however, is the limited cross-reactivity of many antibodies, which often restricts their potential as effective antivirals. In addition to antibodies, other compounds, such as citrate (68, 100) or small molecule compounds with a cyclopenta-a-dimethyl phenanthrene-base structure (233), can interfere with HBGA binding.

Other targets in the norovirus life cycle have also been studied, such as the RdRp. Compounds targeting the RdRp can be divided into nucleoside analogues that bind the active site and non-nucleoside inhibitors. One example is 2’ C-methylcitidine, a nucleoside analogue that has also been studied in other viruses and was able to inhibit norovirus RdRp (170, 171). Moreover, the protease (NS6) also presents a valuable target and therefore also has been the subject of numerous inhibitor studies. Rupintrivir, an antiviral originally developed against rhinovirus was able to effectively inhibit norovirus protease (172).

The only compound that has finished phase II clinical trials is nitazoxanide (NTZ). In these phase II clinical trials, treatment with this compound led to a reduced length of the disease (174). Nevertheless, other studies claim that NTZ is ineffective against norovirus (88). Moreover, the mechanism for norovirus inhibition by NTZ is not identified yet. Additionally, several studies suggested that natural compounds could inhibit norovirus, such as theaflavins (147) or curcumin (232) but for most of these compounds the inhibition mechanism is unknown. Generally, there are several promising candidates, but with most of them only in preclinical development, more studies on potential norovirus inhibitors are urgently needed.

1.6.1. Norovirus inhibition by human milk oligosaccharides

Another large group of compounds that has been shown to have an inhibiting effect on norovirus are the human milk oligosaccharides (HMOs). HMOs are a family of diverse unconjugated glycans that constitute approximately 20% of the carbohydrate content of human milk, with up to 20 g/l in colostrum (211). Usually, HMO concentrations in human milk are between 5-20 g/l (16), making it the third most abundant compound, after lactose and lipids.

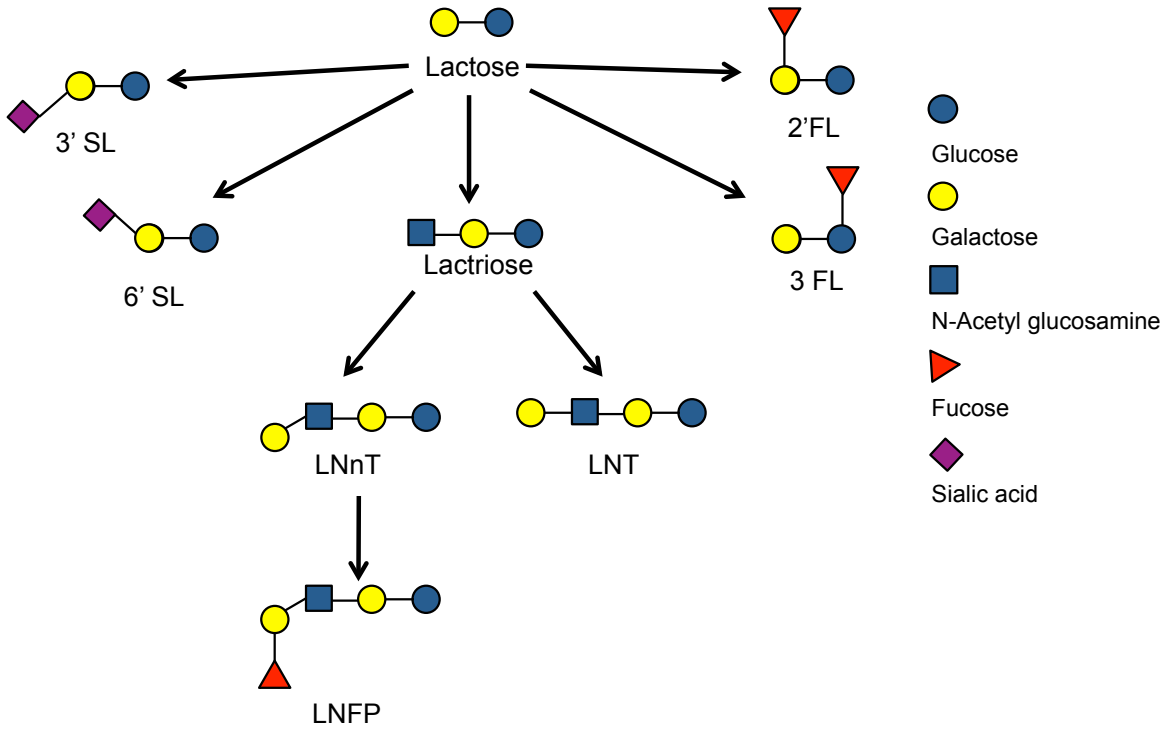

Figure 1-8 | Schematic representation of a section of the HMO synthesis pathway. HMOs are assembled from glucose (blue circle), galactose (yellow circle), N-acetylglucosamine (blue square), fucose (red triangle) and sialic acid (purple diamond). All HMOs are based on lactose. Fucosyltransferases can add fucose to either glucose or galactose and produce 2' fucosyllactose (2'FL) or 3 FL. Lactose can be sialyated, to e.g. produce 3' sialyllactose (3'SL) or 6'SL. Addition of N-acetyl glucosamine to lactose forms lactriose, which can further be processed to Lacto-N-tetraose (LNT) or Lacto-N-neotetraose (LNnT). Further fucosylation produces Lacto-N-fucopentaose (LNFP). This figure represents only a small section of the HMO production pathway, as ~150 different HMOs are known today.

So far, ~150 HMOs have been described (96, 195, 227, 228). The wide variety of HMOs is produced by specific glycosyltransferases in the mammary gland. These enzymes use lactose as acceptor molecule to add various glycosylgroups, as e.g. fucose, galactose, N-acetylneuraminic acid or N-acetylglucosamine (95) (Figure 1-8).

Not every woman is synthesizing the same set of oligosaccharides. Instead, the HMO production is dependent on the expression of different glycosyltransferases and therefore is comparable to blood group characteristics. Similar to what has been described for HBGAs, nonsecretor women do not produce α1-2-fucosylated HMOs, as for example 2' fucosyllactose (2'FL). Therefore, the Lewis blood group and secretor status not only influences the blood type, but also the composition of human milk (108).

Interestingly, HMOs are not digested by infants, instead they pass the digestive tract (48). HMOs exhibit prebiotic effects (65), but also have a high potential to function as antimicrobials, e.g. by prevention of pathogen attachment to host cells (113, 141).

It even has been shown that children that were fed with HMOs had a lower incidence of diarrhea (140). Therefore, many studies focus on the potential of HMOs as prospective antivirals, e.g. for norovirus. HMOs are structurally similar to HBGAs, and can act as cofactor decoys, to block binding sites and inhibit cell attachment. In fact, 2'FL was able to bind to the HBGA binding sites of both GI and GII noroviruses (i.e. GI.1, GII.10, GII.17) and inhibit the attachment to HBGAs in surrogate assays (98, 220). 2'FL is one of the most common HMOs in human milk, and studies suggested that it is safe for consumption in infants at least up to 20 g/l (35).

1.6.2. Nanobodies and norovirus inhibition

Antibodies are glycoproteins that are involved in the immune response. Mammalian immunoglobulin G (IgG) consists of four polypeptide chains, two identical light (L) chains and two heavy (H) chains, forming the typical Y structure (Figure 1-9). The L chains consist of two, the H chains of four distinct domains. At the end of each chain is the variable region that is responsible for antigen binding. In contrast, camelids, such as alpacas or llamas, or cartilaginous fish, are producing immunoglobulins that are lacking the light chain- so-called heavy chain-only antibodies (53, 63, 67). The heavy chain comprises two constant regions and the antigen-binding domain VHH, connected by a linker region (67).

The most variable parts of the VHH domain are the three complementary determining region (CDR) loops that are responsible for epitope attachment. Single domain antibodies (Nanobodies) are engineered proteins, derived from the antigen-binding domain VHH.

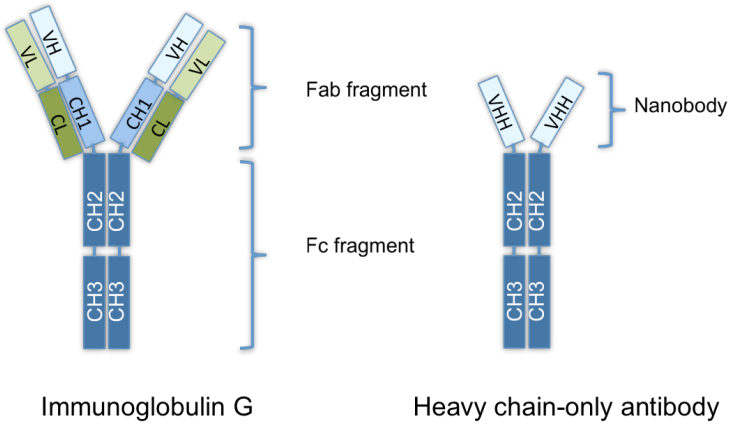

Figure 1-9 | Schematic representation of a conventional antibody (Immunoglobulin G) and a heavy chain-only antibody. Both types of antibodies have constant regions 2 and 3 (CH2/3). IgG consists of another constant region of the heavy chain (CH1) and of the light chain (CL) and variable regions of both light and heavy chains (VL and VH). In contrast, the heavy chain-only antibody only contains a single variable domain, termed VHH.

These single domain antibodies have unique qualities and several advantages over conventional antibodies. Nanobodies bind epitopes, with high affinities in the nano- to picomolar range (124). Usually, Nanobodies have a molecular weight of 12-15 kDa, making them markedly smaller than common IgG antibodies (~150 kDa). Therefore, Nanobodies can bind to hidden epitopes that would be occluded for the larger antibodies. Moreover, structural analysis has shown that often the CDR regions of Nanobodies are longer than the CDR regions of antibodies from most other mammals (179), giving them the possibility to bind to cavities or clefts (33). Nanobodies are only weakly immunogenic *in vivo,* and they exhibit strong tissue penetration (190). Furthermore, Nanobodies have superior biophysical properties compared to conventional antibodies, for example higher solubility and increased stability when exposed to high temperature, extreme pH, or protease treatment (46, 109, 212). They can also easily be fused to various tags and produced in *E. coli* in high yields, which lowers the production costs substantially (105).

Due to their versatility, Nanobodies have a wide use of potential applications, as diagnostic tools for detection of proteins and microorganisms (159, 209), as therapeutic tools against infections (79, 210) or other diseases like Alzheimer's (110). Nanobodies are also currently studied in their function as potential norovirus antivirals. GII.10 specific antibodies have been found to broadly inhibit the attachment of VLPs to HBGAs (101), and their efficacy could

even be proven in human cell culture (unpublished results). As Nanobodies are considered as save for humans, development of norovirus specific Nanobodies could be a promising approach for production of norovirus antivirals or prophylaxis.

1.7. Development of a norovirus vaccine – attempts and difficulties

Next to studies on antivirals, there are increasing efforts to develop a vaccine against norovirus. Effective active immunization would have the advantage that it can be administered prophylactically to prevent viral infection, disease and spread. A vaccine against rotavirus, another gastroenteritis-causing virus, has been developed and implemented with great success in many countries. In fact, since this vaccine is in use, norovirus has replaced rotavirus as the viral agent that is responsible for most gastroenteritis outbreaks in children in many places (20, 72).

Most of the efforts to develop a norovirus vaccine are based on VLPs. VLPs have been shown to be highly immunogenic and safe compared to live attenuated viruses, as they are replication-incompetent. Recombinant VLPs are commonly used as effective agent in other vaccines, for example against human papillomavirus or hepatitis B (104, 136).

There are several challenges hampering the development of an effective norovirus vaccine. One problem is the high antigenic diversity between the genotypes, therefore protection against newly emerging strains could be limited. Moreover, vaccine efficacy might be especially low in high-risk populations, namely the elderly and immunocompromised, due to impaired immune functions in those patients.

As GII.4 is the genotype most commonly associated with outbreaks, vaccine development is mostly directed towards this genotype. Several vaccine candidates that have entered clinical trials use norovirus VLPs in either single formulations or multivalent formulations, with VLPs from different genotypes to broaden efficiency. Efforts to produce a norovirus vaccine include e.g. a mixture of GI.3 and GII.4 VLPs, with rotavirus VP6 as adjuvant that has completed phase I of clinical trials (14, 131), or a single dose, orally administered vaccine containing recombinant adenovirus serotype 5 vectors expressing norovirus GI.1 VP1 (92). The most advanced norovirus vaccine candidate is currently in production by Takeda Pharmaceuticals, and is in phase II clinical trials. This vaccine candidate is bivalent, based on VLPs of GI.1 and GII.4, and is administered intramuscularly (153, 208). In order to confer immunity against several prevalent GII.4 strains, a consensus sequence was designed (GII.4c),

from sequences of three different GII.4 isolates (2006a Yerseke, 2006b Den Haag and 2002 Houston) (153). In first tests, this vaccine was able to induce the production of antibodies that were able to detect GI.1, GII.1, GII.3 and GIV.1 noroviruses (153). However, even though the vaccine was able to elicit broadly reactive antibodies, the vaccine was only associated with modest decreases in severity of the disease. Moreover, neither the duration nor the incubation time to symptom onset could be reduced, and the vaccination failed to significantly reduce the incidence of the illness (10). Another important factor of an effective vaccine is the duration of its protective efficacy. A recent study found that, even though the seroresponse stayed above the baseline when compared to the placebo recipients, the antibody titers waned strongly over a year (5).

Binding of noroviruses to HBGAs at the cell surface was proven to be necessary for infection, therefore, antibodies that are able to block this interaction have been found to correlate with protection against infection (166, 178). One study on mice has shown that immunization with GI VLPs did not elicit HBGA blocking antibodies against GII noroviruses (130). Furthermore, in a human cross-challenge study, patients were immune to the same norovirus genotype, but not to unrelated norovirus strains, implying limited cross-protection after infection (230) Conversely, in a recent clinical trial a multivalent VLP vaccine was able to raise broadly reactive antibodies (120).

Overall, the norovirus vaccines that are in testing can potentially elicit virus-specific antibody responses, and no adverse effects to the vaccines have been observed. Nevertheless, the low levels of efficacy, combined with problems of limited long-term immunity and cross-reactivity among genotypes indicate that still a lot of research is needed on the way towards a highly efficient norovirus vaccine. One potential solution, inspired by the recent progress in the influenza and HIV field, could be to identify and characterize conserved epitopes on the norovirus capsid to advance the structure-based design of novel immunogens.

1.8. Structure determination of proteins - cryo-EM and single particle analysis

Cryo-Electron microscopy (cryo-EM) is a tool to determine the structure of proteins and macromolecular complexes, without the need to crystallize the sample. This is especially of advantage for large complexes and proteins that are complicated to crystallize. With new technological advancements it is now possible to obtain models at near atomic resolution (106). In all types of microscopy, the achievable resolution is influenced by the wavelength of

the chosen radiation. In electron microscopy, this aspect is removed as limiting factor for resolution, as the wavelength of an electron, accelerated by 300 keV, is 0.02 Å.

Nevertheless, resolution was limited in the past, as samples had to be stained and dehydrated in order to provide contrast and limit electron damage. Staining was done by treatment with a heavy metal salt solution, such as uranyl acetate. Negatively stained samples are limited by the granularity of the stain, leading to a maximum achievable resolution of ~20 Å (148). This was overcome when a method was developed to vitrify water in liquid ethane, where the water is frozen rapidly to prevent ice crystal formation (28, 45, 204). A further advantage of this method is that it keeps the particles hydrated and in a near native state.

In EM, electrons are used as radiation source that are scattered by the object. Depositing electrons in a biological sample however destroys the sample over time. To minimize this damage, imaging is done at liquid nitrogen temperatures, leading to a six-fold decrease in damage compared to ambient temperatures (45). To further prevent damage and preserve high resolution information, the electron dose is kept at a low rate (58). This leads to a low signal to noise ratio, as biological macromolecules scatter electrons only weakly. Therefore, imaging is performed under slightly defocused conditions. Defocusing introduces differences in the scattered and unscattered rays, resulting in visible contrast, but also causes loss of information at different spatial frequencies and phase reversals. The influence of microscope imperfections and defocusing can be described by the contrast transfer function (CTF). During processing of the data, the distortions that are introduced can be corrected computationally to obtain the undistorted image and restore the correct phases at all spatial frequencies.

In the single particle approach, first a purified sample is needed, with homogenous, identical particles in random orientations on the grid. Then, a large number of projection images of the protein are collected, to generate a 3D reconstruction of the 2D projections (Figure 1-10). During micrograph acquisition, the images get blurred by beam induced motion, stage drift and charging events. To restore high-resolution information, the micrographs are acquired as movies and the individual frames are aligned relative to one another. After movie alignment, CTF correction is performed. In this step, a model is fitted to the measured CTF of the micrograph, to recover CTF parameters and determine the actual defocus of the image. On the corrected micrographs, particles are picked either manually or in an automated or semi-automated fashion. The first step of sorting is usually 2D classification. Particles are

clustered into homogenous subsets, containing the protein in different views and exclude broken particles or falsely picked noise.

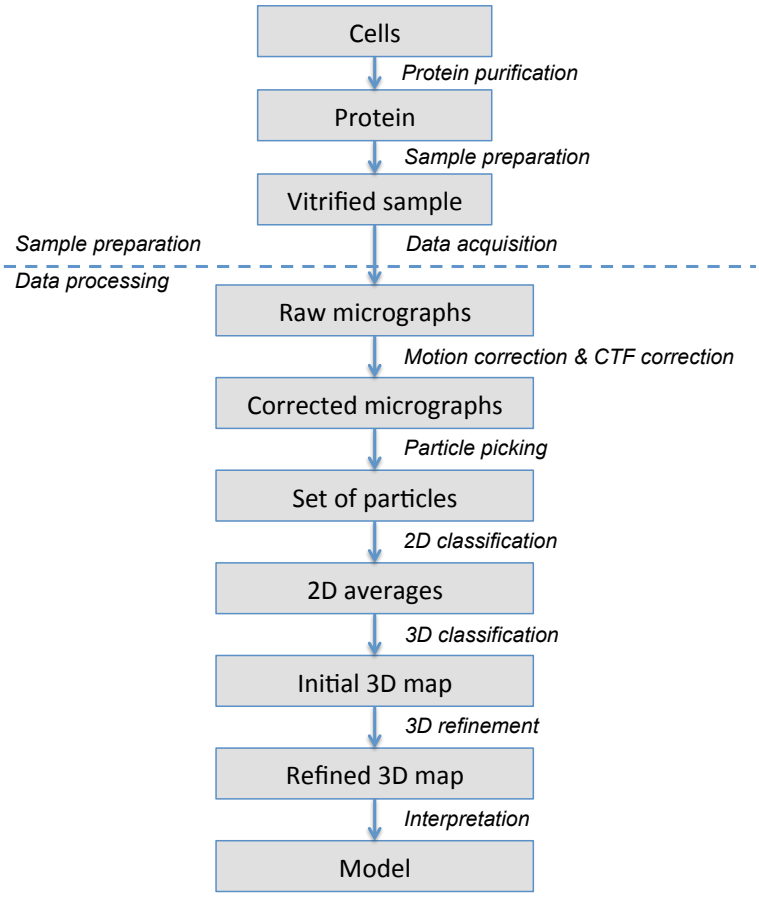

Figure 1-10 | Workflow for structural analysis using single particle cryo-EM. First, protein is purified and vitrified on an EM grid. 2D projections of the protein are acquired at the microscope. These raw images first need to be corrected using motion - and CTF correction. Particles are picked from the corrected micrographs and 2D classification is done, to sort intact from damaged particles or falsely picked noise. For further sorting and to generate an initial 3D map of the protein, 3D classification is done. A subset of particles is used for refinement of the map, to generate a high-resolution structure of the protein. If the resolution allows, the density can be used to build a model of the protein.

In this step, the particle images are compared with class averages and assigned to the class with the best cross-correlation. Then a new set of class averages is computed and the process is repeated over several iterations. 2D classification is followed by a 3D classification by the projection matching technique. In this step, 3D re-projections of the 2D templates are calculated and used to match the experimental 2D particles. After sorting, 3D models are generated and used as the new templates in the following iteration. For generation of a 3D reconstruction from 2D images, one takes advantage of the projection slice theorem: The Fourier transform of each 2D projection is a slice through the Fourier transform of the 3D object. From the intersection of two 2D transforms in 3D Fourier space one can assign relative orientations of the single particles that are needed to build the 3D model. After

determination of the relative angles between the 2D class averages, a 3D model can be reconstructed, using either a real space- or Fourier space-based model, depending on the used processing suite. After a subset of sufficient homogeneity has been selected, these particles are refined to high resolution. In the gold standard method, the dataset is separated into two independent halves that are refined independently to prevent overestimation of the resolution (73). For both datasets, a density is computed. A Fourier shell correlation (FSC) curve is generated by calculation of the correlation coefficient within the resolution shells that were extracted from the Fourier transforms of the two volumes. In single particle cryo-EM, the resolution of the structure is defined as the spatial frequency at a certain FSC cut-off. There are different values used, most commonly an FSC value of 0.5, or 0.143, the latter value being selected on an attempt to enable comparison of EM and crystallographic models (173).

2. Material

Table 2-1 | Used chemicals

Chemicals	Company
2’ Fucosyl-lactose	Jennewein Biotechnologie GmbH
A-Trisaccharide	Dextra
Agarose	Carl Roth
Ampicillin	Sigma-Aldrich
BLOTTO	Bio-Rad Laboratories
Blue White Select Screening Reagent	Sigma-Aldrich
Bromphenol blue	Alfa Aesar
Calcium chloride	Sigma-Aldrich
Cesium chloride	Sigma-Aldrich
Dulbeccos Modified Eagle Medium (DMEM)	Gibco
Dulbeccos Phosphate Buffered Saline (DPBS)	Gibco
Detection Reagent 1 and 2 (Western Blot)	Thermo Scientific
DMSO	Sigma-Aldrich
DNA loading dye purple (6x)	New England BioLabs
EDTA	Thermo Fisher Scientific
Effectene Transfection Reagent	Qiagen
Ethanol	Sigma-Aldrich
Ethidium bromide	BioRad
Ex-Cell 405 Serum-Free Medium	Sigma-Aldrich
EZ-Link™ Sulfo-NHS-LC-Biotin	Thermo Fisher Scientific
Fetal Bovine Serum	Sigma-Aldrich
GCDCA	Sigma-Aldrich
GelCode Blue protein stain	Thermo Fisher Scientific
Gel loading dye purple 6X	New England BioLabs
Gentamycin	Thermo Fisher Scientific
Glucose	Sigma-Aldrich
GlutaMAX	Gibco
Glycerol	Sigma-Aldrich
H_2O_2	Sigma-Aldrich
Hydrochloric acid, 37%, fuming	Merck
Imidazole	Sigma-Aldrich
Isopropanol	Sigma-Aldrich
Isopropyl-β-D-thiogalactopyranosid	Carl Roth
Kanamycin	Carl Roth
LB agar plates	VWR Chemicals
LB broth (Luria/Miller), granulated	Carl Roth
Lipofectamine 2000	Invitrogen
Magnesium-Chloride solution, 1M	Serva
Mini-Protean TGX Precast Gels (4-15%)	BioRad
Natriumchloride	Carl Roth
Natriumhydroxide	Gruessing
Ni-NTA agarose	Sigma-Aldrich
o-Phenylenediamine dihydrochloride	Sigma-Aldrich

Chemicals	Company
Opti-Mem medium	Gibco
PAGE ruler prestained protein ladder	Sigma-Aldrich
PBS 10x powder	Medicago
Penicillin-Streptomycin	Sigma-Aldrich
Phosphate-Citrate buffer tablets	Sigma-Aldrich
Porcine gastric mucin (PGM) type III	Sigma-Aldrich
Puromycin	Gibco
Sf900II SFM (1X)	Gibco
Skim milk powder	Sigma-Aldrich
Sucrose	Sigma-Aldrich
S.O.C medium	Invitrogen
Tetracyclin	VWR International
Terrific Broth (TB-) medium powder	Carl Roth
Trans-Blot Turbo 5x Transfer Buffer	BioRad
Tris-acetate EDTA (TAE) 50x	Carl Roth
Tris-Glycine-SDS 10x	Fisher BioReagents
Trizma hydrochloride solution	Sigma-Aldrich
Trypan blue	BioRad
Tween-20	Sigma-Aldrich
Uranyl acetate	Serva
β-mercaptoethanol	Sigma-Aldrich
Water, sterile filtered, suitable for cell culture	Sigma-Aldrich

Table 2-2 | Used equipment

Equipment and Materials	Company
0.6/1 grids, Cu/Rh, 300 mesh	Quantifoil
1.2/1.3 grids, Cu/Rh, 300 mesh	Quantifoil
96-well maxisorp plates	Nunc
Accublock mini	Labnet
Accu-jet pro pipet boy	Brand
Äkta prime plus	GE Healthcare
AVANTI J-26 XP centrifuge	Beckman Coulter
Beckman Optima LE 80K	Beckman Coulter
Beckman MaxE Ultracentrifuge	Beckman Coulter
Centrifuge 5418	Eppendorf
Centrifuge 5430R	Eppendorf
ChemiDoc	BioRad
Cell Counting slides, Dual Chamber	BioRad
Dialysis Cassettes (slide-a-lyzer)	Thermo Fisher Scientific
DMi1 Light Microscope	Leica
Ecotron Incubator	Infors
Erlenmeyer Flasks	Corning
Erlenmeyer Flask 500 ml	Corning
Filter Paper No.1	Whatman
Gradient master 108	Biocomp
GloMax Explorer	Promega
HiLoad 26/600 Superdex 200 pg	GE Healthcare

Equipment and Materials	Company
HiLoad 26/600 Superdex 75 pg	GE Healthcare
HiPrep 26/60 Sepahcryl S-500 HR	GE Healthcare
iMark Microplate Absorbance Reader	BioRad
Immunowash Microplate Washer	Bio-Rad
Mini Protean Tetra System Apparatus	BioRad
MultiA grids, Cu/Rh, 300 mesh	Quantifoil
MultiTron incubator	Infors
Nanodrop Lite	Thermo Fisher Scientific
OD600 DiluPhotometer	Implen
Rotor JLA 8.1	Beckman Coulter
Rotor JA 25.5	Beckman Coulter
Rotor SW 40	Beckman Coulter
Rotor SW 56	Beckman Coulter
Rotor Ti45	Beckman Coulter
Rotor TLA 55	Beckman Coulter
Shaker DRS-12	NeoLab
Stirred Water Bath WB-4MS	BioSan
Stirrer C-MAG HS10	IKA
Thermomixer Comfort	Eppendorf
Tissue Culture Flask 25 cm2	Falcon
Tissue Culture Flask 175 cm2	Falcon
UP200HT Ultrasonic processor	Hielscher Ultrasonics
Vortex Genie 2	Scientifc Industries
Xplorer plus multipipettes	Eppendorf
Zetasizer Nano S	Malvern

Table 2-3 | *E. coli* strains

Name	Company
MAX efficiency DH10Bac Competent cells	Invitrogen
E. coli DH5α (chemically competent)	Invitrogen
E. coli WK6 (chemically competent)	Invitrogen
E. coli DB3.1 (chemically competent)	Invitrogen
E. coli BL21 (chemically competent)	Invitrogen

Table 2-4 | Cells for protein expression

Name	Company
HIGH FIVE ™	Thermo Fisher Scientific
HEK-293T	Sigma Aldrich
Sf9	Gibco

Table 2-5 | Commercial Kits

Name	Company
QIAprep Spin miniprep Kit	Qiagen
QIAquick Gel Extraction Kit	Qiagen
QIAquick PCR purification Kit	Qiagen

Table 2-6 | Enzymes

Name	Company
Gateway LR Clonase Enzyme Mix	Thermo Fisher Scientific
Phusion High-Fidelity PCR Master Mix	New England BioLabs
Restriction enzyme Bsp1407I	Thermo Fisher Scientific
Restriction enzyme BstEII	New England BioLabs
Restriction enzyme PstI	New England BioLabs
T4 DNA Ligase	New England BioLabs

Table 2-7 | Antibodies

Name	Company
Monoclonal HRP-conjugated goat α-His antibody	Sigma-Aldrich
Monoclonal HRP-conjugated goat α-mouse antibody	Thermo Fisher Scientific
Monoclonal HRP-conjugated goat α-rabbit antibody	Sigma-Aldrich
Polyclonal rabbit α-GII.10 VLP antibodies	In-house production at DKFZ
Polyclonal rabbit α-GII.4 VLP antibodies	In-house production at DKFZ
Precision Protein StrepTactin-HRP conjugate 5,000×	BioRad

Table 2-8 | Primers

Name	Sequence (5'-3')	Function
A6E	GATGTGCAGCTGCAGGAGTCTGGAGGAGG	PCR Nanobody
PMCF	GTAGTGCGGCCGCTGAGGAGACGGTGACCT	PCR Nanobody
Universal Forward	CGC CAG GGT TTT CCC AGT CAC GAC	Sequencing
Universal Reverse	TCACACAGGAAACAGCTATGAC	Sequencing

3. Methods

3.1. VLP expression and purification

3.1.1. Cloning of constructs with the Gateway cloning system

For the production of VLPs, bacmids were produced, containing the recombinant gene for VP1 or VP1/VP2, respectively (Table 3-1). The sequences were ordered from Invitrogen, in a pENTR221 vector. Using the Gateway cloning system, the desired insert was cloned into a pDEST8 vector. 1 µl of pENTR221 plasmid was mixed with 1 µl of pDEST8 plasmid, 6 µl water and 1.5 µl LR Clonase II enzyme mix and incubated for 1 h at RT. The reaction was stopped with proteinase K (10 minutes (min), 37 °C).

3-1 | Used norovirus genotypes for VLP production with accession code.

Genogroup	Name	Accession code	Protein
GI.1	West Chester	AY502016	VP1
GI.1	Norwalk	Q83884	VP1
GI.1	Norwalk	Q83884/Q83885	VP1/VP2
GI.2	Funabashi258	AB078335	VP1
GI.2	Southampton	L07418	VP1
GI.3	Kashiwa645	BD011871	VP1
GI.4	Chiba	AB042808	VP1
GI.11	#8	AB058547	VP1
GII.1	Hawaii Virus	U07611	VP1
GII.4	CHDC	ACT76142	VP1
GII.4	Saga	AB447457	VP1
GII.4	Sydney	K4LM89	VP1
GII.4	Sydney	K4LM89/K4LB50	VP1/VP2
GII.4	c	n.a.	VP1
GII.4	Yerseke	ABL74391	VP1
GII.10	Vietnam 026	AF504671	VP1
GII.17	Kawasaki	LC037415	VP1

3.1.2. Production and transformation of chemically competent *E. coli*

100 ml of LB media were inoculated with a competent *E. coli* preculture. Cells were incubated shaking at 37 °C until an optical density at 600 nm (OD_{600}) of 0.25-0.3 was reached. Following a 15 min cooldown on ice, cells were pelleted for 10 min at 3,300 ×g and resuspended in 40 ml ice cold 0.1 M $CaCl_2$. Cells were pelleted again and resuspended in 6 ml 0.1 M $CaCl_2$ with 15% glycerol. 100 µl of the mix were aliquoted into sterile microcentrifuge tubes, flash frozen in liquid nitrogen and kept at -80 °C.

E. coli DH5α, *E. coli* WK6, *E. coli* BL21, and *E. coli* DB3.1 were transformed using the heat shock method. Aliquots of chemically competent cells were thawed on ice and ~100 ng plasmid were added and incubated for 10 min. Heat shock was done at 42 °C for 45 s. After addition of 600 µl SOC medium, cells were incubated shaking for 1 h at 37 °C and 1,000 rpm. Following the regeneration period, cells were spun down for 2 min at 2,125 ×g, resuspended in 200 µl media and plated on LB Agar plates containing ampicillin. The ampicillin was added on the plates just prior to plating of the cells. Colonies were grown for ~18 h at 37 °C.

3.1.3. Transformation of E. coli MAX efficiency DH10Bac competent cells and bacmid preparation

The cloned plasmid (3.1.1) was used for transformation of *E. coli* DH5α (3.1.2). A single colony was grown in 4 ml LB with ampicillin at 37 °C over night. The plasmid was isolated with a QIAprep miniprep kit after manufacturers instructions and analyzed on an agarose gel, to verify presence of the insert. Positive plasmids were used for transfection of *E. coli* MAX efficiency DH10Bac cells for bacmid production.

60 µl of *E. coli* DH10Bac cells were aliquoted and 1 µl of plasmid was added. After incubation for 10 min on ice, cells were heat shocked for 45 s at 42 °C. 600 µl SOC medium were added and cells were regenerated shaking for 4 h at 37 °C. The cells were plated on LB plates with 50 µg/ml kanamycin, 10 µg/ml tetracycline, 6 µg/ml gentamycin and 40 µl blue/white select and grown for 28 h at 37 °C. White colonies were used to prepare an over night culture in LB with 50 µg/ml kanamycin, 10 µg/ml tetracycline, 6 µg/ml gentamycin. Bacmids were isolated using a QIAprep miniprep kit after manufacturers instructions and stored at 4 °C until transfection.

3.1.4. Production of recombinant baculoviruses

Sf9 cells were transfected with recombinant bacmid DNA encoding the protein of choice, using Effectene transfection reagent. Sf9 cells were seeded into a 6-well plate in 2 ml Sf900 medium. 90 µl EC buffer were mixed with 3.2 µl Enhancer and 8 µl bacmid DNA. 10 µl Effectene were added, mixed and incubated for 5-10 min at RT. When the cells were attached to the plate, old media was aspirated, and 1 ml of new Sf900 media was added. After the incubation, 1 ml Sf900 media was added to the transfection mix and pipetted drop wise onto the cells. Plates were incubated for 7 days at 28 °C. The supernatant and the cells were added to Sf9 cells in a T75 flask, to expand the baculovirus. After 5-7 days of incubation, the baculorvirus-containing supernatant was centrifuged 1057 ×g for 10 min to pellet residual cells, sterile filtered and stored at 4 °C.

3.1.5. Expression and purification of VLPs

If not stated otherwise, VLPs were produced using the baculovirus expression system. Supernatant of infected Sf9 cells, containing the baculovirus, was used for infection of High Five cells (ThermoFisher). 5 days post infection, cells and secreted baculoviruses were removed from the cell culture supernatant by two sequential centrifugation steps at 1057 ×g for 10 min and at 4,960 ×g for 1 h, respectively. Norovirus VLPs in the supernatant were pelleted by ultracentrifugation at 142,032.1 ×g for 2 h at 4 °C. After resuspension in PBS over night, the VLPs were subjected to CsCl gradient centrifugation (18-20 h, 4 °C, 121,780.9 ×g) for further purification. Afterwards, VLPs were pelleted again for 2 h at 71,680 ×g, and resuspended in PBS to remove the CsCl from the solution and concentrate the sample.

3.1.6. Sucrose density gradient centrifugation

Heterogeneous VLP samples were further purified using a sucrose gradient. The 15-45% w/v sucrose gradient was prepared with a gradient maker (Gradient master 10, Biocomp). 200 µl VLP sample were added onto the gradient and centrifuged for 2 h 154,693 ×g and 4 °C.

3.1.7. Generation of mammalian expression vectors

The plasmids used for VLP production in HEK-293T cells were provided by Dr. Stefan Pusch. The used plasmids were pMXs-puro, pDest-puro and pLEX-puro. All constructs contained AttR sequences for cloning with the Gateway cloning system, as described in 3.1.1. Empty vectors contained the *ccdB* gene, which is toxic for *E. coli* DH5α, so for amplification of the empty vectors, *E. coli* DB3.1 were used. To verify that the insert is in the plasmid, the pENTR221, the destination vector and the newly cloned vector were cut with restriction enzyme Bsp1407I and after incubation for 2 h at 37 °C, the cut plasmids were separated on an agarose gel. Positive clones showed DNA corresponding to the backbone of the destination vector and the insert of the pENTR221 vector (i.e. the gene of interest).

3.1.8. Propagation of HEK-293T cells

HEK-293T cells were cultured in Dulbeccos modified Eagles medium (DMEM), supplemented with 1% glutaMAX, 10% fetal bovine serum (FBS) and 1% streptomycin/penicillin, (DMEM complete). Cells were cultured adherent in T175 flasks at 37 °C and 5% CO_2 and passaged when 80-90% confluent.

3.1.9. Transfection of HEK-293T cells

The evening before transfection, $1.5x10^6$ cells/well were seeded into 6 well plates and incubated over night at 37 °C and 5% CO_2. Transfection was done using Lipofectamine 2000

transfection agent. 12 µl Lipofectamine and 2 µg plasmid were added to separate tubes containing 100 µl Opti-Mem Medium each. After incubation for 5 min at RT, the Lipofectamine-containing Opti-Mem was added to the tube containing the plasmid, then the mix was vortexed briefly and incubated for 20 min at RT. Following incubation, 1.5 ml DMEM complete was added. Media was aspirated from the cells and the media containing the transfection mix was added to the cells and incubated at 37 °C and 5% CO_2. After 4-6 h, media was aspirated and new DMEM complete was added. To obtain a stable cell line, cells were propagated in complete DMEM supplemented with 10 µg/ml puromycin starting 24 h post transfection, to maintain only cells containing the plasmid.

3.1.10. Expression and purification of VLPs expressed in HEK-293T cells

HEK-293T cells were transfected as described in 3.1.9 and grown in complete DMEM medium. After 5 days of VLP production, the cell culture supernatant and cells were collected. The cells were pelleted by centrifugation at 300 ×g for 10 min and resuspended in PBS buffer. The cells were lysed by sonication and resulting cell debris was spun down for 30 min at 4 °C and 7,500 ×g. VLPs were purified from the cleared cell lysate and the supernatant by ultracentrifugation and CsCl gradient centrifugation, as described in 3.1.5.

3.1.11. MNV virion production

Murine norovirus CW1 was propagated in RAW 264.7 cells. Cells were infected with the virus and grown for 5 days at 37 °C and 5% CO_2. Cells and medium were subjected to freeze/thaw cycles, and debris was removed by centrifugation for 20 min at 470 ×g. MNV virions were concentrated by ultracentrifugation for 2 h at 142032.1 ×g, resuspended in PBS over night and further purified in a CsCl gradient (121780.9 ×g, 18-20h). The gradient was fractionated and checked for presence of virions in negative stain electron microscopy (3.12.1). Fractions containing MNV were pooled and dialyzed into PBS.

3.2. Expression and purification of Nanobodies

3.2.1. Nanobody selection

Nanobodies were produced by the VIB Nanobody service facility, approved by the ethics commission of the Vrije University in Brussels. An alpaca was injected subcutaneously with purified VLPs. A VHH library was constructed from isolated lymphocytes and screened for VLP specific Nanobodies with a phage display. Three rounds of panning were performed and crude periplasmic extracts were analyzed for antigen specific Nanobodies using ELISA.

3.2.2. Generation of Nanobody expression constructs

The Nanobody constructs were obtained from the VIB Nanobody service facility in a pMECS vector. For expression, the sequences were subcloned into pHEC6c expression vector. The genes were amplified by PCR using PMCF and AGE primers (Table 2-8) that flank the Nanobody sequence on the pMECS vector. The amplified fragments were isolated using the QIAquick PCR purification kit. Fragments were digested with PFSI and BstEII enzymes for 1.5 h at 37 °C and cleaned up using the QIAquick PCR purification kit. The digested fragments were then ligated into the pHEN6c vector that has been cut with the same restriction enzymes. Ligation was done using the T4 ligase for 10 min at RT. 4 µl of the ligation mix were subsequently used for transformation of *E. coli* DH5α (3.1.2).

3.2.3. Sequencing

To verify the sequence of the cloned Nanobody constructs, sequencing service of GATC was used. Universal forward and universal reverse primers (Table 2-8) were used for sequencing. The obtained DNA sequence was analyzed using the Sequencher program.

3.2.4. Nanobody expression

E. coli WK6 cells were transformed as described in 3.1.2, using a pHEN6c vector encoding the Nanobody of interest with a C-terminal His-Tag. The day before expression, a preculture was inoculated in LB media with 100 µg/ml ampicillin and incubated over night at 37 °C and 250 rpm. The preculture was used to inoculate 1l of TB media supplemented with 100 µg/ml ampicillin, 2 mM $MgCl_2$ and 0.1% glucose the following day. Cells were grown at 37 °C and 250 rpm and growth was monitored by measuring the optical density at 600 nm (OD_{600}). Nanobody expression was induced with 1 mM IPTG after reaching an OD_{600} of 0.6-0.8 and cells were grown over night at 28 °C 250 rpm. Cells were harvested by centrifugation for 15 min at 4960 ×g and stored at -20 °C.

3.2.5. Nanobody purification

The cell pellet was thawed and 12 ml TES buffer per liter *E. coli* culture were added. After homogenization, 18 ml TES/4 buffer per liter *E. coli* culture was added and incubated for 30 min in batch to extract the Nanobodies from the periplasm. The cells were then subsequently centrifuged for 30 min at 39191 ×g and the supernatant containing the Nanobodies was incubated with Nickel-NTA (Ni-NTA) resin for 30 min under agitation at 4 °C. The Nanobodies were purified with a Ni-NTA affinity method. After three consecutive rounds of washing with 2 column volumes of 10 mM, 20 mM and 50 mM imidazole buffer, the Nanobodies were eluted using 250 mM imidazole buffer.

After overnight dialysis into gelfiltration buffer (GFB), the Nanobodies were further purified by size exclusion chromatography using a Superdex-200 or Superdex-75 column. The peak fractions were pooled, concentrated to 2-3 mg/ml with a centrifugal filter unit with 5 kDa cut-off, and stored at 4 °C.

Table 3-2 | Buffers for Nanobody purification.

Buffer	Ingredients
TES Buffer	0.2 M Tris-OH (pH 8.0), 0.5 mM EDTA, 0.5 M Sucrose
TES/4 Buffer	50 mM Tris-OH (pH 8.0), 0.125 mM EDTA, 0.125 M Sucrose
10 mM Imidazole Wash Buffer	20 mM Tris-OH (pH 7.6) 0.2 M NaCl, 10 mM Imidazole
20 mM Imidazole Wash Buffer	20 mM Tris-OH (pH 7.6) 0.2 M NaCl, 20 mM Imidazole
50 mM Imidazole Wash Buffer	20 mM Tris-OH (pH 7.6) 0.2 M NaCl, 50 mM Imidazole
250 mM Imidazole Elution Buffer	20 mM Tris-OH (pH 7.6) 0.2 M NaCl, 250 mM Imidazole
Gelfiltration Buffer	25 mM Tris-OH (pH 7.6), 0.3 M NaCl

3.3. P domain expression

Norovirus P domain was expressed in *E. coli* BL21 as a maltose binding protein (MBP) fusion protein. *E. coli* BL21 were transformed with a pMalc2x-P plasmid containing the P domain gene of interest. The *E. coli* were cultured in 100 ml LB with ampicillin over night and used for inoculation (1:100) of 1 l LB media. The cells were grown at 37 °C until an OD_{600} of 0.4-0.6 was reached. The temperature was lowered to 22 °C and P domain expression was induced by addition of 0.75 mM IPTG. The protein was expressed overnight and harvested the following day by centrifugation at 4960 ×g for 15 min, at 4 °C. Pellets were frozen at -20 °C or used immediately for purification.

3.4. P domain purification

Cell pellets were thawed on ice and dissolved in PBS, before lysis of the cells by sonication. Lysates were cleared by centrifugation for 30 min at 39191 ×g and 4 °C. His-tagged MBP-P fusion proteins were purified from the supernatants via Nickel-NTA affinity chromatography, as described in 3.2.5.

To cleave the MBP-P domain fusion protein, HRV-3C protease was added. The mix was dialyzed over night against 10 mM imidazole buffer at 4 °C. To separate MBP-His and P domain, the mix was added to Ni-NTA beads the following day and incubated for 30 min at

4 °C. The flow through, containing the cleaved P domain, was collected, concentrated, and further purified by size exclusion chromatography with a Superdex-200 or Superdex-75 column. The peak fractions were pooled, concentrated to ~3 mg/ml and stored at 4 °C.

3.5. Direct ELISA

Direct binding of Nanobodies or antibodies to VLPs was analyzed by enzyme-linked immunosorbent assay (ELISA). In this assay, Nunc maxisorp 96-well plates were coated with 100 µl VLPs for 1 h at 37 °C. Plates for GI.1 were coated with 5 µg/ml VLPs and 10 µg/ml P domain, GII.4 VLPs were used in a concentration of 1 µg/ml. In GI cross-reactivity assays, 10 µg/ml VLPs were used. Following a blocking step for 1 h at RT with 5% skim milk in PBS, serially diluted Nanobodies, usually with a starting concentration of 100 µg/ml in PBS, were added to the plate and incubated for 1 h at 37 °C. When using antibodies, starting concentrations were at 1:250 if not stated otherwise. Bound Nanobodies were detected using horseradish peroxidase (HRP)-conjugated anti-His antibody (1 h, 37 °C) at a dilution of 1:4,000. Depending on the antibody, bound antibodies were either detected using HRP-conjugated goat anti-rabbit or goat anti-mouse antibody, at 1:40,000 or 1:1,000 dilution, respectively. Plates were developed with *o*-phenylenediamine and H_2O_2 (OPD buffer) in the dark at RT for 30 min. The reaction was stopped by addition of 6% HCl and signal was measured as absorption at 490 nm (OD_{490}) using an iMark plate reader. Between all steps, plates were washed three times with PBS containing 0.1% Tween-20 (PBS-T). Deviations from this protocol are indicated in the results.

3.6. Biotinylation of Nanobodies

To use Nanobodies for detection in ELISAs, Nanobodies had to be biotinylated. Nanobodies were diluted to 1 mg/ml and dialyzed in PBS overnight. 20× molar excess of EZ-Link™ Sulfo-NHS-LC-Biotin to the Nanobody was dissolved in PBS and added to the Nanobody sample. After 30 min incubation at RT, the mix was dialyzed overnight in PBS to remove unbound biotin from the sample.

3.7. Surrogate blocking ELISA

Surrogate blocking ELISAs were performed to analyze the potential of compounds to inhibit the attachment of VLPs to HBGAs. As surrogate HBGAs, either porcine gastric mucin type III (PGM), or saliva samples were used. Saliva samples were collected from adult volunteers; boiled for 10 min and centrifuged for 5 min at 8609 ×g to remove residual debris. Samples were stored at 4 °C. PGM was used in a dilution of 100 µg/ml in PBS, saliva samples were diluted 1:2,000 in PBS prior to coating.

Coating was done for 1 h at 37 °C and plates were subsequently blocked with 5% skim milk in PBS for 1 h at RT. VLPs were diluted and incubated with serially diluted Nanobodies or compounds for 30 min at RT and incubated for 1 h at 37 °C on the plates. For GI.1 inhibition experiments, a final concentration of 0.5 µg/ml VLPs was used. For GII.4, final concentrations were at 1 µg/ml. Nanobody concentrations for inhibition started at 100 µg/ml, for 2'FL the highest concentration was at 250 mM. Untreated VLPs were used as binding control on each plate (0% inhibition). PBS without VLPs was used as negative control.

Following this step, either biotinylated Nanobodies or polyclonal VLP-specific antibodies were incubated on the plate for 1 h at 37 °C. Biotinylated Nanobodies were detected using HRP-conjugated streptavidin monoclonal antibody in a dilution of 1:5,000, polyclonal antibodies were detected using HRP-conjugated anti-rabbit antibody (1:40,000). Deviations from this method are stated in the results. For calculation of the inhibition, the absorbance of untreated VLPs was used as a reference for 0% inhibition and all values were normalized to this value.

3.8. Dynamic light scattering

Size and stability of purified VLPs was determined by dynamic light scattering. 10 µl of the VLPs (1 mg/ml) were diluted with 1 ml H_2Odd prior to measurements. Triplicate measurements were performed at 20 °C with a Zetasizer Nano S with 15 measurement cycles each. VLPs were pre-incubated with Nanobodies or other compounds for 30 min at RT prior to measurements to analyze their effects on VLP integrity. Deviations from this protocol are mentioned in the results.

3.9. SDS-polyacrylamide gel electrophoresis (PAGE)

Proteins were separated for analysis using SDS-PAGE. Commercially available 4-15% mini PROTEAN TGX gels were used. Protein samples were mixed with 5× SDS sample loading dye in 1:4 ratio and boiled at 95 °C for 5 min to denature the proteins. After the run, the proteins were stained with GelCode Blue safe protein stain and visualized using the BioRad Chemidoc.

Table 3-3 | SDS sample loading dye ingredients.

Buffer	Ingredients
5× SDS sample loading dye	250 mM Tris–HCl (pH 6.8), 10% (w/v) sodium dodecyl sulfate (SDS), 0.2% (w/v) bromophenol blue, 43% (v/v) glycerol, 5% (v/v) β-mercaptoethanol

3.10. Western Blot

Specific proteins were detected using western blot. First, proteins were separated via SDS-PAGE (3.9) before transferring the proteins from the gel to a nitrocellulose membrane using a semi-dry method. The gel and the membrane were equilibrated in transfer buffer and placed on transfer buffer soaked blotting paper. Using the Trans blot Turbo protocol, the proteins were transferred onto the nitrocellulose membrane. After a washing step in Tris-buffered saline (TBS), the nitrocellulose membrane was blocked in 5% blotto-TBS with Tween (TBS-T) for 1 h at RT. After 3×5 min of washing in TBS-T, the membrane was incubated with rabbit-anti GII.4 polyclonal antibody [1:1,000, in TBS-T-blotto (5%)], for 1 h at RT. Following another washing step with TBS-T, HRP-coupled goat-anti rabbit antibody was added to the membrane (1:40,000 in TBS-T-blotto). After 1 h incubation, development solution was added and proteins were imaged with a BioRad Chemidoc.

3.11. Agarose Gelelectrophoresis

To analyze the success of PCRs or cloning, the products were analyzed on an agarose gel. 1% agarose in TAE (Tris-acetate-EDTA) buffer was used to prepare the gels. Samples were mixed 1:6 with loading dye, and the gel was run for 30 min at 135 V. Ethidium bromide was added to the running buffer to stain the DNA. After running the gels, the DNA was visualized with a BioRad Chemidoc.

3.12. EM Experiments

3.12.1. Negative stain EM

VLPs and virions were checked for size and integrity using negative stain EM. Samples were diluted 1:30 and subsequently applied to EM grids. The grids were washed with distilled water and stained using 0.75% uranyl acetate. For human infectious virions, samples were fixed with 4% glutaraldehyde prior to staining. Samples were analyzed on a Zeiss 900 electron microscope, operating with an acceleration voltage of 80 keV and images were recorded 50,000 × magnification using a CCD camera.

3.12.2. Sample preparation prior to freezing

In order to be able to image VLPs or MNV virions in complex with Nanobodies using cryo-EM, VLPs were incubated with 5× molar excess of Nanobodies to the binding sites for 30 min at RT prior to sample preparation.

For the complexes of VLPs with small molecule compounds, such as GCDCA, A-trisaccharide or 2'FL, the VLPs were incubated with 100× molar excess of compound to binding sites.

MNV virions in complex with $MgCl_2$ and $CaCl_2$ were incubated with 10 mM of $MgCl_2$ and $CaCl_2$ and incubated at RT for 3 h.

3.12.3. Sample vitrification for cryo-EM

Vitrification of the cryo-EM samples was done with a FEI Mark IV Vitrobot. Purified VLPs were applied on freshly glow discharged Quantifoil holey carbon support films (R1.2/1.3 or R.0.6/1, cu/rh, 300 mesh) and blotted at 12 °C for 18-24 s at 100% humidity, before plunge freezing the sample in liquid ethane. Samples were stored in liquid nitrogen until usage.

3.12.4. Preparation of graphene covered grids

Graphene covered grids were prepared as described before (134). Briefly, 1:10 diluted graphene oxide solution was placed on the grid and blotted away after incubation for 1 min at RT, and washed with distilled water. The grids were dried on a blotting paper and could be used immediately after preparation.

3.12.5. Preparation of carbon-covered grids

For the preparation of carbon-covered grids, first carbon was first evaporated on mica, to generate a thin continuous carbon film. This carbon film was floated onto the EM grids and dried on filter paper prior to sample preparation. The carbon film was provided by Dr. Dirk Flemming.

3.12.6. Cryo-EM data collection

Vitrified specimens were imaged with a Titan Krios (FEI) microscope, operating at 300 keV acceleration voltage. Micrographs were acquired with a K2 or K3 direct electron detector, using DigitalMicrograph Latitude S software. The used direct electron detector and magnification with corresponding pixel size for each dataset are noted in Table 3-4, cryo-EM structures solved within this thesis are mentioned in Table 3-5.

Table 3-4 | Collected cryo-EM datasets.

Sample name	Camera	Magnification	Pixel size (Å/px)	Number of Micrographs
GI.1	K2	130,000	1.08	3,082
GII.4 NSW-2012	K2	64,000	2.27	346
GII.4 CHDC	K3	64,000	1.375	591
GII.4c	K3	64,000	1.369	4,024
GII.4c (HEK cells)	K3	64,000	1.369	483
GII.4 NSW2012 + 1GFV56	K3	64,000	1.369	529
GII.4 NSW2012 + 2GFV20	K3	64,000	1.369	303
GII.4 NSW2012 + 2GFV37	K3	64,000	1.369	373
GII.4 NSW2012 + 2GFV46	K3	64,000	1.369	246
GII.4 NSW2012 + 2GFV104	K3	64,000	1.369	773
GII.4 NSW2012 + 2GFV118	K3	64,000	1.369	153
GII.17	K2	130,000	1.08	2,316
GII.17 + A tri	K3	64,000	1.375	1,407
GII.17 + 2’ FL	K2	130,000	1.08	3,570
MNV – 1. dataset	K3	64,000	1.375	4,046
MNV – 2. dataset	K3	64,000	1.375	1,588
MNV + NB5829	K3	64,000	1.369	3,599
MNV + 10 mM $MgCl_2$	K3	64,000	1.369	611
MNV + 10 mM $CaCl_2$	K3	64,000	1.369	303
MNV + NB5829/$MgCl_2$	K3	64,000	1.369	293

Table 3-5 | Cryo-EM structures solved within the study.

Structure	Particle number	Resolution in Å (0.143 FSC cut-off)	EMDB ID
GII.4c T=1	48,971	4.2	EMD-10757
GII.4c T=3	44,317	8.0	EMD-10756
GII.4c T=4	118,971	4.2	EMD-10755
GII.4c T=4 (HEK cells)	10,135	4.5	EMD-10758
GII.4 CHDC-1974	42,485	6.1	EMD-4549
GII.4 NSW-2012 T=4	10,548	7.3	EMD-4550
GII.4 NSW-2012 T=3	391	15	
GII.4 NSW-2012 +1GFV56	24,597	7.4	
GII.4 NSW-2012 + 2GFV20	8,002	6.5	
GII.4 NSW-2012 + 2GFV37	22,566	6.2	
GII.4 NSW-2012 + 2GFV46	10,401	5.7	
GII.4 NSW-2012 + 2GFV104	43,587	4.6	
GII.4 NSW-2012 + 2GFV118	6,390	8.1	
GII.17	35,709	5.8	EMD-10759
GII.17 + A tri	40,951	7.9	
GII.17 + 2’ FL	55,956	5.8	
MNV	21,424	4.6	EMD-10596
MNV + NB5829	32,612	4.7	EMD-10597
MNV + 10 mM $MgCl_2$	2,783	4.3	EMD-10598
MNV + 10 mM $CaCl_2$	2,637	4.6	EMD-10599
MNV + NB5829/$MgCl_2$	7,386	4.5	EMD-10600

3.12.7. Cryo-EM data processing with Relion

In a first processing step, the micrograph movies were corrected for drift using the software motioncor2 (114), and defocus estimation was done using ctffind4.1 (139), as implemented in Relion 2.1 and 3.0 (181).

An initial set of 1,000 particles was picked manually, to perform 2D classification and produce templates for the automated particle picking procedure. After automated particle picking, the particles were first sorted in 2D classifications. A subset of particles was used to produce an initial 3D model. Using this model as reference, 3D classification was done with the particles as another sorting step. A subgroup of particles generating the highest resolution structure was used for 3D refinement. For all VLP datasets, icosahedral symmetry I2 was imposed on the dataset for 3D classification, initial model generation and 3D refinement.

3.12.8. Cryo-EM data processing with cryoSPARC

Alternatively to Relion, datasets were processed with cryoSPARC (163). Analogous to processing in Relion, the micrograph stacks were first drift corrected with motioncor2 (114), and then CTF correction was done using ctffind4.1 (139). A subset of particles was manually picked and templates for automated picking were generated using 2D classification. All picked particles were subjected to several rounds of 2D classification, to exclude falsely picked particles and noise. With this subset of particles, first a 3D initial model was prepared that was then used as starting point for the 3D refinement. cryoSPARC has the opportunity to perform homogenous – as well as non-uniform refinement that can correct for intrinsic variabilities. For all VLP datasets, icosahedral symmetry I2 was imposed on the dataset for 3D classification, initial model generation and 3D refinement.

3.12.9. Focused reconstruction

When imposing icosahedral symmetry on particles, variabilities in the asymmetric units are not accounted for, resulting in a lower resolution in those variable regions. To resolve these structural differences, focused refinement was performed in Relion 3.0. First, the dataset was processed as described in 3.12.7, until 3D refinement. Following this step, the dataset is expanded by symmetry, using the *relion_expand_symmetry* command, so that each particle is assigned 60 orientations, corresponding to the 60 asymmetric units and redundant views in the particle. Using spider (54), a cylindrical mask was prepared and positioned in chimera, to cover only the region of interest on the particle, i.e. a symmetry axes or single VP1 dimers. Using these input files, 3D classification was performed without angular refinement, to resolve the structural deviations between the asymmetric units.

4. Chapter 1: Characterisation of potential antivirals for GI noroviruses, using antibodies, Nanobodies and the HMO 2'FL

4.1. Summary

In this chapter, we analyzed the potential of GI.1 specific antibodies, Nanobodies and the human milk oligosaccharide 2'FL, to function as norovirus inhibitors.

In the antibody panel we identified five antibodies that inhibited VLP attachment to HBGA, but these antibodies were unable to block other genotypes.

For the Nanobodies, we discovered two that inhibited VLP binding to HBGAs by aggregation (Nano-94), and in a manner that kept particle integrity intact (Nano-7). The binding site was occluded, giving proof that such sites on the capsid can represent vulnerable epitopes. A third Nanobody, Nano-62, exhibited as similar binding site, but inhibition was only low.

We also showed that 2'FL was able to inhibit HBGA attachment of several GI genotypes, showing its broad specificity.

Importantly, we found that combination of Nanobodies and 2'FL improved attachment inhibition substantially. In the case of Nano-94, the increase could be defined as synergistic. Combining cross-reactive with highly efficient compounds could present a treatment alternative to combat the issue of low cross-reactivity in potential norovirus treatments.

4.2. Contributions

Parts of this chapter (Nanobodies) were a collaborative work: Alexander Hempelmann, Celina Geiss, Juliane Graf, Michelle Haas, and Imme Roggenbach expressed and purified the Nanobodies, X-ray crystallography was performed by Dr. Turgay Kilic. ELISA experiments were performed and analyzed jointly with Alessa Ringel and Kerstin Ruoff and me. Kerstin Ruoff and me performed EM and DLS experiments. Dr. Grant Hansman, Kerstin Ruoff, Alessa Ringel, Anna Koromyslova and I wrote the manuscript. It has been published as:

Ruoff K*, Kilic T*, Devant J*, Koromyslova A, Ringel A, Hempelmann A, Geiss C, Graf J, Haas M, Roggenbach I, Hansman G. 2019. Structural Basis of Nanobodies Targeting the Prototype Norovirus. Journal of Virology 93:e02005-18

(* = equal contribution)

Figures in this chapter were taken from this publication and are labeled accordingly.

4.3. Results

Production of GI VLPs

In order to be able to identify broadly reactive antibodies and Nanobodies, we produced a panel of GI VLPs (GI.2 Southampton, GI.2 Fusabashi258, GI.3 Kashiwa645, GI.4 Chiba Virus and GI.11 #8). Purified VLPs were mostly a mixture of small and native VLPs, with the typical norovirus morphology (Figure 4-1).

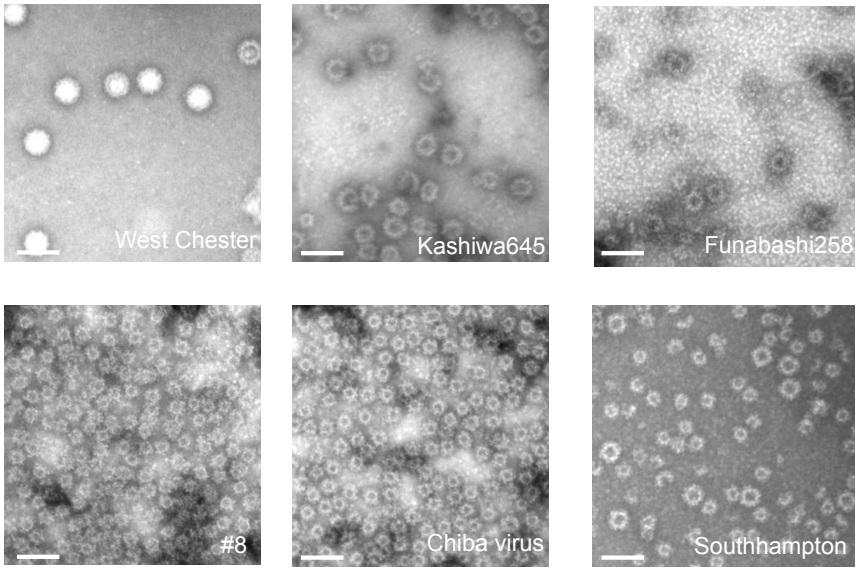

Figure 4-1 | Negative stain EM of different GI genotypes. Shown are VLPs from GI.1 West Chester, GI.2 Southampton, GI.2 Funabashi258, GI.3 Kashiwa645, GI.4 Chiba Virus and GI.11 #8. The scale bar represents 50 nm. All VLPs exhibit the typical norovirus morphology, but particles varied in size.

Binding abilities of GI specific antibodies

A panel of 16 antibodies raised against GI.1 VLPs was obtained from virostat inc. These antibodies were first tested for their ability to bind GI VLPs in a direct binding ELISA.

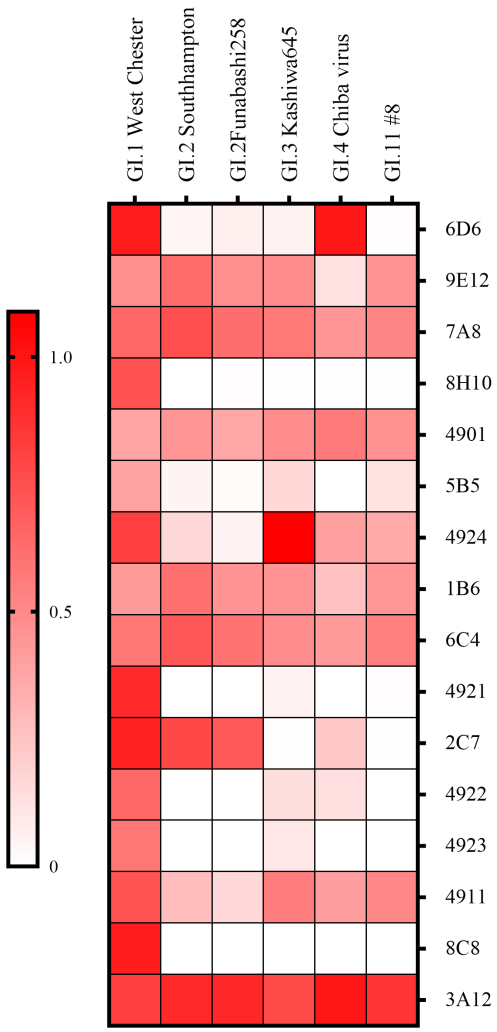

Figure 4-2 | Cross-reactivity of antibodies binding to different GI genotypes. The color scheme represents measured OD_{490} values. All antibodies were able to attach GI.1 VLPs, but binding patterns to other GI VLPs varied between the analyzed antibodies.

All of the tested antibodies bound to GI.1 VLPs. The strongest binders were mAb 6D6, 4921, 2C7 and 8C8 (Figure 4-2). Remarkably, mAb 7A8, 4901, 6C4 and 3A12 were cross-reactive with all other GI VLPs. Of these cross-reactive antibodies, mAb 3A12 exhibited the strongest overall binding. Conversely, mAbs 8H10, 4921, 4922,4923 and 8C8 were specific to GI.1.

HBGA attachment inhibition of GI VLPs by GI.1 specific antibodies

In a surrogate HBGA binding assay, the ability of the antibodies to inhibit the attachment of VLPs to PGM was analyzed. Prior to these experiments, the VLPs were examined for their HBGA binding properties. GI.11 #8 VLPs neither bound saliva A/B/O samples nor PGM, indicating that this genotype was a non-binder. Therefore, the inhibition for these VLPs could

not be not further tested in the HBGA surrogate ELISA. Conversely, GI.2, GI.3 and GI.4 VLP samples were able to bind to PGM.

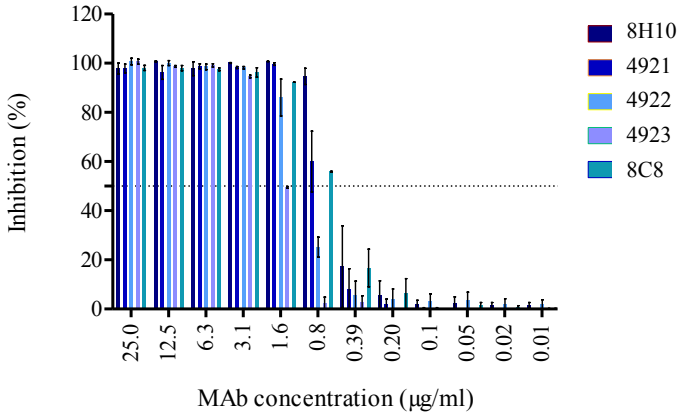

Figure 4-3 | Inhibitory properties of GI.1 specific antibodies. Out of the panel of 16 antibodies, only five were able to inhibit HBGA attachment of GI.1 VLPs in a dose dependent manner. The inhibition experiments were performed in triplicates (error bars indicate standard deviation).

Table 4-1 | IC_{50} values of mAbs inhibiting GI.1 PGM attachment.

Antibody	IC_{50} (µg/ml)
8H10	3.39
4921	5.33
4922	11.90
4923	36.98
8C8	5.46

Five of the 16 mAbs were able to inhibit the attachment of GI.1 to PGM. The best inhibitor was mAb 8H10, with an IC_{50} value of 3.39 µg/ml (Table 4-1 and Figure 4-3). mAb 4921 had an IC_{50} of 5.33 µg/ml, followed by 8C8, at 5.46 µg/ml. mAb 4922 had a ~two-fold lower IC_{50} at 11.9 µg/ml, and the lowest inhibition was measured for mAb 4923 at 36.98 µg/ml. The inhibiting antibodies were non-cross reactive for other genotypes (Figure 4-2), therefore the attachment inhibition could not be tested for other GI genotypes.

HBGA attachment inhibition of GI VLPs by 2'FL

To further characterize the GI VLPs, the inhibition ability of 2'FL was analyzed. In previous studies, 2'FL was able to inhibit the attachment of VLPs to HBGAs in both GI and GII genotypes, suggesting a broad activity of this compound (98, 220).

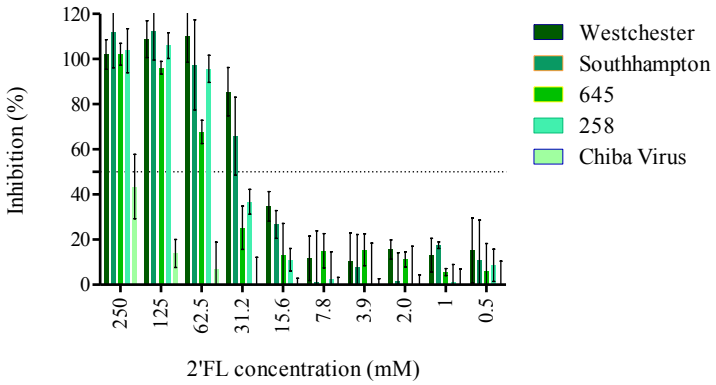

Figure 4-4 | Inhibition of GI VLP PGM attachment by 2'FL. 2'FL was able to inhibit the attachment of all tested GI VLPs to PGM in an ELISA surrogate experiment in a dose dependent manner. Inhibition for GI.4 Chiba virus did not reach a plateau. All experiments were performed in triplicates. Error bars indicate standard deviation.

Table 4-2 | IC_{50} values of 2'FL inhibiting PGM attachment of GI VLPs.

Norovirus genotype	IC_{50} (mM)
GI.1 West Chester	18.27
GI.2 Southampton	23.48
GI.2 Funabashi258	34.75
GI.3 Kashiwa645	44.89
GI.4 Chiba407	Not defined

2'FL was able to inhibit the attachment of all VLPs to PGM, with IC_{50} values ranging from 18.27 to 44.89 mM (Figure 4-4 and Table 4-2). For GI.4 Chiba Virus, the inhibition was too weak to calculate an IC_{50} value. Even in this case, a dose dependent inhibition was observed, although the curve did not reach a plateau at the tested concentrations. 2'FL is soluble in H_2O up to 240 g/l, which corresponds to a maximum molar concentration of 491.8 mM. Therefore, the concentration could not be increased to a concentration necessary to reach the plateau.

Structural and functional characterization of GI.1 specific Nanobodies

A Nanobody library was obtained from the VIB Nanobody Service Facility in Brussels, where an alpaca was immunized with GI.1 VLPs. Nanobodies were expressed and purified by Alexander Hempelmann, Celina Geiss, Juliane Graf, Michelle Haas, and Imme Roggenbach. Based on results from preliminary binding ELISA experiments by Kerstin Ruoff, three Nanobodies, Nano-7, Nano-62 and Nano-94 were chosen for further characterization.

Binding properties of GI.1 specific Nanobodies

In order to identify, how the Nanobodies were interacting with GI.1 VLPs and isolated GI.1 P domains, we performed direct ELISAs with Nano-7, Nano-94 and Nano-62 (Figure 4-5).

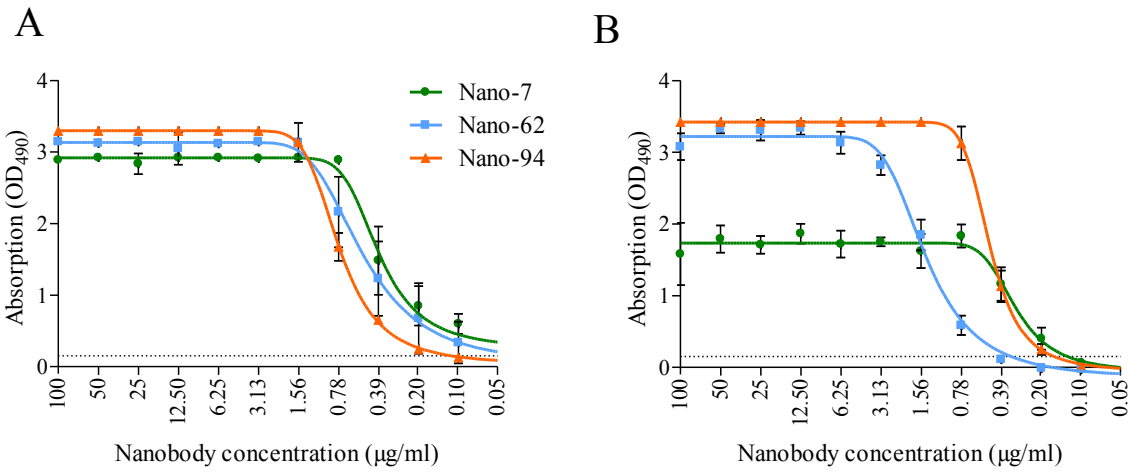

Figure 4-5 | Nanobodies binding to GI.1. (A) All Nanobodies were able to detect GI.1 P domain in a dose dependent manner. (B) All three Nanobodies were able to detect GI.1 VLPs. For Nano-7, the maximum signal at the plateau was ~two-fold lower than for Nano-62 and Nano-94. All experiments were performed in triplicates (error bars indicate standard deviation), together with Kerstin Ruoff and Alessa Ringel. The figure was adapted from (176).

All three Nanobodies bound comparably well to the GI.1 P domain, with similar cut-off values. However, for binding of VLPs, only Nano-62 and Nano-94 displayed a similar binding pattern, whereas Nano-7 had a ~two-fold lower absorption value at the highest concentration.

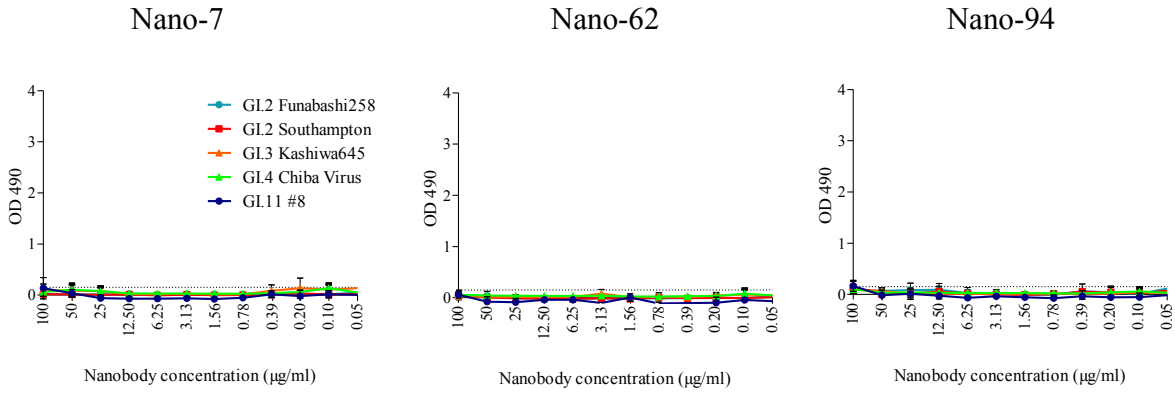

Figure 4-6 | Cross-reactivity of GI.1 specific Nanobodies. The cross reactivity in ELISA was tested with VLPs from GI.2 Southampton, GI.2 Fusabashi258, GI.3 Kashiwa645, GI.4, Chiba Virus and GI.11 #8. The Nanobodies were specific to GI.1, no cross-reactivity with any other GI genotype VLPs was observed. All experiments were performed in triplicates (error bars show standard deviation).

Cross-reactivity binding ELISAs revealed that Nano-7, Nano-62 and Nano-94 were unable to bind to VLPs of genotypes other than GI.1. Tested were GI.2, GI.3, GI.4 and GI.11 VLPs (Figure 4-6). These results suggested that the binding sites of all three Nanobodies were not conserved in other GI genotypes.

Structural analysis of Nanobodies in complex with GI.1 P domain

The structure for GI.1 P domain in complex with Nano-94, Nano-62 and Nano-7 was solved using X-ray crystallography (experiments performed by Dr. Turgay Kilic). Nano-94 bound to the top of the P domain (Figure 4-7A), whereas Nano-62 and Nano-7 attached to epitopes located at the lower part of the P domain (Figure 4-7B/C). Interestingly, superposition of the P domain/Nano-7 or P domain/Nano-62 structure onto the structure of intact VLPs [PDB: 1IHM (162)] revealed that in context of the whole particle, the Nanobodies would clash with the S domains, as well as neighboring P domains (Figure 4-8 and Figure 4-9).

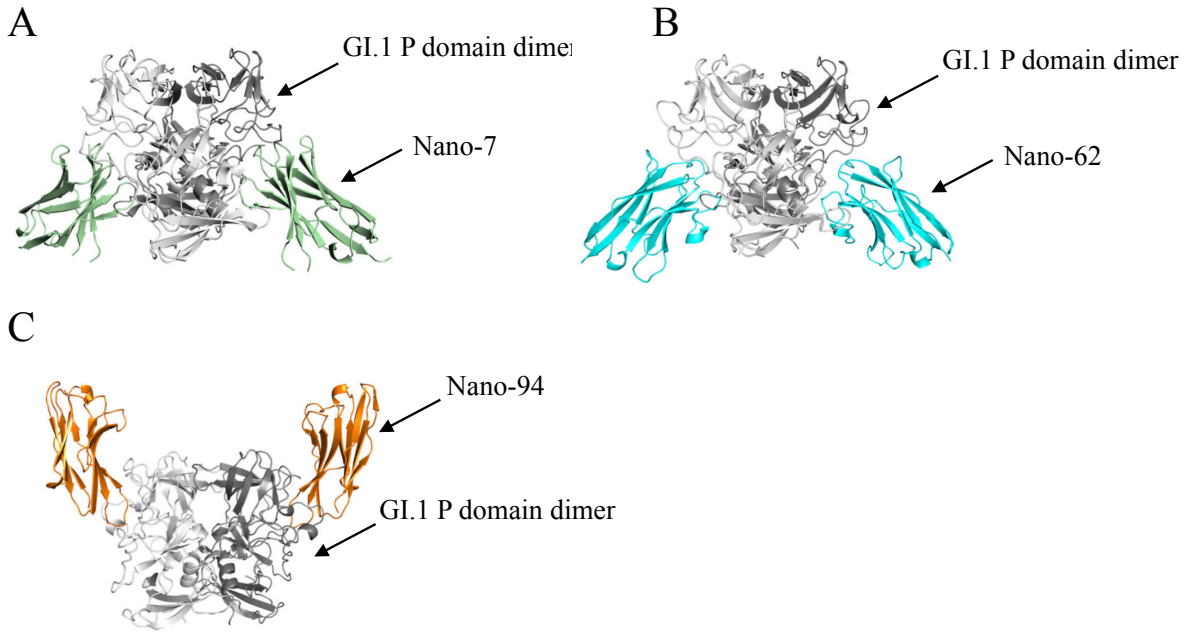

Figure 4-7 | X-ray crystal structures of GI.1 P domain with Nanobodies. (A) GI.1 P domain in complex with Nano-7. The binding site of Nano-7 was located at the bottom of the P domain. Two Nanobodies and one P domain dimer were forming the asymmetric unit. The Nanobody was held in place by side- and main chain interactions from both monomers. (B) X-ray crystal structure of GI.1 P domain bound to Nano-62. The asymmetric unit comprised one P domain dimer and two Nanobodies, with binding sites located at the lower part of the P domain. Also here, the Nanobody was held by side chain interactions and main chain interactions from both P domain monomers. (C) GI.1 P domain in complex with Nano-94. Two Nanobodies were bound per P domain dimer. The interaction was formed solely between one Nanobody and a single P domain monomer, as the binding site was located at the top of the P domain. All structures were solved by Dr. Turgay Kilic. The figure was adapted from (176).

When the P domain/Nano-94 complex was superpositioned on the VLP structure, there were no clashes with the S domain or neighboring P domains, as it bound to an epitope located at the top (Figure 4-10). However, steric hindrance between individual neighboring Nanobody molecules was observed at full occupancy.

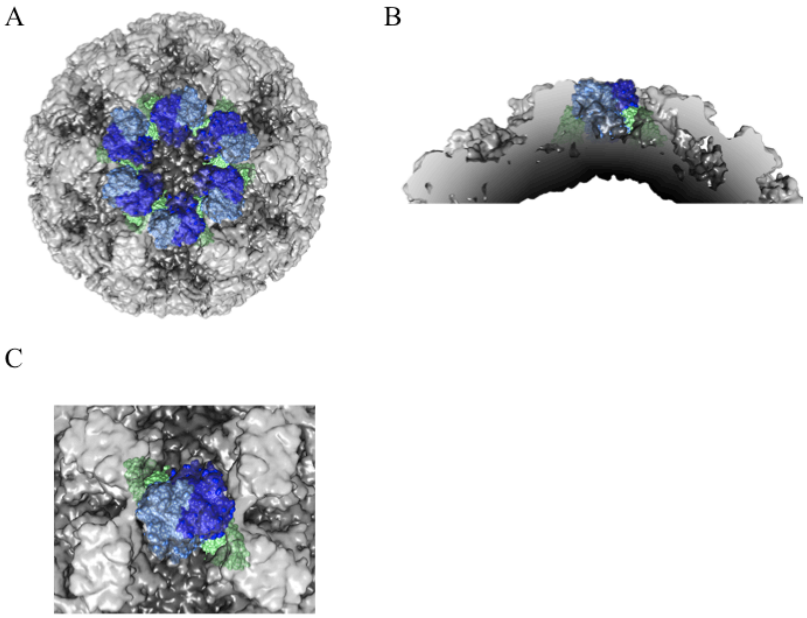

Figure 4-8 | Model of Nano-7 binding to GI.1 VLPs. (A) The X-ray crystal structure of the GI.1 P domain/Nanobody complex was fitted into the X-ray crystal structure of the GI.1 VLP (PDB: 1IHM). The P domain/Nano-7 structure is colored blue and green, respectively. The VLP structure is shown in grey (light grey: P domain, dark grey: S domain). (B) A cutout section demonstrates that Nano-7 clashes with neighboring P domains and S domains. (C) Close-up view on a C/C dimer shows Nano-7 would clash with neighboring P domains in this position. The X-ray crystal structures were solved by Dr. Turgay Kilic, the modeling was performed by me. The figure was adapted from (176).

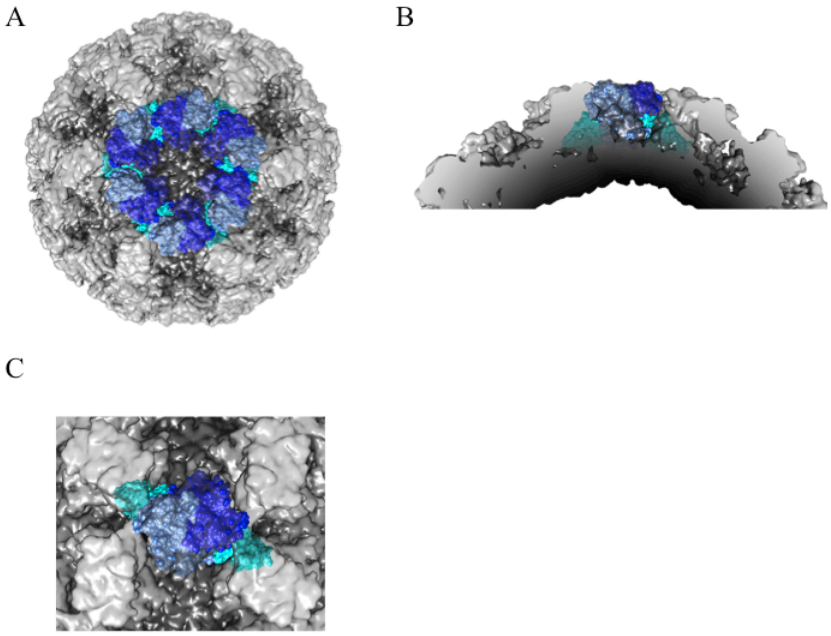

Figure 4-9 | Model of Nano-62 binding to GI.1 VLPs. (A) The X-ray crystal structure of the GI.1 P domain/Nanobody complex was fitted into the X-ray crystal structure of the GI.1 VLP (PDB: 1IHM). The P domain/Nano-62 structure is colored blue and cyan, respectively; the VLP structure is illustrated in grey (light grey: P domain, dark grey: S domain). (B) A cutout section shows that Nano-62 clashes with neighboring P domains and S domains. (C) Close-up view on a C/C dimer shows Nano-62 would clash with neighboring P domains in this position. The X-ray crystal structures were solved by Dr. Turgay Kilic, the modeling was performed by me. The figure was adapted from (176).

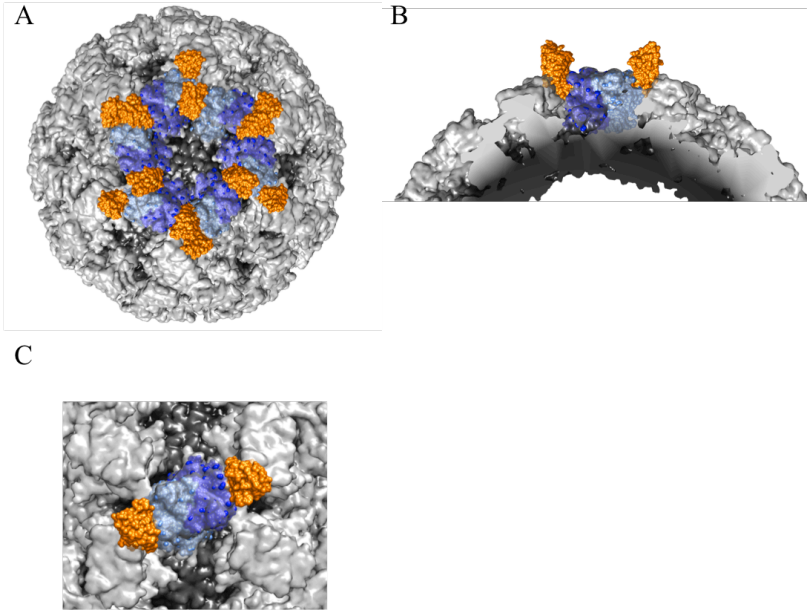

Figure 4-10 | Model of Nano-94 binding to GI.1 VLPs. (A) The X-ray crystal structure of the GI.1 P domain/Nanobody complex was fitted into the X-ray crystal structure of the GI.1 VLP (PDB: 1IHM). The P domain/Nano-94 structure is colored blue and orange, respectively. The VLP is shown in grey (light grey: P domain, dark grey: S domain). Neighboring Nanobodies would clash at full occupancy. (B) A cutout section shows that Nano-94 is binding to the top of the P domain, forming the outermost layer of the capsid/Nanobody complex. (C) Model of a close-up top view on a C/C dimer bound with Nano-94. As this Nanobody binds to the top, no steric hindrance with neighboring P domains would occur. The X-ray crystal structures were solved by Dr. Turgay Kilic, the modeling was performed by me.

Attachment inhibition of Nanobodies

In previous studies it was shown that GII.10 specific Nanobodies could block the attachment of VLPs to PGM in a surrogate HBGA binding assay (101). Therefore, we determined if these VLPs were able to block the binding of GI.1 VLPs to PGM in an adapted blocking assay (Figure 4-11).

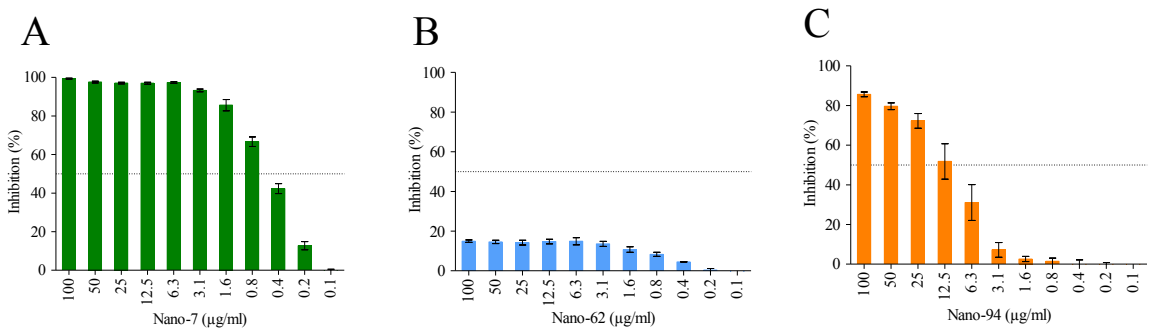

Figure 4-11 | Inhibition of GI.1 VLP HBGA binding by Nanobodies. (A) Nano-7 was able to inhibit the attachment of GI.1 VLPs to PGM in a dose dependent manner, with an IC_{50} value of 0.4 µg/ml. (B) Nano-62 only exhibited weak inhibitory properties, with a maximum inhibition of 15% at the highest Nanobody concentration. (C) Nano-94 blocked the binding of VLPs to PGM, with an IC_{50} of 9.2 µg/ml. The inhibition experiments were performed in triplicates (error bars indicate standard deviation). The experiments were performed by Alessa Ringel, Kerstin Ruoff and me. The figure was adapted from (176).

Nano-7 showed the strongest inhibition, with a half maximal inhibitory concentration of 0.4 µg/ml. Nano-94 also exhibited dose dependent inhibition, with an IC_{50} of 9.2 µg/ml. Despite the binding site similarity of Nano-7 and Nano-62, Nano-62 had only minimal effect on PGM attachment, with a maximum inhibition of ~15% at 100 µg/ml Nanobody concentration.

The influence of Nanobodies on the GI.1 capsid morphology

To further characterize the mode of inhibition, we performed DLS and negative stain EM experiments on VLPs treated with Nanobodies (Figure 4-12).

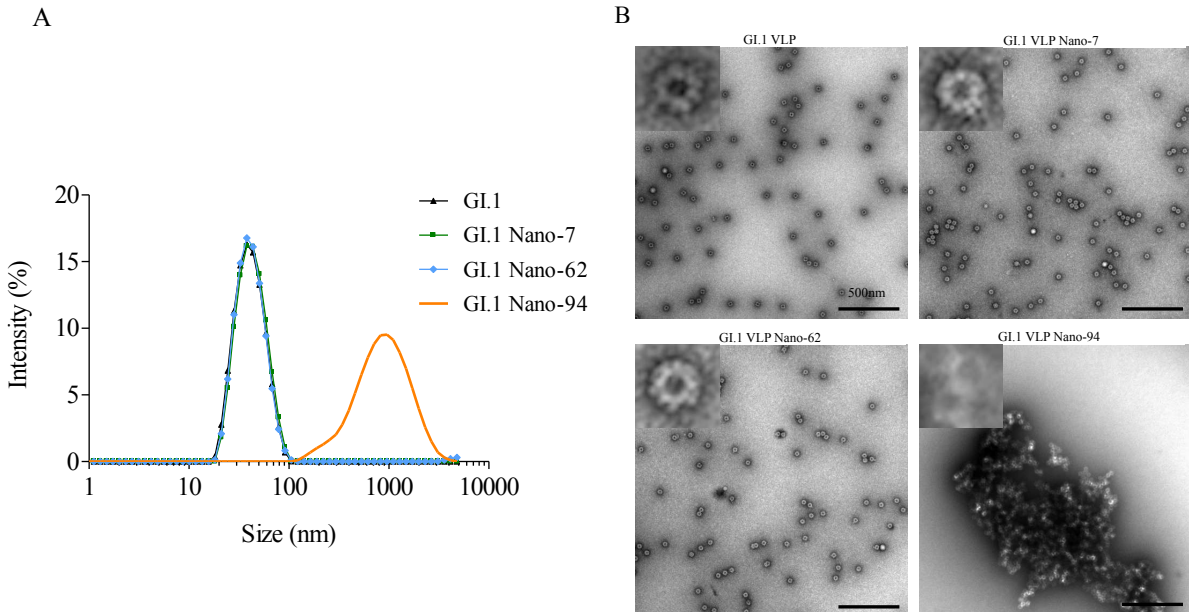

Figure 4-12 | GI.1 VLPs after Nanobody treatment. (A) In DLS, incubation with Nano-94 (orange) led to an increase in hydrodynamic diameter. In contrast, VLPs treated with Nano-7 (green) or Nano-62 (cyan), exhibited a comparable hydrodynamic diameter as the untreated VLPs (black). (B) Negative stain EM of VLPs with Nanobodies confirmed these results: Nano-94 led to formation of large VLP aggregates, whereas Nano-7 and Nano-62 kept the particle morphology intact. DLS measurements and EM images were prepared by Kerstin Ruoff and me. The figure was adapted from (176).

The untreated VLPs showed a single peak with a diameter of ~42 nm. Neither Nano-62 nor Nano-7 treatment influenced the particle size, and the peaks were comparable to the peak exhibited for untreated VLPs. Correspondingly, in negative stain images of the VLPs treated with Nano-62 or Nano-7, the VLPs exhibited a morphology that was undistinguishable from untreated VLPs. In contrast, incubation with Nano-94 led to a peak shift in DLS to ~1,000 nm, suggesting particle aggregation or disintegration of the capsid. Negative stain-EM confirmed that the addition of the Nanobody led to formation of VLP aggregates.

Combinational treatment of Nanobodies and 2'FL

Earlier studies suggested that several compounds block HBGA attachment to norovirus VLPs by mimicking the binding factor and occupying the HBGA binding site. One example for this was 2'FL, which inhibited GI.1 VLP-HBGA attachment with an IC_{50} of ~50 mM (98). Therefore, we wanted to explore, if the combination of two independently working inhibitors could improve the blocking potential. For this experiment, the inhibition ELISA was adapted: Constant concentrations of 2'FL (10, 20, 30, 40 and 50 mM) were combined with serially diluted Nanobodies (Nano-7 and Nano-94) and incubated with GI.1 VLPs, to determine their combined blocking potential (Figure 4-13). In both cases, the combination led to enhanced

inhibition, suggesting that the compounds did not influence each other negatively. Instead, the extent of inhibition increased with higher 2'FL concentrations. We applied the mathematical model of Bliss (15, 160), to define if the observed effect was synergistic or additive. In this model, an expected value for additivity is calculated from the inhibition values of the two compounds alone. If the observed inhibitory effect is more than 20% above this value, the compounds act synergistically.

For combinations with 40 and 50 mM 2'FL (Figure 4-13 D/E/I/J), the effects could not be defined as synergistic, as the calculated expected additive effect exceeded 100% inhibition. With Nano-94, several values could be defined as synergistic according to our 20% criteria: 10 mM 2′FL combined with 25, 12.5, and 6.3 μg/ml of Nano-94 (Figure 4-13A) and 20 and 30 mM 2′FL combined with 12.5 to 3.1 μg/ml of Nano-94 (Figure 4-13B/C). The differences between synergistic values and expected additivity were determined as statistically significant in all cases by paired t-test and two-way analysis of variance (ANOVA). Combination of 2'FL with Nano-7 increased inhibition additively at all tested concentrations, but no synergistic effects were observed (Figure 4-13F/G/H/I/J).

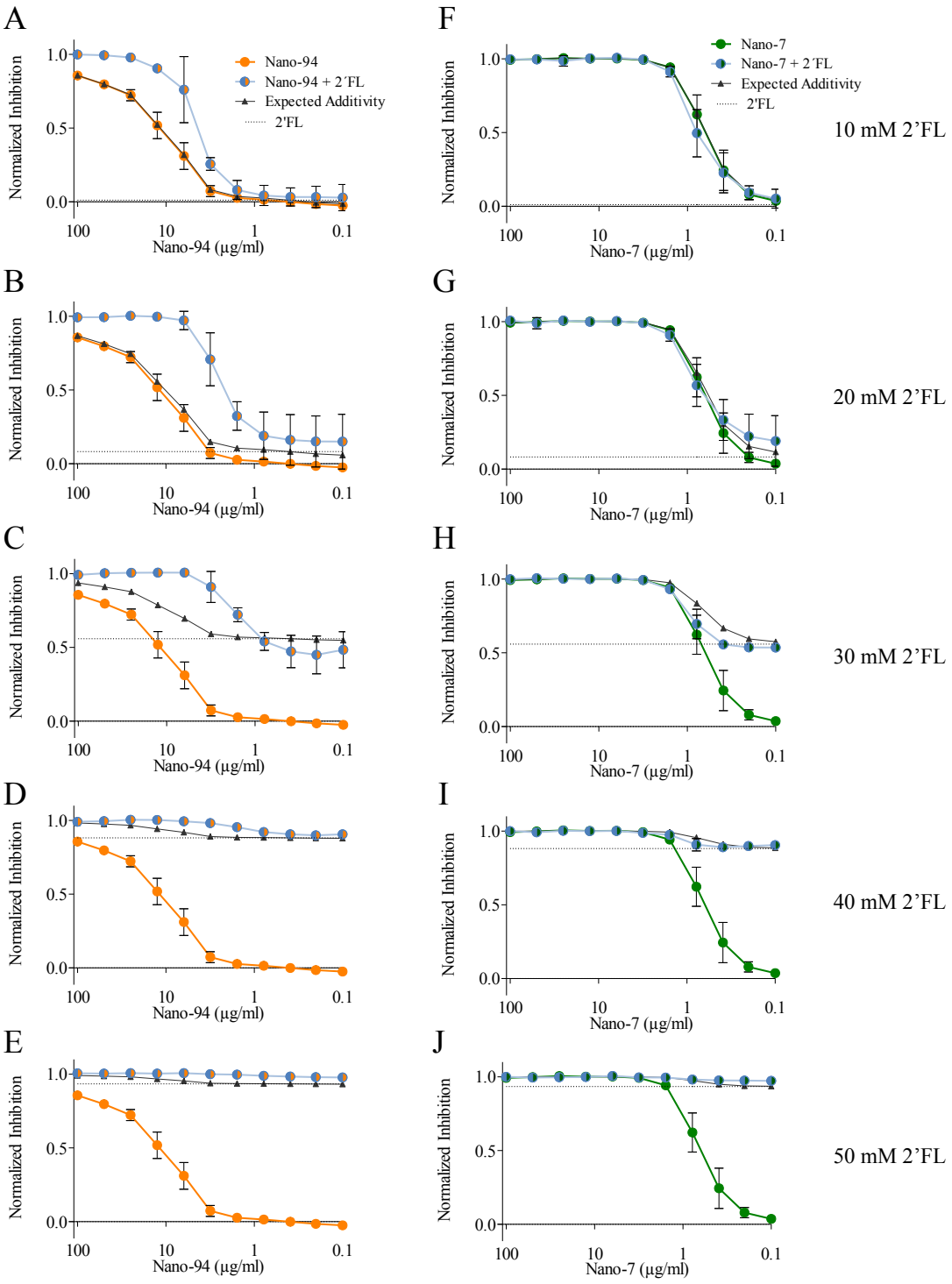

Figure 4-13 | Combinational inhibitory effects of Nano-7 and Nano-94 with 2'FL. Serially diluted Nanobodies were combined with constant concentrations of 2'FL. (A-E) The graphs demonstrate inhibition of Nano-94 alone (orange circles), 2'FL alone (dashed line), expected values for additivity according to the mathematical model of Bliss (black triangles), and the observed inhibition of the combination (blue/orange circles). For several combinations of Nano-94 and 2'FL, the effect could be defined as synergistic. (F-J) The graphs show inhibition of Nano-7 alone (green circles), 2'FL alone (dashed line), the expected values for additivity according to the Bliss model (black triangles) and the observed inhibition of the combination (blue/green circles). The observed inhibition values closely matched the expected values for additivity, suggesting an additive effect for this combination. Experiments were performed in triplicates; error bars represent the standard deviation. Kerstin Ruoff, Alessa Ringel and me performed and analyzed the experiments. The figure was adapted from (176).

Cryo-EM analysis of GI.1 VLPs

As mentioned, Nano-7 and Nano-62 bound to seemingly sterically occluded sites on the capsid. Therefore, we sought to analyze the structure of Nanobody-bound VLPs more in detail using single particle cryo-EM.

The X-ray crystal structure of an unliganded GI.1 VLP had already been solved in 1999 (162). In this structure, the P domains were located on the shell and the hinge region was not extended. This structure was in contrast with published calicivirus structures from other genotypes, where the P domains were linked to the S domain by an extended hinge region (69, 87). As most other VLP structures were solved using single particle cryo-EM, this raised the question whether the differential conformations of the P domains were genotype dependent, or if they represent two states of the virus. Therefore, our first aim was to determine the structure of a native GI.1 VLP using cryo-EM and evaluate the positioning of the P domains.

In the vitreous ice, GI.1 particles tended to aggregate (Figure 4-14A). To circumvent this issue, we deposited a carbon layer onto the grids prior to freezing, a procedure, which considerably improved particle distribution und uniformity (Figure 4-14B). Similar improvements could be observed with graphene oxide covered grids (Figure 4-14C). In general, graphene oxide has superior properties compared to carbon, as it is thinner and therefore introduces less background signal. However, the amount of deposited graphene flakes on the grid was too low to allow efficient data collection on these grids. Therefore, we used carbon-covered grids for GI.1 data collection.

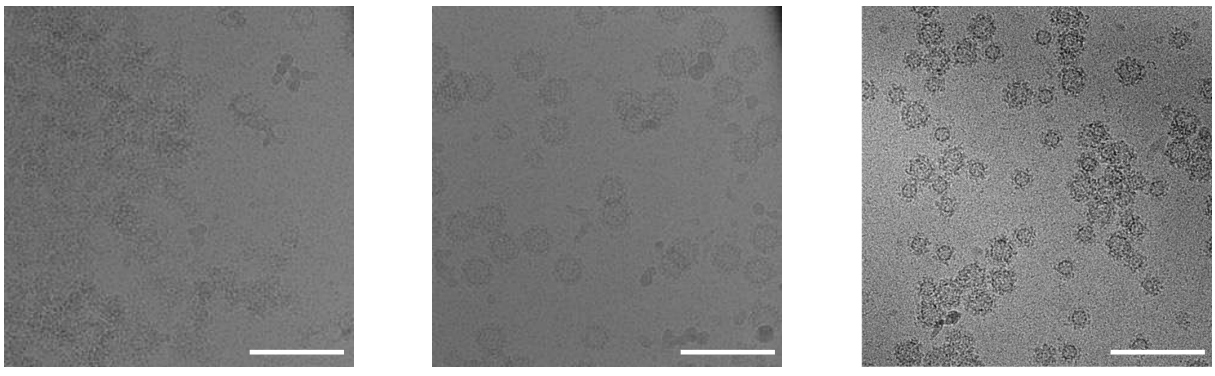

No support film | Graphene oxide | Carbon

Figure 4-14 | Particle distribution of GI.1 VLPs in vitrified ice with different support films. Without support film, the VLPs tended to form large clusters. On grids with either graphene oxide or carbon film backing, the VLPs were preferentially monodisperse. The scale bar represents 100 nm.

After treatment of the grids with a carbon support film, the particles were preferentially monodisperse in the ice (Figure 4-14C). GI.1 particles were not homogenous and two differently sized populations of particles were observed.

The particles with larger diameter were the supposedly native sized T=3 icosahedral VLPs. Particles were picked automatically from 3,082 images and sorted in 2D classification. The particles appeared to have a distorted shape (Figure 4-15A). Because of the heterogeneity within the particles, the 3D structure of those VLPs could not be solved.

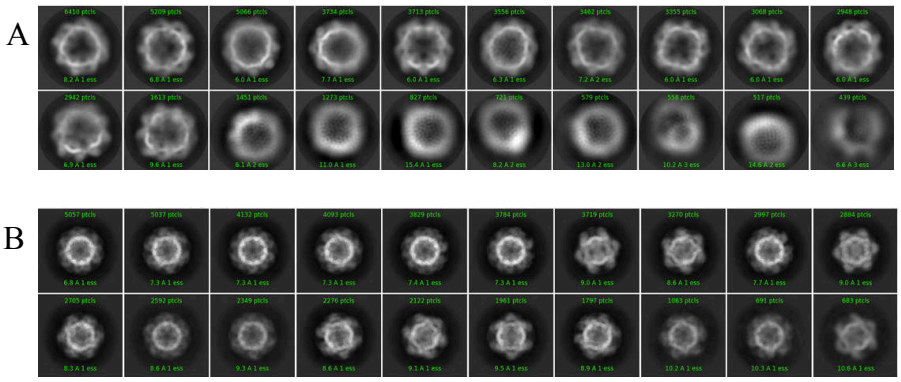

Figure 4-15 | 2D classification of GI.1 VLPs. (A) T=3 icosahedral particles showed a blurred, distorted morphology. (B) T=1 icosahedral particles showed well-resolved S domains with clearly visible features, and low contrast P domains.

Smaller particles were picked and classified separately (Figure 4-15B). 56,732 particles were used for 3D reconstruction, which revealed a T=1 icosahedral capsid. The shell of the particles was resolved to a nominal resolution of 3.9 Å. GI.1 S domain monomers could be fitted unambiguously into the densities and revealed the icosahedral cage of the T=1 capsid (Figure 4-16A/B). The closed shell consisted of 60 individual VP1 subunits. The P domains could not be resolved in this structure and appeared as smeared densities (Figure 4-16C/D). The resolution of the shell indicated that in general the dataset was of good quality and the lack of resolution in the T=3 particles and the T=1 P dimers was likely caused by heterogeneity within the particles. Surprisingly, the densities corresponding to the P dimers appeared to be located at the three-fold axes, instead of the two-fold axes.

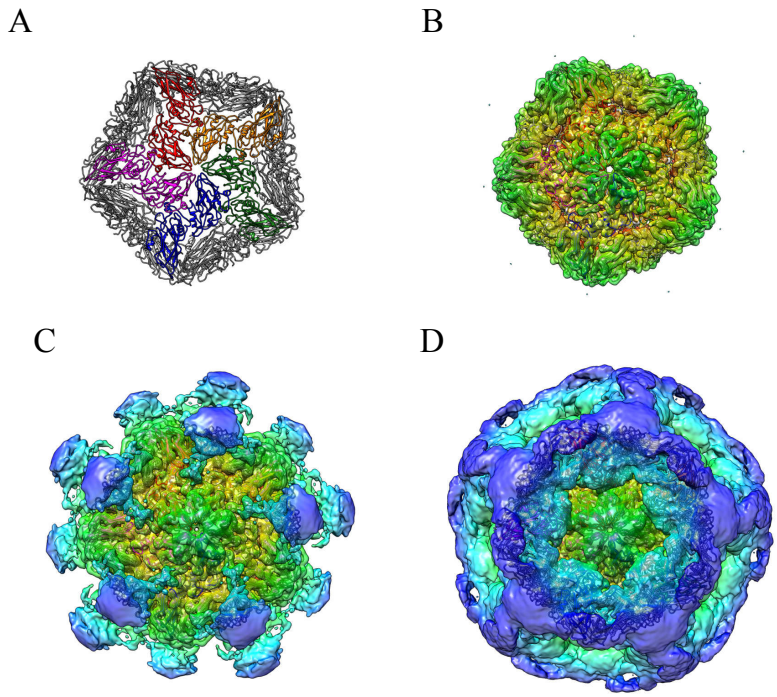

Figure 4-16 | Structure of the GI.1 T=1 icosahedral particle. (A) Fitted X-ray crystal structures of the GI.1 S domain (PDB: 1IHM) revealed the icosahedral cage of the particle. The S domain dimers around the five-fold axes are colored. (B) Structure at a threshold of 0.3 shows only the shell. Fitted into the structure are the S domains of GI.1, as shown in (A). (C) At a threshold of 0.23, a density was visible at the three-fold axes, with three spikes extending out to the five-fold axes. (D) At a threshold of 0.15, also densities at the two-fold axes were observable.

To improve the resolution of the smeared P domains, we applied focused reconstruction, but resolution was still limited. Nevertheless, two different main classes emerged after this classification: One with the P domains at the expected position at the two-fold axes with three P domain dimers located around the three-fold axes and one where the P domains appeared to form a trimeric assembly at the three-fold axes. However, resolution was not sufficient to allow detailed analysis of the complex. Nevertheless, this suggests that in this particle the P domain might form trimeric complexes instead of the typical dimeric arch like structures. Higher resolution information would be required here, in order to characterize this apparently trimeric complex in detail.

4.4. Discussion

Neutralizing antibodies represent one promising class of potential antivirals against norovirus. High-risk populations could be treated with passive immunoprophylaxis or immunotherapy to prevent acute norovirus outbreaks. Antibodies are currently evaluated for their potential to combat different viral infections in clinical trials, such as cytomegalovirus, influenza or respiratory syncytial virus (64, 74, 80).

Numerous antibodies have been described that are able to block the HBGA binding of VLPs to HBGAs in surrogate assays (26, 118, 120, 122). The antibodies we tested in our array were raised against GI.1 and many of those were able to detect other GI genotypes as well, indicating that these cross-reactive antibodies bound to parts of the VLP that are conserved between the different genotypes. The tested GI VLPs exhibit amino acid identities ranging from 67,16% (GI.3 Kashiwa645 to GI.2 Funabashi258 and GI.2 Southampton) to 99.63%, (GI.2 Funabashi258 and GI.2 Southampton). The most sequence differences were located in the P2 subdomain. Therefore it is conceivable that the non-cross-reactive antibodies bound to the P2 subdomain. Of note, this subdomain contains the HBGA binding site (19, 21, 29). Five antibodies were able to block HBGA binding. As these inhibiting antibodies were not cross-reactive, it is likely that these antibodies bound to the P2 subdomain, thereby blocking access to the HBGA binding site on the VLPs.

Cross-reactivity plays a vital role in determining whether a potential agent could be used as an efficient antiviral. This is particularly true for norovirus, where a multitude of strains are existing and new strains are emerging constantly (187). Unfortunately, the only inhibiting antibodies we discovered were not cross-reactive against other strains and could therefore most likely not serve as a potent antiviral against norovirus, especially as GI infections are comparably rare. Moreover, blockage potency of the antibodies was relatively low compared to other previously described norovirus specific antibodies (26, 118).

Conversely to the antibodies, the HMO 2'FL showed a broad inhibition profile across all tested GI genotypes. Only for GI.4 Chiba virus, inhibition was too low to determine an IC_{50} value. In a prior HBGA binding study, it was determined that in contrast to GI.1, GI.2 and GI.3 VLPs, GI.4 VLPs were not able to bind synthetic H type 1/2/3, HBGA carbohydrates, suggesting differences in the HBGA binding sites of this genotype (185). These differences could also translate to a reduced affinity to 2'FL, as it blocks the HBGA binding site.

In recent years, Nanobodies have been extensively investigated as potential therapeutics (2, 180). Nanobodies have several advantages over conventional antibodies, such as their stability

and small size that could allow them to bind to occluded sites on the viral particle. In our GI.1 Nanobody study, we characterized three different GI.1 specific Nanobodies. We found that two of the Nanobodies (Nano-7 and Nano-62) bound to the P1 sub-region of the P domain. Modeling the X-ray crystal structure of the complex on to the intact particle revealed clashes with adjacent P domains and S domains, suggesting that in this P domain conformation the Nanobodies would be unable to bind. Steric hindrance between Nanobodies was also observed for Nano-94 that bound to the top of the P domain. Therefore, it is likely that the P domains structurally rearrange upon binding of the Nanobodies to allow full occupancy. This could be possible due to the flexible nature of the hinge region. Moreover, the VLPs appeared undistorted in EM, suggesting that the intrinsic flexibility allows Nanobody attachment to these occluded sites, to prevent disassembly of the particle. Likewise, with GII specific Nanobodies (101) and one antibody (69), clashing with the shell has been observed when modeling the X-ray crystal structure into the intact capsid. This suggests that the shift of P domains is a common occurrence and possible in both GI and GII noroviruses.

GI.1 and GII.10 VLPs exhibit marked differences in their P domains, with GI.1 P domains being lowered and GII.10 P domains being raised (69, 162). It was suspected that these differences could be due to the differences in visualizing techniques (X-ray crystallography versus cryo-EM) and that the pH and ionic strength of the crystallization conditions could contribute to the lowering of the P domains. Because of high heterogeneity in the sample, we could not solve the GI.1 structure in cryo-EM to resolve this issue. Nevertheless, recently a cryo-EM structure of GI.1 was solved that reported lowered P domains as well, suggesting this state could indeed be a feature of GI.1 noroviruses and was not caused by the crystallization conditions (82).

In context of the intact particles, Nano-7 exhibited a lowered maximal detection signal in direct ELISAs than Nano-94 and Nano-62. This might be due to steric hindrances in the particle that could prevent all binding sites from being occupied. When binding to P domains only, steric hindrance would not be a problem, thus explaining the similar detection levels that were observed in the binding ELISA using isolated P domains.

Despite the similarities of the binding sites of Nano-7 and Nano-62, only Nano-7 was able to efficiently inhibit the binding of VLPs to HBGAs (Figure 4-11). This suggests that small differences in binding can have a strong impact on inhibitory properties. This is also highlighted by the fact that Nano-62 bound to a similar binding site as GII specific Nano-26 (101), a Nanobody that efficiently disassembled VLPs upon binding. Conversely, Nano-7 did

not compromise particle integrity. As direct steric interference of the HBGA binding site can be ruled out, no clear mode of action could be defined for this Nanobody. However, our results indicated that this Nanobody has a very large footprint, burying more residues than any other norovirus-specific Nanobody characterized so far. It could be possible that binding to that site triggers internal rearrangements within the P domain that allosterically influence the HBGA binding site.

The third Nanobody studied here, Nano-94, had a distinct binding site, located at the top part of the P domain. This Nanobody most likely inhibited HBGA attachment by aggregation of the capsids. Particle aggregation has previously been observed for GII specific Nanobody Nano-32 as well (101). However, in this case, rearrangement of several loops in the P domain was observed that altered hydrophobicity of the capsid, which was not observed for Nano-94.

Furthermore, we showed that combinational treatment of Nanobodies and the HMO 2'FL led to improvement in attachment inhibition. Combination of 2'FL and Nano-94 could be defined as synergistic for several conditions. This increase in inhibition might occur as follows: Nano-94 binding led to inhibition of VLPs, and remaining available binding sites were then blocked by 2'FL attachment to the binding site. With the addition of Nano-94, the concentration of 2'FL was higher relative to the remaining free binding sites, explaining the synergistic effect. For Nano-7 the effect was defined as additive, but as no clear mode of inhibition was defined for Nano-7, also the additive effect could not be explained in detail. Most likely however, the additive effect was only caused by the increased total concentration of inhibitor in the sample. Nevertheless, we could show that the positive effect of combining two different compounds is not limited to a single mode of action of Nanobodies and could therefore be exploited in a therapeutic setting.

Nanobodies have shown promising results as treatments against various viral infections, such as HIV or influenza (39). One study demonstrated that a rotavirus-specific Nanobody could be used to treat human rotavirus induced symptoms in gnotobiotic pigs (214). Generally, Nanobodies are considered as safe and of high efficacy and are therefore of great interest as potential therapeutics (2, 152, 213). Combining these efficient antivirals with other compounds, such as the broadly-reactive compound 2'FL, could provide higher cross-reactivity of the antiviral and higher efficacy without increasing the individual dose of the active compounds. Different compounds can act together to increase their effects, or work independently on different target sites, to maximize the efficacy. For drug discovery, synergistic effects of compounds play a pivotal role and are investigated for a broad range of

different viruses, such as dengue virus or hepatitis C (51, 157, 161). Moreover, combined activity of antiviral compounds has also previously been shown for rotavirus, another gastroenteritis causing virus: Two studies found that plant-derived compounds were able to synergistically inhibit replication in *in vitro* experiments (94, 123).

So far, 2'FL has been shown to inhibit GI.1, GII.10, GII.4, GII.17 (98, 220) and also GI.2 and GI.3 as shown in this study. However, the IC_{50} values are relatively high. Nevertheless, as 2'FL is present in mother's milk with concentrations up to 20 g/l (16), corresponding to a molar concentration of ~40 mM. This shows that 2'FL is safe for consumption at high concentrations, even for infants. Combinatorial treatment of 2'FL with a more specific, but highly efficient compound could improve the degree of inhibition. It could also be possible to combine a Nanobody that inhibits the HBGA binding with a differently acting drug class, such as an RdRp inhibitor (170, 171), to target different stages of norovirus infection simultaneously. This method is employed in several drugs, such as the state-of-the-art HIV treatment, where three synergistically acting compounds are used to suppress different stages of the viral life cycle (17, 52, 107). Combination of differently acting drug classes can also prevent the emergence of escape mutants for specific antivirals, which is especially problematic in fast evolving viruses, such as norovirus.

In summary, we could show that norovirus HBGA attachment inhibition can be synergistically improved by combinatorial treatment. As in the case of norovirus, limited cross-reactivity between different genogroups is one of the major impediments for the development of antivirals, combination treatment could be a remedy and should be considered in further studies.

5. Chapter 2: Expression of GII.4 VP1 forms T=4 icosahedral particles

5.1. Summary

In this chapter we solved the structures of VLPs from different GII.4 variants using single particle cryo-EM. Surprisingly, we found that all examined GII.4 variants mainly formed particles of T=4 icosahedral symmetry. We showed that this is also the case for the vaccine candidate GII.4c, which could have implications for vaccine efficacy. Conversely, negative stain experiments suggested that the infectious virion has T=3 icosahedral symmetry, indicating that GII.4 VLPs mainly adopted a non-native conformation. Moreover, the formation of T=4 particles appeared to be independent of the expression system, as expression in insect as well as mammalian cells favored T=4 VLP formation.

5.2. Contributions

A part of the results in this chapter was published as:

Devant JM, Hofhaus G, Bhella D, Hansman GS. 2019. Heterologous expression of human norovirus GII.4 VP1 leads to assembly of T=4 virus-like particles. Antiviral Research 168:175-182

Figures were adapted from this publication, as mentioned in the figure legend. All experiments were performed by me. Dr. Götz Hofhaus helped with data collection and processing; Dr. David Bhella helped with data processing. The paper was written by Dr. Grant Hansman and me, and all authors commented on the manuscript.

5.3. Results

Structural analysis of GII.4 NSW-2012 VLPs

In recent years, structural studies on human noroviruses were mostly focusing on isolated P dimers, and information about intact particles was limited. Only two structures, of GI.1 (162) and GII.10 VLPs (69) were available, both of which were less clinically relevant genotypes. In order to gather additional structural information in terms of the intact particle, we decided to solve the structure of VLPs representing the clinically prevalent human norovirus genotype GII.4.

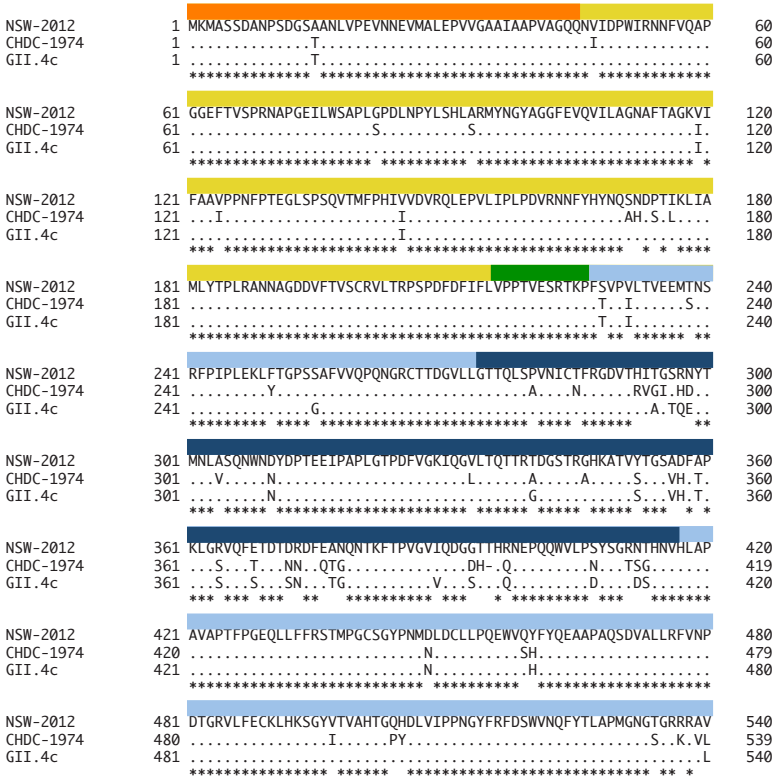

Figure 5-1 | Sequence alignment of GII.4 VP1. NSW-2012 (JX459908), CHDC-1974 (ACT76142), and GII.4c (153) VP1 amino acid sequences were compared in ClustalX (111). The N-terminus (orange), S domain (yellow), hinge region (green) P1 subdomain (light blue) and P2 subdomain (dark blue) are marked. The S domain exhibited the highest conservation rate, most substitutions were found in the P domain, especially the P2 subdomain. Compared to CHDC-1974, NSW-2012 and GII.4c had an amino acid insertion at position 394 (numbering according to NSW-2012). The figure was adapted from (41).

In our first analysis, we focused on two different GII.4 isolates from 1974 and 2012, termed CHDC-1974 and NSW-2012, respectively. Sequence alignment revealed that the genotypes had 89% sequence identity. Most substitutions (45 out of 54) were located in the P2 domain, whereas the hinge region and the S domain were mostly conserved (Figure 5-1). Additionally, NSW-2012 had a single aa insertion at position 394 compared to CHDC-1974.

Negative stain comparison of different norovirus VLPs

Negative stain EM revealed that the GII.4 VLP samples were homogenous and exhibited the typical norovirus characteristics, with clearly visible spikes on the surface. However, the diameters appeared enlarged compared to VLPs from other genotypes. GII.4 VLPs exhibited diameters of ~52 nm, whereas e.g. GII.10 and GI.1 VLPs, for which the structure had already been solved, had a smaller diameter of ~43 and 38 nm, respectively (69, 162).

Comparison of different genotypes revealed that in fact, exclusively GII.4 (CHDC-1974, Saga-2006, Yerseke-2006 and NSW-2012, both VP1 only and VP1/VP2 VLPs) exhibited these larger assemblies (Figure 5-2). All other examined genotypes, from both GI and GII, exhibited particle sizes between 40-45 nm. Interestingly, in several cases, smaller VLPs of ~28 nm could be observed as well. These particles were found for several different genotypes, e.g. GI.1, GII.4 or GII.10.

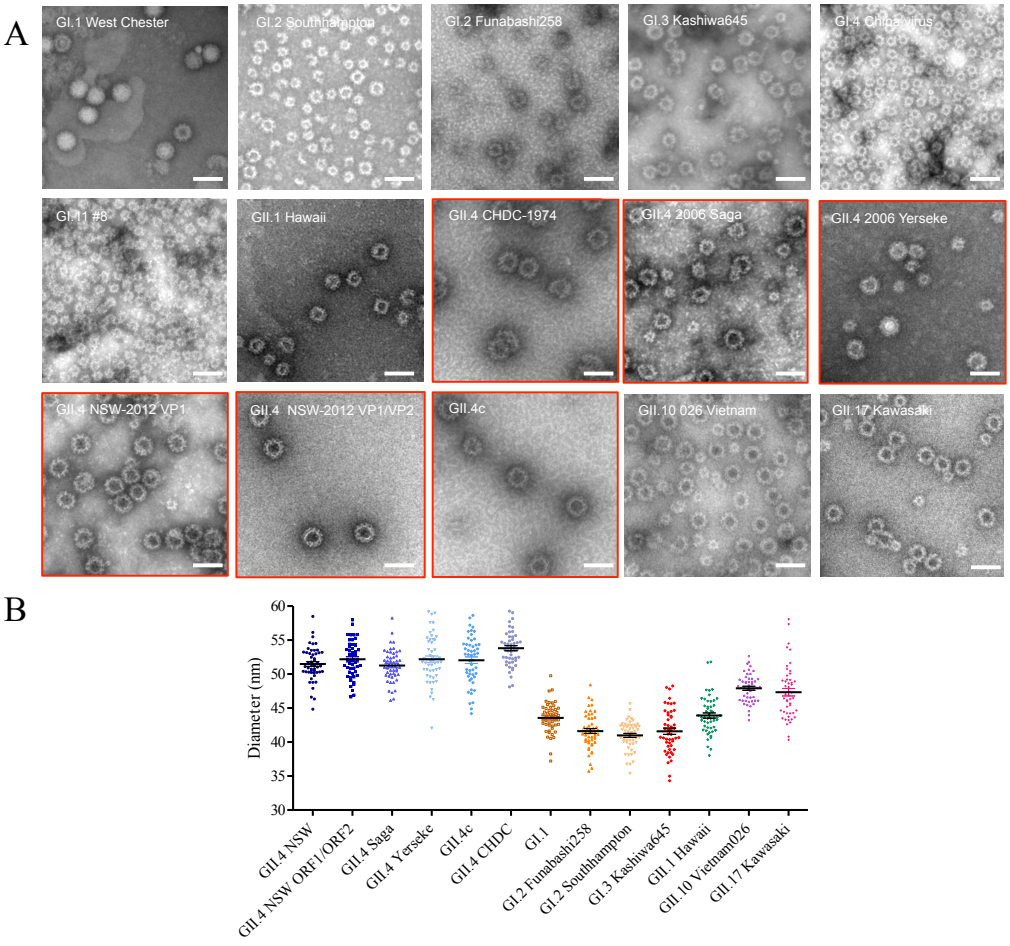

Figure 5-2 | Size comparison of different VLPs. (A) Negative stain EM micrographs of different norovirus VLPs. VLPs from GII.4 genotypes exhibit a larger diameter than VLPs from GI or GII.1 Hawaii, GII.10 026 Vietnam or GII.17 Kawasaki. The GII.4 genotypes are marked in red. The scale bar represents 50 nm. (B) Scatterplot of different VLP sizes. 50 single VLPs per genotype were measured in Fiji (182). GII.4 VLPs are marked in shades of blue.

Single particle analysis of GII.4 NSW-2012 VLPs

We applied single particle cryo-EM to determine the structure of NSW 2012 VLPs to a resolution of 7.3 Å. The particles were separated evenly in the ice and were mainly homogenous (Figure 5-3A/B). 364 images were acquired, from which 10,548 particles were used for the final icosahedral reconstruction of the structure, which had a resolution of 7.3 Å (Figure 5-3C).

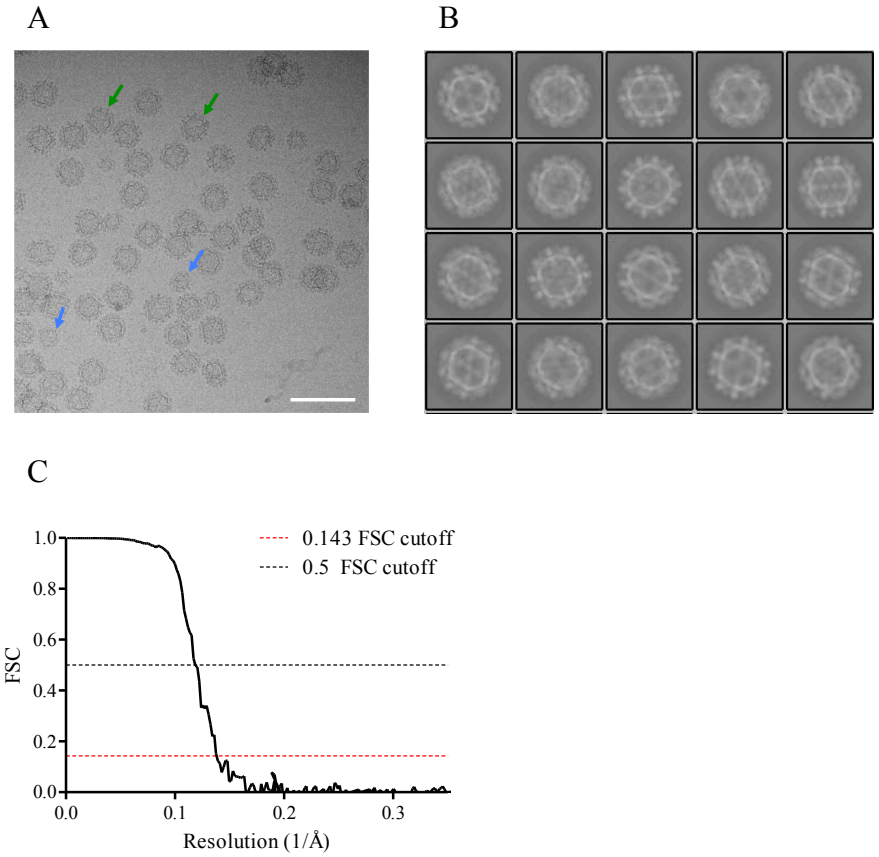

Figure 5-3 | Data processing of NSW-2012 VLPs. (A) Representative cryo-EM micrograph of NSW-2012 VLPs, acquired at 64,000× magnification. The arrows indicate VLPs with 46 nm (blue) nm and 50 nm (green) diameters. The scale bar represents 100 nm. (B) 2D classification of T=4 icosahedral particles. (C) FSC plot of the icosahedral reconstruction of NSW-2012 VLPs reveals a resolution of 7.3 Å (0.143 FSC cut-off) and 8.2 Å (using 0.5 FSC cut-off). The figure was adapted from (41).

Interestingly, NSW-2012 VLPs exhibited T=4 icosahedral symmetry (Figure 5-4A), meaning the VLPs were composed of 240 copies of VP1, instead of 180, which would correspond to T=3 icosahedral symmetry. The VLPs had an inner and outer diameter of 32 and 50 nm, respectively (Figure 5-4B). The shell volume was calculated to be ~12,724 nm^3. This is ~2.1× the volume of GII.10 VLPs, which represent a typical calicivirus structure (69). With an inner diameter of 23 nm, the volume of GII.10 was calculated to be ~5,985 nm^3.

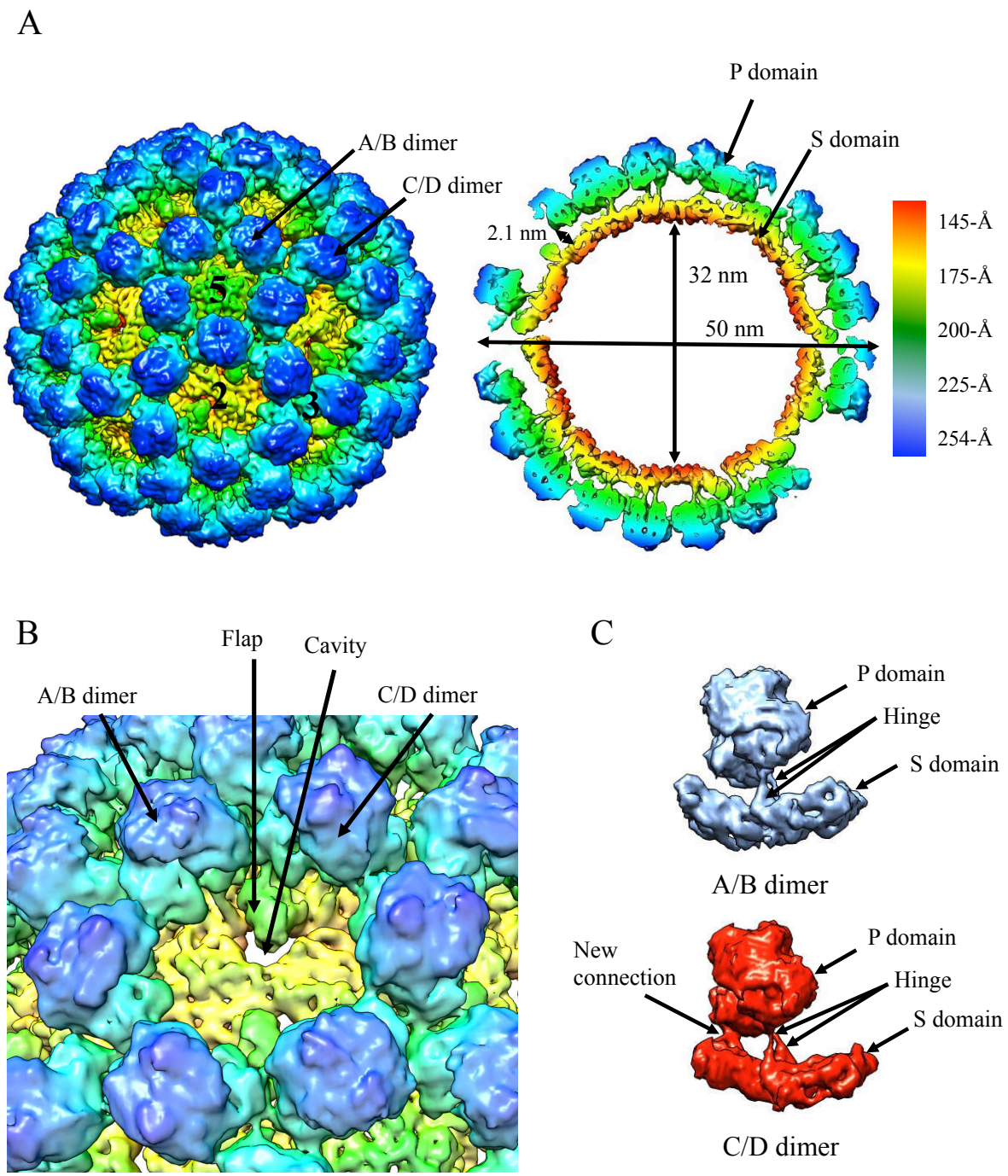

Figure 5-4 | Cryo-EM reconstruction of NSW-2012 VLPs. (A) The left side shows an intact particle, exhibiting T=4 icosahedral symmetry. Symmetry axes are labeled as 2, 3 and 5. The VLPs were composed of 240 VP1 molecules that formed two types of dimers; A/B and C/D. B, C and D subunits were at the icosahedral two-fold axes, whereas A subunits were located around the icosahedral five-fold axes. The right image is a cutaway section of the particle, indicating the inner and outer diameter (32 and 50 nm, respectively) and the elevation of the P domains (2.1 nm). (B) The S domain associated with the D subunit was forming a cavity and flap like structure that was disrupting the shell. (C) For NSW-2012 T=4 VLPs, both A/B and C/D dimers were in a bent S domain conformation. For the C/D dimer, an additional connection was visible between S domain and the P1 subdomain. The figure was adapted from (41).

In the T=4 icosahedral capsid, VP1 adopted four quasiequivalent conformations, termed A, B, C and D that were forming two distinct classes: A/B and C/D. 60 A/B and 60 C/D dimers

formed the capsid. This was markedly different from T=3 particles, which were assembled from only 60 A/B and 30 C/C dimers. The A subunit was located at the five-fold axes, whereas B, C and D subunits alternated around the two-fold axes (Figure 5-4A/B). Close inspection of the isolated dimers showed that both A/B and C/D dimers exhibited a similar S domain conformation. In both cases, the S domain was in a convex conformation with upwards facing S domains (Figure 5-4C). Conversely, in GI.1 only A/B dimers exhibited a convex conformation, whereas the C/C dimers were flat (162).

In both A/B and C/D dimers, the P domains were raised 21 Å off the shell. Therefore, the structure more closely resembled the GII.10 structure (69), than the structure of GI.1 (162), even though in GII.10 the P domains were raised only 14 Å.

Another main difference to typical T=3 structures was found in the shell. Usually, the S domains form a contiguous capsid, protecting the enclosed RNA genome. In the T=4 particles the shell was disrupted by a cavity and flap like structure (Figure 5-4B and Figure 5-5). This feature was located at the two-fold axes and formed by the S domain of subunit D, likely a result of the convex C/D dimer.

For verification of the structure, we modeled the X-ray crystal structures of the GI.1 S domain (PDB: 1IHM) and the P domain of NSW-2012 [PDB: 4OOS (189)] into the obtained density map (Figure 5-5). The P domains were fitted unambiguously into both A/B and C/D dimers, with cross-correlation coefficients of 0.96, suggesting that no large structural rearrangements in the P domain occurred between A/B and C/D dimers. For the S domain, the model could be fitted into the A, B and C subunits, but for the elevated S domain of the D subunit, it had to be shifted upwards to accommodate the formation of the flap like structure. Nevertheless, the X-ray crystal structure could be fitted easily into the density, indicating that mainly rigid body movement was involved in this structural rearrangement. A connection between the C-terminus of the P domain and the S domain was present that appeared to stabilize this untypical conformation (Figure 5-4C and Figure 5-5B).

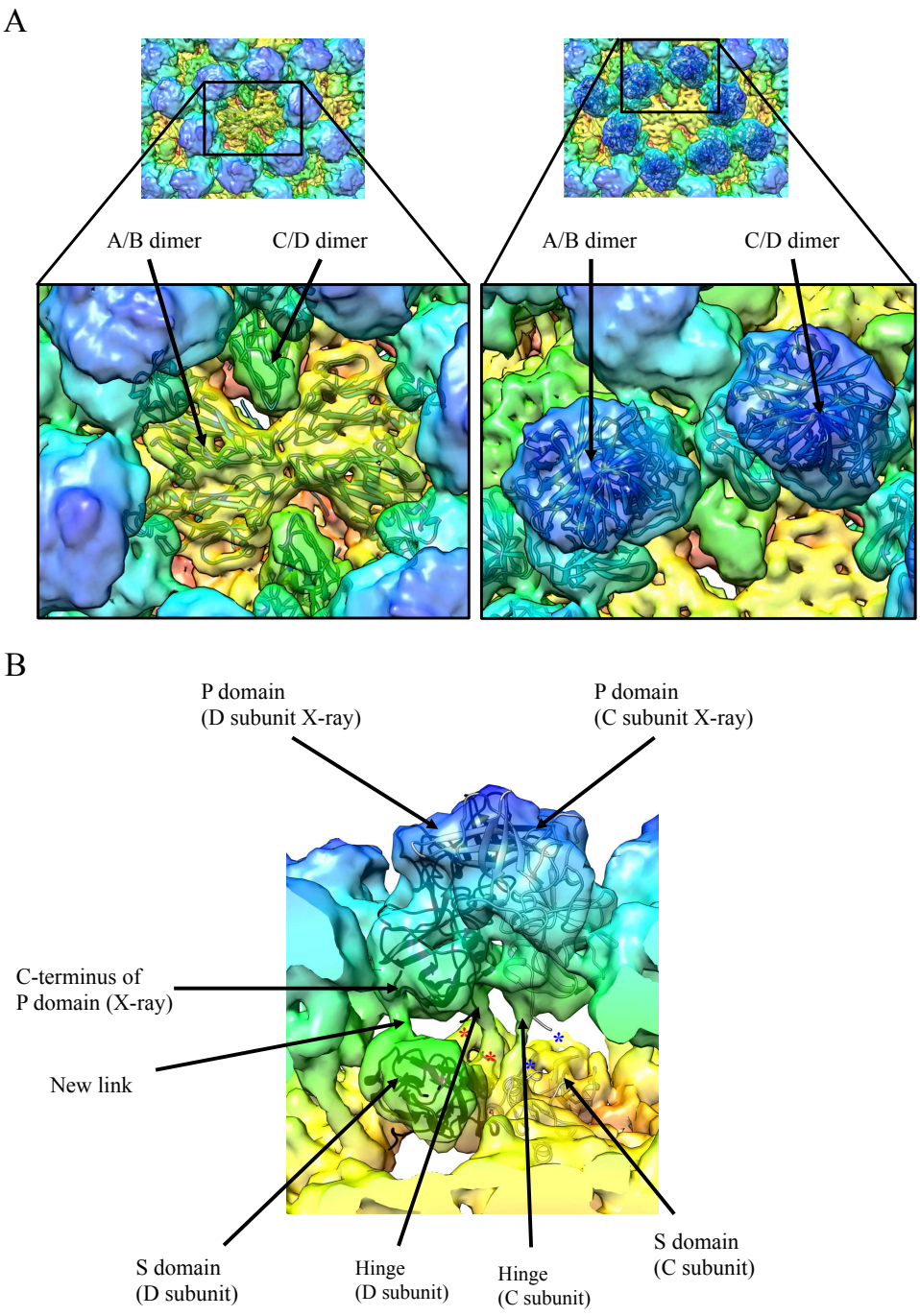

Figure 5-5 | X-ray crystal structures of NSW-2012 P domain and GI.1 S domain fitted into the density map of NSW-2012 VLPs. (A) Left shows a close-up on the three-fold axis, with GI.1 S domain (PDB: 1IHM, cartoon) fitted into A/B and C/D densities. Right shows a close-up on a two-fold axis, with NSW-2012 P domain X-ray crystal structure (PDB: 4OOS, cartoon) fitted into A/B and C/D P domain dimers. (B) Close-up on a single C/D dimer of NSW-2012. The new connection between S and P domain is visible. The asterisk is representing the hinge region that was not visible in either of the X-ray crystal structures. The hinge region was visible and connected S and P domain in both C subunit (blue) and D subunit (red). The figure was adapted from (41).

T=3 icosahedral symmetry of GII.4 NSW-2012 VLPs

Most of the VLPs in the raw micrographs were homogenous and exhibited the untypical T=4 symmetry. Notably, a small subset of 391 particles exhibited a smaller diameter, indicating a native T=3 icosahedral symmetry (Figure 5-6A). Icosahedral reconstruction of these particles revealed that in fact the particles exhibited T=3 icosahedral symmetry (Figure 5-6C). The particle had an inner diameter of ~24 nm, and an outer diameter of ~46 nm, corresponding to the particle size that has been determined for GII.10 VLPs (69).

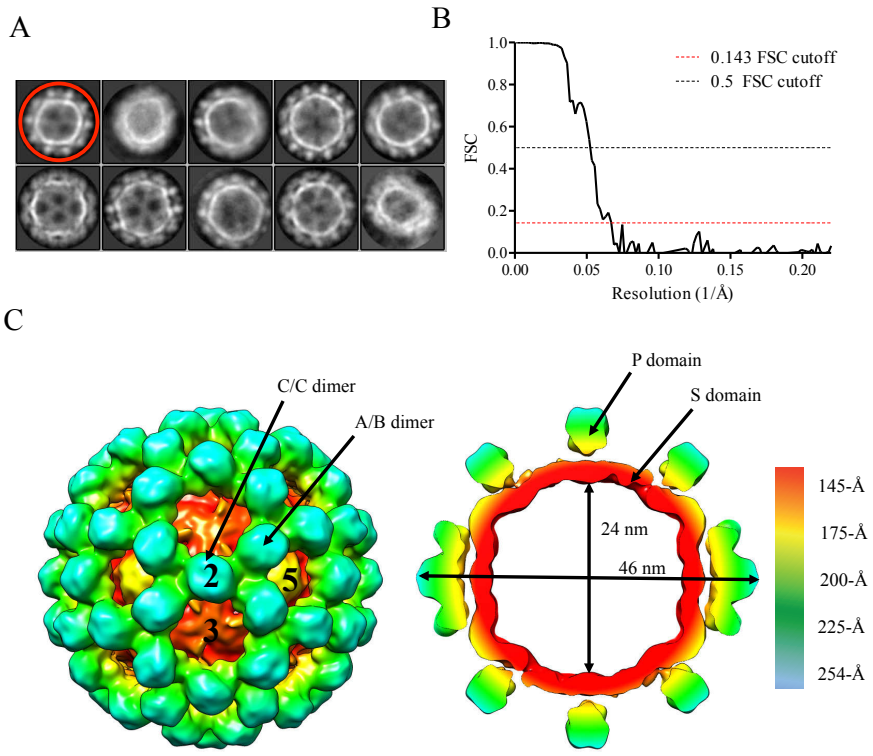

Figure 5-6 | Cryo-EM structure of NSW-2012 T=3 icosahedral VLPs. (A) 2D classification of 1,780 manually picked particles showed two differently sized assemblies. The first class (red circle) contained 391 particles with a smaller diameter and was used for further refinement. (B) The FSC plot of the T=3 VLPs indicates a resolution of 15 Å and 19 Å, using 0.143 and 0.5 FSC cut-off, respectively. (C) The left side shows NSW-2012 T=3 VLP structure with symmetric axes labeled (2, 3, 5). The right figure is a cutaway section, indicating an inner and outer diameter of 24 and 46 nm, respectively. At this low resolution, the hinge region was not resolved, but a large gap between S and P domain suggests that the P domains were raised up from the shell. The figure was adapted from (41).

Due to the low number of particles, the structure was only solved to a maximal resolution of 15 Å (Figure 5-6B). The hinge region was not resolved at this resolution, but a gap between S and P domain indicated that the P domains were raised up from the shell, similarly as in the T=4 icosahedral particle. Interestingly, it appeared as if the shell was fully closed in this particle. However, higher resolution information would be necessary to unambiguously answer this question.

Comparison of different GII.4 VLP preparations

Comparison of negative stain images of different GII.4 VLPs preparations revealed that the diameter was comparable across all samples, suggesting that the T=4 particles are formed reproducibly, excluding batch effects. To eliminate the possibility that the T=4 particles were produced due to an error in the expressed VP1 sequence, we cloned and expressed a new construct of GII.4 NSW-2012 VP1 and VP1/VP2. However, also in these cases, the diameter of the resulting VLPs suggested the formation of T=4 particles.

In general, our results revealed that VP1 from NSW-2012 mainly formed two types of particles, with T=4 and T=3 icosahedral symmetry. Surprisingly, the non-native T=4 symmetry was highly favored and only ~5% of the population exhibited T=3 symmetry. This proportion was found in several different VLP preparations.

Structural analysis of GII.4 CHDC-1974 VLPs

In order to verify T=4 symmetry as a universal property of GII.4 norovirus VLPs, we determined the structure of GII.4 CHDC-1974 VLPs. In raw micrographs the VLPs appeared mostly monodisperse and homogenous, with a similar appearance to GII.4 NSW-2012 VLPs (Figure 5-7A/B). 42,485 particles were used for the final reconstruction that had a resolution of 6.1 Å (0.143 FSC cut-off, Figure 5-7C).

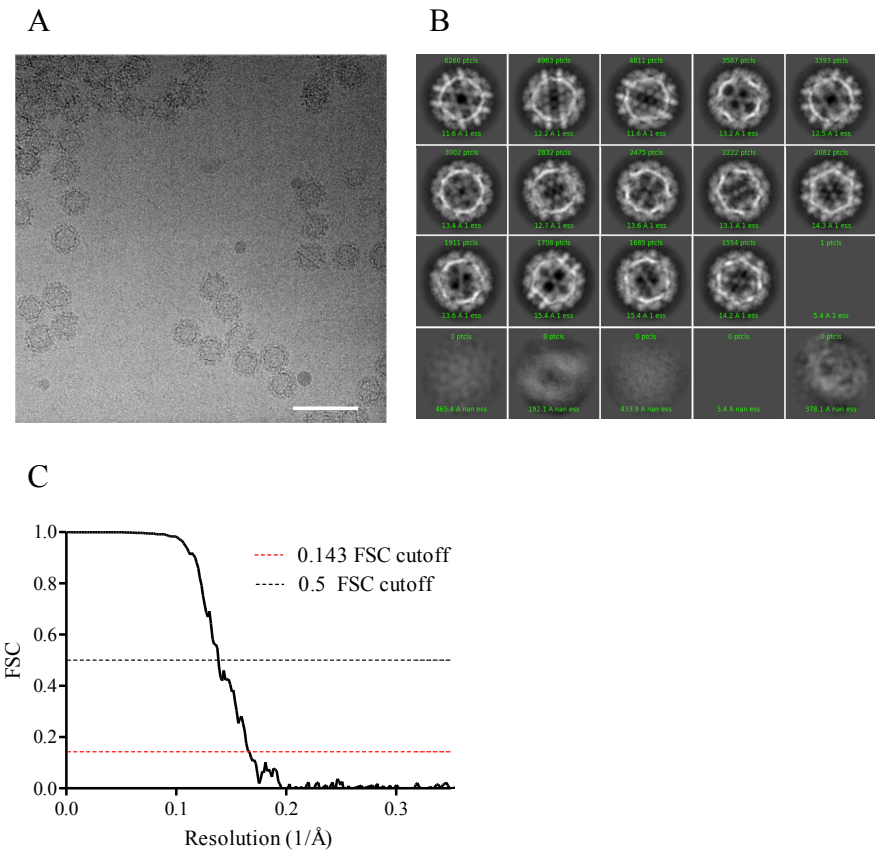

Figure 5-7 | Data processing of CHDC-1974 VLPs. (A) Representative cryo-EM micrograph of CHDC-1974 VLPs, acquired at 64,000× magnification. The scale bar represents 100 nm. (B) 2D classification of CHDC-1974 VLPs. (C) The FSC plot of the icosahedral reconstruction indicates a resolution 6.1 Å and 7.2 Å using FSC cut-off at 0.143 and 0.5, respectively. The figure was adapted from (41).

In general, the structure of the GII.4 CHDC-1974 VLPs closely resembled the structure of the newer GII.4 NSW-2012 isolate. 240 copies of VP1 formed 60 A/B and 60 C/D dimers that made up the T=4 icosahedral capsid (Figure 5-8A).

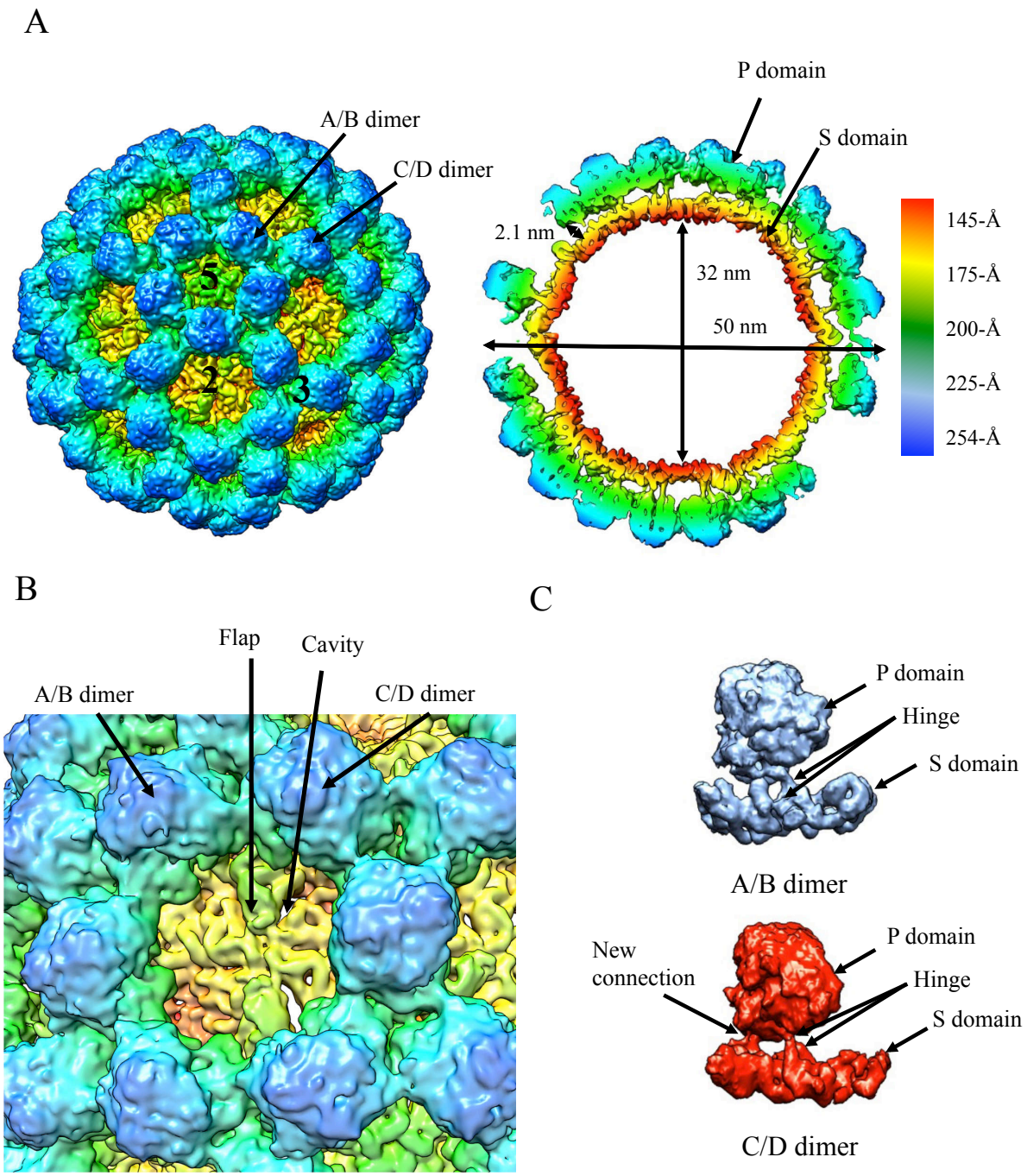

Figure 5-8 | Cryo-EM structure of CHDC-1974 VLPs. (A) Shown on the left is an intact particle with T=4 icosahedral symmetry. The symmetry axes are labeled accordingly (2, 3, 5). The VLPs contained 240 subunits of VP1 that were assembling into distinct dimers, A/B and C/D. A subunits were located at the five-fold axes, whereas B, C and D subunits were alternating at the two-fold axes. On the right is a cutaway section, which indicates the diameters of the structure (32 nm inner diameter, 50 nm outer diameter). The hinge region was visible and measured 2.1 nm. (B) The cavity and flap like structures were also observed on the CHDC-1974 two-fold axes. As in NSW-2012, the structure was formed by the D subunit S domain. (C) Both A/B and C/D dimers exhibited a bent S domain conformation, with the S domain being slightly less bent in the C/D dimer. Also here, an additional connection between S and P domain was found in the C/D dimer. The figure was adapted from (41).

The inner diameter was measured to be 32 nm, the outer diameter was 50 nm, and the hinge region was 2.1 nm (Figure 5-8B). Also in this structure, the shell was disrupted by a cavity

and flap like structure, although the curvature was slightly less pronounced than in NSW-2012 VLPs (Figure 5-8B). Concomitantly, the C/D dimer was less convex than the A/B dimer. Nevertheless, the connection between S domain and C-terminus of the P domain was still observed (Figure 5-8C).

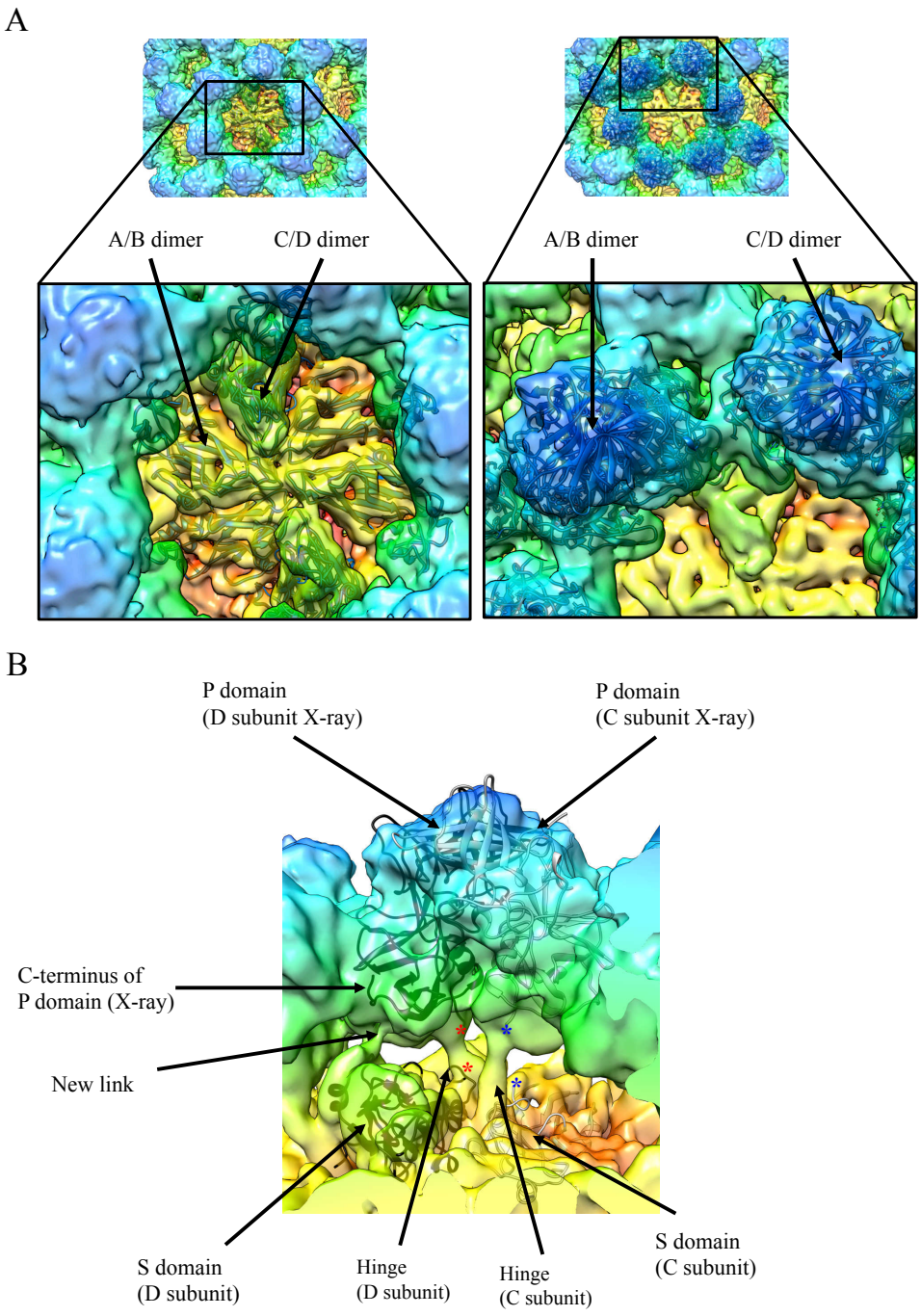

Figure 5-9 | X-ray crystal structures of CHDC-1974 P domain and GI.1 S domain fitted into the density map of CHDC-1974 VLPs. (A) In the left image, the X-ray crystal structure of GI.1 S domain (PDB: 1IHM, cartoon) was fitted into the S domain densities at a two-fold axis. On the right, the X-ray crystal structure of CHDC-1974 P domain (PDB: 5IYN) was fitted into P domain densities. (B) Detailed view of a single CHDC-1974 C/D dimer. The new connection between S domain and P1 subdomain is shown. The asterisks are representing the hinge regions that are not visible in the X-ray crystal structures and could not be fitted into the densities of the C subunit (blue) and D subunit (red) hinge regions. The figure was adapted from (41).

The X-ray crystal structure of GII.4 CHDC-1974 P domain (PDB: 5IYN) and GI.1 S domain (PDB: 1IHM) were fitted into the density well (Figure 5-9). Similarly to the NSW-2012 structure, the S domains appeared to be conserved, and only fitting of the D subunit S domain the X-ray crystal structure had to be positioned up, in order to fit into the flap-like density.

Vaccine candidate GII.4c VLPs

A norovirus vaccine candidate, using GII.4c VLPs as immunogen, has recently entered phase IIb clinical trials (112, 208). As our experiments suggested that the formation of T=4 particles is GII.4 specific, we wanted to determine, whether GII.4c would form T=4 symmetric particles as well, as this could have implications on the efficacy of the vaccine. The sequence of GII.4c VLPs is a consensus sequence derived from the sequences of GII.4 2002 Houston, 2006a Den Haag and 2006b Yerseke (153), but also closely matched the sequence of GII.4 NSW-2012 and CHDC-1974 VLPs, with sequence identities of 94.26% and 92.39% respectively (Figure 5-1).

As for other tested VLPs, GII.4c VLPs were expressed in HighFive insect cells, using a baculovirus expression system. In negative stain images, the VLPs exhibited a diameter comparable to other GII.4 VLPs, suggesting that also here, T=4 particles were formed. The sample appeared to be heterogeneous, with smaller particles present, that most likely were of T=1 and T=3 symmetry. In a first test we could show that the VLPs were functional and could bind to A and B saliva samples and PGM.

Separation of differently sized GII.4c particles and antigenic differences

Because of the heterogeneity in the sample, we tried to separate the particles by size in a sucrose gradient centrifugation or size exclusion chromatography. Two bands were visible in the sucrose gradient, corresponding to T=1 and a mixture of T=3 and T=4 particles, as confirmed by negative stain EM.

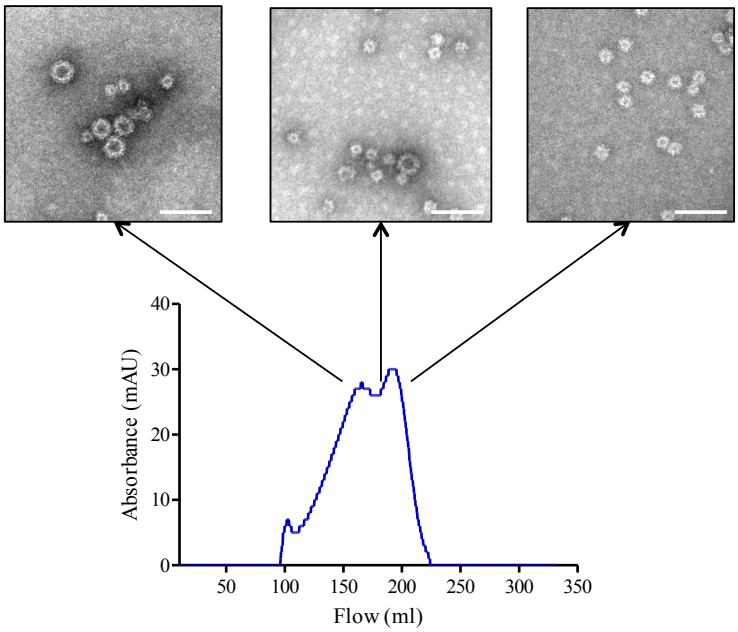

Figure 5-10 | Size exclusion chromatography of purified GII.4c VLPs. The chromatogram exhibits two overlapping peaks at 150 and 200 ml flow. Negative stain EM verified that the first peak contained mainly T=4 icosahedral symmetric particles, whereas the second peak contained the small T=1 icosahedral particles. No peak corresponding to T=3 icosahedral particles was observed. The scale bar in the negative stain EM micrographs corresponds to100 nm.

Separation using size exclusion chromatography only succeeded to separate T=1 particles from the larger particles, only two peaks were visible in the chromatogram (Figure 5-10). Negative stain EM confirmed that the first peak mainly consisted of T=1 particles, whereas the second peak contained both T=3 and T=4 particles. Unfortunately it was not possible to separate T=3 and T=4 particles.

Therefore, in order to identify if there are antigenic differences between differently sized particles, we compared the antigenicity between separated T=1 and T=3/T=4 particles.

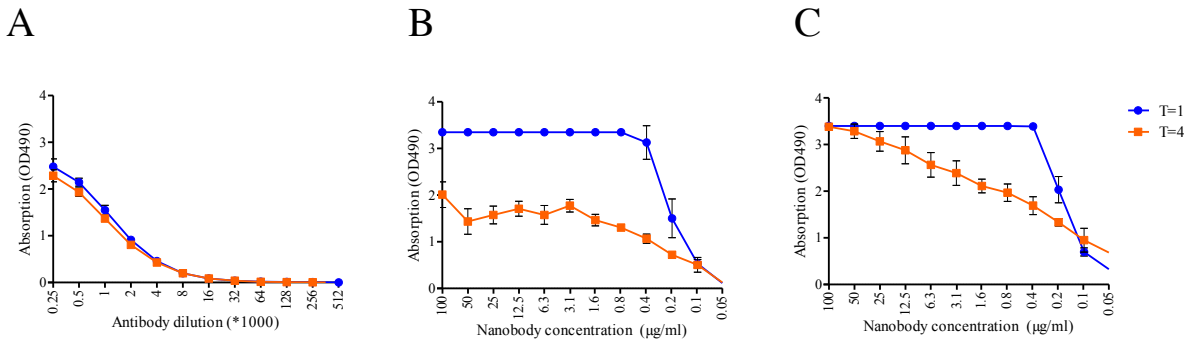

Figure 5-11 | Antigenic comparison of GII.4c T=1 and T=4 particles using direct binding ELISA. (A) Binding curves of a polyclonal GII.4 specific antibody to T=1 (blue) and T=4 (red) particles. The binding curves exhibited a similar plateau value and slope for both VLP types. (B) Antigenic comparison using Nano-26 indicates a stronger binding to T=1 particles, as shown by a higher plateau value. (C) Antigenic comparison using Nano-85 exhibits a similar starting value, but lower affinity to T=4 particles at lower Nanobody concentrations.

Previous studies revealed that the GII.10 specific Nanobodies Nano-85 and Nano-26 were able to bind GII.4 VLPs, with distinct epitopes at the lower part of the P domain (99, 101). In a binding ELISA, both Nanobodies had higher binding affinities to the smaller particles than to larger assemblies (Figure 5-11B/C). For Nano-26, maximum absorption was measured for T=1 particles up to a concentration of 0.4 µg/ml. In contrast, the measured maximum absorption value for T=3/4 particles was ~two-fold lower. For Nano-85, the maximum absorption was similar for both T=1 and T=3/4 particles at 100 µg/ml. However, for larger particles the binding value already declined from this concentration, whereas maximum absorption was measured until 0.4 µg/ml Nano-85 concentration for T=1 particles. Conversely, binding assays using a polyclonal GII.4 specific antibody revealed no difference in binding to either large or small VLPs (Figure 5-11A) and the slope of the dilution curve and maximum absorption value were similar.

Structural analysis of GII.4c particles

Despite the heterogeneity in the sample, we proceeded with determining the structures of the VLPs by single particle cryo-EM, as the particles can be separated computationally. Structure determination of the differently sized particles was done by collecting a large dataset of heterogeneous particles and picking and refining the differently sized assemblies separately. In general, the particles were mostly monodisperse with few aggregates of the particles (Figure 5-12A).

We found that 56% of the particles exhibited T=4 icosahedral symmetry and these particles were refined to 4.2 Å resolution (Figure 5-12B/C). The particle had an outer and inner diameter of 50 and 32 nm, respectively. The particle consisted of 240 copies of VP1 that exhibited four quasiequivalent conformations (A, B, C and D). These gave rise to 60 A/B and C/D dimers each. As described for GII.4 NSW-2012 and CHDC-1974, the A subunits assembled at the five-fold axes, and B, C and D subunits alternated at the two-fold axes.

The structures closely resembled the structures of GII.4 NSW-2012 and CHDC-1974. P domains were raised ~20 Å, and the cavity and flap like structure was present. This revealed that also in this structure, both A/B and C/D dimers had a convex S domain conformation (Figure 5-13B).

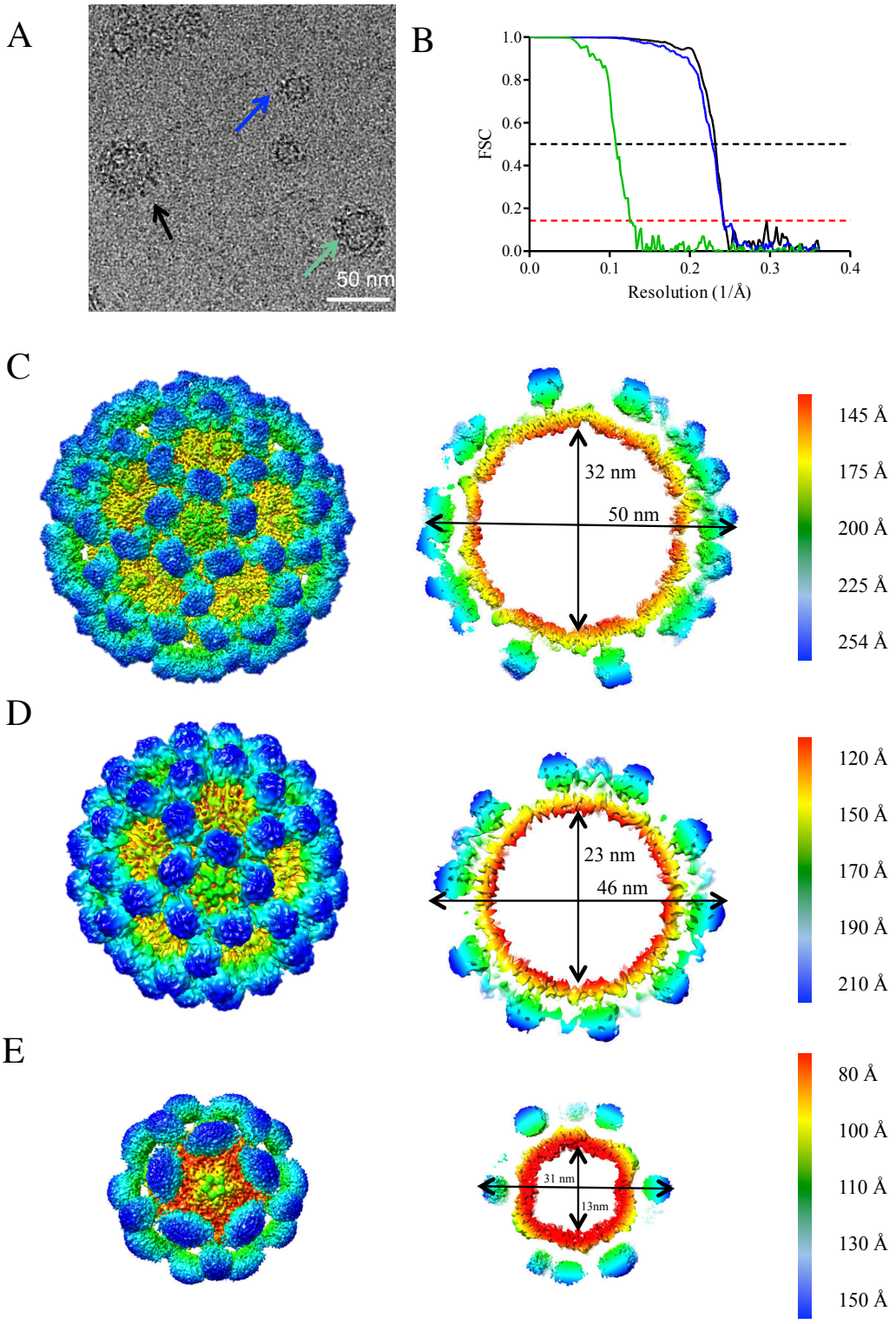

Figure 5-12 | GII.4c VP1 assembles in VLPs of various sizes. (A) Cutout of a representative cryo-EM micrograph of GII.4c VLPs shows T=4 (black arrow), T=3 (green arrow) and T=1 (blue arrow) particles. The scale bar indicates 50 nm. (B) FSC curves indicate resolutions of 4.2 Å for both T=1 (blue) and T=4 (black) particles and 8 Å for T=3 icosahedral VLPs (green), using the cut-off of 0.143 (red dashed line, black line shows FSC cutoff of 0.5). (C) T=4 icosahedral structure of GII.4c VLPs. The VLP has an inner and outer diameter of 32 and 50 nm, respectively. These particles comprised 240 copies of VP1 that form A/B and C/D dimers. (D) T=3 icosahedral structure of GII.4c VLPs. T=3 icosahedral symmetric particles consisted of 180 VP1 molecules, assembling into A/B and C/C dimers. The inner diameter was 23 nm; the outer diameter was measured to be 46 nm. (E) T=1 icosahedral structure of GII.4c VLPs. The particles were assembled from 60 VP1 proteins and had an inner and outer diameter of 13 and 31 nm, respectively. All structures are colored by radius, as indicated by the respective color scales.

The lowest number of particles (~20%), was found in native sized T=3 icosahedral assemblies (Figure 5-12B/D). These particles were only refined to 8 Å resolution. The VLPs consisted of A, B and C quasiequivalent conformations that formed 60 A/B and 30 C/C dimers. The diameter of 46 nm was similar to what we found for the low-resolution structure of the T=3 icosahedral GII.4 NSW-2012 VLPs, suggesting these structures are conserved between different genotypes. The inner diameter of the particle was 23 nm. Comparison of the P domain conformation between T=3 and T=4 particles revealed that both P domains were elevated off the shell and, despite the differences in symmetry, the hinge region appeared similar (Figure 5-13A). This indicated that the raise of the P domain was not influenced by particle symmetry.

Usually, the S domain of norovirus particles is relatively rigid, which enables determination of the S domain to a comparably high resolution. In this structure however, the S domain at the three-fold axis was not clearly resolved. Therefore, we applied focused reconstruction on this region, for further structural analysis.

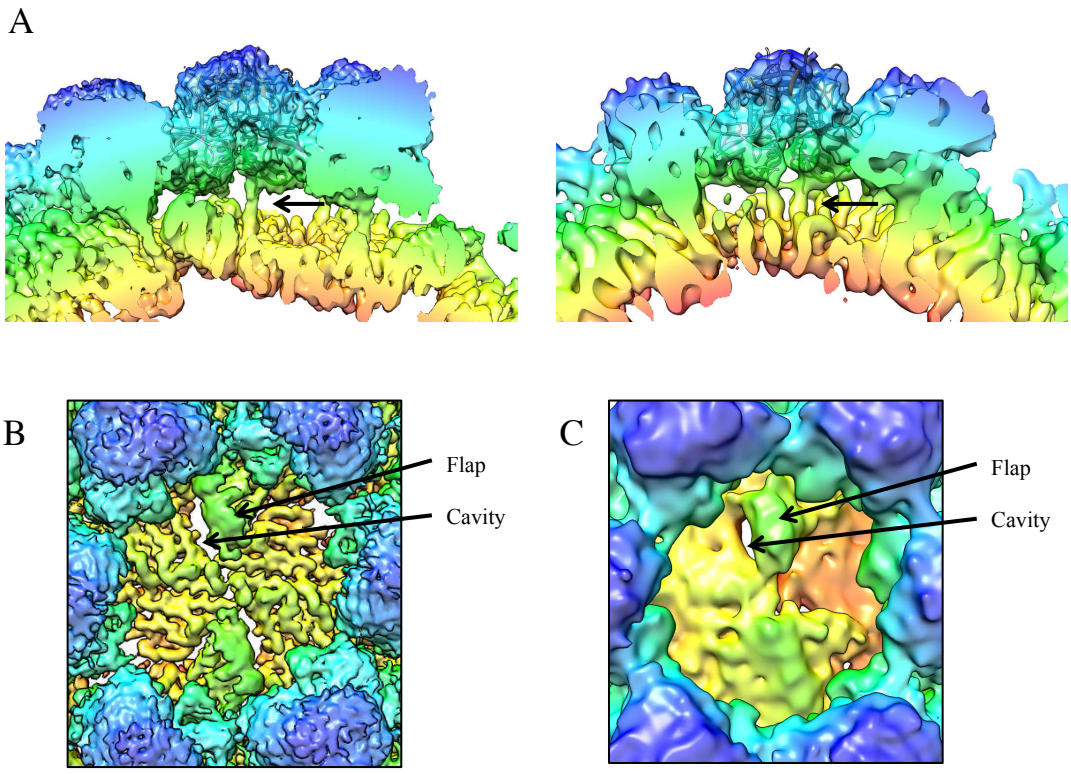

Figure 5-13 | Comparison GII.4c VLPs with T=4 and T=3 icosahedral symmetry. (A) Close-up view of a single C/D dimer of the T=4 particle (left) and a C/C dimer of a T=3 symmetric particle (right). The X-ray crystal structure of GII.4 NSW-2012 (PDB: 4OOS, cartoon) was fitted into the P domain dimers. Both P domain dimers were raised up from the shell by an extended hinge region (black arrows) that measured 2.1 nm. (B) Close-up view of the two-fold axis of a T=4 icosahedral particle. A flap and cavity like structure, formed by the S domain of the D subunit was disrupting the shell. (C) Close-up view of a focused reconstruction class of the three-fold axis of the T=3 icosahedral particle. Despite the low resolution, the capsid shell appeared disrupted by a cavity and flap like structure, comparably as in the T=4 particle. Here, the flap structure was formed by the S domain of a C subunit.

Interestingly, we found several classes, in which the S domain exhibited a similar conformation to what we found for the T=4 icosahedral particle: Two S domains, associated with the C/C dimer, were raised up and forming a flap-like structure that disrupted the closed shell (Figure 5-13C). Although resolution was limited, these results indicated that in T=3 icosahedral particles the shell was not fully closed as well. This is at odds with the results from the GI.1 X-ray crystal structure, where the S domains at the three-fold axis were coming together to form a fully closed capsid (162), but explains the lower resolution found for the S domains.

Approximately 23% of particles were small particles that exhibited T=1 icosahedral symmetry (Figure 5-12E). The particles were assembled from 60 VP1 monomers that form 30 identical dimers. For these particles however, we found that only the shell was well resolved, whereas the P domains appeared as blurred densities. This density blurring indicated pronounced movement of the dimers. Because of this, the hinge region could not be resolved, but a large gap existed between P and S domains. This suggested that in this structure the P domains were raised. Superposition of the density onto the T=3 and T=4 particles verified this theory. Moreover, the superposition of the particles suggested that in the T=1 particle, the P domains were separated stronger than in the larger sized assemblies.

A

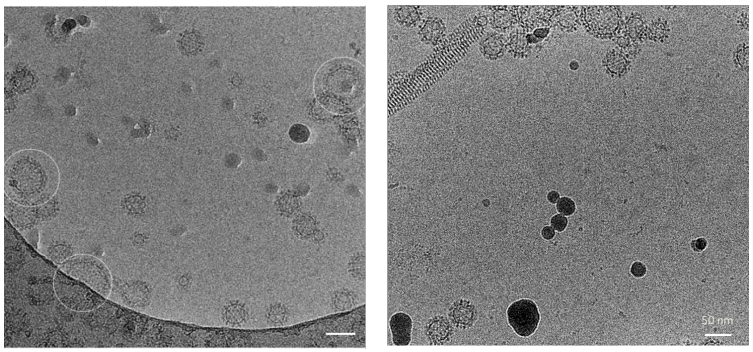

B

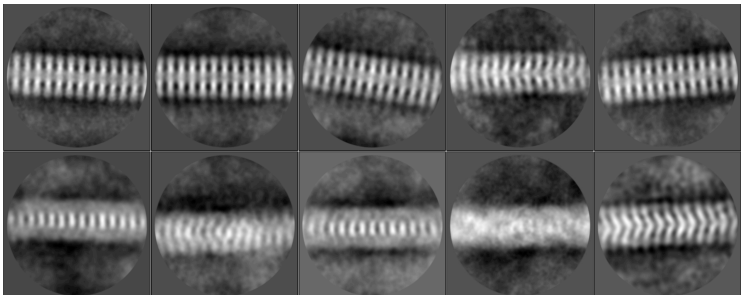

Figure 5-14 | Non-icosahedral assemblies formed by GII.4c VP1. (A) On the micrograph on the right, assemblies larger than T=4 icosahedral VLPs were found (white circle). On the right, a helical assembly can be observed. The scale bar represents 50 nm. (B) 2D classification of the helical filaments found in the preparations.

Curiously, also other, non-icosahedral assemblies were present in this sample, of which unfortunately the structures could not be solved. In some cases, we found assemblies with an enlarged diameter (Figure 5-14A). The particles were not uniform in size and shape, preventing structure determination using single particle analysis. Helical assemblies were also observed in the sample that appeared to be made up of VP1 (Figure 5-14A). However, a high-resolution structure could not be determined, as the helical raise and twist could not be defined and therefore we could only perform 2D classification (Figure 5-14B).

Overall, these results reveal that also for this engineered GII.4 strain, mostly T=4 icosahedral particles were formed, but in general, the samples exhibited T-number polymorphism.

Expression and structural analysis of GII.4c VP1 in mammalian cells

In order to determine if the unusual size of the VLPs was due to the expression system, we wanted to express GII.4 VLPs in a mammalian cell culture system. Transfected HEK-293T cells were cultured in DMEM complete with puromycin, to generate a stable VP1 expressing cell line. Comparison of supernatant and cell lysate showed that VP1 was expressed, but the VLPs mainly remained inside the cells and were not secreted into the medium. We expressed both GII.4 NSW-2012 and GII.4c VLPs in HEK-293T cells and examined their morphology using negative stain EM.

VLPs purified from HEK-293T cells exhibited a similar diameter as GII.4 VLPs that were expressed in insect cells. In EM, no differences between VLPs expressed in High Five cells and HEK-293T cells could be observed, but HEK-293T expressed VLPs were more homogenous and no T=1 or T=3 particles appeared to be produced, leading to higher homogeneity of the sample. This was the case for both GII.4 NSW-2012 and GII.4c. Therefore, further structural analysis was done only on GII.4c VLPs.

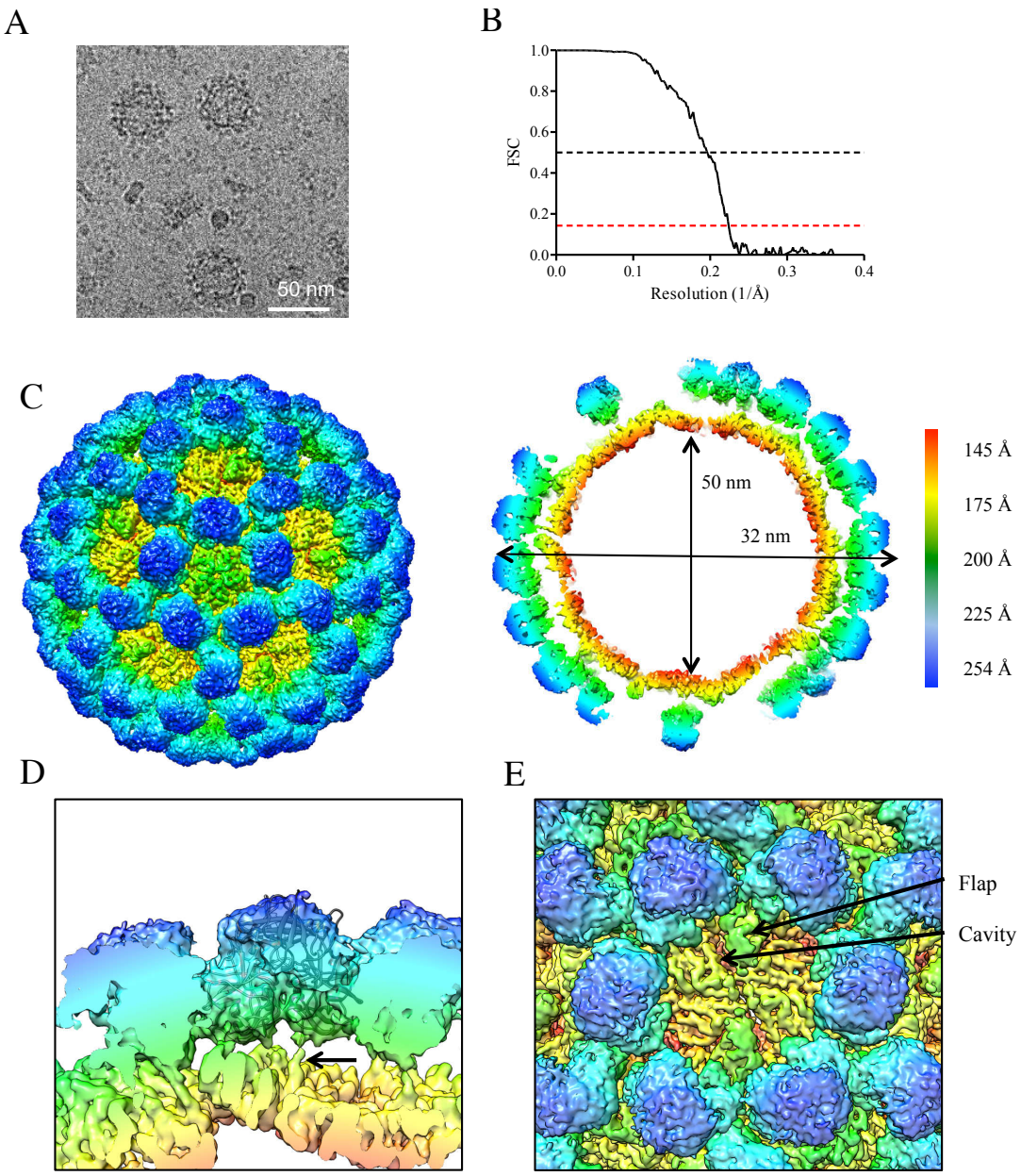

Figure 5-15 | Cryo-EM structure of GII.4c VLPs, expressed in mammalian HEK-293T cells. (A) Cutout of a representative cryo-EM micrograph of HEK-293T cell expressed GII.4c VLPs shows a homogenous sample. The scale bar represents 50 nm. (B) FSC plot of the icosahedral reconstruction reveals a resolution of 4.5 Å, at 0143 FSC cut-off (red dashed line, black lines indicates FC cutoff of 0.5). (C) The cryo-EM structure revealed a particle of T=4 icosahedral symmetry, assembled from 120 VP1 dimers (A/B and C/D). The particle had an inner diameter of 50 nm and an outer diameter of 32 nm. (D) Close-up on a single C/D dimer, fitted with the X-ray crystal structure of GII.4 NSW-2012 P domain (PDB: 4OOS, cartoon). The hinge region was extended and measured ~2.1 nm (black arrow). (E) Close-up on an icosahedral two-fold axis. As observed in the T=4 particles expressed in insect cells, the D subunit S domains are forming a flap like structure, disrupting the continuous shell.

To analyze if there were structural differences between VLPs expressed in HEK-293T cells and VLPs from insect cells, the structure of GII.4c VLPs from the mammalian system was determined using single particle cryo-EM (Figure 5-15A). 10,135 particles were refined to a structure of 4.5 Å (Figure 5-15B/C). The structures matched the insect cell produced T=4 VLP structure closely, with a cross-correlation coefficient of 0.99 and, at that resolution, no

visible differences in structure. In both cases, the particle had T=4 icosahedral symmetry, and the characteristic cavity and flap- like structure was observable in both densities, with the flap being raised equally (Figure 5-15B/D). Moreover, P domains were raised to the same extent (Figure 5-15C). This verified that, at least on a structural basis, the expression system did not have an influence.

Negative stain analysis of infectious GII.4 virions

To determine if authentic GII.4 virions assemble into T=4 particles, we measured the diameter of infectious virions in negative stain images (Figure 5-16). Unfortunately, the amount of virions produced in the cell culture system was not sufficient to allow cryo–EM single particle analysis, but virions from stool samples could be imaged using negative stain EM. The virions had a diameter of ~44 nm. This size corresponded to the diameter that we found for T=3 particles (~46 nm), indicating that GII.4 virions likely exhibit T=3 icosahedral symmetry.

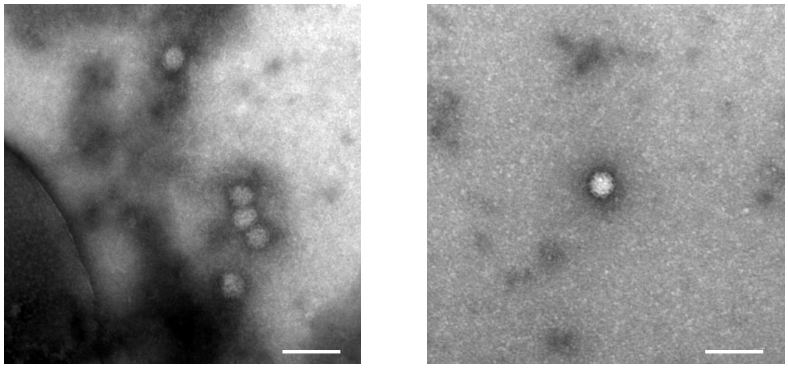

Figure 5-16 | Negative stain images of intact GII.4 virions. The diameter of the virions was ~44 nm, which corresponded to the diameter of a T=3 icosahedral particle. The scale bar measures 100 nm. The figure was adapted from (41). The images were taken by Dr. Anna Koromyslova.

Taken together, our data revealed that GII.4 VLPs tend to mainly assemble into T=4 icosahedral particles, a structure deviating from the commonly assumed T=3 symmetry for caliciviruses. Moreover, intact virions appear to be of T=3 icosahedral symmetry, suggesting these larger assemblies are an artifact of VLP production that is unique for GII.4 VLPs. Importantly, the vaccine candidate GII.4c mainly forms T=4 particles as well, which could have important implications on the vaccine efficacy.

5.4. Discussion

It is commonly assumed that norovirus VLPs are morphologically identical to intact norovirus capsids. However, in our study we showed that, when GII.4 VP1 is expressed in insect cells, mostly T=4 icosahedral symmetric particles are formed. Moreover, we found that this was the case for at least five different GII.4 strains, and for three, GII.4 NSW-2012, CHDC-1974 and GII.4c, the structures were solved within this study.

In a study on RHDV the authors found that an insertion at the N-terminus led to formation of T=4 icosahedral particles, but prior to this, no formation of norovirus T=4 icosahedral norovirus particles has been described (127). Our data indicates however, that these particles are the predominant form in which GII.4 VLPs are occurring. Moreover, this assembly remained structurally conserved over time, as GII.4 CHDC-1974 and GII.4 NSW-2012 were isolated 38 years apart and have only 89% sequence identity. Our findings were supported by a later study, where VLPs of GII.4 Minerva exhibited T=4 icosahedral symmetry (82). Conversely, a study on GII.4 Grimsby VLPs, produced in insect cells, revealed a T=3 icosahedral capsid (24).

Our results are contradicting the T=3 symmetry that is likely encoded for by the GII.4 virion (Figure 5-16). With our experiments using HEK-293T cells, we excluded that formation of these particles was caused by differences in post-translational modifications of the protein in insect and mammalian cells. Expression in insect cells and mammalian cells mostly differs in the obtained glycosylation patterns. In insect cells, the N-linked glycosylation is simpler than in mammalian cells, as only simple mannose based structures can be attached. For VP1 of norovirus no glycosylation pattern has been observed so far, therefore our observed results were not unexpected.

Formation of native virions includes the encapsidation of RNA, the genome linked protein VPg and several copies of VP2, all of which are not included in the empty VLPs. Expression of VP1 from other norovirus genotypes in the baculoviral expression system leads to formation of T=3 particles (69, 162). Therefore, these factors are presumably not solely defining the type of symmetry, but their presence could tilt the scale towards formation of the native T=3 capsids. Moreover, for other single stranded RNA viruses it was shown that the capsid assembles around its genome (93, 196), suggesting that the absence of the genome in the VLPs could play a role in the formation of the non-native capsids. In fact, it recently has been shown that bacteriophage MS2 forms T=4 icosahedral particles instead of T=3 particles in absence of full-length RNA (38).

Due to these observations, we speculate that the formation of T=4 icosahedral particles might be sequence-dependent. Sequence comparison of GII.4 NSW-2012, CHDC-1974, GII.4c with GI.1 and GII.10, two genotypes which have been proven to have T=3 icosahedral symmetry (69, 162), revealed that only 18.5% of the VP1 sequence are conserved between T=3 and T=4-forming genotypes. 5% of these amino acids exhibit conservation between the two T=3 icosahedral genotypes. Therefore, it could be of great interest for further studies to focus on these parts of the sequence to characterize, which part of the protein is responsible for the formation of these particles. Production of chimeric VLPs from sequences of T=3 and T=4 producing VP1 could be of value to pinpoint the sequence or domain that is the major contributor to the particle size determination. Studies on calicivirus particle size have been done before with contradicting results: Experiments on RHDV suggested that the N-terminal arm is the determining factor for particle size (6, 127). Conversely, a study on GI.1 came to the conclusion that the N-terminus does not influence particle symmetry. Instead, they found that deletions at the C-terminus, as well as deletions at the P2 subdomain mediated changes in VLP size (11).

Even though the symmetric difference was the most obvious variation to the previously solved structures, the particles also exhibited other distinct structural features, in particular the disruption of the closed shell by flap like S domain conformation. This most likely arises as a consequence of the bent C/D dimers. Usually in T=3 icosahedral particles, only A/B dimers have a curvature of the S domains, whereas C/C dimers are flat, in order to facilitate the curvature of a fully closed capsid structure. In our structures however, we found that the C/D dimer was bent as well. This could prevent the S domain from forming the necessary contacts with the adjacent B and C subunits, leading to the disruption of the shell. Interestingly, we found that, at least to some extent, this was also the case for GII.4c T=3 icosahedral particles. This was contradicting the results for GI.1, where the C/C dimer was flat and subsequently the shell was forming the expected contacts and formed a fully closed capsid (162). Additionally, this suggests that the formation of T=3 icosahedral particles does not necessarily rely on the alternating assembly of flat and bent dimers. In consequence this also could mean that the absence of flat dimers is not responsible for formation of the T=4 particles. If this opening of the shell has a biological function within the norovirus life cycle, or if it is a result of the heterologous expression of VP1 in an artificial system remains to be determined.

The result that particles can adopt differently sized particles is, at first glance, not surprising. Capsid polymorphism for norovirus (i.e. formation of T=3 and T=1 particles) has been described several times, for production of VLPs (222), as well as *in vivo* (202) and as a result

of infection in a human tissue culture system (49). The presence of these smaller VLPs in infected patients suggests that they serve a biological function, however their role remains elusive so far. Due to spatial limitations, these T=1 particles are most likely not capable of encapsidating a complete genome. Moreover, these smaller VLPs have been observed in several different genotypes. Conversely, the formation of T=4 particles has only been described as a result of heterologous expression of GII.4 VP1 in artificial cell culture systems. Therefore, these particles likely constitute an artifact of VLP production. However, this artifact is still of importance, as many studies, most importantly the vaccine studies with GII.4c, have been conducted under the assumption that the VLPs are identical to virions (153). Our results prove that it cannot be automatically assumed that this is the case, and careful examination of the particles is essential. Most importantly, we showed that the VLPs used in a vaccine candidate indeed mainly form these non-native assemblies.

For caliciviruses, the most readily accessible epitopes are on top of the P domain, where receptor and cofactor binding sites area located. These epitopes should be easily recognized on particles of either symmetry. However, P2 subdomain associated regions are often hypervariable and under selective pressure, leading to high genetic and antigenic drift. Therefore, antibodies against these epitopes would most likely not be cross-reactive to other genotypes or strains emerging after vaccination. Conversely, the P1 subdomain exhibits a more stable sequence and therefore might constitute a superior epitope for cross-reactive antibodies. In fact, different studies described antibodies and Nanobodies that bound to the lower part of the P domain, suggesting that these epitopes possibly represent sites of vulnerability for caliciviruses (69, 101, 122, 176).

Our ELISA results suggest that epitopes, which appear occluded in larger virions, could be more easily accessible on T=1 particles, due to increased flexibility of the P domains. Higher P domain flexibility could be associated with better accessibility to occluded epitopes. Therefore the larger, more rigid particles could serve as a suboptimal antigen due to structural constraints. A study on tick borne encephalitis virus also demonstrated differences in affinity for several envelope specific antibodies, depending on the quaternary structure of the assembly (89). However, in our experiments, overall antigenicity was comparable (as determined with the polyclonal antibody). This could mean that in general, smaller and larger particles are both strongly immunogenic, both being highly ordered repeats of the antigen, but elicitation of neutralizing antibodies binding to occluded regions might be not optimal in the larger particles. Conversely, it might also be possible, that a mixture of differently sized VLPs could elicit a more diverse panel of antibodies, as availabilities of epitopes vary between the

particles. Moreover, previous studies proved that the vaccine candidate was in fact able to elicit a robust immune response and at least some antibodies were able to detect different norovirus genotypes (120, 153). This is in accordance with our results, as the more occluded epitopes were still detectable on the larger assemblies, only affinity was reduced.

Unfortunately, it was not possible to separate T=3 and T=4 icosahedral particles, and therefore antigenic comparisons between particle sizes were limited to T=1 and T=4 particles. Such experiments between T=3 and T=4 particles could help ensure that vaccination with a non-native immunogen is not antigenically problematic. So far, clinical trials indicated that the vaccine is only associated with modest levels of protection when compared to placebo groups (10). Hence, it is important to rule out the particle symmetry as a hindering factor for efficacy. Nevertheless, immune responses to viruses and vaccines are complex and highly impacted by the pre-exposure history of the patients (especially in common viruses such as influenza or norovirus) (9, 60, 121). Therefore, the moderate efficacy of the vaccine candidate could stem from a multitude of other factors as well.

Taken together, one could speculate that the differences between the native virion and the T=4 icosahedral vaccine only play a limited role in affecting its efficacy, but clearly more studies on this are needed to answer this question. Nonetheless, there are important consequences from our studies on these larger particles: Even though particles appear to be morphologically similar to typical norovirus genotypes, they could have symmetric deviations; therefore, cautious examination of the used particles is of importance. Moreover, further studies are required, to specify whether differences in symmetry translate into differences in antigenicity.

6. Chapter 3: Characterization of GII.4 specific Nanobodies

6.1. Summary

In this study we characterized a panel of GII.4 NSW-2012 specific Nanobodies. We found that most of the Nanobodies were able to inhibit attachment of GII.4 to PGM in a dose dependent manner in the micromolar range. We commonly found that Nanobody binding led to particle aggregation, thereby preventing attachment of VLPs to HBGAs. Unfortunately none of the tested Nanobodies were able to bind VLPs other than GII.4.

Moreover, we structurally characterized the binding of six Nanobodies using single particle cryo-EM. Interestingly, we found that most Nanobodies were binding to the lower part of the P domain. In all cases we observed a shift of the P domain to accommodate Nanobody binding, highlighting the flexibility of the capsid.

6.2. Contributions

In total, 33 Nanobodies were produced and characterized, together with Kerstin Ruoff and Dr. Charles Sabin. 11 of these, Nanobodies were characterized by me. For cross-reactivity studies, I used all 33 available Nanobodies. I performed the cryo-EM structural analysis.

6.3. Results

Production of GII.4-specific Nanobodies

For initial production of Nanobodies, we employed the service from VIB Nanobody service facility in Vrije University Brussels. Alpacas were immunized with GII.4 NSW-2012 VLPs, and 100 Nanobody clones were generated. 33 different Nanobodies were expressed and characterized, selected to obtain a wide variety of different Nanobodies, based on the sequence. I characterized the binding and inhibitory potential of 11 of these Nanobodies.

Nanobody binding to GII.4 NSW-2012 VLPs

In first tests, we defined the affinity of the Nanobodies for GII.4 NSW-2012 VLPs. In a direct binding ELISA, the plates were coated with 2 µg /ml VLPs and the binding of serially diluted Nanobodies was measured.

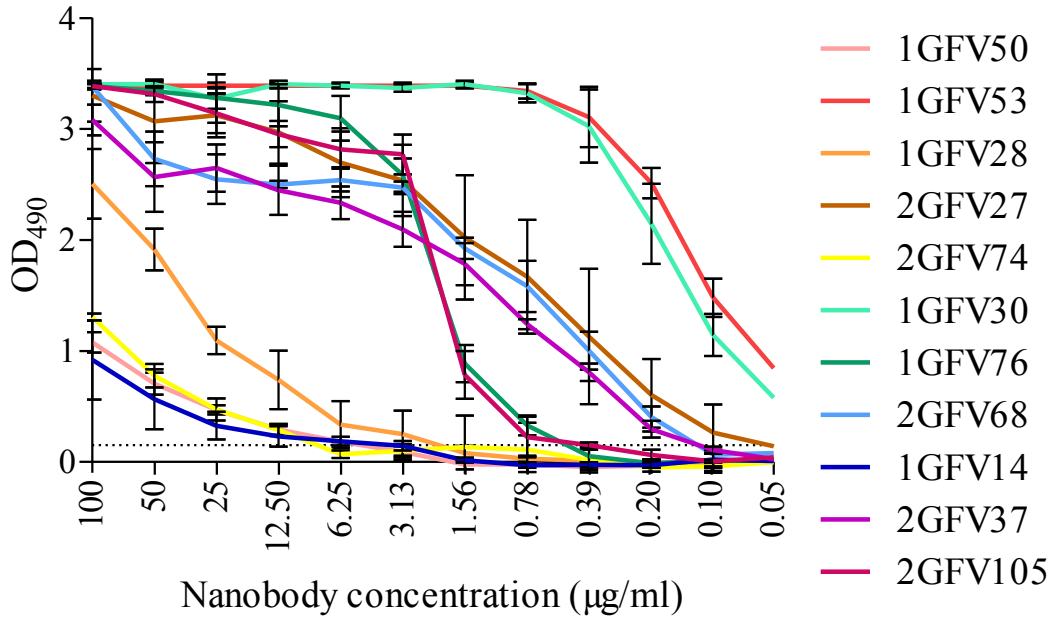

Figure 6-1 | Nanobodies binding to GII.4 NSW-2012 VLPs. All Nanobodies were able to detect GII.4 VLPs in a direct binding ELISA. The dashed line shows a cut-off value of 0.15 OD_{490}.

All Nanobodies were able to attach to GII.4 NSW-2012 VLPs, but the tested Nanobodies exhibited marked differences in their binding affinities (Figure 6-1). The strongest binders were 2GFV53 and 1GFV30, with a maximum OD_{490} signal measured up to a concentration of 0.78 µg/ml. Lowest binding was measured for 1GFV14, 1GFV50 and 2GFV74, where the cut-off level of OD_{490} = 0.15 was reached already at 6.25 µg/ml.

In order to identify, whether the Nanobodies were cross-reactive against other norovirus genotypes and different GII.4 isolates, we performed binding ELISAs with VLPs from GI.1 West Chester, GI.11 #8, GII.1 Hawaii, GII.10 026-Vietnam, GII.17 Kawasaki, GII.4 CHDC-1974, GII.4 Saga-2006, GII.4 Yerseke-2006, GII.4c and GII.4 NSW-2012.

All 33 expressed Nanobodies were tested for cross-reactivity by me. In this analysis, triplicates of the highest Nanobody concentration (100 µg/ml) were tested for their ability to bind to 2 µg/ml of the different VLPs.

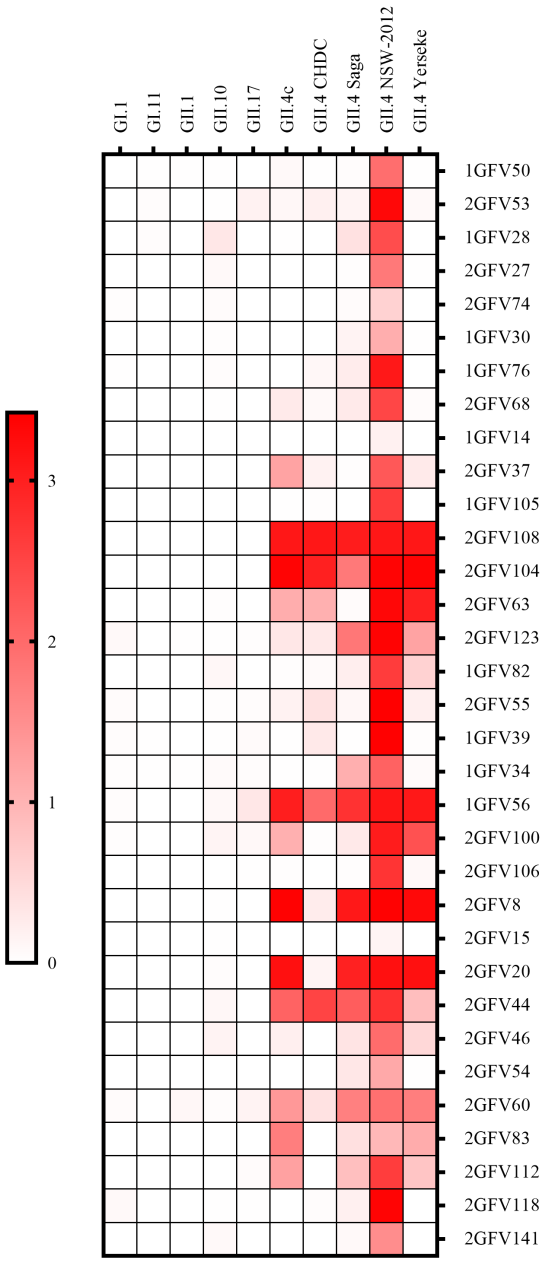

Figure 6-2 | Cross-reactivity of GII.4 Nanobodies. The Nanobodies were analyzed at 100 µg/ml, for their ability to bind to GI.1, GI.11, GII.1, GII.10, GII.17, GII.4c, GII.4 CHDC-1974, GII.4 Saga, GII.4 NSW-2012 and GII.4 Yerseke at 2 µg/ml. The color scheme represents measured OD_{490} values. Nanobodies were not able to bind to GI or GII genotypes other than GII.4. Binding assays were done in triplicates.

None of the tested Nanobodies were able to cross-react with other genotypes. Most Nanobodies (15) were specific to GII.4 NSW-2012, but some of the Nanobodies were able to attach to GII.4 isolates other than GII.4 NSW-2012 (Figure 6-2). Three Nanobodies (2GFV108, 2GFV104 and 1GFV56) were able to attach to all tested GII.4 variants. Interestingly, we found that five Nanobodies (2GFV8, 2GFV20, 2GFV60, 2GFV83 and 2GFV112) were binding all GII.4 VLPs except CHDC-1974.

HBGA inhibition of Nanobodies

To analyze if the Nanobodies were able to inhibit the attachment of VLPs to HBGAs, a surrogate binding ELISA was performed (Figure 6-3). Except 1GFV14, all Nanobodies were able to inhibit PGM binding, with IC_{50} values ranging from 0.74 µg/ml to 6.31 µg/ml (Table 6-1). The best inhibitor was Nanobody 2GFV68. Interestingly, only 1GFV30 and 1GFV76 were able to inhibit 100% of binding, up to a concentration of 25 µg/ml and 6.25 µg/ml, respectively. Most Nanobodies reached a plateau at 60-80% inhibition, suggesting that even at the highest Nanobody concentrations some HBGA binding sites on the VLPs were still available.

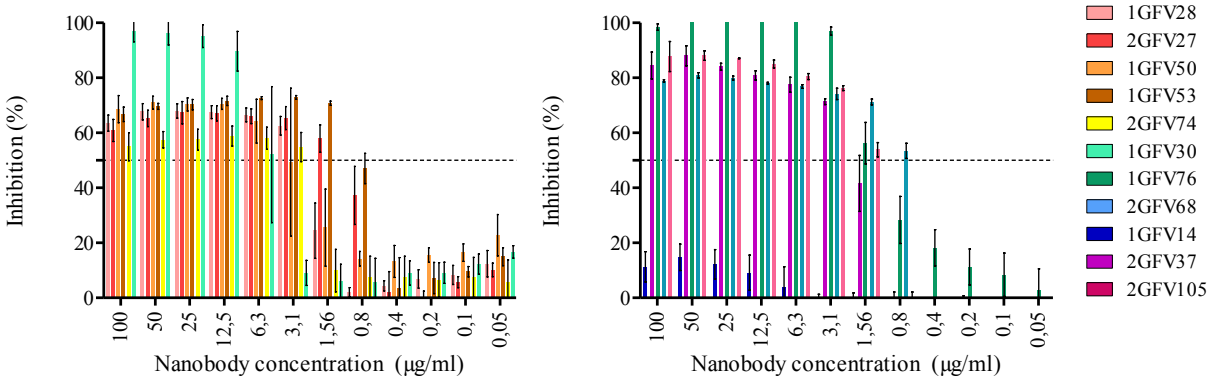

Figure 6-3 | Inhibition of GII.4 PGM attachment by Nanobodies. In this surrogate HBGA blocking assay, all Nanobodies except 1GFV14 were able to inhibit the attachment of GII.4 NSW-2012 VLPs to PGM. In most cases, except for 1GFV76 and 1GFV30, we found that the maximum inhibition was only at 60-80%.

Table 6-1 | IC_{50} values of Nanobodies inhibiting PGM attachment of GII.4 VLPs.

Nanobody	IC_{50} (µg/ml)
1GFV50	2.70
2GFV53	0.77
1GFV28	1.84
2GFV27	0.76
2GFV74	2.19
1GFV30	6.31
1GFV76	1.41
2GFV68	0.74
1GFV14	Not defined
2GFV37	1.54
1GFV105	1.34

The influence of Nanobody binding on the structural integrity of GII.4 VLPs

To further characterize how these Nanobodies inhibit the HBGA attachment, we performed DLS and negative stain experiments.

After incubation of GII.4 NSW-2012 VLPs with Nanobodies, we observed a pronounced peak shift in the DLS measurements, indicating an increase in hydrodynamic diameter. These results were confirmed by negative stain EM, where in most samples VLPs were aggregated after treatment. Nevertheless, the nature of the complexes varied between the Nanobodies. In several cases, as for 1GFV50, 2GFV27, 1GFV76 and 1GFV105 the complexes were dense and large, whereas other Nanobodies only moderately aggregated the particles (2GFV74, 1GFV30, 2GFV68) and in some cases, only small aggregates were observed (2GFV53, 1GFV28, 2GFV37). VLPs incubated with 1GFV14 did not exhibit a peak shift in DLS, and VLPs appeared morphologically identical to untreated VLPs in EM. This was in line with our inhibition results, since this Nanobody failed to inhibit PGM attachment. These results indicated that likely all inhibiting Nanobodies were preventing PGM binding by aggregating the particles.

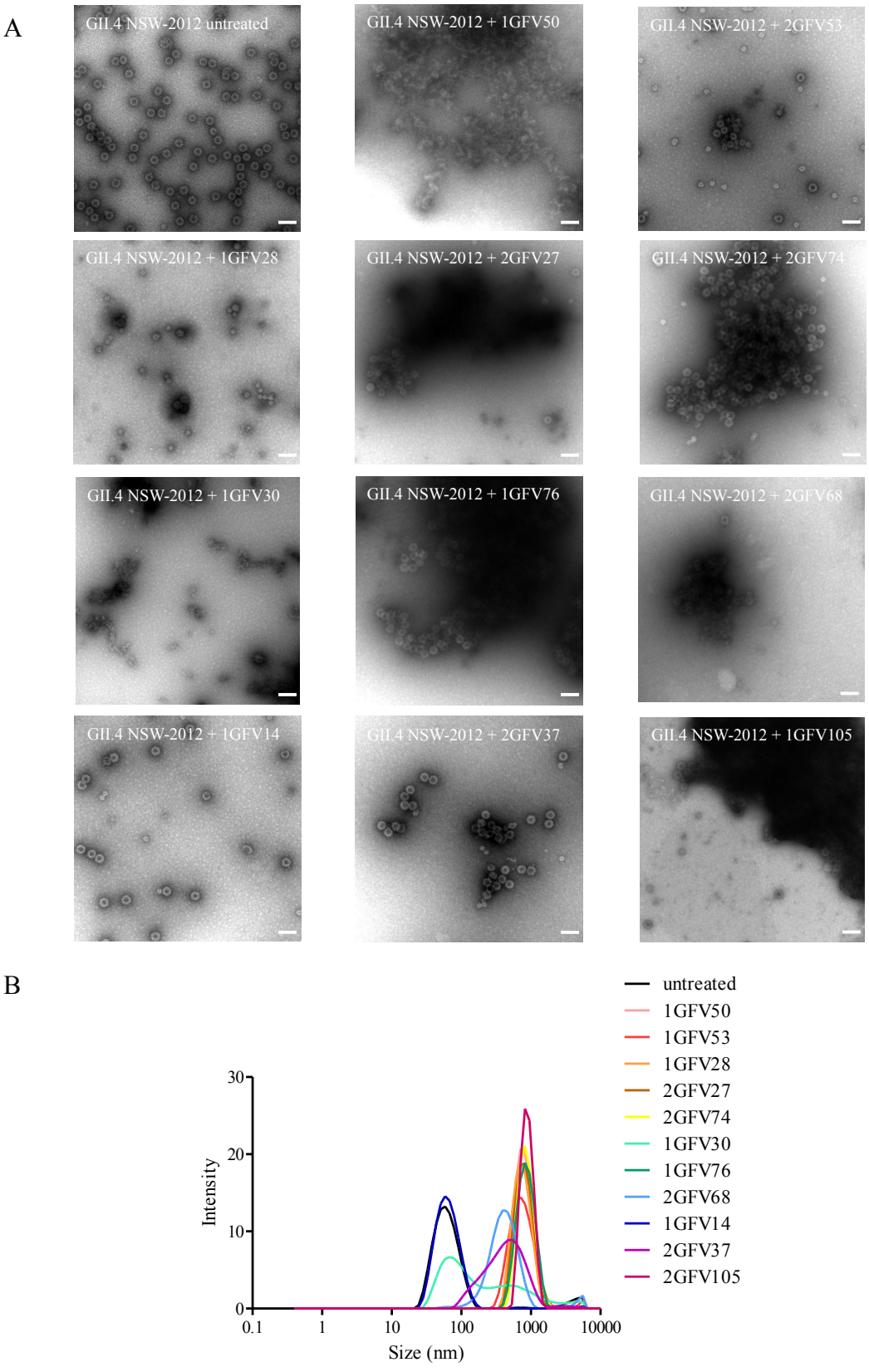

Figure 6-4 | Treatment of GII.4 NSW-2012 VLPs with different GII.4-specific Nanobodies. (A) Negative stain EM and (B) DLS measurements of untreated VLPs and VLPs treated with different Nanobodies. Untreated VLPs were mostly monodisperse. 1GFV14 treated VLPs did not differ from untreated VLPs, but treatment with all other tested Nanobodies led to aggregation of the particles. The scale bar indicates 100 nm.

Structural analysis of GII.4-Nanobody complexes

Despite these results, we decided to structurally analyze some of the Nanobodies in complex with GII.4 NSW-2012 VLPs, using single particle cryo-EM. For these experiments, I also used Nanobodies that were not characterized by me (2GFV37, 1GFV56, 2GFV20, 2GFV46, 2GFV54, 2GFV118, 2GFV83 and 2GFV104). In the ice, most particles appeared aggregated, but several datasets could be collected where single particles were still observable and only weak aggregation occurred (Figure 6-5A). It was possible to pick particles from the smaller and more loosely packed aggregates, and for six different combinations, structures could be calculated. In several cases, such as 2GFV54 or 2GFV83, grids were prepared, but the high degree of aggregation precluded structure determination using single particle cryo-EM.

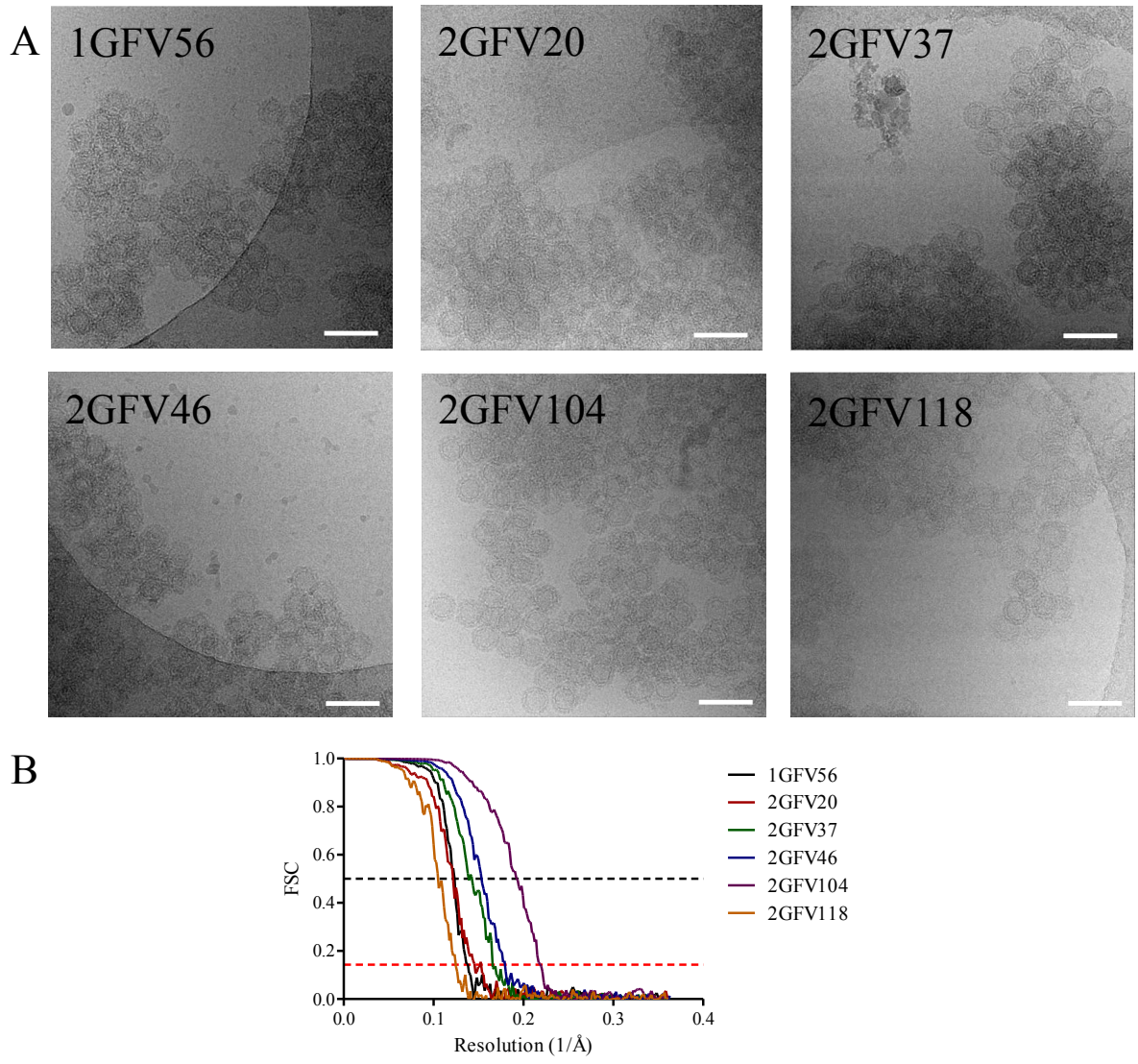

Figure 6-5 | Cryo-EM data of GII.4 NSW-2012 VLPs with different Nanobodies. (A) Exemplary cryo-EM micrographs for NSW-2012 VLPs with Nanobodies. In all cases aggregation occurred, but particles were still clearly visible. The scale bar indicates 100 nm. (B) FSC plot indicates resolutions of 7.4 Å for 1GFV56, 6.5 Å for 2GFV20, 6.2 Å for 2GFV37, 5.7 Å for GII.4 with 2GFV46, 4.62 Å for 2GFV104 and 8.1 Å for 2GFV118 using an FSC cut-off of 0.143 (red dashed line; black line indicates FSC cut-off of 0.5).

The Nanobodies selected for structural studies exhibited distinct binding patterns: 2GFV37, 2GFV46, and 2GFV118 bound specifically to GII.4 NSW-2012; 2GFV20 bound all GII.4 VLPs except GII.4 CHDC-1974, and 1GFV56 and 2GFV104 bound to all tested GII.4 isolates.

The highest resolution structure was obtained for GII.4 and 2GFV104, with 4.6 Å. For the 2GFV118 complex, resolution was only at 8.1 Å (Figure 6-5B). This could be due to the strong aggregation that allowed only a small dataset to be acquired, and only few particles could be used for final reconstruction of the structure.

Generally, the Nanobodies did not disrupt the particle integrity and the capsids were still present as T=4 icosahedral assemblies with raised P domains. In all structures we found two bound Nanobodies per P domain dimer. Interestingly, we found that in all cases the binding sites were located at the lower part of the P domain. The binding sites were at the dimeric interface of the two P monomers, suggesting that the Nanobodies interacted with both P domain subunits. Moreover this suggests that despite their marked differences in VLP binding, the epitopes were located in close vicinity.

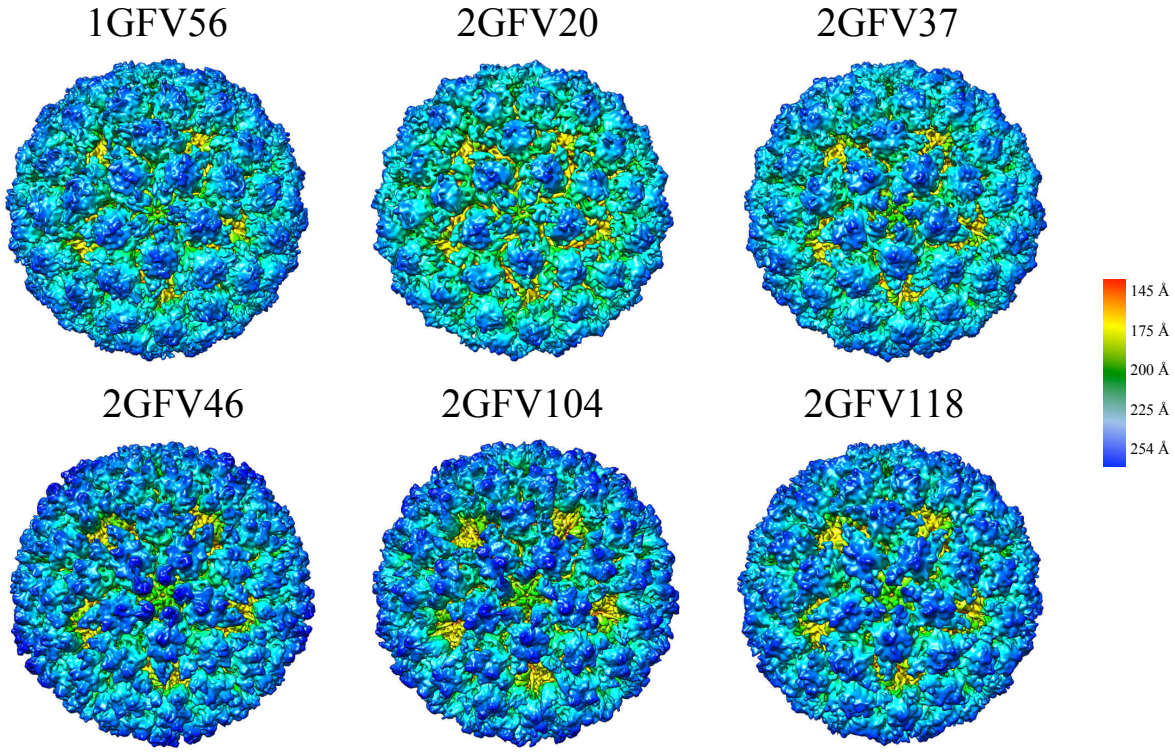

Figure 6-6 | Cryo-EM structures of GII.4 NSW-2012 with different Nanobodies. In all cases, Nanobodies bound to the lower site of the P domains, at all available binding sites of the capsid. All structures are colored by radius, as indicated by the color scale.

In all complexes except with 2GFV104, the P domains were rotated similarly and the Nanobodies were pointing to the center of the three-fold and five-fold axes (Figure 6-6). For 2GFV104 however, the Nanobodies were bound to a similar position of the P domain, but orientation was different: In this case, the Nanobodies were pointing upwards. Moreover, the C-terminal part of the Nanobody was connected to the upper part of the P domain. In this conformation, the shell was more surface-exposed than in the other complexes.

Comparison of the GII.4 NSW-2012 apo structure to the complexed structures revealed that in all cases, the P domain was rotated in a clockwise direction in respect to the apo structure after Nanobody binding (Figure 6-7). Possibly this movement occurred to allow the Nanobodies to efficiently bind to all available binding sites.

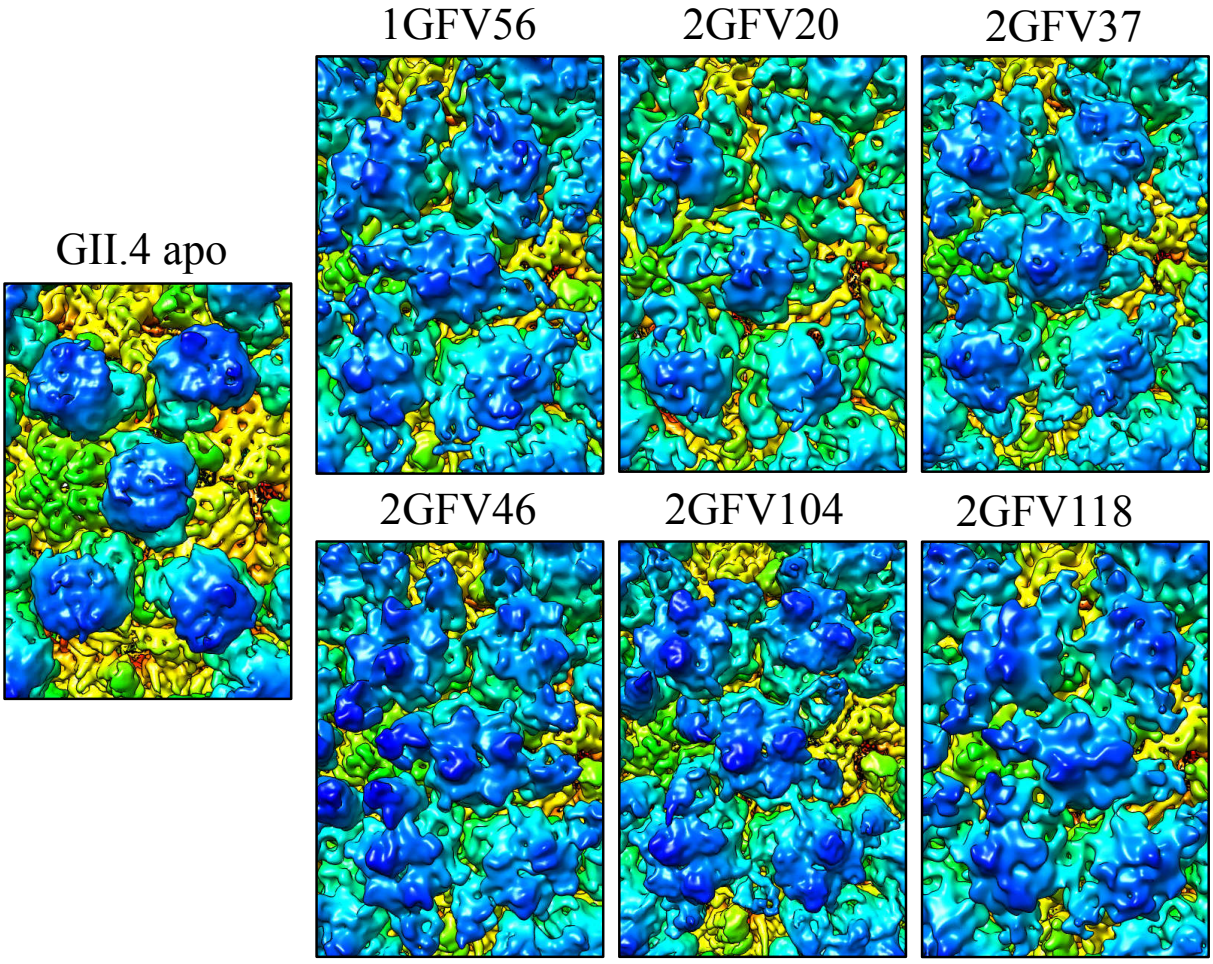

Figure 6-7 | Close-up on an A/B dimer of the GII.4 NSW-2012 apo structure and GII.4 NSW-2012 in complex with different Nanobodies. In all cases, the P domain was rotated as a result of Nanobody binding.

The measured tilts ranged from ~5º for the 1GFV56 C/D dimer, to 18º for the 2GFV20 A/B dimer (Table 6-2). This highlights the high flexibility of the hinge region, as the particles still remained intact. The rotation of the A/B dimers remained relatively similar between the

different complexes (ranging from 11-18º), whereas the C/D dimer rotation ranged from 5º up to 17º. Moreover, in some cases, such as 2GFV46 or 2GFV104, the P domain was resolved to a higher resolution, when compared to the P domain in the apo structure. This indicates that Nanobody binding stabilized the P domain conformation in these structures, resulting in a higher overall resolution.

Table 6-2 | Rotations of the A/B and C/D complex dimers, respective to the P domains in the apo structure.

Nanobody complex	A/B dimer rotation	C/D dimer rotation
1GFV56	12º	5º
2GFV20	18º	16º
2GFV37	12º	17º
2GFV46	12º	10º
2GFV104	11º	6º
2GFV118	13º	8º

In all structures, there were no differences observable in the S domains, suggesting that the influence of Nanobody binding was restricted to the P domain, while the S domain remained rigid.

6.4. Discussion

Many successful RNA viruses exhibit extensive antigenic diversity. Nevertheless, it is integral to retain the structural integrity of the capsid and important sites, such as receptor or cofactor binding sites. These conserved sites could be of interest in the development of a potent antiviral.

Nanobodies are of great interest as potential therapeutics. In this study, we analyzed Nanobodies raised against the most clinically important genotype of norovirus. GII.4 VLPs, as described in Chapter 2, exhibit an unusual symmetry. Nevertheless, the VLPs were proven to be highly immunogenic, and a high number of Nanobodies were produced. In former studies on Nanobodies [(101) and Chapter 1], usually different inhibition modes were present. However in our case, the results indicated that all Nanobodies that were inhibiting PGM binding aggregated the particles. Aggregation of VLPs appears to be a common mode of inhibition for Nanobodies, as this has also been observed for Nanobodies from other libraries [(101) and Chapter 1].

Ten out of 11 Nanobodies were able to inhibit GII.4 NSW-2012 binding to HBGAs, with IC_{50} values that were comparable to values found in other studies (101, 176). HBGA binding facilitates cell attachment *in vivo*. Therefore the inhibition of HBGA binding is handled as correlate for protection (166). Interestingly, we found that for most Nanobodies, 100% inhibition was not reached. This could imply that the Nanobodies might not be able to hinder the attachment of all VLPs or that sufficient binding sites were unoccupied to still allow binding. From preliminary X-ray crystallography data (unpublished data, performed by Dr. Charles Sabin) and the cryo-EM results performed within this thesis, we know that most Nanobodies had epitopes located at the lower site of the P domain. Only the epitope of 1GFV76, one of the two Nanobodies that was able to inhibit 100% of the binding in our assay, was located at the top of the P domain. Of note, in studies with GI.1 and GII.10 specific Nanobodies [(101) and Chapter 1], highly efficient bottom-binding Nanobodies were discovered, suggesting that lower efficiency might not be linked to the location of the binding site on the P1 subdomain.

In a cross-reactivity binding assay we found that none of the Nanobodies were able to bind VLPs from genotypes other than GII.4. Most of the Nanobodies were specific to GII.4 NSW-2012, the genotype they were raised against. Nevertheless, several Nanobodies were able to bind to all tested GII.4 VLPs, suggesting that they bound to an epitope that is conserved only within the GII.4 genotype. As GII.4 infections are by far the most frequent

(42, 165), these Nanobodies could be of therapeutic interest, despite their inability to bind genotypes other than GII.4. Moreover, the fact that these Nanobodies are able to attach to GII.4 isolates that were isolated 38 years apart (GII.4 CHDC-1974 vs. GII.4 NSW-2012) suggests that their epitopes are especially conserved. They could therefore represent important sites on the P domain. Unfortunately, these cross-reactive Nanobodies showed only moderate inhibition in surrogate blocking ELISAs (data not shown, performed by Kerstin Ruoff), limiting the usability of these Nanobodies as potential therapeutics. Nevertheless, determination of the exact binding site could provide a target for GII.4 genotypes that could be exploited in the development of a GII.4 antiviral.

Interestingly, one group of Nanobodies (2GFV8, 2GFV20, 2GFV60, 2GFV83 and 2GFV112) was able to bind all newer isolates of GII.4, but not GII.4 CHDC-1974, suggesting that the epitope evolved after isolation of this variant, but is conserved in the newer isolates.

Using single particle cryo-EM, we solved the structures of six different Nanobodies in complex with GII.4 NSW-2012 VLPs. Notably, in all cases the Nanobodies forced the P domains in diverse positions. This becomes necessary, as the binding sites were located at the bottom of the P domain, and the Nanobodies would likely otherwise clash with neighboring Nanobodies or P domains. This suggests that the capsid in general is flexible and allows for diverse positioning of the P domain. Binding of a Nanobody to a sterically unfavourable position did not lead to capsid disruption, as has been shown e.g. for hepatitis E virus (234). Instead, the flexibility of the hinge region allowed the P domain/Nanobody complex to adopt different conformations to accommodate Nanobody binding at all epitopes, while maintaining the general structure of the capsid. As disruption of the particle is generally a non-reversible process, the high flexibility, allowing the particle to remain intact even at unfavourable conditions, could ultimately contribute to the high environmental stability and infectivity of noroviruses and in particular GII.4 isolates.

Despite the apparent similarity in binding sites, the binding pattern of the evaluated Nanobodies varied substantially. Structurally most diverse from the others was 2GFV104. In this case, the Nanobodies were protruding out from the capsid instead of pointing towards the center of the five- or three-fold axes. Cryo-EM is an important tool to analyze how the Nanobody binding influences the structural integrity of the intact particles. Nevertheless, due to limited resolution of the complexes, it would be of great interest to solve the structures of Norovirus P domain and Nanobodies using X-ray crystallography. Determining the exact

binding sites and interacting amino acids could provide a structural basis for the differences in VLP binding.

In most structures, the P domains were resolved relatively well when compared to the apo structure. This indicated that the binding of the Nanobody additionally stabilized the P domain and restricted the movement of the flexible hinge region, most likely by steric hindrance. Preventing conformational changes in the capsid has been shown to be an effective mode of inhibition e.g. in rhinovirus, where binding of WIN compounds stabilized the capsid, subsequently precluding the uncoating (167, 191). Nevertheless, inhibition by preventing virus particle breathing can only in detail be assessed in neutralization studies, as often these structural rearrangements occur only after receptor binding. As no conformational changes are necessary in our HBGA binding assay, the influence of the stabilization of the P domain on the inhibition could not directly be determined. Neutralization studies using the enteroid system could shed further light on this potential mode of inhibition.

Overall, this study provides additional examples of Nanobodies as efficient inhibitors of norovirus attachment, building a mandate for further research into the development of Nanobody-based therapeutics. Due to their limited cross-reactivity, the therapeutic potential of the Nanobodies characterized in this study might be limited on their own, but in a combinatorial therapy with other Nanobodies or active compounds, as described in Chapter 1, these Nanobodies could be of therapeutic interest. Moreover, the use of Nanobodies is not limited to therapeutic applications. Nanobodies could be of use in laboratory settings or as detection tools. Their high specificity and affinity could be exploited in the development of norovirus detection kits that are of higher specificity and more cost-effective than the current detection kits that use conventional antibodies for detection (40).

7. Chapter 4: Structural characterization of GII.17 VLPs

7.1. Summary

In this chapter, we solved the structure of VLPs from the currently prevalent genotype GII.17 Kawasaki. We found that the VLP exhibited T=3 icosahedral symmetry, which is the typical structure of caliciviruses. The P dimers were raised from the shell, as observed for other calicivirus structures, giving further prove that this appears to be the most common P domain conformation. Moreover we attempted to solve the structure of GII.17 in complex with a binding factor (A-trisaccharide) and a small molecule inhibitor (2'FL), but the addition of these compounds did not induce structural deviations in the capsid.

7.2. Contributions

All experiments in this chapter were performed by me. Benedikt Wimmer helped with data processing for the GII.17 apo structure.

7.3. Results

Single particle analysis of GII.17 VLPs

Norovirus GII.4 is generally assumed to be the most clinically relevant norovirus genotype. However, in the recent years, genotype GII.17 superseded GII.4 in prevalence in some regions of the world. Therefore, we wanted to analyze the structure of GII.17 VLPs in detail using single particle cryo-EM.

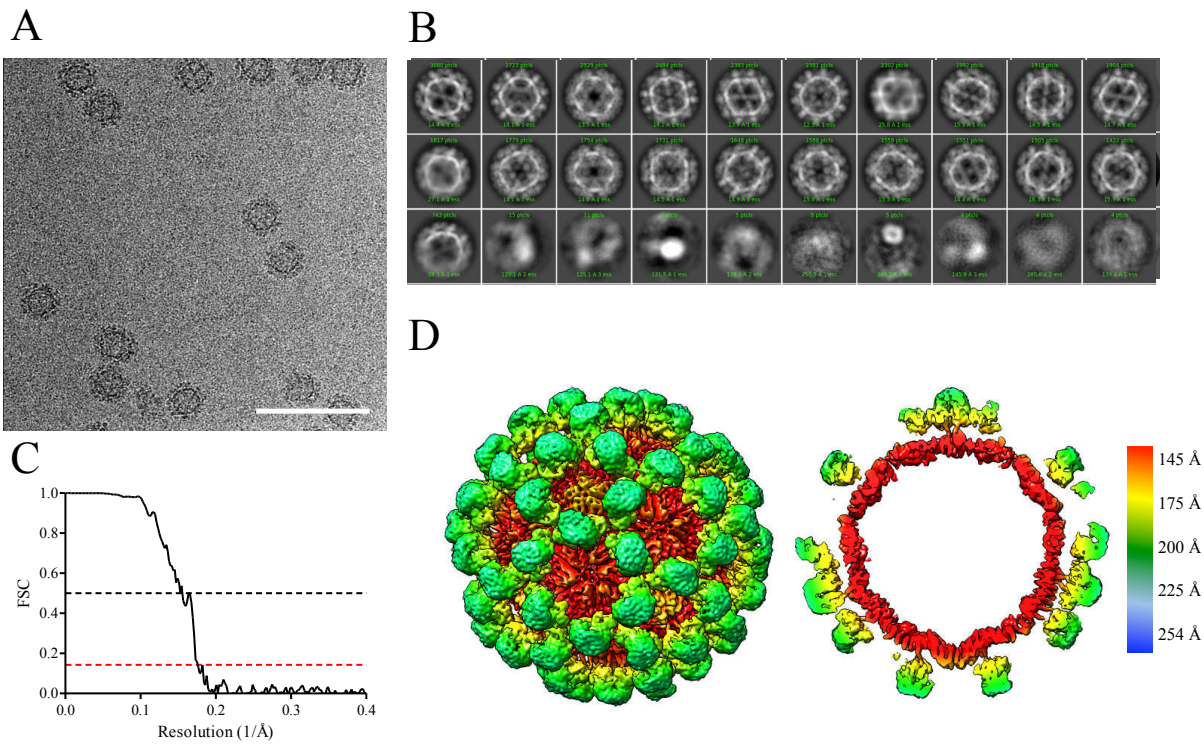

Figure 7-1 | The cryo-EM structure of GII.17 VLPs. (A) Representative raw micrograph of GII.17 VLPs. (B) 2D classification shows structurally homogeneous particles. (C) The FSC curve indicates a resolution of 5.8 Å at FSC cut-off of 0.143 (red dashed line, 0.5 FSC cut-off indicated as black dashed line). (D) Cryo-EM structure of GII.17 VLPs exhibited T=3 icosahedral symmetry. The particle is colored by radius, as indicated by the color scale.

GII.17 Kawasaki VLPs were expressed in HighFive insect cells and purified from the cell supernatant via a CsCl gradient. The purified VLPs appeared as homogenous and monodisperse particles in the vitrified ice (Figure 7-1A/B). A dataset of 2,316 images was collected. 35,709 particles were refined to a structure of 5.8 Å resolution (Figure 7-1C/D).

GII.17 VLPs exhibited T=3 icosahedral symmetry, which is typical for the *Caliciviidae* family. The particle comprised 180 VP1 monomers, dimerizing at the P domain to form the characteristic arch-like structures. VP1 dimers can be divided into two classes: A/B and C/C. 60 A/B dimers were located at the icosahedral five-fold axes, whereas 30 C/C dimers were

positioned at the two-fold axes. B and C subunits were alternating at the three-fold axes. The VLPs had an inner diameter of ~24 nm and an outer diameter of ~45 nm.

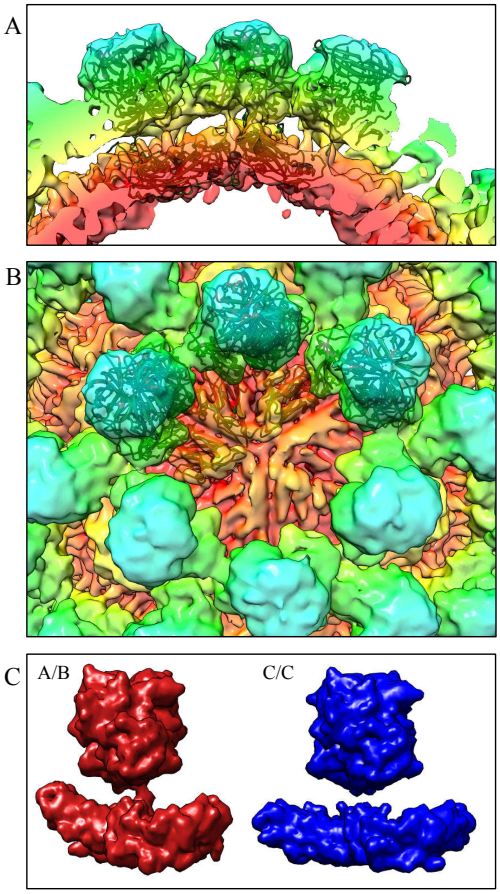

Figure 7-2 | Detailed view of the GII.17 VLP structure. (A) Cutout view of the structure, and (B) top view on a three-fold axis, fitted with GI.1 S domain (PDB: 1IHM) and GII.17 P domain (PDB: 5F4O). (C) Extracted A/B (red) and C/C (blue) VP1 dimers revealed that A/B dimers had a convex conformation, whereas C/C dimers had a flat S domain conformation.

A flexible hinge connected P and S domain and the P domains were rising from the shell. The S domain was resolved to a higher resolution than the P domain, which is linked to stronger flexibility in the extended P domain, compared to the more rigid S domain.

Fitting of the X-ray crystal structure of the GII.17 P domain [PDB: 5F4O (188)] revealed a cross-correlation coefficient of 0.96 for both A/B and C/C dimers. This indicates that at the given resolution there were no, or only small deviations between A/B and C/C P domain dimers. As no structure for GII.17 S domain was available so far, the X-ray crystal structure of GI.1 S domain (PDB: 1IHM) was used as S domain model. The S domain of GI.1 and GII.17 is relatively well conserved, with a sequence identity of 57%. The structure fitted well into the density, indicating that the common jelly-roll fold of the calicivirus S domain is

conserved in GII.17. Close inspection of the dimers showed that the A/B dimer had a bent conformation, whereas the C/C dimer was flat.

GII.17 VLPs in complex with binding factor A-trisaccharide

So far, little is known about how the norovirus interacts with the cell prior to entry. In viral infections, often binding to cofactors or receptors leads to structural rearrangements facilitating infection. As for human norovirus no proteinaceous receptor is known, we wanted to analyze whether the binding of HBGAs primes the virus for subsequent steps in the infection cycle. In a former study it was shown that GII.17 Kawasaki was able to bind A-trisaccharide (A-tri), a core antigen fragment in ABO blood group system (98). Therefore, we used A-tri as a model to determine if the capsid morphology is influenced by HBGA binding. Structurally, A-tri is a branched amino trisaccharide, comprised of a beta-D-galactose with an alpha-L-fucosyl residue at position 2 and an N-acetyl-alpha-D-galactosaminyl residue at position 3. From previous studies, the X-ray crystal structure of GII.17 P domain in complex with the compound was available (98).

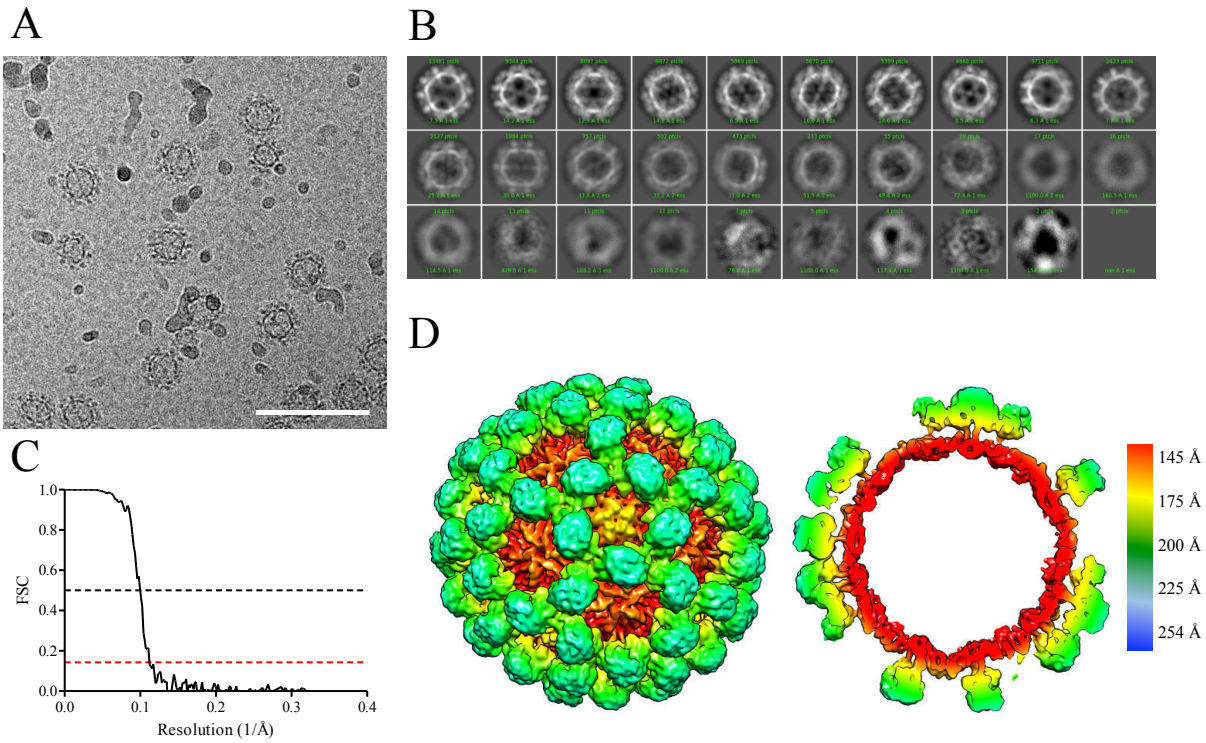

Figure 7-3 | The cryo-EM structure of GII.17 VLPs in complex with A-tri. (A) Representative raw micrograph of GII.17 VLPs with A-trisaccharide. (B) 2D classification reveals structurally homogeneous particles. (C) The FSC curve indicates a resolution of 7.9 Å at FSC cut-off of 0.143 (red dashed line, 0.5 FSC cut-off indicated as black dashed line). (D) Cryo-EM structure of GII.17 VLPs with A-tri show T=3 icosahedral symmetry. The particle is colored by radius, as indicated by the color scale.

Prior to sample preparation, purified VLPs were incubated with 100× molar excess of A-tri to the binding sites. In the vitrified ice, no differences to unbound viruses were detectable (Figure 7-3B). Moreover, addition of A-tri did not introduce noticeable background.

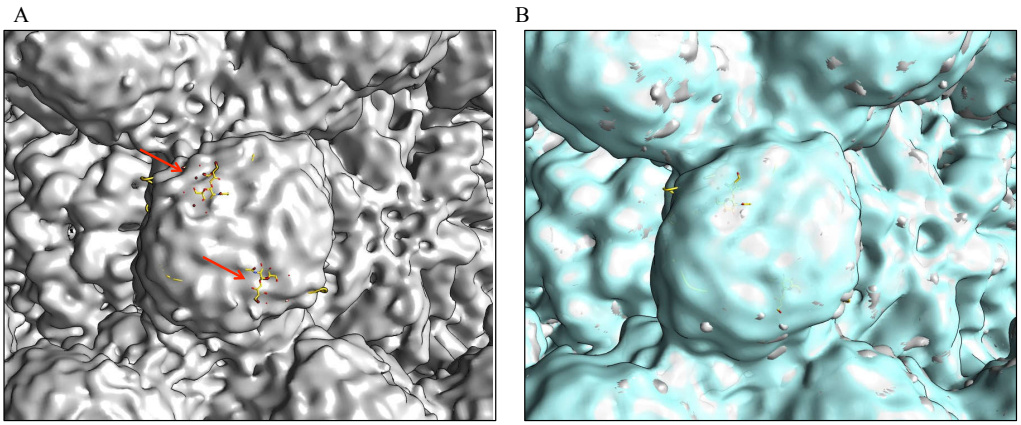

Figure 7-4 | The X-ray crystal structure of GII.17 P domain with A-tri (PDB: 5LKC), fitted into the cryo-EM structure of GII.17 apo (A) and GII.17 with A-tri (B). The ligands are shown as yellow sticks and highlighted by red arrows. Ligands were not covered by density in the unbound structure and covered by density in the complexed structure.

After refinement of 40,951 particles, we obtained a structure at 7.9 Å resolution (Figure 7-3C/D). Comparison of the unbound to the liganded structure revealed that the structures appeared identical and no obvious structural rearrangements had occurred. When fitting the GII.17-A-tri complex X-ray crystal structure [PDB: 5LKC (98)] into the density, the A-tri molecules were covered, whereas at the same threshold they were not covered in the apo structure (Figure 7-4). However, at lower threshold also in the liganded structure the A-tri ligand was not covered by density. This could imply that not all binding sites were occupied, leading to a lower density threshold. Unfortunately, the resolution of the P domains was not sufficient to unambiguously define if the small A-tri molecules were present in the structure. As the P domains in norovirus are relatively flexible and therefore resolution is limited, we applied focused reconstruction on the P domains. However, resolution of the separate classes was not sufficient to unambiguously detect the small ligand bound to the receptor site. All classes exhibited a comparable tilt and rise of the P domain, suggesting no strong conformational differences within the particles.

GII.17 in complex with the small molecule inhibitor 2'FL

In a similar experiment, we wanted to determine, whether the binding of the inhibitor 2'FL led to structural rearrangements. 2'FL is known to broadly inhibit attachment of noroviruses to HBGAs by occupying the HBGA binding site.

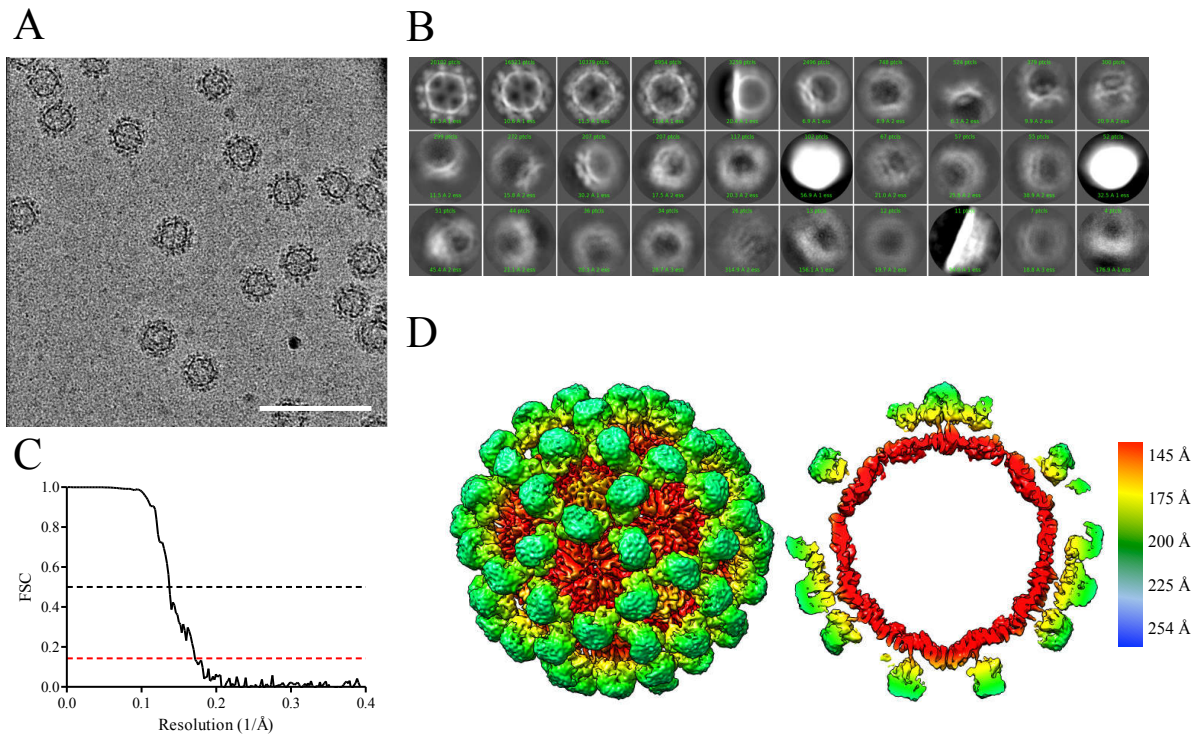

Figure 7-5 | The Cryo-EM structure of GII.17 VLPs with 2'FL. (A) Representative raw micrograph of GII.17 VLPs with 2'FL shows not obvious differences to unbound particles. (B) 2D classification indicates structurally homogeneous particles. (C) The FSC curve indicates a resolution of 5.8 Å with FSC cut-off of 0.143 (red dashed line, 0.5 FSC cut-off illustrated as black dashed line). (D) Cryo-EM structure of GII.17 VLPs with 2'FL exhibits T=3 icosahedral symmetry and no structural deviations from the apo structure were observable at this resolution. The particle is colored by radius, as demonstrated by the color scale.

GII.17 HBGA binding can be inhibited by 2'FL, and the X-ray crystal structure of the P domain/2'FL complex was solved in a previous study (98). For structural analysis of the capsids with the compound, VLPs were incubated with 100× molar excess of 2'FL to the binding site and flash frozen on the cryo-EM grid. As observed with A-tri, liganded VLPs in vitrified ice exhibited a similar morphology as the untreated VLPs and no noticeable background was introduced by addition of the compound (Figure 7-5A). A dataset with 3,570 images was collected. From 55,956 particles, we obtained a structure of 5.8 Å resolution (Figure 7-5 C/D). However, no large differences were visible when compared to the apo structure. The particles exhibited a diameter of 45 nm, with clearly raised P domains. Only when fitting the X-ray crystal structure of GII.17 P domain with 2'FL [PDB: 5LKG (98)] in

the complexed structure and in the apo structure, a difference was visible: In the complex, the 2'FL molecules where covered by EM density (Figure 7-6). Conversely, when fitting the complex in the cryo-EM apo structure, no density was visible corresponding to the 2'FL molecules. Nevertheless, due to the high flexibility and low resolution of the P domain, it was not possible to definitely determine, whether the ligand was bound to the capsid.

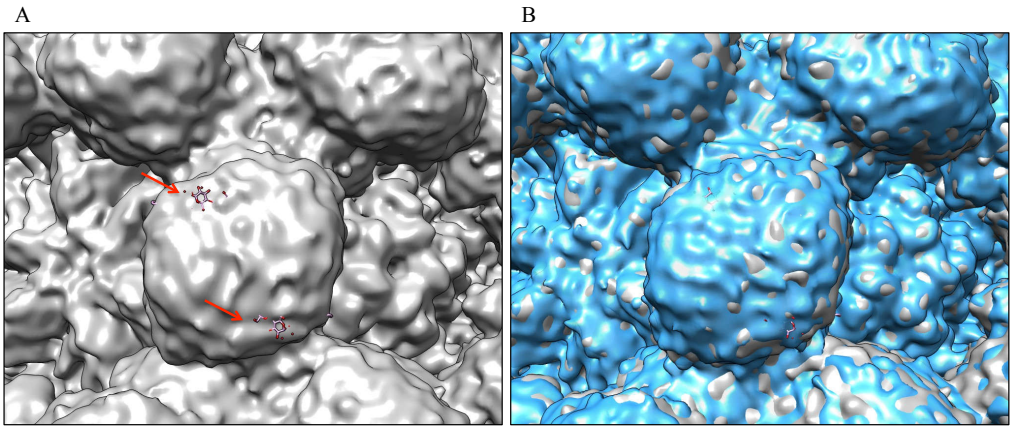

Figure 7-6 | X-ray crystal structure of GII.17 P domain in complex with 2'FL (PDB: 5LKG), fitted into the cryo-EM densities of GII.17 apo (A) and GII.17 with 2'FL (B). Ligands are colored in purple and highlighted by red arrows. In the unliganded structure, the ligands were not covered by density, in the complexed cryo-EM structure, the 2'FL molecules were covered.

7.4. Discussion

In this chapter we determined the structure of the VLPs of the newly clinically relevant genotype GII.17 Kawasaki. While the structure in general resembled the typical capsid morphology, several features were distinct from previously solved structures (Figure 7-7 and Figure 7-8). The P domains of the GII structures were raised up from the S domain, whereas the P domains of GI.1 Norwalk VLPs rested directly on the shell. Extended P domains have previously been observed for RHDV, MNV, vesivirus 2117, sapovirus and FCV (31, 86, 87). Due to the extension of the P domain, GII.17 VLPs were notably larger than GI.1 VLPs. Similarly, T=3 GII.4 VLPs had a diameter of 46 nm [Chapter 2 and (41)]. The diameter of GII.10 was 42 nm, 3 nm smaller than the T=3 structures of GII.17 and GII.4. This fits well with the observation that GII.10 had P domains that were raised, but not as pronounced as in GII.4 and GII.17 (Figure 7-8). T=4 GII.4 VLPs exhibited a larger capsid size of ~50 nm, with an inner diameter of ~32 nm (41). This can be explained by the fact that the GII.4 T=4 capsid incorporated 60 subunits more into the capsid than T=3 structures, leading to an overall increase in inner and outer diameter.

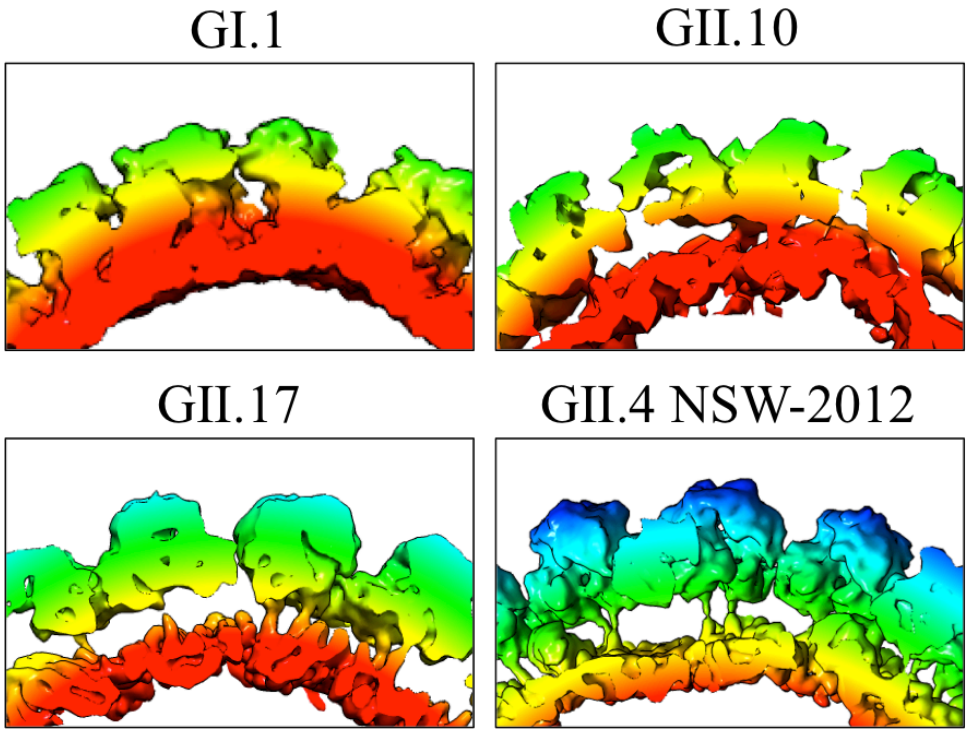

Figure 7-7 | Cutout sections of different VLP structures. In GI.1, the P domains were resting directly on the shell. All GII structures had elevated P domains. The diameter of GII.17 was larger than GII.10, due to stronger extension of the hinge region. The structures are colored by diameter.

A common feature of GII.4 and GII.17 VLPs is an extended hinge region connecting P and S domain (Figure 7-8). Both GII.4 and GII.17 are clinically relevant, so one can speculate that

the outstretched hinge region could confer an advantage during infection. The P domain is responsible for host interactions. This elongation could allow for more flexibility, permitting more efficient interactions with host cells, thereby increasing infectivity.

The hinge regions of GI.1, GII.10, GII.4 and GII.17 have a sequence identity of 60-70%. Sequence comparison did not provide obvious reasons for the observed structural differences. For MNV-1 the P domains were extended as well (86). Comparison with the MNV hinge region demonstrated a sequence identity of only 20-30% compared to the human norovirus hinge regions, suggesting that the extension of the hinge was not dependent on the sequence. Moreover, there were no insertions within the GII genotypes compared to GI.1. In the X-ray crystal structure of GI.1, the hinge region formed a loop (162). Therefore, the extension could be due to differential intramolecular interactions, forcing the hinge into an extended conformation. Since all caliciviruses share the flexible hinge between the P and S domain, it could be possible that raised and lowered P domains are not exclusive conformations of certain genotypes but rather are different states occurring throughout the norovirus infection cycle. Indications that this might be the case have been found for MNV, where P domains were collapsed after treatment with the cofactor bile (183).

Another main difference between the structures was the tilt of the P domains (Figure 7-8). GII P domains were similar in appearance, whereas the P dimers of GI.1 were rotated distinctly. In the GI.1 structure, the P domains were only connected via a loop at the quasi-three-fold axes, exhibiting only few intramolecular contacts between the neighboring dimers. In contrast, the GII P domains were tilted and the flatter part of the P domain was pointing towards the quasi-three-fold axes. This rotation of the P domains enabled more interactions between adjacent P domains, allowing the formation of a stabilizing network. The P1 domains were not only involved in intradimeric interactions that facilitated dimer formation, but also participated in interdimeric interactions between individual dimers. As this tilt occurred only in the structures with raised P domains, it is possible that these interactions are necessary for stabilization and prevent the P domains from collapsing onto the shell. Extensive interactions between the P domains at the quasi-three-fold axes have also been observed in the structure of elevated MNV P domains (86).

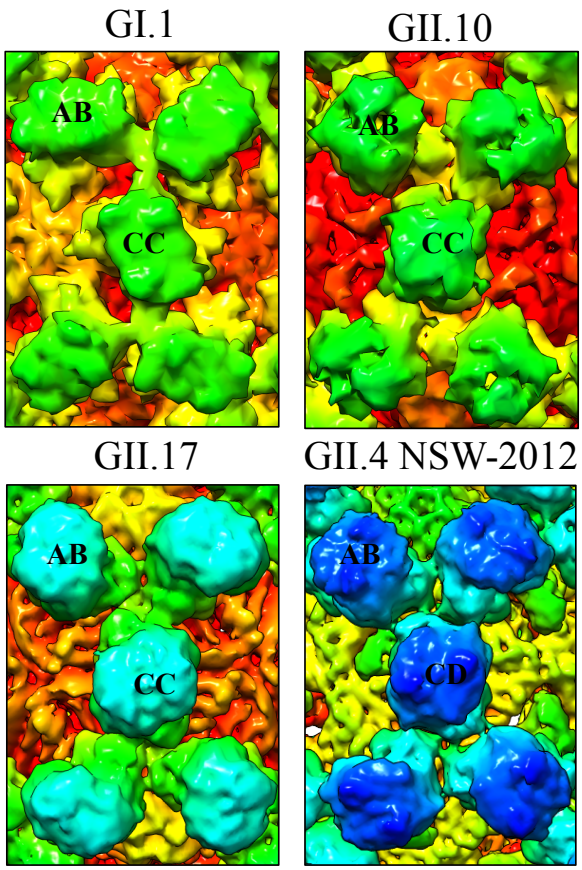

Figure 7-8 | Close-up on the P domains of different VLPs. For GI.1 VLPs, the P domains were distinctly rotated when compared to the GII structures. This was caused by the rotation due to the lowering of the P domains onto the shell in this capsid morphology.

Attachment factors are commonly used to concentrate the virus on the cell surface without induction of conformational changes. Conversely, true receptors can often promote conformational rearrangements in the capsid to prime the virus for cell entry (231). In calicivirus, this has also been shown recently, where the addition of the proteinaceous receptors fJAM-A to FCV initiated movement of the P domains. Most importantly, receptor binding resulted in the formation of a portal vertex of 12 VP2 monomers that is thought to enter the host cell membrane and facilitate the genome delivery (32). Interestingly, the addition of the cofactor bile salt to MNV virions resulted in a structural rearrangement where the P domains were lowered onto the shell from their normally extended position (183). The conformational change is thought to initiate infection. This shows that in the case of MNV, also cofactors can induce structural rearrangements on the capsid. However, in our case, no structural rearrangements were observed after incubation of the VLPs with the cofactor A-tri. As the resolution was limited at the P domain, we could not definitively prove that the ligand was attached to the binding sites. Nevertheless, it is conceivable that binding of A-tri did not induce any major structural rearrangements. So far, the knowledge about how human

norovirus enters the cell is scarce. Several important cofactors, such as HBGAs and bile acids are known (49, 133), but their roles are not completely clear. A human norovirus host receptor still remains elusive. It could be possible that only binding to a receptor triggers the changes that are necessary for infection, as observed in FCV (32). HBGAs, such as A-tri, might only be important for initial attachment of the virus to the cell, thus no structural changes would be necessary at this point. Many viruses, e.g. herpesviruses (184, 229), flaviviruses (7, 25, 56) or picornaviruses (81) bind to molecules of the negatively charged glycocalyx as a first step of infection, only to concentrate the virus on the cell surface and enhance infection. Moreover, not all virus receptors are imposing structural rearrangements on the capsids. In some cases, binding to the receptor triggers signaling pathways that in turn enable cell entry (61). Due to this high variability of possible virus/binding factor-interactions, more detailed studies on which roles the different norovirus binding factors are assuming are urgently needed. Additionally, higher resolution information, where the small cofactors are visible would be needed to determine unambiguously that the HBGAs did not introduce structural rearrangements.

Another possibility is that rearrangements can only occur in the context of the intact virion and not in VLPs only assembled from VP1. In both cases where extensive structural rearrangements have been reported for caliciviruses [MNV (183) and FCV (32)], experiments were done with intact virions, as opposed to empty VLPs in our experimental setup. Additional interactions of VP1 with VP2, or the VPg-linked genome could aid in facilitating the necessary rearrangements.

In former studies, it has been shown that 2'FL was able to inhibit the attachment of VLPs to PGM, by acting as a cofactor decoy and blocking the HBGA binding site (98, 220). However, it is possible that next to this direct blocking effect, the sugar has additional effects on the virus that lead to the loss of HBGA binding ability. In our structure, the P domains appeared to be bound to 2'FL, but due to the high flexibility of the P domain and the lowered resolution, the ligand could not be placed unambiguously. Nevertheless, it is conceivable that binding of 2'FL has no effect on the structural integrity of the virus, as simple blocking the binding site would suffice to efficiently inhibit HBGA binding.

In summary, we found that GII.17 VLPs exhibited the characteristic norovirus morphology. P domains were in a raised state, which further indicates that extended P dimers are the most common P domain state in norovirus. Moreover, our results suggest that neither the binding factor A-tri, nor the small molecule inhibitor 2'FL induced large structural rearrangements on

the GII.17 capsid. Whether the human norovirus capsid is primed by structural rearrangements to initiate infection is still to be determined.

8. Chapter 5: Structural analysis of MNV in complex with Nanobodies and ions

8.1. Summary

In this chapter we solved the structure of murine norovirus (MNV) virions alone and in complex with a neutralizing Nanobody. In the apo state, MNV appeared as a typical T=3 icosahedral norovirus, with raised P domains.

In the complexed structure, the Nanobody forced the MNV P domains into distinct conformations to allowed binding at all available epitopes. Incubation of MNV virions with divalent cations (Mg^{2+} and Ca^{2+}) led to a collapse of the P domain onto the shell, a conformational rearrangement that seems to enable efficient MNV infection. Importantly, binding of the Nanobody appeared to inhibit this structural rearrangement, thereby effectively inhibited viral infection.

8.2. Contributions

The results in this chapter were gained as a part of collaborative work: Dr. Anna Koromyslova and Virginie Malak cloned and purified the Nanobodies and MNV virions. Dr. Anna Koromyslova performed the biochemical characterization of the Nanobodies (ELISA, cell attachment and entry assays, ITC). Dr. Turgay Kilic and Dr. Charles Sabin did X-ray crystallography experiments. I was working on the cryo-EM structures of MNV apo, together with Dr. Charles Sabin, and MNV in complex with NB-5829, $MgCl_2$ and $CaCl_2$, and NB-5829/$MgCl_2$. All authors analyzed the data, and wrote and commented on the paper that is currently under review and published on a preprint server:

Koromyslova AD*, Devant JM*, Kilic T, Sabin CD, Malak V, Hansman GS. 2020. Nanobody mediated neutralization reveals an Achilles heel for norovirus. bioRxiv doi:10.1101/2020.02.07.938506:2020.02.07.938506.

(* = equal contribution)

Figures from this chapter were taken and adapted from this manuscript.

8.3. Results

Prior results: Biochemical and structural characterization of MNV-specific Nanobodies

MNV is commonly used as a model system for human norovirus, as a reliable cell culture and reverse genetics system are available. In this study, we focused on Nanobodies raised against MNV virions, to characterize their neutralization potential and define how those Nanobodies are inhibiting infection.

Generally, two types of Nanobodies were found and structurally characterized by X-ray crystallography: One type bound to the upper part of the P domain and was able to neutralize infection by competing with the cellular receptor CD300lf (150). The second group of Nanobodies bound to an epitope at the lower part of the P domain, so no direct interference with binding factors or receptors was found (Figure 8-1). Cell culture assays indicated that the Nanobodies binding to the lower part of the P domain were most likely affecting post-receptor binding steps, but from cell culture assays and ITC measurements alone, no mode of inhibition could be determined.

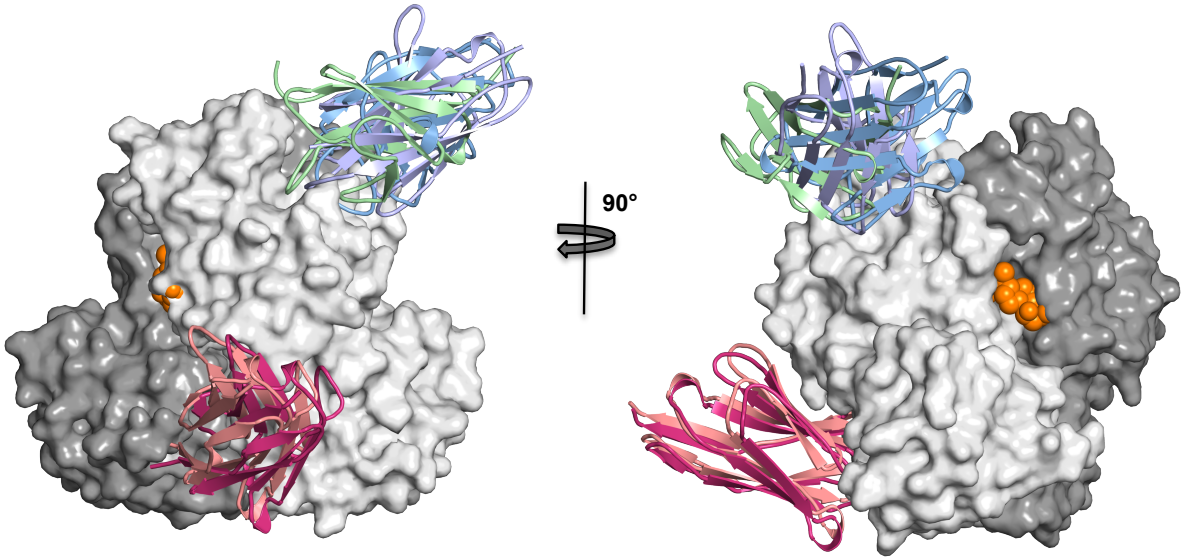

Figure 8-1 | Binding sites of MNV specific Nanobodies. X-ray crystallographic data revealed that NB-5853 (blue) and NB-5867 (lavender) bound to the top of the MNV P domain. The binding sites of these Nanobodies overlapped with the binding sites of the proteinaceous receptor CD300lf (green). NB-5820 (salmon) and NB-5829 (pink) were binding to the lower side of the P domain and interacted with both VP1 monomers in a P dimer. Also shown is the binding site of the bile acid GCDCA (orange). Dr. Turgay Kilic and Dr. Charles Sabin solved and refined the X-ray crystal structures; Dr. Charles Sabin prepared the figure. Figure adapted from (103).

Dr. Anna Koromyslova, Dr. Turgay Kilic and Dr. Charles Sabin have performed these prior experiments. In the following experiments, we used single particle cryo-EM to elucidate the mode of inhibition for the Nanobodies binding to the bottom of the P domain.

The structure of MNV virions in an unbound state

In former studies, the MNV structure has been elucidated using cryo-EM to a resolution of ~8 Å (87). In order to have higher resolution information to compare how Nanobodies influence the structure, we first determined the structure of MNV in an unbound state. In a first dataset 4,046 images were collected. 15,770 particles were used for final reconstruction with a nominal resolution of 4.1 Å. However, the P domains were only visible as blurred densities. Smearing of densities can be caused by incoherent averaging. Therefore, we applied focused reconstruction on the VP1 dimers, to resolve this heterogeneity between the single VP1 dimers. Indeed, application of focused reconstruction on the P domain dimers revealed that 20% of the A/B- and 25% of the C/C dimers showed a lowered P domain morphology, instead of the typical elongated hinge region and subsequently elevated P domain (Figure 8-2).

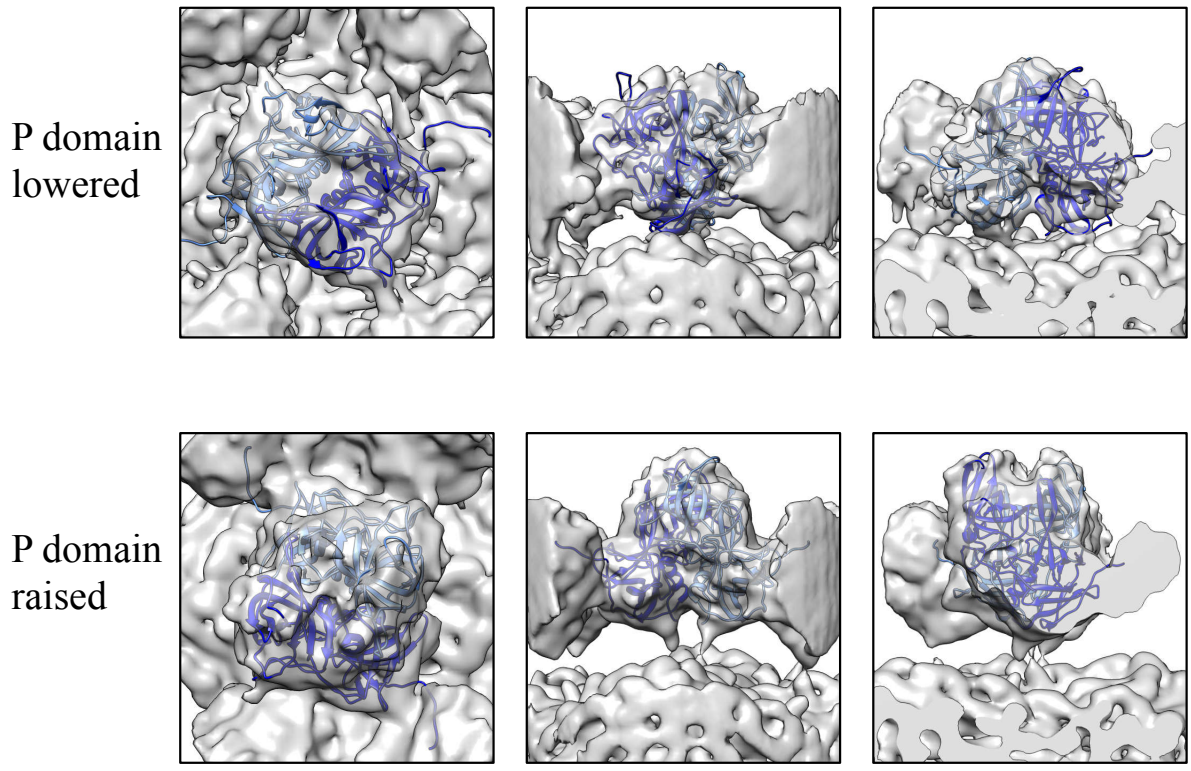

Figure 8-2 | Comparison of raised and lowered P domains on the MNV capsid. The classes were separated by focused reconstruction on the P domain dimers. Shown are two representative classes of raised and lowered P domains of a C/C dimer (grey) fitted with the X-ray crystal structure of MNV (PDB: 3LQ6, blue cartoon).

Comparison of different P domain conformations indicated that upon collapse of the hinge region, the P domain dimers were rotated by ~104º relative to the extended P domain conformation.

To confirm that this was not due to two separate populations of virions, one with only lowered and one with only extended P domains, a heterologous refinement was performed in cryoSPARC, where two distinct starting models are presented [GI.1 – lowered P domains (162) and MNV- raised P domains (87)], to facilitate the separation of two distinct classes. Both obtained structures were similar, with well-resolved S domains and fuzzy P domains. This suggested that the two conformations indeed were present on the same particles.

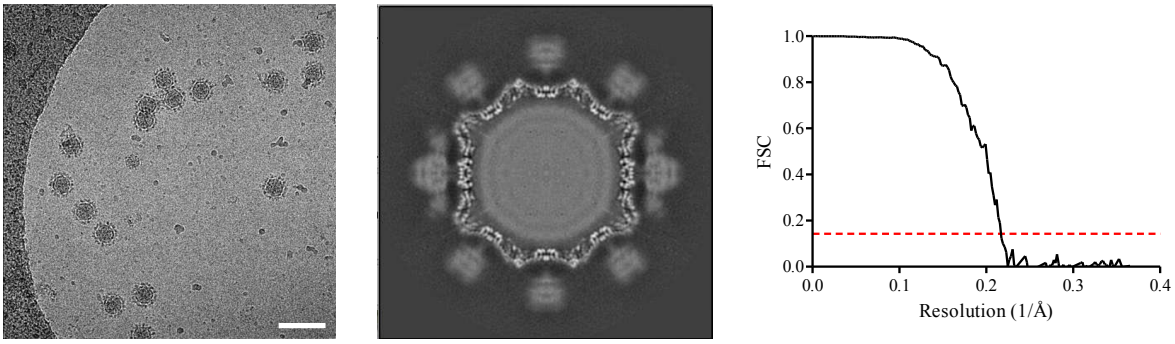

Figure 8-3 | Cryo-EM processing of MNV virions. Left shows a raw micrograph of the virions (scale bar represents 100 nm), the middle figure is the central section of the reconstruction, revealing that the P domains are of lower resolution than the shell. The FSC curve (right) indicates a resolution of 4.6 Å at 0.143 FSC cut-off. Figure adapted from (103)**.**

The sample we used for this first structure determination was stored for several months at 4 ºC. As so far, only raised P domains were reported for MNV (87) we decided to repeat the experiment with a freshly purified MNV sample. Also here, particles were well distributed in the ice and a dataset with 1,588 images was collected (Figure 8-3).

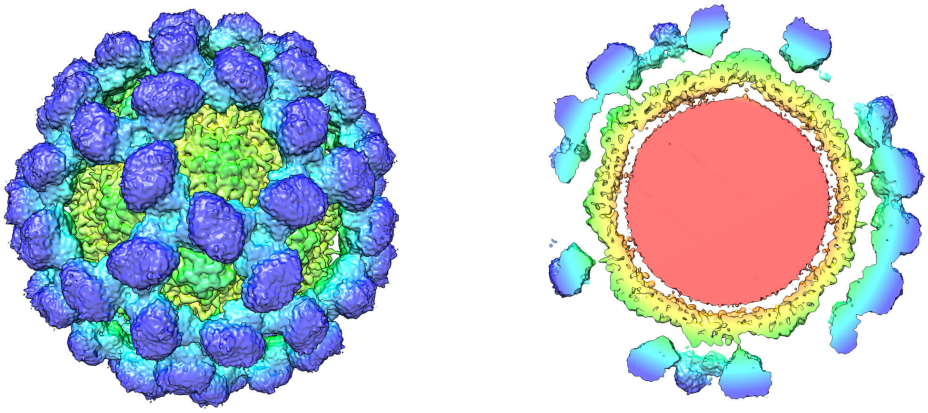

Figure 8-4 | Cryo-EM structure of the MNV virion. The capsid is shown in whole (left) and in cutout section (right). The P domains were all extended. Nevertheless, the P domain resolution was lower than for the S domain. Due to the icosahedral reconstruction, the RNA (red) could not be resolved.

From the raw data, no obvious differences were observed compared to the first dataset. 21,424 particles were used for the final reconstruction that had a resolution of 4.6 Å, and P domains that appeared to be all raised (Figure 8-3 and Figure 8-10 left). Subsequent focused refinement on both A/B and C/C dimers confirmed that all P domains were indeed in a raised state. This result suggested that during the long storage, the virions used in the first preparation became unstable, causing a proportion of the P domains to collapse onto the particles. As both samples were purified in the same way and stored in PBS, effects due to differences in the buffer or purification method could be excluded.

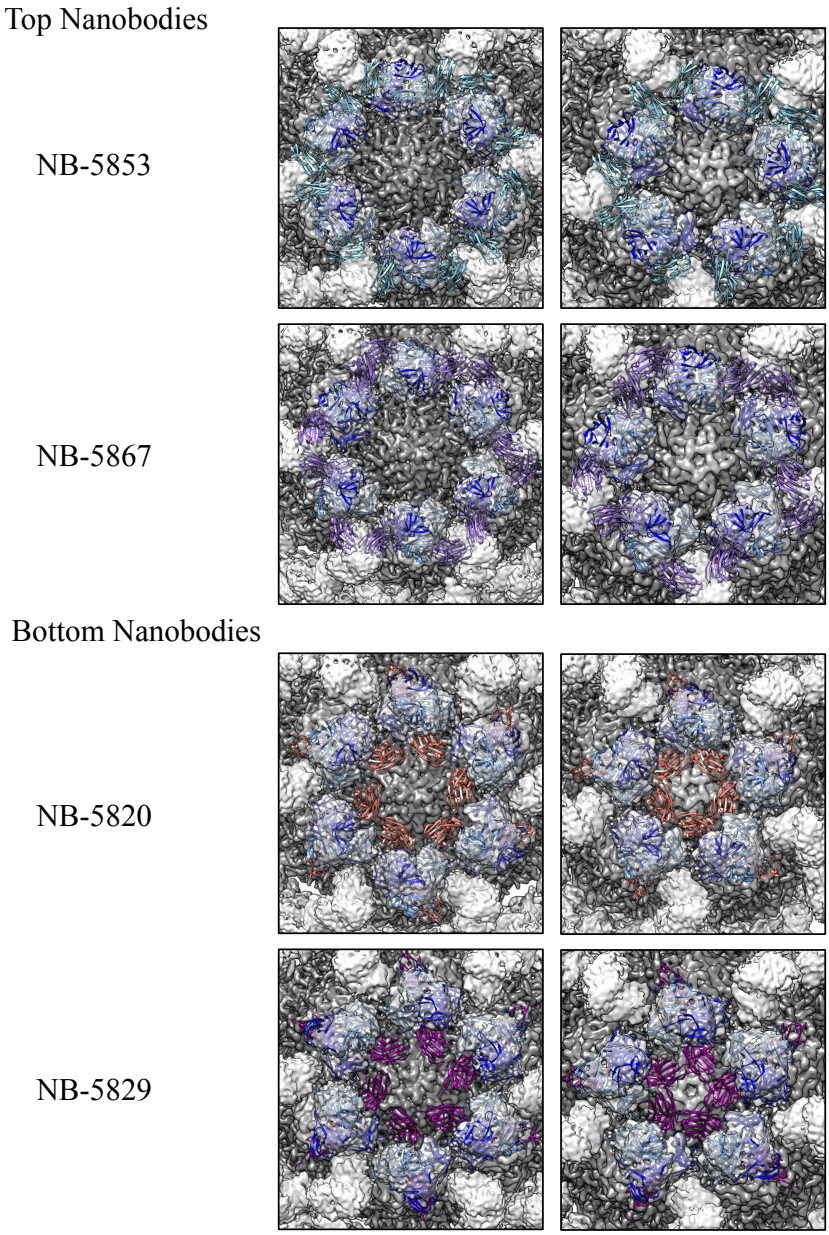

Figure 8-5 | Model of top and bottom Nanobodies bound to the MNV capsid. The X-ray crystal structure of P domain and Nanobody (cartoon, P domain in blue, NB-5853 turquoise, NB-5867 lavender, NB-5820 salmon, NB-5829 purple) was fitted into the cryo-EM density of the MNV virion. In all cases, Nanobodies were clashing with adjacent Nanobodies at full occupancy at both three-fold (left) and five-fold (right) icosahedral axes.

Fitting of P domain/Nanobody X-ray crystal structures onto the apo cryo-EM density revealed clashes at full occupancy: For both, top (NB-5853 and NB-5867), and bottom binding Nanobodies (NB-5820 and NB-5829), the Nanobodies were clashing with adjacent Nanobodies when all binding sites were occupied, suggesting that in this capsid conformation not all epitopes were available (Figure 8-5). Consequently, this would indicate that either, Nanobodies were not able to bind to all available binding sites due to space restraints, or that the Nanobody binding forced structural rearrangements onto the capsid to facilitate the occupation of all epitopes.

The structure of MNV in complex with NB-5829

To further define how the Nanobodies were neutralizing the MNV infection, and if and how the Nanobody binding influenced the virion structure, we wanted to determine the structures of virions in complex with Nanobodies. Binding of Nanobodies with epitopes overlapping the CD300lf binding site (NB-5853 and NB-5867) led to aggregation of the particles, so no single-particle analysis could be performed.

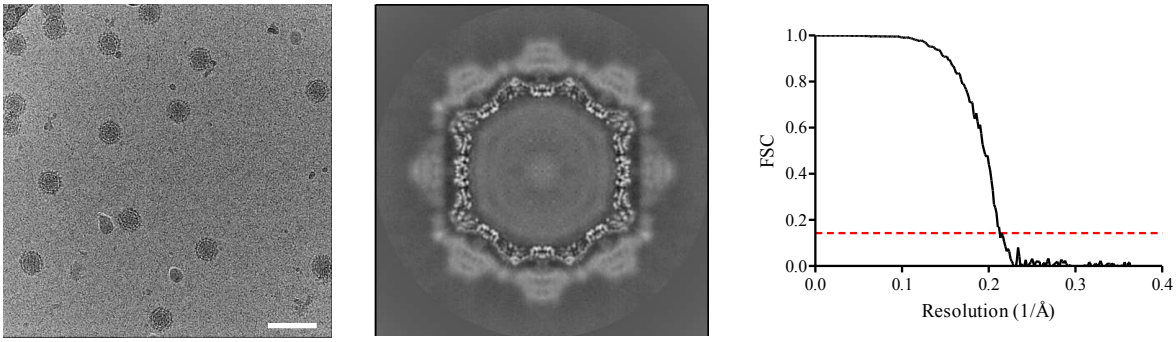

Figure 8-6 | Cryo-EM processing of MNV virions in complex with NB-5829. Left shows a raw micrograph of the complexes (scale bar represents 100 nm), the middle figure is the central section of the reconstruction. The FSC curve (right) indicates a resolution of 4.7 Å at 0.143 FSC cut-off. Figure adapted from (103)**.**

Virions bound to the bottom-binding Nanobody NB-5829 however, were still separated in the ice and a dataset of 3,599 images was collected and analyzed (Figure 8-6). 32,612 particles were used for the final icosahedral reconstruction of 4.7 Å resolution (0.143 cut-off). Even though the S domains were resolved well, the P domains appeared as smeared densities and were of lower resolution than the S domain, again indicating structural differences within the P domain dimers on the capsid (Figure 8-7).

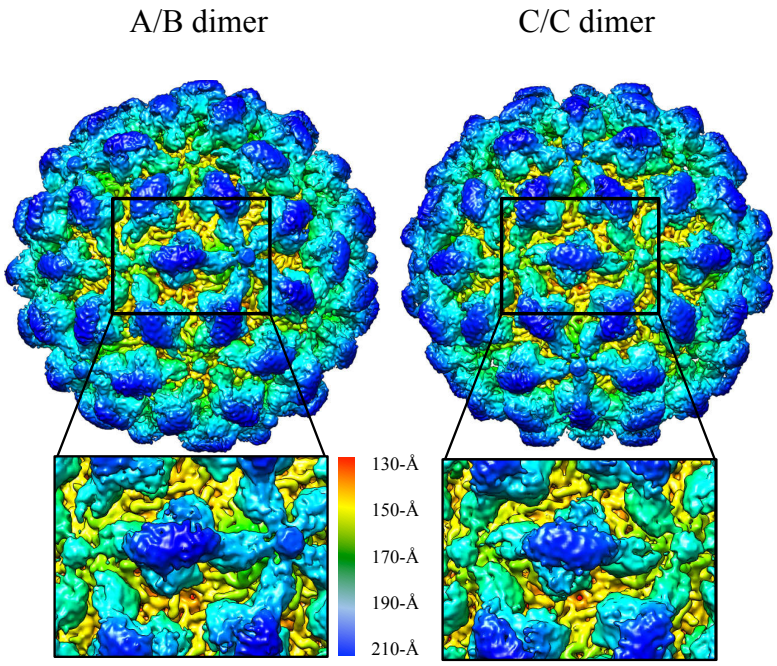

Figure 8-7 | The cryo-EM structure of MNV virion in complex with NB-5829. After icosahedral reconstruction, additional densities at the P domains were visible, indicating bound Nanobodies. The structure is colored by radius, as indicated by the color scale. The P domains were of lower resolution than the shell, suggesting movement of this domain. Figure adapted from (103)**.**

By applying focused reconstruction on the P domain/Nanobody complexes, we found that indeed all classes had two Nanobodies bound to the P domain dimers. This indicated that also in context of the intact particle, two Nanobodies had bound per dimer (Figure 8-8A). Overlay of the complexed X-ray crystallography structure indicated a good fit. This revealed that the Nanobodies bound to the same binding site and in the same manner on the virions as they did to isolated P domains.

Moreover, we found that the P domains exhibited several different rotations, relative to the S domain, with up to 31° tilt between different A/B dimer conformations and 34° tilt between C/C dimer conformations (Figure 8-8B). These differences could result in incoherent averaging of the P domains and smearing of the P domain densities, as observed in the icosahedral reconstruction of the particles. In contrast, in the apo structure a tilt of only 2° in A/B- and 12° in C/C dimers was measured, indicating the Nanobody attachment did not stabilize the P dimer. Instead, it led to stronger structural deviations within the single P dimers on the capsid. Moreover, when compared to the apo structure, we found that the P domains were rotated by ~70°. These results indicated that the Nanobodies were forcing the P domains in new and diverse positions, most likely to accommodate the binding of Nanobodies to all binding sites. This movement of the P domain upon binding of the Nanobody highlights the high flexibility of the capsid, in particular of the hinge region connecting S and P domains.

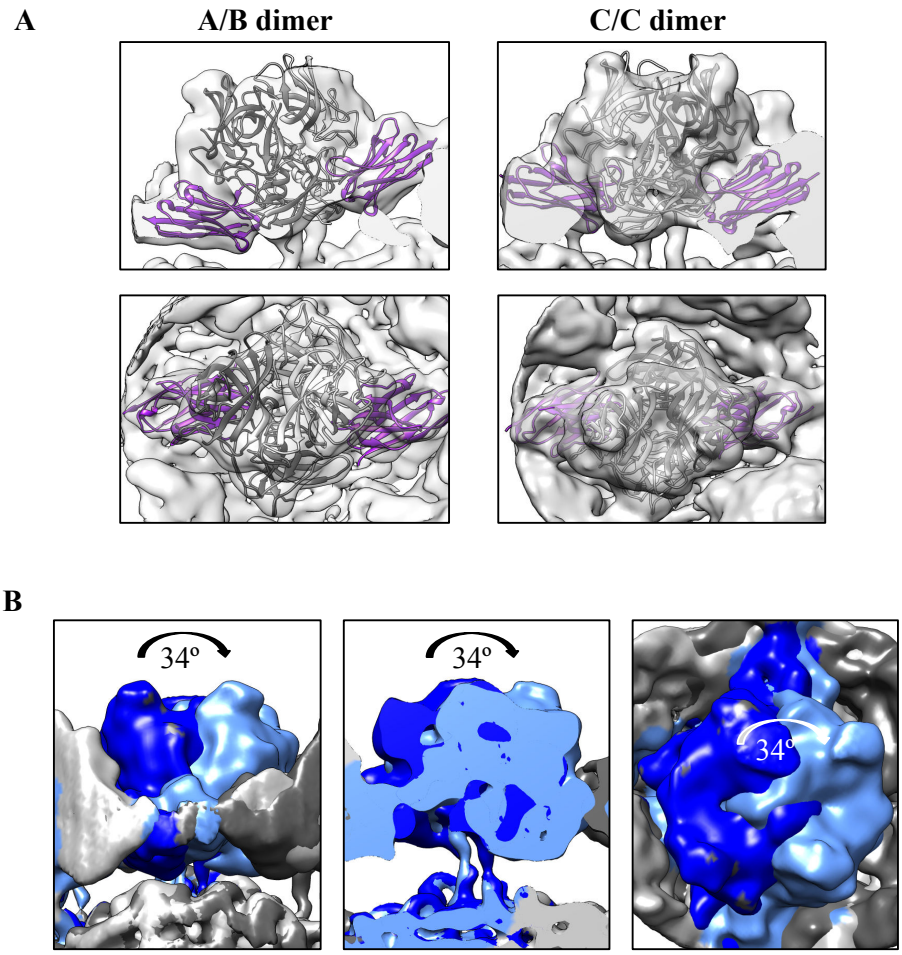

Figure 8-8 | Focused reconstruction of P domains in complex with NB-5829. (A) Representative classes of A/B and C/C dimers after focused reconstruction. The densities have the X-ray crystal structure of MNV P domain (grey cartoon) and NB-5829 (purple cartoon) fitted. (B) To compare the of P domain tilt, two focused reconstruction C/C dimer classes were overlaid (light blue and dark blue). P domains are shown in side view (left panel), cutout section (middle panel) and top view (right panel). The P domains showed strong tilt of the P domain between the different classes, up to 34º. Conversely, the shell remained rigid. Figure adapted from (103)**.**

The influence of $MgCl_2$ or $CaCl_2$ on the MNV capsid morphology

All these results however, did not aid in elucidating the exact mechanism of neutralization. Recently, it was proven that binding of an important cofactor, bile salt, induced structural rearrangements in the MNV capsid: The P domain collapsed onto the shell, thereby causing a rotation of the P domains (183). Even though it is not yet known why this movement is important, infectivity is decreased in the absence of bile, suggesting that this structural rearrangement facilitated infection. Interestingly, in ITC experiments done by Dr. Anna Koromyslova, we found that the addition of $CaCl_2$ to MNV P domain had the same effect on Nanobody binding as the addition of bile salt.

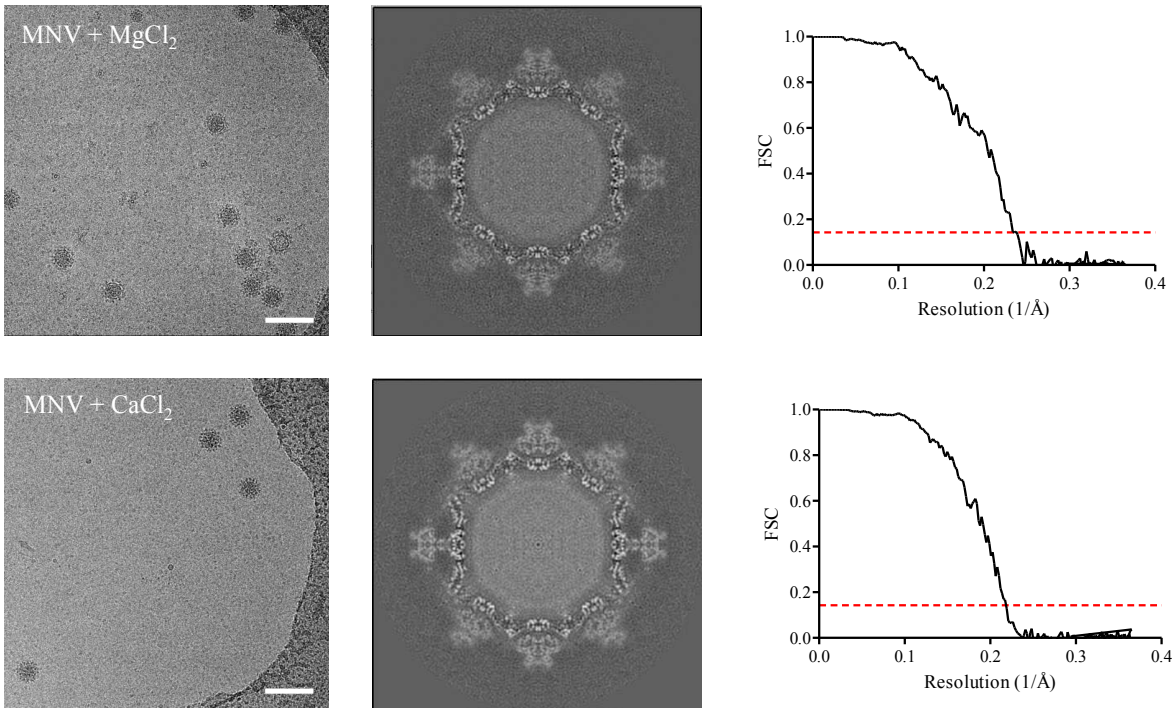

Figure 8-9 | Cryo-EM processing of MNV virions in complex with Ca^{2+} and Mg^{2+}. Left shows raw micrographs of the virions (scale bar represents 100 nm), the middle figures are the central sections of the reconstructions. In these structures, both P and S domain were well resolved. The FSC curve (right) indicates resolutions of 4.6 and 4.3 Å for MNV with Ca^{2+} and Mg^{2+}, respectively (0.143 FSC cut-off). Figure adapted from (103).

Therefore, we went on to determine the structure of the capsid in complex with Ca^{2+} and Mg^{2+} in order to analyze potential structural rearrangements of the capsid as a result of ion binding (Figure 8-9).

Two datasets for MNV virions incubated with 10 mM $CaCl_2$ or 10 mM $MgCl_2$ were collected and data was processed using icosahedral reconstruction. The structures were solved to 4.6 and 4.3 Å resolution, respectively. In both structures, the P domains were clearly resting on the shell, and were remarkably similar to the structure of virions in complex with bile salts (183). This suggests that the different compounds induced the same conformational changes (Figure 8-10). Moreover, the P domains were resolved to a higher resolution than in the apo structure. This suggests that the lowering of the P domain onto the shell stabilized the structure and reduced the movements of the P domains that, in the apo structure, prevent the averaging of the P domains to a high resolution.

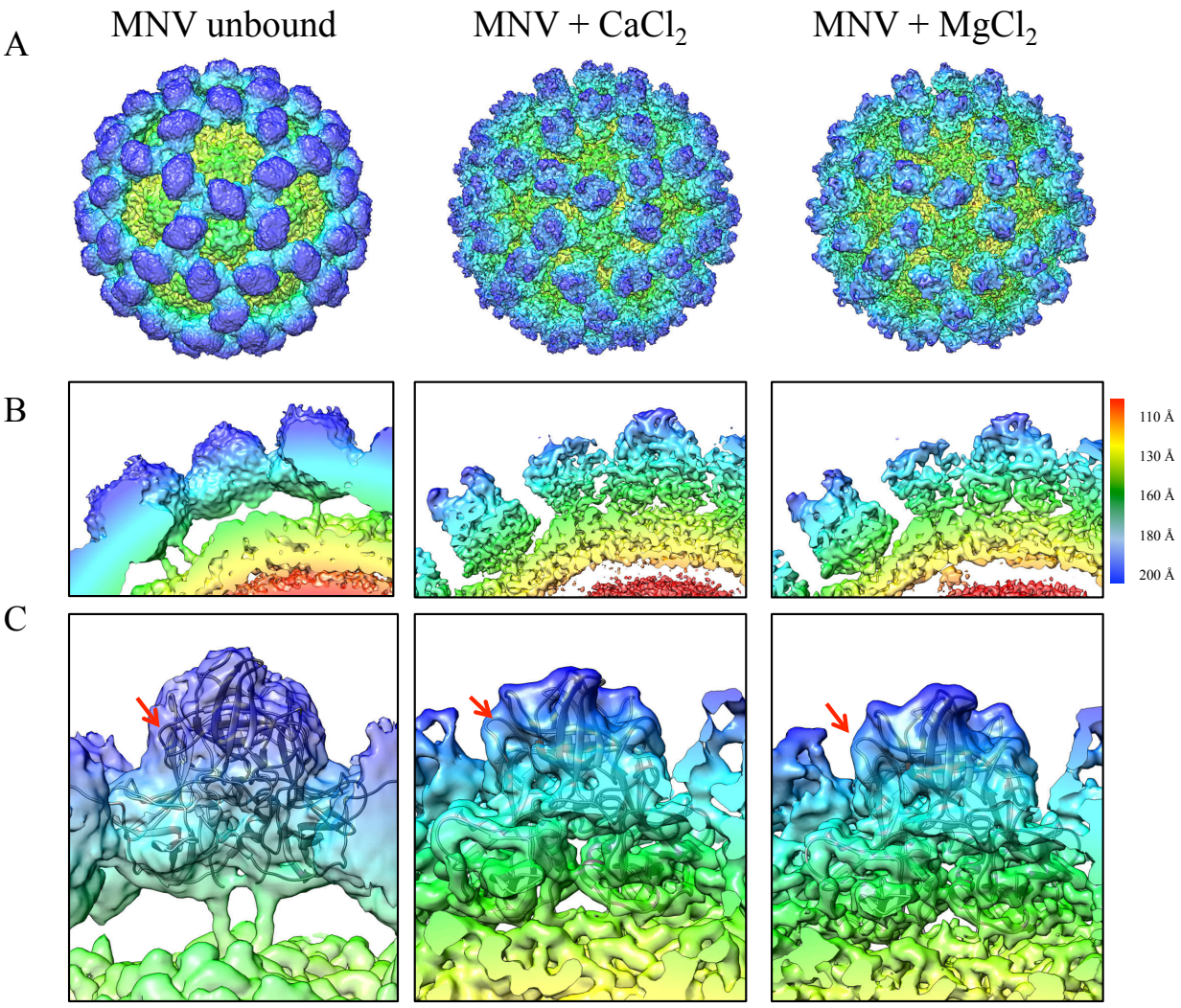

Figure 8-10 | Comparison of the unbound MNV structure with the ion bound MNV capsids. (A) Intact capsids show that the ions induced a collapse of the P domain onto the shell that subsequently led to a stabilization of the structure. Addition of $CaCl_2$ and $MgCl_2$ had an equal effect on the capsid. (B) Cutout sections of the capsid show the elongated hinge region in the apo structure, compared to the collapsed structures, where the hinge was folded into a loop. Consequently, the gap between the P and S domain that is present in the unbound structure is absent in the collapsed form. (C) Close-up on a single VP1 dimer, fitted with the X-ray crystal structure of MNV P domain (PDB: 3LQ6) shows how the C'D' loop was folded down in the apo structure and in an upwards conformation upon ion binding. For the apo structure, a representative focused reconstruction class is shown, as in the icosahedral structure, resolution was limited in the P domains The loop is highlighted by a red arrow. The structures are colored by radius, according to the color scale.

Comparison of collapsed and extended P domains showed that, when collapsing, P domains were moving 114º in a clockwise direction (Figure 8-10B). Moreover, we found that the C'D loop, which was in a closed conformation in the apo structure, was in an opened conformation in the lowered state (Figure 8-10C). This loop movement is thought to facilitate the binding of the receptor to the P domain, as in a closed conformation, affinity of the receptor to the P domain was only low (145).

The cryo-EM structure of MNV in complex with both Mg^{2+} and NB-5829

Superposition of the MNV P domain/NB-5829 X-ray crystal structure onto the lowered-state capsid density indicated that in this conformation, the Nanobodies would clash with neighboring Nanobodies and adjacent P domains (Figure 8-11).

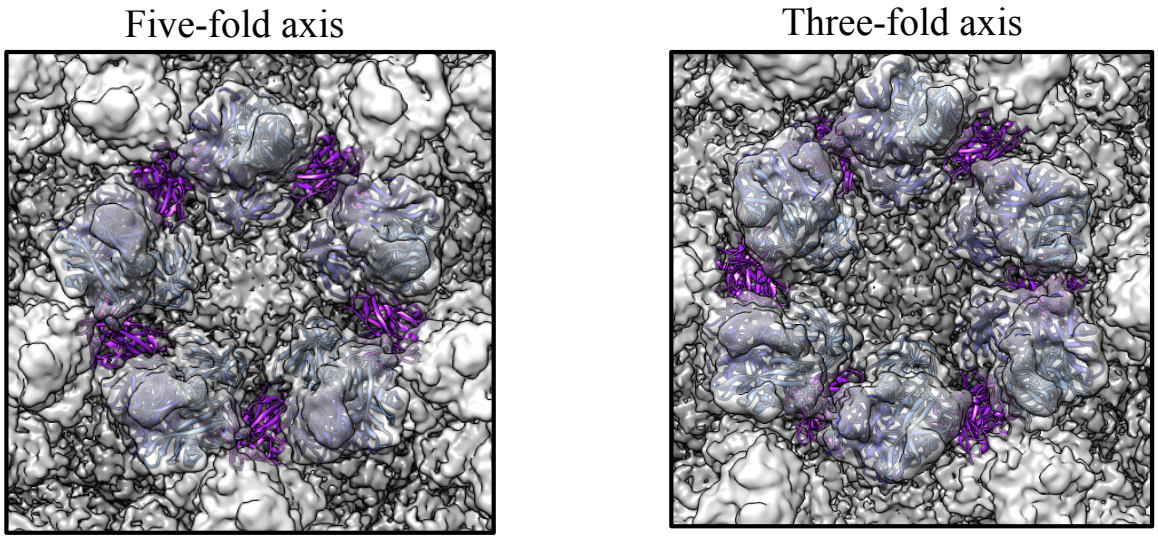

Figure 8-11 | Model of NB-5829 binding to lowered P domains. As a model, MNV in complex with Mg^{2+} was used (grey density), to fit the X-ray crystal structure of the P domain/Nanobody complex (cartoon, P domain in blue, NB-5829 in purple). In this state, the Nanobody would clash with neighboring P domains. Figure adapted from (103)**.**

This finding suggested that Nano-5829 binding prevented the structural rearrangement from the raised- to the lowered-state capsid, thereby inhibiting infection. To confirm this, we incubated virions with NB-5829 for 30 min at RT and then added 10 mM $MgCl_2$ and determined the structure of the complex (Figure 8-12).

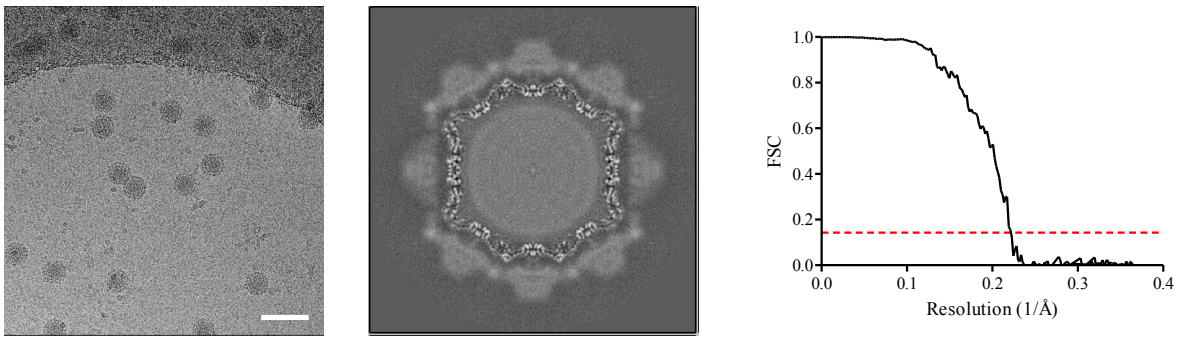

Figure 8-12 | Cryo-EM processing of MNV virions in complex with NB-5829 and Mg^{2+}. Left shows a raw micrograph of the virions (scale bar represents 100 nm), the middle figure is the central section of the reconstruction, showing that the S domain was more sharply resolved than the P domains. The FSC curve (right) indicates a resolution of 4.5 Å at 0.143 FSC cut-off. Figure adapted from (103).

The structure was solved to a resolution of 4.5 Å and bound to NB-5829 at all available binding sites (Figure 8-13). The structure closely resembled the structure of the virion/NB-5829 complex, suggesting that after addition of the Nanobody, the ions could either not bind at all or at least could not induce the lowering of the P domain onto the shell.

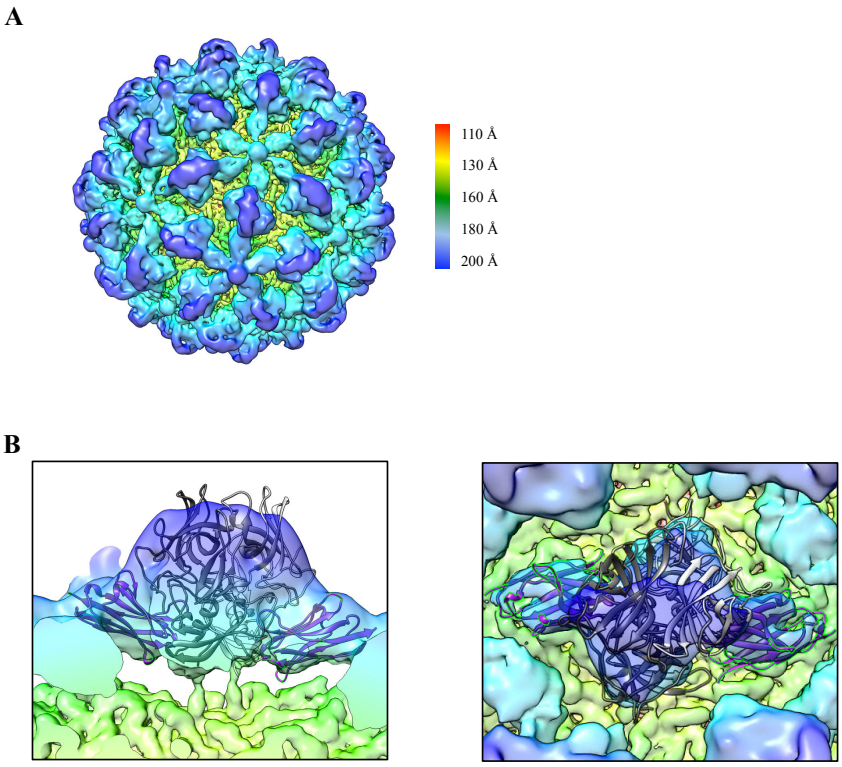

Figure 8-13 | Cryo-EM structure of MNV virion in complex with NB-5829 and Mg^{2+}. (A) Intact particle shows additional densities at the P domains at all possible binding sites, indicating bound Nanobodies. The structure is colored by radius, according to the color scale. (B) Close-up on a P domain dimer in side view and top view. The P domains were raised up from the shell by an elongated hinge region. Overall, the structure closely resembled the structure of MNV in complex with only NB-5829. Figure adapted from (103).

8.4. Discussion

MNV is a popular system to study norovirus. Being segregated in the same genus, it is more closely related to human norovirus than other available model systems, such as FCV or Tulane virus, that are of the *Vesivirus* and *Recovirus* genus, respectively. Moreover, as cell culture- and reverse genetics systems are readily available (219, 225, 226), the viral life cycle can be studied more closely.

Recently, CD300lf has been identified as the cellular receptor for MNV (150) and the discovery of this receptor has explained the inhibition modes for several already described antibodies (86, 97). The receptor-binding site is located at the P2 subdomain, the outermost part of the P domain (90). This domain harbors binding sites for cofactors, such as bile acids (91). Nanobodies and antibodies that bind to the upper part of the P domain often interfere with the binding of cofactors or the receptor, as has been shown for the top binding Nanobodies NB-5853 and NB-5867 that interfere with CD300lf binding.

For the Nanobodies binding to the lower part of the P domain, the mode of inhibition was unclear, as the receptor was still able to bind to the capsid. Many details about the norovirus infection cycle are still unknown. Nevertheless, many studies in the recent years have shed light on at least certain aspects of the infection. It is known that cofactors, such as bile salts or cations, improve infection (49, 66, 91, 150, 183). Studying the cryo-EM structure of MNV with bile salts revealed that the P domains were collapsed instead of elevated, as they are in an unbound state (183), and our study confirmed that this is the case also when cations were added. In fact, our structures were closely matching the MNV capsid after bile salt addition, suggesting that cations and bile induce the same structural rearrangements. Moreover, our results have, unknowingly, been confirmed in another study, where the cryo-EM structure of MNV was solved in a buffer that contained both $MgCl_2$ and $CaCl_2$. In the study, collapsed P domains were reported, but the reason was unclear to the authors. Nevertheless, our findings imply that the structural rearrangement they observed was caused by the presence of $MgCl_2$ and $CaCl_2$ in the buffer (192).

Taken together, this indicates that the lowering of the P domains onto the shell is an essential conformational change to enable infection. Our data suggests that NB-5829 inhibits the P domain rotation and collapse onto the P domain, thereby effectively preventing infection (Figure 8-14). The fact that several compounds induce this conformational rearrangement highlights its importance, but raises the question if the presence of all compounds is required

for efficient infection, or if it is redundant and the presence of one type of molecule is sufficient to enable infection.

To date it is not known why the collapse of the P domain is important for infection. Therefore, we cannot with certainty pinpoint the exact stage of the viral entry mechanism that is inhibited. A cryo-EM structure of a complex of MNV, bile salts and CD300lf indicated that due to spatial restraints it is unlikely that all binding sites can be covered by the receptor, even though the clashes were reduced compared to binding to the apo structure (183). It could therefore be possible that the P domain movement opens up more potential binding sites for the receptor, thereby increasing the effective valency of the viral particle. However, we cannot exclude that this structural change is needed for a later step in the infection cycle, e.g. cell entry or RNA release, and that by binding of the Nanobody not the receptor binding, but another, later stage of infection is prevented.

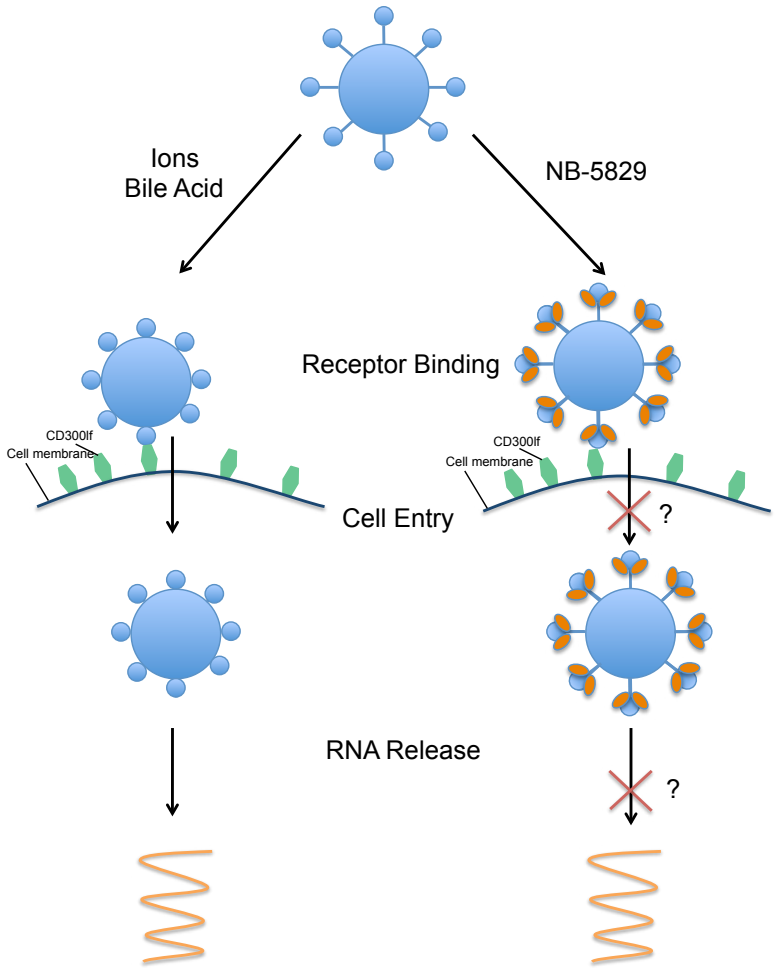

Figure 8-14 | Model for mode of inhibition of the neutralizing Nanobody NB-5829. Without inhibitor, divalent cations, such as Mg^{2+} or Ca^{2+}, or bile acids induce structural rearrangements of the P domain, in turn leading to the collapse of P domain onto the S domain. When NB-5829 is bound to the capsid, P domain collapse is prevented. The particle is still able to attach to the receptor CD300lf, but most likely, a later step in the infection cycle, such as cell entry or RNA release is impaired, subsequently inhibiting infection.

The intracellular concentration of Ca^{2+} is 20,000x lower than outside the cell (30), thus it is possible these that structural rearrangements also allow the virus to detect whether they are outside or inside a cell. Considering the high concentration of ions and bile salt outside of the cell compared to inside, it is conceivable that the collapsed form is required for cell entry. Our finding that ions lead to structural rearrangements are not entirely surprising, as structural dependence on Ca^{2+} has been shown for a number of non-enveloped viruses. For rotavirus, VP7, a protein of the rotavirus capsid, is able to bind Ca^{2+}, and upon chelation of the ions, the protein undergoes antigenic changes that prevent binding of monoclonal antibodies (43). In high calcium environments, VP7 is arranged in a trimeric assembly that dissociates under low calcium conditions. This structural rearrangement was shown to facilitate capsid uncoating *in vitro* (44, 175). This is only one of many cases, where divalent cations play a role in capsid assembly and loss of the ions translates into capsid destabilization (18, 44, 169).

It is still unknown whether our findings can be translated into human norovirus infections. For human norovirus, both raised and lowered state P domains have been reported, but only in different genotypes and a comparable structural rearrangement has not been observed so far (69, 82, 162). Therefore, it remains to be determined if a P domain collapse plays a vital role in the infection cycle of human noroviruses, or if this is a feature unique to MNV. For several genotypes, the addition of bile acid could enhance infection *in vitro* (49), suggesting that bile plays a role in human norovirus infection as well. However, so far the exact role is yet to be determined. Bile acid was able to attach to different human norovirus P domains (91). Moreover, addition of the bile acid GCDCA was able to restore HBGA binding in a supposed non-binder genotype, by inducing structural modifications on the P domain (91). These results suggested that the bile acids have the capacity to directly interact with the virus, possibly influencing cell attachment. Nevertheless, structural studies in context of human norovirus particles with bile have not been done so far. Conversely, another study found that bile acids influence cellular mechanisms of the host cells to provide optimal conditions for norovirus infection, suggesting an indirect influence of the cofactor (144). Future studies, both in cells and on capsids, will have to clarify the role of bile acids as a cofactors in the infection cycle of human norovirus.

So far it is also not known how exactly the binding of the ions/bile salt to the upper part of the P domain leads to the collapse of the hinge region. The regions are distant from each other, but are connected through a stretch of residues. Therefore, it is possible that long-range interactions are causing the hinge region to ultimately collapse and lower the P domain onto the S domain.

Surprisingly, we found that also on the unliganded capsid, lowering of the P domain is possible, apparently without the addition of external triggers. Moreover, this was not the case for the whole capsid but only few P domains, suggesting that both states can be present on the same capsid. As so far, P domains were observed only either all elevated or all lowered, this is a new feature that certainly will have to be studied in more detail. This sample had neither bile nor ions added, therefore this result could entail that other factors could trigger the collapse of the P domain as well.

Epitopes at the bottom of the P domains are more conserved and therefore, antibodies and Nanobodies binding to this region are more likely to be cross-reactive. In fact, even though the lower part of the P domain is less accessible; it appears to be relatively strongly immunogenic. Various different antibodies and Nanobodies have been reported to bind to the lower part of the P domain, and many of those have been proven to effectively inhibit norovirus (69, 99, 101, 176). Therefore, the lower part of the P domain might represent a vulnerable part of norovirus, independent of the genogroup. Of note, despite the similar binding epitopes, antibodies and Nanobodies were inhibiting with remarkably different mechanisms: GII.10 specific Nano-26 and Nano-85 for example bound to the lower part of the P domain of different norovirus VLPs, thereby effectively destroying the particles (99, 101). GI.1 specific Nano-7 also bound to a lower part of the P domain, but here, no clear inhibition mode could be defined, as the particles remained intact and not aggregated. Nevertheless, HBGA binding was abolished effectively upon binding of this Nanobody (176). Conversely, another GI.1 specific Nanobody, Nano-62, bound an epitope close to the Nano-7 binding site, but was not able to inhibit the attachment of VLPs to HBGAs, suggesting that not all epitopes at this site of the domain are vulnerable.

In summary, we have identified a potential intermediate conformation in the norovirus entry pathway, while simultaneously providing an explanation how Nanobodies can prevent those structural rearrangements to inhibit infection. We confirmed that in an unbound state, the P domains of MNV are elevated and found that a P domain collapse could be induced by addition of divalent metal ions. This movement can be blocked by addition of a Nanobody that is binding to the lower part of the P domain, and this interaction effectively inhibited MNV infection. This highlights the importance of this movement for infection and could inform the future development of antivirals by targeting this essential entry pathway intermediate.

9. References

1. **Adler JL, Zickl R.** 1969. Winter Vomiting Disease. The Journal of Infectious Diseases **119**:668-673.
2. **Aladin F, Einerhand AW, Bouma J, Bezemer S, Hermans P, Wolvers D, Bellamy K, Frenken LG, Gray J, Iturriza-Gomara M.** 2012. In vitro neutralisation of rotavirus infection by two broadly specific recombinant monovalent llama-derived antibody fragments. PLoS One **7**:e32949.
3. **Alvarado G, Ettayebi K, Atmar RL, Bombardi RG, Kose N, Estes MK, Crowe JE.** 2018. Human Monoclonal Antibodies That Neutralize Pandemic GII.4 Noroviruses. Gastroenterology **155**:1898-1907.
4. **Atmar RL, Opekun AR, Gilger MA, Estes MK, Crawford SE, Neill FH, Graham DY.** 2008. Norwalk virus shedding after experimental human infection. Emerging Infectious Diseases **14**:1553-7.
5. **Atmar RL, Baehner F, Cramer JP, Lloyd E, Sherwood J, Borkowski A, Mendelman Paul M.** 2019. Antibody persistence to two Virus-Like Particle norovirus vaccine candidate formulations in healthy adults: one-year follow-up with memory probe vaccination. The Journal of Infectious Diseases **220**:603-614.
6. **Barcena J, Verdaguer N, Roca R, Morales M, Angulo I, Risco C, Carrascosa JL, Torres JM, Caston JR.** 2004. The coat protein of Rabbit hemorrhagic disease virus contains a molecular switch at the N-terminal region facing the inner surface of the capsid. Virology **322**:118-34.
7. **Barth H, Schäfer C, Adah MI, Zhang F, Linhardt RJ, Toyoda H, Kinoshita-Toyoda A, Toida T, van Kuppevelt TH, Depla E, von Weizsäcker F, Blum HE, Baumert TF.** 2003. Cellular Binding of Hepatitis C Virus Envelope Glycoprotein E2 Requires Cell Surface Heparan Sulfate. Journal of Biological Chemistry **278**:41003-41012.
8. **Bartsch SM, Lopman BA, Ozawa S, Hall AJ, Lee BY.** 2016. Global Economic Burden of Norovirus Gastroenteritis. PloS one **11**:e0151219-e0151219.
9. **Belongia EA, Skowronski DM, McLean HQ, Chambers C, Sundaram ME, De Serres G.** 2017. Repeated annual influenza vaccination and vaccine effectiveness: review of evidence. Expert Review of Vaccines **16**:723-736.
10. **Bernstein DI, Atmar RL, Lyon GM, Treanor JJ, Chen WH, Jiang X, Vinje J, Gregoricus N, Frenck RW, Jr., Moe CL, Al-Ibrahim MS, Barrett J, Ferreira J, Estes MK, Graham DY, Goodwin R, Borkowski A, Clemens R, Mendelman PM.** 2015. Norovirus vaccine against experimental human GII.4 virus illness: a challenge study in healthy adults. The Journal of Infectious Diseases **211**:870-8.
11. **Bertolotti-Ciarlet A, White LJ, Chen R, Prasad BV, Estes MK.** 2002. Structural requirements for the assembly of Norwalk virus-like particles. Journal of Virology **76**:4044-55.
12. **Bertolotti-Ciarlet A, Crawford SE, Hutson AM, Estes MK.** 2003. The 3' end of Norwalk virus mRNA contains determinants that regulate the expression and stability of the viral capsid protein VP1: a novel function for the VP2 protein. Journal of Virology **77**:11603-15.
13. **Bhella D, Goodfellow IG.** 2011. The cryo-electron microscopy structure of feline calicivirus bound to junctional adhesion molecule A at 9-angstrom resolution reveals receptor-induced flexibility and two distinct conformational changes in the capsid protein VP1. Journal of Virology **85**:11381-90.

14. **Blazevic V, Lappalainen S, Nurminen K, Huhti L, Vesikari T.** 2011. Norovirus VLPs and rotavirus VP6 protein as combined vaccine for childhood gastroenteritis. Vaccine **29**:8126-8133.
15. **Bliss CI.** 1939. The toxicity of poisons applied jointly. Annals of Applied Biology **26**:585-615.
16. **Bode L.** 2012. Human milk oligosaccharides: every baby needs a sugar mama. Glycobiology **22**:1147-1162.
17. **Borroto-Esoda K, Vela JE, Myrick F, Ray AS, Miller MD.** 2006. In vitro evaluation of the anti-HIV activity and metabolic interactions of tenofovir and emtricitabine. Antiviral therapy **11**:377-384.
18. **Brady JN, Winston VD, Consigli RA.** 1977. Dissociation of polyoma virus by the chelation of calcium ions found associated with purified virions. Journal of Virology **23**:717.
19. **Bu W, Mamedova A, Tan M, Xia M, Jiang X, Hegde RS.** 2008. Structural basis for the receptor binding specificity of Norwalk virus. Journal of Virology 82:5340-7.
20. **Burnett E, Parashar U, Tate J.** 2018. Rotavirus Vaccines: Effectiveness, Safety, and Future Directions. Paediatric drugs **20**:223-233.
21. **Cao S, Lou Z, Tan M, Chen Y, Liu Y, Zhang Z, Zhang XC, Jiang X, Li X, Rao Z.** 2007. Structural basis for the recognition of blood group trisaccharides by norovirus. Journal of Virology **81**:5949-57.
22. **Carlsson B, Kindberg E, Buesa J, Rydell GE, Lidon MF, Montava R, Abu Mallouh R, Grahn A, Rodriguez-Diaz J, Bellido J, Arnedo A, Larson G, Svensson L.** 2009. The G428A nonsense mutation in FUT2 provides strong but not absolute protection against symptomatic GII.4 Norovirus infection. PLoS One **4**:e5593.
23. **Chan MC, Lee N, Hung TN, Kwok K, Cheung K, Tin EK, Lai RW, Nelson EA, Leung TF, Chan PK.** 2015. Rapid emergence and predominance of a broadly recognizing and fast-evolving norovirus GII.17 variant in late 2014. Nature Communications **6**:10061.
24. **Chen R, Neill JD, Noel JS, Hutson AM, Glass RI, Estes MK, Prasad BV.** 2004. Inter- and intragenus structural variations in caliciviruses and their functional implications. Journal of Virology **78**:6469-79.
25. **Chen Y, Maguire T, Hileman RE, Fromm JR, Esko JD, Linhardt RJ, Marks RM.** 1997. Dengue virus infectivity depends on envelope protein binding to target cell heparan sulfate. Nature Medicine **3**:866-871.
26. **Chen Z, Sosnovtsev SV, Bok K, Parra GI, Makiya M, Agulto L, Green KY, Purcell RH.** 2013. Development of norwalk virus-specific monoclonal antibodies with therapeutic potential for the treatment of norwalk virus gastroenteritis. Journal of Virology **87**:9547-57.
27. **Chiang JYL.** 2013. Bile acid metabolism and signaling. Comprehensive Physiology **3**:1191-1212.
28. **Chiu W.** 1986. Electron microscopy of frozen, hydrated biological specimens. Annual Review of Biophysics and Biophysical Chemistry **15**:237-257.
29. **Choi JM, Hutson AM, Estes MK, Prasad BV.** 2008. Atomic resolution structural characterization of recognition of histo-blood group antigens by Norwalk virus. Proceedings of the National Academy of Sciences of the United States of America **105**:9175-80.
30. **Clapham DE.** 2007. Calcium Signaling. Cell **131**:1047-1058.
31. **Conley M, Emmott E, Orton R, Taylor D, Carneiro DG, Murata K, Goodfellow IG, Hansman GS, Bhella D.** 2017. Vesivirus 2117 capsids more closely resemble sapovirus and lagovirus particles than other known vesivirus structures. Journal of General Virology **98**:68-76.

32. **Conley MJ, McElwee M, Azmi L, Gabrielsen M, Byron O, Goodfellow IG, Bhella D.** 2019. Calicivirus VP2 forms a portal-like assembly following receptor engagement. Nature **565**:377-381.
33. **Conrath KE, Lauwereys M, Galleni M, Matagne A, Frère JM, Kinne J, Wyns L, Muyldermans S.** 2001. Beta-lactamase inhibitors derived from single-domain antibody fragments elicited in the camelidae. Antimicrobial agents and chemotherapy **45**:2807-2812.
34. **Cortes-Penfield NW, Ramani S, Estes MK, Atmar RL.** 2017. Prospects and Challenges in the Development of a Norovirus Vaccine. Clinical therapeutics **39**:1537-1549.
35. **Coulet M, Phothirath P, Allais L, Schilter B.** 2014. Pre-clinical safety evaluation of the synthetic human milk, nature-identical, oligosaccharide 2'-O-Fucosyllactose (2'FL). Regulatory Toxicology and Pharmacology **68**:59-69.
36. **de Graaf M, van Beek J, Vennema H, Podkolzin AT, Hewitt J, Bucardo F, Templeton K, Mans J, Nordgren J, Reuter G, Lynch M, Rasmussen LD, Iritani N, Chan MC, Martella V, Ambert-Balay K, Vinjé J, White PA, Koopmans MP.** 2015. Emergence of a novel GII.17 norovirus – End of the GII.4 era? Euro surveillance : bulletin Europeen sur les maladies transmissibles = European communicable disease bulletin **20**:21178.
37. **de Graaf M, van Beek J, Koopmans MPG.** 2016. Human norovirus transmission and evolution in a changing world. Nature Reviews Microbiology **14**:421.
38. **de Martín Garrido N, Crone MA, Ramlaul K, Simpson PA, Freemont PS, Aylett CHS.** 2019. Bacteriophage MS2 displays unreported capsid variability assembling T = 4 and mixed capsids. Molecular Microbiology n/a.
39. **De Meyer T, Muyldermans S, Depicker A.** 2014. Nanobody-based products as research and diagnostic tools. Trends in Biotechnology **32**:263-70.
40. **Derrington P, Schreiber F, Day S, Curtis C, Lyon M.** 2009. Norovirus Ridaquick: a new test for rapid diagnosis of norovirus. Pathology **41**:687-688.
41. **Devant JM, Hofhaus G, Bhella D, Hansman GS.** 2019. Heterologous expression of human norovirus GII.4 VP1 leads to assembly of T=4 virus-like particles. Antiviral Research **168**:175-182.
42. **Donaldson EF, Lindesmith LC, Lobue AD, Baric RS.** 2008. Norovirus pathogenesis: mechanisms of persistence and immune evasion in human populations. Immunological Reviews **225**:190-211.
43. **Dormitzer PR, Greenberg HB.** 1992. Calcium chelation induces a conformational change in recombinant herpes simplex virus-1-expressed rotavirus VP7. Virology **189**:828-832.
44. **Dormitzer PR, Greenberg HB, Harrison SC.** 2000. Purified Recombinant Rotavirus VP7 Forms Soluble, Calcium-Dependent Trimers. Virology **277**:420-428.
45. **Dubochet JAM, Chang J, Homo J, Lepaul J, McDowall A, Schutz P.** 1988. Cryo-electron microscopy of vitrified specimens. Quarterly Review of Biophsics **21**:129-228.
46. **Dumoulin M, Conrath K, Van Meirhaeghe A, Meersman F, Heremans K, Frenken LGJ, Muyldermans S, Wyns L, Matagne A.** 2002. Single-domain antibody fragments with high conformational stability. Protein science : a publication of the Protein Society **11**:500-515.
47. **Eden JS, Tanaka mM, Boni MF, Rawlinson WD, White PA.** 2013. Recombination within the pandemic norovirus GII.4 lineage. Journal of Virology **87**:6270-82.
48. **Engfer MB, Stahl B, Finke B, Sawatzki G, Daniel H.** 2000. Human milk oligosaccharides are resistant to enzymatic hydrolysis in the upper gastrointestinal tract. The American Journal of Clinical Nutrition **71**:1589-1596.

49. **Ettayebi K, Crawford SE, Murakami K, Broughman JR, Karandikar U, Tenge VR, Neill FH, Blutt SE, Zeng XL, Qu L, Kou B, Opekun AR, Burrin D, Graham DY, Ramani S, Atmar RL, Estes MK.** 2016. Replication of human noroviruses in stem cell-derived human enteroids. Science **353**:1387-1393.
50. **Farkas T, Cross RW, Hargitt E, 3rd, Lerche NW, Morrow AL, Sestak K.** 2010. Genetic diversity and histo-blood group antigen interactions of rhesus enteric caliciviruses. Journal of Virology **84**:8617-25.
51. **Feld JJ, Kowdley KV, Coakley E, Sigal S, Nelson DR, Crawford D, Weiland O, Aguilar H, Xiong J, Pilot-Matias T, DaSilva-Tillmann B, Larsen L, Podsadecki T, Bernstein B.** 2014. Treatment of HCV with ABT-450/r–Ombitasvir and Dasabuvir with Ribavirin. New England Journal of Medicine **370**:1594-1603.
52. **Feng JY, Ly JK, Myrick F, Goodman D, White KL, Svarovskaia ES, Borroto-Esoda K, Miller MD.** 2009. The triple combination of tenofovir, emtricitabine and efavirenz shows synergistic anti-HIV-1 activity in vitro: a mechanism of action study. Retrovirology **6**:44.
53. **Flajnik MF, Kasahara M.** 2010. Origin and evolution of the adaptive immune system: genetic events and selective pressures. Nature reviews Genetics **11**:47-59.
54. **Frank J, Radermacher M, Penczek P, Zhu J, Li Y, Ladjadj M, Leith A.** 1996. SPIDER and WEB: Processing and Visualization of Images in 3D Electron Microscopy and Related Fields. Journal of Structural Biology **116**:190-199.
55. **Frenck R, Bernstein DI, Xia M, Huang P, Zhong W, Parker S, Dickey M, McNeal M, Jiang X.** 2012. Predicting susceptibility to norovirus GII.4 by use of a challenge model involving humans. The Journal of Infectious Diseases **206**:1386-93.
56. **Germi R, Crance J-M, Garin D, Guimet J, Lortat-Jacob H, Ruigrok RWH, Zarski J-P, Drouet E.** 2002. Heparan Sulfate-Mediated Binding of Infectious Dengue Virus Type 2 and Yellow Fever Virus. Virology **292**:162-168.
57. **Gerondopoulos A, Jackson T, Monaghan P, Doyle N, Roberts LO.** 2010. Murine norovirus-1 cell entry is mediated through a non-clathrin-, non-caveolae-, dynamin- and cholesterol-dependent pathway. Journal of General Virology 91:1428-38.
58. **Glaeser RM.** 2008. Retrospective: Radiation damage and its associated "Information Limitations". Journal of Structural Biology **163**:271-276.
59. **Goodfellow I, Taube S**. 2016. Calicivirus Replication and Reverse Genetics, p 355-378.
60. **Gostic KM, Ambrose M, Worobey M, Lloyd-Smith JO.** 2016. Potent protection against H5N1 and H7N9 influenza via childhood hemagglutinin imprinting. Science **354**:722-726.
61. **Greber UF.** 2002. Signalling in viral entry. Cellular and Molecular Life Sciences CMLS **59**:608-626.
62. **Green KY. 2013.** Caliciviridae: the Noroviruses, p 582-608. *In* Knipe DM HP, Cohen JI , Griffin DE , Lamb RA , Martin MA , Racaniello VR , Roizman B (ed), Fields Virology 6th ed, vol 1. Lippincott Williams & Wilkins, Philadelphia, PA.
63. **Greenberg AS, Avila D, Hughes M, Hughes A, McKinney EC, Flajnik MF.** 1995. A new antigen receptor gene family that undergoes rearrangement and extensive somatic diversification in sharks. Nature **374**:168-173.
64. **Griffin MP, Khan AA, Esser MT, Jensen K, Takas T, Kankam MK, Villafana T, Dubovsky F.** 2017. Safety, Tolerability, and Pharmacokinetics of MEDI8897, the Respiratory Syncytial Virus Prefusion F-Targeting Monoclonal Antibody with an Extended Half-Life, in Healthy Adults. Antimicrobial Agents and Chemotherapy **61**:e01714-16.

65. **György P, Norris RF, Rose CS.** 1954. Bifidus factor. I. A variant of Lactobacillus bifidus requiring a special growth factor. Archives of Biochemistry and Biophysics **48**:193-201.
66. **Haga K, Fujimoto A, Takai-Todaka R, Miki M, Doan YH, Murakami K, Yokoyama M, Murata K, Nakanishi A, Katayama K.** 2016. Functional receptor molecules CD300lf and CD300ld within the CD300 family enable murine noroviruses to infect cells. Proceedings of the National Academy of Sciences U S A **113**:E6248-E6255.
67. **Hamers-Casterman C, Atarhouch T, Muyldermans S, Robinson G, Hammers C, Songa EB, Bendahman N, Hammers R.** 1993. Naturally occurring antibodies devoid of light chains. Nature **363**:446-448.
68. **Hansman GS, Shahzad-Ul-Hussan S, McLellan JS, Chuang GY, Georgiev I, Shimoike T, Katayama K, Bewley CA, Kwong PD.** 2012. Structural basis for norovirus inhibition and fucose mimicry by citrate. Journal of Virology **86**:284-92.
69. **Hansman GS, Taylor DW, McLellan JS, Smith TJ, Georgiev I, Tame JR, Park SY, Yamazaki M, Gondaira F, Miki M, Katayama K, Murata K, Kwong PD.** 2012. Structural basis for broad detection of genogroup II noroviruses by a monoclonal antibody that binds to a site occluded in the viral particle. Journal of Virology **86**:3635-46.
70. **Hardy ME.** 2005. Norovirus protein structure and function. FEMS Microbiology Letters **253**:1-8.
71. **Hassan E, Baldridge MT.** 2019. Norovirus encounters in the gut: multifaceted interactions and disease outcomes. Mucosal Immunology **2**:1259-1267
72. **Hemming M, Räsänen S, Huhti L, Paloniemi M, Salminen M, Vesikari T.** 2013. Major reduction of rotavirus, but not norovirus, gastroenteritis in children seen in hospital after the introduction of RotaTeq vaccine into the National Immunization Programme in Finland. European Journal of Pediatrics **172**:739-746.
73. **Henderson R, Sali A, Baker Matthew L, Carragher B, Devkota B, Downing Kenneth H, Egelman Edward H, Feng Z, Frank J, Grigorieff N, Jiang W, Ludtke Steven J, Medalia O, Penczek Pawel A, Rosenthal Peter B, Rossmann Michael G, Schmid Michael F, Schröder Gunnar F, Steven Alasdair C, Stokes David L, Westbrook John D, Wriggers W, Yang H, Young J, Berman Helen M, Chiu W, Kleywegt Gerard J, Lawson Catherine L.** 2012. Outcome of the First Electron Microscopy Validation Task Force Meeting. Structure **20**:205-214.
74. **Hershberger E, Sloan S, Narayan K, Hay CA, Smith P, Engler F, Jeeninga R, Smits S, Trevejo J, Shriver Z, Oldach D.** 2019. Safety and efficacy of monoclonal antibody VIS410 in adults with uncomplicated influenza A infection: Results from a randomized, double-blind, phase-2, placebo-controlled study. EBioMedicine **40**:574-582.
75. **Hsu CC, Wobus CE, Steffen EK, Riley LK, Livingston RS.** 2005. Development of a microsphere-based serologic multiplexed fluorescent immunoassay and a reverse transcriptase PCR assay to detect murine norovirus 1 infection in mice. Clinical and Diagnostic Laboratory Immunology **12**:1145-51.
76. **Huang P, Farkas T, Marionneau S, Zhong W, Ruvoen-Clouet N, Morrow AL, Altaye M, Pickering LK, Newburg DS, LePendu J, Jiang X.** 2003. Noroviruses bind to human ABO, Lewis, and secretor histo-blood group antigens: identification of 4 distinct strain-specific patterns. The Journal of Infectious Diseases **188**:19-31.
77. **Huang P, Farkas T, Zhong W, Tan M, Thornton S, Morrow AL, Jiang X.** 2005. Norovirus and histo-blood group antigens: demonstration of a wide spectrum of strain specificities and classification of two major binding groups among multiple binding patterns. Journal of Virology **79**:6714-22.

78. **Hutson AM, Atmar RL, Graham DY, Estes MK.** 2002. Norwalk virus infection and disease is associated with ABO histo-blood group type. The Journal of Infectious Diseases **185**:1335-7.
79. **Ibañez LI, De Filette M, Hultberg A, Verrips T, Temperton N, Weiss RA, Vandevelde W, Schepens B, Vanlandschoot P, Saelens X.** 2011. Nanobodies With In Vitro Neutralizing Activity Protect Mice Against H5N1 Influenza Virus Infection. The Journal of Infectious Diseases **203**:1063-1072.
80. **Ishida JH, Patel A, Mehta AK, Gatault P, McBride JM, Burgess T, Derby MA, Snydman DR, Emu B, Feierbach B, Fouts AE, Maia M, Deng R, Rosenberger CM, Gennaro LA, Striano NS, Liao XC, Tavel JA.** 2017. Phase 2 Randomized, Double-Blind, Placebo-Controlled Trial of RG7667, a Combination Monoclonal Antibody, for Prevention of Cytomegalovirus Infection in High-Risk Kidney Transplant Recipients. Antimicrobial agents and chemotherapy **61**:e01794-16.
81. **Jackson T, Ellard FM, Ghazaleh RA, Brookes SM, Blakemore WE, Corteyn AH, Stuart DI, Newman JW, King AM.** 1996. Efficient infection of cells in culture by type O foot-and-mouth disease virus requires binding to cell surface heparan sulfate. Journal of Virology **70**:5282-5287.
82. **Jung J, Grant T, Thomas DR, Diehnelt CW, Grigorieff N, Joshua-Tor L.** 2019. High-resolution cryo-EM structures of outbreak strain human norovirus shells reveal size variations. Proceedings of the National Academy of Sciences of the United States of America **116**:12828-12832.
83. **Kapikian AZ, Wyatt RG, Dolin R, Thornhill TS, Kalica AR, Chanock RM.** 1972. Visualization by immune electron microscopy of a 27-nm particle associated with acute infectious nonbacterial gastroenteritis. Journal of Virology **10**:1075-1081.
84. **Kapikian AZ, Wyatt RG, Dolin R, Thornhill TS, Kalica AR, Chanock RM.** 1972. Visualization by immune electron microscopy of a 27-nm particle associated with acute infectious nonbacterial gastroenteritis. Journal of Virology 10:1075-81.
85. **Karst SM, Wobus CE, Lay M, Davidson J, Virgin HWt.** 2003. STAT1-dependent innate immunity to a Norwalk-like virus. Science **299**:1575-8.
86. **Katpally U, Wobus CE, Dryden K, Virgin HWt, Smith TJ.** 2008. Structure of antibody-neutralized murine norovirus and unexpected differences from viruslike particles. Journal of Virology **82**:2079-88.
87. **Katpally U, Voss NR, Cavazza T, Taube S, Rubin JR, Young VL, Stuckey J, Ward VK, Virgin HWt, Wobus CE, Smith TJ.** 2010. High-resolution cryo-electron microscopy structures of murine norovirus 1 and rabbit hemorrhagic disease virus reveal marked flexibility in the receptor binding domains. Journal of Virology **84**:5836-41.
88. **Kempf B, Edgar JD, Mc Caughey C, Devlin LA.** 2017. Nitazoxanide Is an Ineffective Treatment of Chronic Norovirus in Patients With X-Linked Agammaglobulinemia and May Yield False-Negative Polymerase Chain Reaction Findings in Stool Specimens. The Journal of Infectious Diseases **215**:486-487.
89. **Kiermayr S, Stiasny K, Heinz FX.** 2009. Impact of Quaternary Organization on the Antigenic Structure of the Tick-Borne Encephalitis Virus Envelope Glycoprotein E. Journal of Virology **83**:8482.
90. **Kilic T, Koromyslova A, Malak V, Hansman GS.** 2018. Atomic Structure of the Murine Norovirus Protruding Domain and Soluble CD300lf Receptor Complex. Journal of Virology **92**:e00413-18.
91. **Kilic T, Koromyslova A, Hansman GS.** 2019. Structural Basis for Human Norovirus Capsid Binding to Bile Acids. Journal of Virology **93**:e01581-18.

92. **Kim L, Liebowitz D, Lin K, Kasparek K, Pasetti MF, Garg SJ, Gottlieb K, Trager G, Tucker SN.** 2018. Safety and immunogenicity of an oral tablet norovirus vaccine, a phase I randomized, placebo-controlled trial. JCI insight **3**:e121077.
93. **Klug A.** 1999. The tobacco mosaic virus particle: structure and assembly. Philosophical transactions of the Royal Society of London Series B, Biological sciences **354**:531-535.
94. **Knipping K, Garssen J, van't Land B.** 2012. An evaluation of the inhibitory effects against rotavirus infection of edible plant extracts. Virology Journal 9:137-137.
95. **Kobata A.** 1992. Structures and functions of the sugar chains of glycoproteins. European Journal of Biochemistry **209**:483-501.
96. **Kobata A.** 2010. Structures and application of oligosaccharides in human milk. Proceedings of the Japan Academy Series B, Physical and biological sciences **86**:731-747.
97. **Kolawole AO, Smith HQ, Svoboda SA, Lewis MS, Sherman MB, Lynch GC, Pettitt BM, Smith TJ, Wobus CE.** 2017. Norovirus Escape from Broadly Neutralizing Antibodies Is Limited to Allostery-Like Mechanisms. mSphere **2**:e00334-17.
98. **Koromyslova A, Tripathi S, Morozov V, Schroten H, Hansman GS.** 2017. Human norovirus inhibition by a human milk oligosaccharide. Virology **508**:81-89.
99. **Koromyslova AD, Hansman GS.** 2015. Nanobody binding to a conserved epitope promotes norovirus particle disassembly. Journal of Virology **89**:2718-30.
100. **Koromyslova AD, White PA, Hansman GS.** 2015. Treatment of norovirus particles with citrate. Virology **485**:199-204.
101. **Koromyslova AD, Hansman GS.** 2017. Nanobodies targeting norovirus capsid reveal functional epitopes and potential mechanisms of neutralization. PLoS Pathogens 13:e1006636.
102. **Koromyslova AD, Morozov VA, Hefele L, Hansman GS.** 2019. Human Norovirus Neutralized by a Monoclonal Antibody Targeting the Histo-Blood Group Antigen Pocket. Journal of Virology **93**:e02174-18.
103. **Koromyslova AD, Devant JM, Kilic T, Sabin CD, Malak V, Hansman GS.** 2020. Nanobody mediated neutralization reveals an Achilles heel for norovirus. bioRxiv doi:10.1101/2020.02.07.938506:2020.02.07.938506.
104. **Koutsky LA, Ault KA, Wheeler CM, Brown DR, Barr E, Alvarez FB, Chiacchierini LM, Jansen KU.** 2002. A controlled trial of a human papillomavirus type 16 vaccine. New England Journal of Medicine **347:**1645-1651.
105. **Kubala MH, Kovtun O, Alexandrov K, Collins BM.** 2010. Structural and thermodynamic analysis of the GFP:GFP-nanobody complex. Protein science : a publication of the Protein Society **19**:2389-2401.
106. **Kühlbrandt W.** 2014. The Resolution Revolution. Science 343:1443.
107. **Kulkarni R, Hluhanich R, McColl DM, Miller MD, White KL.** 2014. The Combined Anti-HIV-1 Activities of Emtricitabine and Tenofovir plus the Integrase Inhibitor Elvitegravir or Raltegravir Show High Levels of Synergy In Vitro. Antimicrobial Agents and Chemotherapy **58**:6145-6150.
108. **Kunz C, Meyer C, Collado MC, Geiger L, García-Mantrana I, Bertua-Ríos B, Martínez-Costa C, Borsch C, Rudloff S.** 2017. Influence of Gestational Age, Secretor, and Lewis Blood Group Status on the Oligosaccharide Content of Human Milk. Journal of Pediatric Gastroenterology and Nutrition **64**:789-798
109. **Kunz P, Zinner K, Mücke N, Bartoschik T, Muyldermans S, Hoheisel JD.** 2018. The structural basis of nanobody unfolding reversibility and thermoresistance. Scientific reports **8**:7934-7934.

110. **Lafaye P, Achour I, England P, Duyckaerts C, Rougeon F.** 2009. Single-domain antibodies recognize selectively small oligomeric forms of amyloid β, prevent Aβ-induced neurotoxicity and inhibit fibril formation. Molecular Immunology **46**:695-704.
111. **Larkin MA, Blackshields G, Brown NP, Chenna R, McGettigan PA, McWilliam H, Valentin F, Wallace IM, Wilm A, Lopez R, Thompson JD, Gibson TJ, Higgins DG.** 2007. Clustal W and Clustal X version 2.0. Bioinformatics **23**:2947-2948.
112. **Leroux-Roels G, Cramer JP, Mendelman PM, Sherwood J, Clemens R, Aerssens A, De Coster I, Borkowski A, Baehner F, Van Damme P.** 2018. Safety and immunogenicity of different formulations of norovirus vaccine candidate in healthy adults: A randomized, controlled, double-blind clinical trial. Journal of Infectious Diseases **217**:597-607.
113. **Li M, Monaco MH, Wang M, Comstock SS, Kuhlenschmidt TB, Fahey GC, Jr., Miller MJ, Kuhlenschmidt MS, Donovan SM.** 2014. Human milk oligosaccharides shorten rotavirus-induced diarrhea and modulate piglet mucosal immunity and colonic microbiota. The ISME journal **8**:1609-1620.
114. **Li X, Mooney P, Zheng S, Booth C, Braunfeld MB, Gubbens S, Agard DA, Cheng Y.** 2013. Electron counting and beam-induced motion correction enable near atomic resolution single particle cryoEM. Nature methods **10**:584-590.
115. **Lindesmith L, Moe C, Marionneau S, Ruvoen N, Jiang X, Lindblad L, Stewart P, LePendu J, Baric R.** 2003. Human susceptibility and resistance to Norwalk virus infection. Nature Medicine **9**:548-53.
116. **Lindesmith L, Moe C, Lependu J, Frelinger JA, Treanor J, Baric RS.** 2005. Cellular and humoral immunity following Snow Mountain virus challenge. Journal of Virology **79**:2900-9.
117. **Lindesmith LC, Donaldson EF, Lobue AD, Cannon JL, Zheng DP, Vinje J, Baric RS.** 2008. Mechanisms of GII.4 norovirus persistence in human populations.PLoS Medicine **5**:e31.
118. **Lindesmith LC, Beltramello M, Donaldson EF, Corti D, Swanstrom J, Debbink K, Lanzavecchia A, Baric RS.** 2012. Immunogenetic mechanisms driving norovirus GII.4 antigenic variation. PLoS Pathogens **8**:e1002705.
119. **Lindesmith LC, Donaldson EF, Beltramello M, Pintus S, Corti D, Swanstrom J, Debbink K, Jones TA, Lanzavecchia A, Baric RS.** 2014. Particle conformation regulates antibody access to a conserved GII.4 norovirus blockade epitope. Journal of Virology **88**:8826-42.
120. **Lindesmith LC, Ferris MT, Mullan CW, Ferreira J, Debbink K, Swanstrom J, Richardson C, Goodwin RR, Baehner F, Mendelman PM, Bargatze RF, Baric RS.** 2015. Broad blockade antibody responses in human volunteers after immunization with a multivalent norovirus VLP candidate vaccine: immunological analyses from a phase I clinical trial.PLoS Medicine **12**:e1001807.
121. **Lindesmith LC, Mallory ML, Jones TA, Richardson C, Goodwin RR, Baehner F, Mendelman PM, Bargatze RF, Baric RS.** 2017. Impact of Pre-Exposure History and Host Genetics on Antibody Avidity Following Norovirus Vaccination. The Journal of Infectious Diseases **215**:984-991
122. **Lindesmith LC, McDaniel JR, Changela A, Verardi R, Kerr SA, Costantini V, Brewer-Jensen PD, Mallory ML, Voss WN, Boutz DR, Blazeck JJ, Ippolito GC, Vinje J, Kwong PD, Georgiou G, Baric RS.** 2019. Sera Antibody Repertoire Analyses Reveal Mechanisms of Broad and Pandemic Strain Neutralizing Responses after Human Norovirus Vaccination. Immunity **50**:1530-1541.e8.

123. **Lipson SM, Karalis G, Karthikeyan L, Ozen FS, Gordon RE, Ponnala S, Bao J, Samarrai W, Wolfe E.** 2017. Mechanism of Anti-rotavirus Synergistic Activity by Epigallocatechin Gallate and a Proanthocyanidin-Containing Nutraceutical. Food and Environmental Virology **9**:434-443
124. **Liu W, Song H, Chen Q, Yu J, Xian M, Nian R, Feng D.** 2018. Recent advances in the selection and identification of antigen-specific nanobodies. Molecular Immunology **96**:37-47.
125. **Lopman BA, Reacher MH, Vipond IB, Sarangi J, Brown DWG.** 2004. Clinical Manifestation of Norovirus Gastroenteritis in Health Care Settings. Clinical Infectious Diseases **39**:318-324.
126. **Ludwig-Begall LF, Mauroy A, Thiry E.** 2018. Norovirus recombinants: recurrent in the field, recalcitrant in the lab – a scoping review of recombination and recombinant types of noroviruses. Journal of General Virology **99**:970-988.
127. **Luque D, Gonzalez JM, Gomez-Blanco J, Marabini R, Chichon J, Mena I, Angulo I, Carrascosa JL, Verdaguer N, Trus BL, Barcena J, Caston JR.** 2012. Epitope insertion at the N-terminal molecular switch of the rabbit hemorrhagic disease virus T = 3 capsid protein leads to larger T = 4 capsids. Journal of Virology **86**:6470-80.
128. **Makino A, Shimojima M, Miyazawa T, Kato K, Tohya Y, Akashi H.** 2006. Junctional adhesion molecule 1 is a functional receptor for feline calicivirus. Journal of Virology **80**:4482-90.
129. **Mallory ML, Lindesmith LC, Graham RL, Baric RS.** 2019. GII.4 Human Norovirus: Surveying the Antigenic Landscape. Viruses **11**:177.
130. **Malm M, Tamminen K, Lappalainen S, Uusi-Kerttula H, Vesikari T, Blazevic V.** 2015. Genotype considerations for virus-like particle-based bivalent norovirus vaccine composition. Clinical and vaccine immunology : CVI **22**:656-663.
131. **Malm M, Tamminen K, Lappalainen S, Vesikari T, Blazevic V.** 2016. Rotavirus Recombinant VP6 Nanotubes Act as an Immunomodulator and Delivery Vehicle for Norovirus Virus-Like Particles. Journal of immunology research **2016**:9171632-9171632.
132. **Marionneau S, Cailleau-Thomas A, Rocher J, Le Moullac-Vaidye B, Ruvoën N, Clément M, Le Pendu J.** 2001. ABH and Lewis histo-blood group antigens, a model for the meaning of oligosaccharide diversity in the face of a changing world. Biochimie **83**:565-573.
133. **Marionneau S, Ruvoen N, Le Moullac-Vaidye B, Clement M, Cailleau-Thomas A, Ruiz-Palacois G, Huang P, Jiang X, Le Pendu J.** 2002. Norwalk virus binds to histo-blood group antigens present on gastroduodenal epithelial cells of secretor individuals. Gastroenterology **122**:1967-77.
134. **Martin TG, Boland A, Fitzpatrick AWP, Scheres SHW.** 2016. Graphene Oxide Grid Preparation doi:10.6084/m9.figshare.3178669.v1.
135. **Matsushima Y, Ishikawa M, Shimizu T, Komane A, Kasuo S, Shinohara M, Nagasawa K, Kimura H, Ryo A, Okabe N, Haga K, Doan YH, Katayama K, Shimizu H.** 2015. Genetic analyses of GII.17 norovirus strains in diarrheal disease outbreaks from December 2014 to March 2015 in Japan reveal a novel polymerase sequence and amino acid substitutions in the capsid region. Euro Surveillance 20: 21173
136. **McAleer WJ, Buynak EB, Maigetter RZ, Wampler DE, Miller WJ, Hilleman MR.** 1984. Human hepatitis B vaccine from recombinant yeast. Nature **307**:178-180.

137. **McFadden N, Bailey D, Carrara G, Benson A, Chaudhry Y, Shortland A, Heeney J, Yarovinsky F, Simmonds P, Macdonald A, Goodfellow I.** 2011. Norovirus regulation of the innate immune response and apoptosis occurs via the product of the alternative open reading frame 4. PLoS Pathogens **7**:e1002413.
138. **Mead PS, Slutsker L, Dietz V, McCaig LF, Bresee JS, Shapiro C, Griffin PM, Tauxe RV.** 1999. Food-related illness and death in the United States. Emerging infectious diseases **5**:607-625.
139. **Mindell JA, Grigorieff N.** 2003. Accurate determination of local defocus and specimen tilt in electron microscopy. Journal of Structural Biology 142:334-347.
140. **Morrow AL, Ruiz-Palacios GM, Altaye M, Jiang X, Guerrero ML, Meinzen-Derr JK, Farkas T, Chaturvedi P, Pickering LK, Newburg DS.** 2004. Human milk oligosaccharides are associated with protection against diarrhea in breast-fed infants. The Journal of Pediatrics **145**:297-303.
141. **Morrow AL, Ruiz-Palacios GM, Jiang X, Newburg DS.** 2005. Human-Milk Glycans That Inhibit Pathogen Binding Protect Breast-feeding Infants against Infectious Diarrhea. The Journal of Nutrition **135**:1304-1307.
142. **Müller B, Klemm U, Mas Marques A, Schreier E.** 2007. Genetic diversity and recombination of murine noroviruses in immunocompromised mice. Archives of Virology **152**:1709-1719.
143. **Mumphrey SM, Changotra H, Moore TN, Heimann-Nichols ER, Wobus CE, Reilly MJ, Moghadamfalahi M, Shukla D, Karst SM.** 2007. Murine norovirus 1 infection is associated with histopathological changes in immunocompetent hosts, but clinical disease is prevented by STAT1-dependent interferon responses. Journal of Virology **81**:3251-63.
144. **Murakami K, Tenge VR, Karandikar UC, Lin S-C, Ramani S, Ettayebi K, Crawford SE, Zeng X-L, Neill FH, Ayyar BV, Katayama K, Graham DY, Bieberich E, Atmar RL, Estes MK.** 2020. Bile acids and ceramide overcome the entry restriction for GII.3 human norovirus replication in human intestinal enteroids. Proceedings of the National Academy of Sciences of the United States of America **117**:1700-1710
145. **Nelson CA, Wilen CB, Dai Y-N, Orchard RC, Kim AS, Stegeman RA, Hsieh LL, Smith TJ, Virgin HW, Fremont DH.** 2018. Structural basis for murine norovirus engagement of bile acids and the CD300lf receptor. Proceedings of the National Academy of Sciences of the United States of America **115**:E9201-E9210.
146. **Nenonen NP, Hannoun C, Svensson L, Toren K, Andersson LM, Westin J, Bergstrom T.** 2014. Norovirus GII.4 detection in environmental samples from patient rooms during nosocomial outbreaks. Journal of Clinical Microbiology **52**:2352-8.
147. **Ohba M, Oka T, Ando T, Arahata S, Ikegaya A, Takagi H, Ogo N, Zhu C, Owada K, Kawamori F, Wang Q, Saif LJ, Asai A.** 2016. Antiviral effect of theaflavins against caliciviruses. The Journal of Antibiotics **70**:443–447
148. **Ohi M, Li Y, Cheng Y, Walz T.** 2004. Negative Staining and Image Classification - Powerful Tools in Modern Electron Microscopy. Biological procedures online **6**:23-34.
149. **Oka T, Wang Q, Katayama K, Saif LJ.** 2015. Comprehensive review of human sapoviruses. Clinical microbiology reviews **28**:32-53.
150. **Orchard RC, Wilen CB, Doench JG, Baldridge MT, McCune BT, Lee YC, Lee S, Pruett-Miller SM, Nelson CA, Fremont DH, Virgin HW.** 2016. Discovery of a proteinaceous cellular receptor for a norovirus. Science **353**:933-6.
151. **Pan L, Xue C, Fu H, Liu D, Zhu L, Cui C, Zhu W, Fu Y, Qiao S.** 2016. The novel norovirus genotype GII.17 is the predominant strain in diarrheal patients in Shanghai, China. Gut Pathogogens **8**:49.

152. **Pant N, Hultberg A, Zhao Y, Svensson L, Pan-Hammarstrom Q, Johansen K, Pouwels PH, Ruggeri FM, Hermans P, Frenken L, Boren T, Marcotte H, Hammarstrom L.** 2006. Lactobacilli expressing variable domain of llama heavy-chain antibody fragments (lactobodies) confer protection against rotavirus-induced diarrhea. The Journal of Infectious Diseases **194**:1580-8.
153. **Parra GI, Bok K, Taylor R, Haynes JR, Sosnovtsev SV, Richardson C, Green KY.** 2012. Immunogenicity and specificity of norovirus Consensus GII.4 virus-like particles in monovalent and bivalent vaccine formulations. Vaccine **30**:3580-6.
154. **Parra GI, Squires RB, Karangwa CK, Johnson JA, Lepore C, Sosnovtsev SV, Green KY.** 2017. Static and Evolving Norovirus Genotypes: Implications for Epidemiology and Immunity. PLoS Pathogens 13:e1006136.
155. **Patel mM, Widdowson M-A, Glass RI, Akazawa K, Vinjé J, Parashar UD.** 2008. Systematic literature review of role of noroviruses in sporadic gastroenteritis. Emerging infectious diseases **14**:1224-1231.
156. **Patterson T, Hutchings P, Palmer S.** 1993. Outbreak of SRSV gastroenteritis at an international conference traced to food handled by a post-symptomatic caterer. Epidemiology and infection **111**:157-162.
157. **Pelliccia S, Wu Y-H, Coluccia A, La Regina G, Tseng C-K, Famiglini V, Masci D, Hiscott J, Lee J-C, Silvestri R.** 2017. Inhibition of dengue virus replication by novel inhibitors of RNA-dependent RNA polymerase and protease activities. Journal of Enzyme Inhibition and Medicinal Chemistry **32**:1091-1101.
158. **Perry JW, Taube S, Wobus CE.** 2009. Murine norovirus-1 entry into permissive macrophages and dendritic cells is pH-independent. Virus Research **143**:125-9.
159. **Pinto Torres JE, Goossens J, Ding J, Li Z, Lu S, Vertommen D, Naniima P, Chen R, Muyldermans S, Sterckx YGJ, Magez S.** 2018. Development of a Nanobody-based lateral flow assay to detect active Trypanosoma congolense infections. Scientific reports **8**:9019-9019.
160. **Pöch G, Dittrich P, Reiffenstein RJ, Lenk W, Schuster A.** 1990. Evaluation of experimental combined toxicity by use of dose–frequency curves: comparison with theoretical additivity as well as independence. Canadian Journal of Physiology and Pharmacology **68**:1338-1345.
161. **Pomeroy JJ, Drusano GL, Rodriquez JL, Brown AN.** 2017. Searching for synergy: Identifying optimal antiviral combination therapy using Hepatitis C virus (HCV) agents in a replicon system. Antiviral Research **146**:149-152.
162. **Prasad BV, Hardy ME, Dokland T, Bella J, Rossmann MG, Estes MK.** 1999. X-ray crystallographic structure of the Norwalk virus capsid. Science **286**:287-90.
163. **Punjani A, Rubinstein JL, Fleet DJ, Brubaker MA.** 2017. cryoSPARC: algorithms for rapid unsupervised cryo-EM structure determination. Nature Methods **14**:290-296.
164. **Rackoff LA, Bok K, Green KY, Kapikian AZ.** 2013. Epidemiology and evolution of rotaviruses and noroviruses from an archival WHO Global Study in Children (1976-79) with implications for vaccine design. PLoS One **8**:e59394.
165. **Ramani S, Atmar RL, Estes MK.** 2014. Epidemiology of human noroviruses and updates on vaccine development. Curr Opin Gastroenterol **30**:25-33.
166. **Reeck A, Kavanagh O, Estes MK, Opekun AR, Gilger MA, Graham DY, Atmar RL.** 2010. Serological correlate of protection against norovirus-induced gastroenteritis. The Journal of Infectious Diseases **202**:1212-8.
167. **Reisdorph N, Thomas JJ, Katpally U, Chase E, Harris K, Siuzdak G, Smith TJ.** 2003. Human rhinovirus capsid dynamics is controlled by canyon flexibility. Virology **314**:34-44.
168. **Robilotti E, Deresinski S, Pinsky BA.** 2015. Norovirus. Clin Microbiol Rev **28**:134-164.

169. **Robinson IK, Harrison SC.** 1982. Structure of the expanded state of tomato bushy stunt virus. Nature **297**:563-568.
170. **Rocha-Pereira J, Jochmans D, Dallmeier K, Leyssen P, Cunha R, Costa I, Nascimento MSJ, Neyts J.** 2012. Inhibition of norovirus replication by the nucleoside analogue 2′-C-methylcytidine. Biochemical and Biophysical Research Communications **427**:796-800.
171. **Rocha-Pereira J, Jochmans D, Debing Y, Verbeken E, Nascimento MSJ, Neyts J.** 2013. The Viral Polymerase Inhibitor 2′-C-Methylcytidine Inhibits Norwalk Virus Replication and Protects against Norovirus-Induced Diarrhea and Mortality in a Mouse Model. Journal of Virology **87**:11798.
172. **Rocha-Pereira J, Nascimento MSJ, Ma Q, Hilgenfeld R, Neyts J, Jochmans D.** 2014. The enterovirus protease inhibitor rupintrivir exerts cross-genotypic anti-norovirus activity and clears cells from the norovirus replicon. Antimicrobial agents and chemotherapy **58**:4675-4681.
173. **Rosenthal PB, Henderson R.** 2003. Optimal Determination of Particle Orientation, Absolute Hand, and Contrast Loss in Single-particle Electron Cryomicroscopy. Journal of Molecular Biology **333**:721-745.
174. **Rossignol JF, El-Gohary YM.** 2006. Nitazoxanide in the treatment of viral gastroenteritis: a randomized double-blind placebo-controlled clinical trial. Alimentary Pharmacology & Therapeutics **24**:1423-1430.
175. **Ruiz MC, Charpilienne A, Liprandi F, Gajardo R, Michelangeli F, Cohen J.** 1996. The concentration of Ca2+ that solubilizes outer capsid proteins from rotavirus particles is dependent on the strain. Journal of Virology **70**:4877-4883.
176. **Ruoff K, Kilic T, Devant J, Koromyslova A, Ringel A, Hempelmann A, Geiss C, Graf J, Haas M, Roggenbach I, Hansman G.** 2019. Structural Basis of Nanobodies Targeting the Prototype Norovirus. Journal of Virology **93**:e02005-18.
177. **Ruvoen-Clouet N, Ganiere JP, Andre-Fontaine G, Blanchard D, Le Pendu J.** 2000. Binding of rabbit hemorrhagic disease virus to antigens of the ABH histo-blood group family. Journal of Virology **74**:11950-4.
178. **Ryder RW, Singh N, Reeves WC, Kapikian AZ, Greenberg HB, Sack RB.** 1985. Evidence of immunity induced by naturally acquired rotavirus and Norwalk virus infection on two remote Panamanian islands. The Journal of Infectious Diseases **151**:99-105.
179. **Salvador JP, Vilaplana L, Marco MP.** 2019. Nanobody: outstanding features for diagnostic and therapeutic applications. Analytical and Bioanalytical Chemistry **411**:1703-1713.
180. **Sarker SA, Jäkel M, Sultana S, Alam NH, Bardhan PK, Chisti MJ, Salam MA, Theis W, Hammarström L, Frenken LGJ.** 2013. Anti-Rotavirus Protein Reduces Stool Output in Infants With Diarrhea: A Randomized Placebo-Controlled Trial. Gastroenterology **145**:740-748.e8.
181. **Scheres SHW.** 2012. RELION: implementation of a Bayesian approach to cryo-EM structure determination. Journal of structural biology **180**:519-530.
182. **Schindelin J, Arganda-Carreras I, Frise E, Kaynig V, Longair M, Pietzsch T, Preibisch S, Rueden C, Saalfeld S, Schmid B, Tinevez J-Y, White DJ, Hartenstein V, Eliceiri K, Tomancak P, Cardona A.** 2012. Fiji: an open-source platform for biological-image analysis. Nature Methods **9**:676-682.
183. **Sherman MB, Williams AN, Smith HQ, Nelson C, Wilen CB, Fremont DH, Virgin HW, Smith TJ.** 2019. Bile salts alter the mouse norovirus capsid conformation; possible implications for cell attachment and immune evasion. Journal of Virology **19**:e00970-19.

184. **Shieh MT, WuDunn D, Montgomery RI, Esko JD, Spear PG.** 1992. Cell surface receptors for herpes simplex virus are heparan sulfate proteoglycans. The Journal of cell biology **116**:1273-1281.
185. **Shirato H, Ogawa S, Ito H, Sato T, Kameyama A, Narimatsu H, Xiaofan Z, Miyamura T, Wakita T, Ishii K, Takeda N. 2008.** Noroviruses distinguish between type 1 and type 2 histo-blood group antigens for binding. Journal of Virology **82**:10756-67.
186. **Shivanna V, Kim Y, Chang KO. 2014.** Endosomal acidification and cathepsin L activity is required for calicivirus replication. Virology **464-465**:287-95.
187. **Siebenga JJ, Vennema H, Renckens B, de Bruin E, van der Veer B, Siezen RJ, Koopmans M.** 2007. Epochal evolution of GGII.4 norovirus capsid proteins from 1995 to 2006. Journal of Virology **81**:9932-41.
188. **Singh BK, Koromyslova A, Hefele L, Gurth C, Hansman GS.** 2015. Structural evolution of the emerging 2014/15 GII.17 noroviruses. Journal of Virology **90**:2710-5.
189. **Singh BK, Leuthold MM, Hansman GS.** 2015. Human noroviruses' fondness for histo-blood group antigens. Journal of Virology **89**:2024-40.
190. **Siontorou CG. 2013.** Nanobodies as novel agents for disease diagnosis and therapy. International journal of nanomedicine **8**:4215-4227.
191. **Smith TJ, Kremer MJ, Luo M, Vriend G, Arnold E, Kamer G, Rossmann MG, McKinlay MA, Diana GD, Otto MJ.** 1986. The site of attachment in human rhinovirus 14 for antiviral agents that inhibit uncoating. Science **233**:1286.
192. **Snowden JS, Hurdiss DL, Adeyemi OO, Ranson NA, Herod MR, Stonehouse NJ.** 2019. High-Resolution Cryo-EM Reveals Dynamics in the Murine Norovirus Capsid. bioRxiv doi:10.1101/693143:693143.
193. **Sosnovtsev SV, Belliot G, Chang KO, Onwudiwe O, Green KY.** 2005. Feline calicivirus VP2 is essential for the production of infectious virions. Journal of Virology **79**:4012-24.
194. **Sosnovtsev SV, Sandoval-Jaime C, Parra GI, Tin CM, Jones RW, Soden J, Barnes D, Freeth J, Smith AW, Green KY.** 2017. Identification of Human Junctional Adhesion Molecule 1 as a Functional Receptor for the Hom-1 Calicivirus on Human Cells. mBio **8**:e00031-17.
195. **Stahl B, Thurl S, Zeng JR, Karas M, Hillenkamp F, Steup M, Sawatzki G.** 1994. Oligosaccharides from Human Milk as Revealed by Matrix-Assisted Laser Desorption/Ionization Mass Spectrometry. Analytical Biochemistry **223**:218-226.
196. **Stockley PG, Ranson NA, Twarock R.** 2013. A new paradigm for the roles of the genome in ssRNA viruses. Future Virology **8**:531-543.
197. **Stuart AD, Brown TD.** 2006. Entry of feline calicivirus is dependent on clathrin-mediated endocytosis and acidification in endosomes. Journal of Virology **80**:7500-9.
198. **Stuart AD, Brown TD.** 2007. Alpha2,6-linked sialic acid acts as a receptor for Feline calicivirus. Journal of General Virology **88**:177-86.
199. **Tan M, Hegde RS, Jiang X.** 2004. The P domain of norovirus capsid protein forms dimer and binds to histo-blood group antigen receptors. Journal of Virology **78**:6233-42.
200. **Tan M, Jiang X.** 2005. Norovirus and its histo-blood group antigen receptors: an answer to a historical puzzle. Trends Microbiol **13**:285-93.
201. **Tan M, Jiang X.** 2014. Histo-blood group antigens: a common niche for norovirus and rotavirus. Expert Reviews in Molecular Medicine **16**:e5.
202. **Taniguchi K, Urasawa S, Urasawa T.** 1981. Further studies of 35-40-nm virus-like particles associated with outbreaks of acute gastroenteritis. Journal of Medical Microbiology **14**:107-118.

203. **Taube S, Perry JW, McGreevy E, Yetming K, Perkins C, Henderson K, Wobus CE. 2012.** Murine noroviruses bind glycolipid and glycoprotein attachment receptors in a strain-dependent manner. Journal of Virology **86**:5584-93.
204. **Taylor KA, Glaeser RM**. 1974. Electron diffraction of frozen, hydrated protein crystals. Science 186:1036-1037.
205. **Teunis PF, Moe CL, Liu P, Miller SE, Lindesmith L, Baric RS, Le Pendu J, Calderon RL.** 2008. Norwalk virus: how infectious is it? J Med Virol **80**:1468-76.
206. **Thackray LB, Wobus CE, Chachu KA, Liu B, Alegre ER, Henderson KS, Kelley ST, Virgin HWt.** 2007. Murine noroviruses comprising a single genogroup exhibit biological diversity despite limited sequence divergence. Journal of Virology **81**:10460-73.
207. **Thorne LG, Goodfellow IG. 2014**. Norovirus gene expression and replication. Journal of General Virology **95**:278-291.
208. **Treanor JJ, Atmar RL, Frey SE, Gormley R, Chen WH, Ferreira J, Goodwin R, Borkowski A, Clemens R, Mendelman PM.** 2014. A novel intramuscular bivalent norovirus virus-like particle vaccine candidate--reactogenicity, safety, and immunogenicity in a phase 1 trial in healthy adults. The Journal of Infectious Diseases **210**:1763-71.
209. **Tu Z, Chen Q, Li Y, Xiong Y, Xu Y, Hu N, Tao Y.** 2016. Identification and characterization of species-specific nanobodies for the detection of Listeria monocytogenes in milk. Analytical Biochemistry **493**:1-7.
210. **Unger M, Eichhoff AM, Schumacher L, Strysio M, Menzel S, Schwan C, Alzogaray V, Zylberman V, Seman M, Brandner J, Rohde H, Zhu K, Haag F, Mittrücker H-W, Goldbaum F, Aktories K, Koch-Nolte F.** 2015. Selection of nanobodies that block the enzymatic and cytotoxic activities of the binary Clostridium difficile toxin CDT. Scientific reports **5**:7850-7850.
211. **Urashima T, Asakuma S, Leo F, Fukuda K, Messer M, Oftedal OT.** 2012. The predominance of type I oligosaccharides is a feature specific to human breast milk. Advances in nutrition **3**:473S-82S.
212. **van der Linden RHJ, Frenken LGJ, de Geus B, Harmsen mM, Ruuls RC, Stok W, de Ron L, Wilson S, Davis P, Verrips CT.** 1999. Comparison of physical chemical properties of llama VHH antibody fragments and mouse monoclonal antibodies. Biochimica et Biophysica Acta (BBA) - Protein Structure and Molecular Enzymology **1431**:37-46.
213. **Vanlandschoot P, Stortelers C, Beirnaert E, Ibanez LI, Schepens B, Depla E, Saelens X**. 2011. Nanobodies(R): new ammunition to battle viruses. Antiviral Research **92**:389-407.
214. **Vega CG, Bok M, Vlasova AN, Chattha KS, Gomez-Sebastian S, Nunez C, Alvarado C, Lasa R, Escribano JM, Garaicoechea LL, Fernandez F, Bok K, Wigdorovitz A, Saif LJ, Parreno V**. 2013. Recombinant monovalent llama-derived antibody fragments (VHH) to rotavirus VP6 protect neonatal gnotobiotic piglets against human rotavirus-induced diarrhea. PLoS Pathogens **9**:e1003334.
215. **Verhoef L, Depoortere E, Boxman I, Duizer E, van Duynhoven Y, Harris J, Johnsen C, Kroneman A, Le Guyader S, Lim W, Maunula L, Meldal H, Ratcliff R, Reuter G, Schreier E, Siebenga J, Vainio K, Varela C, Vennema H, Koopmans M**. 2008. Emergence of new norovirus variants on spring cruise ships and prediction of winter epidemics. Emerging Infectious Diseases **14**:238-43.
216. **Vinje J. 2015.** Advances in laboratory methods for detection and typing of norovirus. Journal of Clinical Microbiology **53**:373-81.

217. **Vinjé J, Estes MK, Esteves P, Green KY, Katayama K, Knowles NJ, L'Homme Y, Martella V, Vennema H, White PA, Consortium IR**. 2019. ICTV Virus Taxonomy Profile: Caliciviridae. Journal of General Virology **100**:1469-1470.
218. **Vongpunsawad S, Venkataram Prasad BV, Estes MK.** 2013. Norwalk Virus minor Capsid Protein VP2 Associates within the VP1 Shell Domain. Journal of Virology **87**:4818-25.
219. **Ward JM, Wobus CE, Thackray LB, Erexson CR, Faucette LJ, Belliot G, Barron EL, Sosnovtsev SV, Green KY.** 2006. Pathology of Immunodeficient Mice With Naturally Occurring Murine Norovirus Infection. Toxicologic Pathology **34**:708-715.
220. **Weichert S, Koromyslova A, Singh BK, Hansman S, Jennewein S, Schroten H, Hansman GS.** 2016. Structural Basis for Norovirus Inhibition by Human Milk Oligosaccharides. Journal of Virology **90**:4843-8.
221. **White LJ, Ball JM, Hardy ME, Tanaka TN, Kitamoto N, Estes MK.** 1996. Attachment and entry of recombinant Norwalk virus capsids to cultured human and animal cell lines. Journal of Virology **70**:6589-97.
222. **White LJ, Hardy ME, Estes MK.** 1997. Biochemical characterization of a smaller form of recombinant Norwalk virus capsids assembled in insect cells. Journal of Virology **71**:8066-72.
223. **Wobus CE, Karst SM, Thackray LB, Chang KO, Sosnovtsev SV, Belliot G, Krug A, Mackenzie JM, Green KY, Virgin HW.** 2004. Replication of Norovirus in cell culture reveals a tropism for dendritic cells and macrophages. PLoS Biology **2**:e432.
224. **Wobus CE, Thackray LB, Virgin HWt.** 2006. Murine norovirus: a model system to study norovirus biology and pathogenesis. Journal of Virology **80**:5104-12.
225. **Wobus CE, Karst SM, Thackray LB, Chang KO, Sosnovtsev SV, Belliot G, et al.** . 2004. Replication of Norovirus in cell culture reveals a tropism for dendritic cells and macrophages. PLoS Biology **2**:e432
226. **Wobus CE, Thackray LB, Virgin HW**. 2006. Murine norovirus: a model system to study norovirus biology and pathogenesis. Journal of Virology **80**:5104-5112.
227. **Wu S, Tao N, German JB, Grimm R, Lebrilla CB.** 2010. Development of an annotated library of neutral human milk oligosaccharides. Journal of proteome research **9**:4138-4151.
228. **Wu S, Grimm R, German JB, Lebrilla CB.** 2011. Annotation and structural analysis of sialylated human milk oligosaccharides. Journal of proteome research **10**:856-868.
229. **WuDunn D, Spear PG.** 1989. Initial interaction of herpes simplex virus with cells is binding to heparan sulfate. Journal of Virology **63**:52-58.
230. **Wyatt RG, Dolin R, Blacklow NR, DuPont HL, Buscho RF, Thornhill TS, Kapikian AZ, Chanock RM.** 1974. Comparison of Three Agents of Acute Infectious Nonbacterial Gastroenteritis by Cross-Challenge in Volunteers. The Journal of Infectious Diseases **129**:709-714.
231. **Yamauchi Y, Helenius A.** 2013. Virus entry at a glance. Journal of Cell Science **126**:1289.
232. **Yang M, Lee G, Si J, Lee SJ, You HJ, Ko G.** 2016. Curcumin Shows Antiviral Properties against Norovirus. Molecules 21:1401
233. **Zhang XF, Tan M, Chhabra M, Dai YC, Meller J, Jiang X**. 2013. Inhibition of histo-blood group antigen binding as a novel strategy to block norovirus infections. PLoS One **8**:e69379.
234. **Zheng Q, Jiang J, He M, Zheng Z, Yu H, Li T, Xue W, Tang Z, Ying D, Li Z, Song S, Liu X, Wang K, Zhang Z, Wang D, Wang Y, Yan X, Zhao Q, Zhang J, Gu Y, Li S, Xia N**. 2019. Viral neutralization by antibody-imposed physical disruption. Proceedings of the National Academy of Sciences **116**:26933.

Acknowledgements

This work would not have been possible without the help of a lot of people. My gratitude goes to…

…My supervisor

Dr. Grant Hansman. Thank you for giving me the chance to do my PhD in your lab. Even though the cryo-EM part was not always easy to set up, you always provided me with whatever I needed to get it running– from getting me a workstation to sending me to India and Glasgow to learn more about the methods. Thank you so much for giving me all this opportunities.

…My Referees

Prof. Dr. Dr. Delecluse, for agreeing to be my first advisor and helpful discussions in the TAC meetings.

Prof. Dr. Ralf Bartenschlager, for agreeing to be my thesis chair.

Dr. Petr Chlanda, for saying yes to be my committee member on short notice. And of course also for all the help at the microscope and providing me with grid boxes.

Dr. Erec Stebbins for support and advice during the TAC meetings.

…All my past and present lab members

Kerstin Ruoff – You were my longest lab companion. We made it together :) Thanks for all the discussions and help with everything and your willingness to always discuss new possibilities or ideas.

Alessa Ringel – even though you left way too soon, you will always be my favorite "lab-wife".

Dr. Anna Koromyslova – Thank you for all your help with everything – from telling us how everything works to where all the stuff is located – Without you we would have been so clueless in the beginning (and not only then :D).

Dr. Turgay Kilic – For the beautiful X-ray structures that completed my (not so high resolution) cryo-EM.

Virginie Malak – Thank you for keeping everything in order and having our backs with all the paperwork and lab stuff. I think we did not fully understand what you did for us until you were gone – and then we appreciated it even more.

Satoko Hansman – for caring beautifully for the insect cells and providing me with cells whenever I needed them.

Benedikt Wimmer – Thank you for setting up the workstation and all the programs. Otherwise, I would probably still be stuck at trying to compile Relion.

Dr. Charles Sabin – Thank you for being my cryo-EM companion, and also providing nice X-ray crystal structures that I needed to help make sense of my data. And thanks for all the delicious cakes and pastries.
Dr. Jennifer Lun – Your always-positive attitude really impressed me. Thank you for making the last year in the lab a really fun one. Also, I think it is great you are willing to try out everything – from Wasen to carnival or even Tatort :D
Angelika Schmidt-Zitouni – even though officially you are not part of our lab, you are definitely honorary F150 member. Thank you for all your administrative wizardry that made impossible admin tasks suddenly possible.

…Collaborators and supporters
Dr. Götz Hofhaus – Thanks for showing me everything I needed to know to work with the Krios, from sample prep to data collection and trying to get jobs to run on the cluster. And of course thanks for all the fast help, whenever the Krios decided to be a diva again.
Also thanks to all other people from the cryo-EM community in Heidelberg, who were always happy to help and provide tips and guidance.
Dr. David Bhella – Thank you for making me believe that the T=4 capsid was actually not a processing error. And of course for giving me the opportunity to stay in your lab to learn, and the super fast emails, whenever I had processing issues.
Dr. Karsten Richter and Dr. Michelle Nüssling, for their introduction and assistance in EM.
Dr. Stefan Pusch, for providing me with plasmids and cells for the mammalian expression system.

…All the rest:
My friends –that made that time such a memorable one. Thanks for all the wine and cheese, the happy hours, botanik-evenings, and cooking sessions, and all the other stuff that sometimes also did not include food or drinks :P
Nick –Thank you for all the chocolate whenever I had a bad day, and everything else I needed to get here. And thanks for coming to Australia with me and turning a work trip into one of the greatest road trips – even with our gravel road adventures. Also thanks for proofreading and helping me make these beautiful heatmaps.
My family – I am very grateful I have a family that actually understands (mostly) what I do :D Without you, I would not have made it so far (literally, because I would never have sent that second email without your encouragement). And of course, Pascal, thanks for all the lab tips and protocols and the (slow but thorough :P) proofreading; and for being willing to travel here from Boston, just to ask stupid questions at my defense ;)